Signatures of present and past melt distribution at fast and intermediate spreading centers

Milena Marjanović

Submitted in partial fulfillment of the
requirements for the degree of
Doctor of Philosophy
in the Graduate School of Arts and Sciences

COLUMBIA UNIVERSITY

2013

ABSTRACT

Signatures of present and past melt distribution at fast and intermediate spreading centers

Milena Marjanović

The work presented in this dissertation depicts past and present signatures of melt distribution at fast and intermediate spreading centers. The primary goal of the studies included in this thesis is to provide better understanding of melt distribution and variation in melt physical properties within and at the base of oceanic crust formed at these spreading centers. Furthermore, this work examines effects that melt presence might have on formation and structural characteristics of oceanic crust. To explore the above we use geophysical data collected during two expeditions conducted along the Juan de Fuca Ridge (intermediate) and the East Pacific Rise (fast).

The major part of the thesis is based on the work conducted on high resolution reflection seismic data that investigate present day intracrustal melt distribution along the East Pacific Rise (EPR) axis extending between 8º20’ and 10º10’N. Here, the character of the melt reservoir is examined from different aspects and by using different seismic data analysis methods. By systematic analysis of the seismic reflection data, we show that the axial melt lens (AML) is segmented at different segment scales. Locations of the mapped disruptions in the AML correspond to previously identified tectonic discontinuities well expressed in the seafloor bathymetry. The above result corroborates genetic relationship between tectonic and magmatic segmentation. To examine melt distribution along the EPR, here for the first time we use

amplitude variation with angle of incidence (AVA) crossplotting technique that was developed by oil and gas industry experts to look for presence of hydrocarbons. Further data examination for the first time for the mid-ocean ridges show presence of deeper lenses (lenses that are present below the AML). Presence of gaps in these sub-events and their collocation with what is believed to be the location of origin of the last documented eruption occurred in 2005-06, may shed light on the mechanisms behind the mid-ocean ridges volcanic processes.

To explore variation in crustal structure and melt distribution at present day along the Juan de Fuca Ridge and relicts of past melt presence near ridge propagators wakes, a combination of gravity and multi-channel seismic data was used. Gravity modeling, constrained by seismic data, showed that robust topography (shallow axial depth and wide axial high) and thicker crust observed for the southern portion of this ridge system originate from enhanced melt supply at the base of the crust. In addition, prominent crustal thickening on the younger crust side of the inner propagators wakes (now on the ridge flanks) is brought into relationship with collocated frozen magma lenses imaged at the base of the crust. Spatial relationship of the two argues for their causal relationship at the time of the crustal formation on the axis. Our study suggests that these frozen lenses represent the record of once molten reservoir that most probably actively participated in the formation of the thicker crust.

TABLE OF CONTENTS

* This chapter has 15 figures.

ACKNOWLEDGEMENTS

Completing a PhD is truly a marathon event, which instead of kilometers as a unit of distance counts in years. As in each sport discipline the results of PhD work is not reflecting only efforts and hard work of one individual, but the work of entire team that needs to be acknowledged.

Foremost, I would like to thank my advisory committee Spahr Webb, Mladen Nedimović and John Mutter and especially to my primary research advisor Suzanne Carbotte, who guided me and transferred to me the passion for mid-ocean ridges. Also, I am extremely grateful to my advisors for the opportunities to participate in expeditions at the East Pacific Rise, Juan de Fuca and Valu Fa Ridge. I would also like to show my gratitude to Roger Buck and Paul Olsen for serving on my examination committee and everyone else at Lamont-Doherty Earth Observatory, in particular: Helene Carton, Bill Ryan, Walter Pittman, John Diebold, Donna Shillington, Peter de Menocal, Bill Menke, Maya Tolstoy, Peter Kelemen, Tim Crone, Collin Stark, Mark Anders, Mia Leo, Sally Odland, Regina Giacinto, Missy Pinkert, Carol Mountain, Rob Kakascik, Bob Arko, Doug Shearer, David Lentrichia, Rose Anne Weissel, Kori Newman, Chadwick Holmes, Robert Bialas, Martin Collier, Byrdie Renik, Adrienne Block, Ivan Mihajlov and Shuoshuo Han. I would also like to thank Juan Pablo Canales at Woods Hole Oceanographic Institution.

Over the years, I enjoyed the aid of Columbia Fellowship and SEG awards, which have supported my work. I also had a chance to do internships with two leading oil-industry companies ExxonMobil and ConocoPhillips to which teams I worked with I owe sincere and earnest thankfulness. I am especially obliged to Douglas Foster and Jeff Malloy from ConocoPhillips. I am also grateful to Paradigm's and Landmark's support team.

Finally, I would like to thank my friends, and most of all I would like to thank my family

for supporting me and for putting up with my stress while I struggled to complete this dissertation.

"There is something within me that might be illusion as it is often case with young delighted people, but if I would be fortunate to achieve some of my ideals, it would be on the behalf of the whole of humanity. If those hopes would become fulfilled, the most exciting thought would be that it is a deed of a Serbian"

Nikola Tesla
Belgrade, 1892

PREFACE

Mid-ocean ridges are places on Earth where two plates are separating and where new oceanic crust has been forming. Sometimes they are also described as the longest continuous mountain chain (~70,000 km long) that wraps around the Globe. However, extensive mapping of the seafloor showed that the mid-ocean ridge mountain chain is not continuous, but rather segmented into hierarchically different segment scales [*Whitehead et al.*, 1984; *Schouten et al.,* 1987; *Macdonald et al.,* 1988]. The segmentation and standing out topography of the ridge crest are reflecting processes that operate below the seafloor. Our knowledge about these processes and their mechanism is limited because of inaccessibility to direct observation and challenges associated with drilling and sampling of the sub-seafloor. To explore and better understand these processes marine geophysicists use different methods (seismic reflection and refraction, tomography, gravity, magnetic, etc.).

During the past four decades, active source reflection seismology, supported by complementary field studies in ophiolites (obducted oceanic crust) and other geophysical studies, has provided us with important information on crustal structure formed at different spreading centers, and suggested different mechanisms to explain oceanic crust formation. Results from these studies indicate that the top-most part of the crust is composed of relatively thin layer of basalts (~ seismic layer 2a), below which a layer of vertically intruded dikes is present (~ seismic layer 2b); these layers are underlain by a relatively thick gabbroic complex (~ seismic layer 3). The above crustal layers (basalts, dikes and gabbro) overlay peridotites, rocks that make the uppermost mantle and separated from the crustal rocks by Mohorovičić (Moho) discontinuity. At fast (> 60 mm/a half rate) to intermediate (> 25-60 mm/a half rate) spreading centers, layers 2b

and 3 at the ridge axis are separated by a narrow (200-4000 m) [*Kent et al.,* 1993] and thin (16-82 m) [*Hussenoeder et al.,* 1996; *Canales et al.,* 2006; *Singh et al.,* 1998; *Xu,* 2012] intracrustal axial melt lens (AML).

Since the AML discovery, it has been hypothesized that the crystallization of melt within it is responsible for formation of the most of oceanic crust. While there is a consensus on how the upper crust (above the AML) is formed, the mechanism behind the formation of the lower crust is still debated. Currently, the debate is centered on two end-member models: gabbro-glacier [e.g. *Nicolas et al.,* 1988; *Quick and Denlinger,* 1993; *Henstock et al.,* 1993] and sheeted sill model [*Boudier et al.,* 1996; *Kelemen et al.,* 1997]. To reconcile the two end-member models with observations from ophiolites and ridge seismic structure, intermediate (or combined) models have been suggested [e.g. *Natland and Dick,* 2009]. Regardless of mechanism behind crustal formation, different seismic studies on limited examples indicated that changes in the physical properties and reflectivity of the AML [e.g. *Mutter et al.,* 1988; *Kent et al.,* 1993; *Babcock et al.,* 1998; *Carbotte et al.,* 2000] are collocated with the tectonic discontinuities observed at the seafloor. These discoveries lead scientists to speculate that there is a strong genetic relationship between tectonic discontinuities expressed in morphology of the ridge axis and available melt beneath the seafloor.

Due to the important role that the AML has in processes of crustal formation, and morpho-tectonic segmentation, different studies over the past two decades have been focused on determining the available amount of melt within it [*Hussenoeder et al.,* 1996; *Collier and Singh* 1997; *Singh et al.,* 1998; *Canales et al.,* 2006; *Xu,* 2010]. Some of the above studies were regional and qualitative and the others were more quantitative, but investigated crustal structure at only a small number of single point locations (i.e., mostly in 1D). These studies cast some

light onto the melt distribution within the intracrustal reservoir and have motivated application of novel methods for melt determination.

In addition to the well-imaged axial zones, a limited number of studies have explored the oceanic lithosphere beneath the ridge flanks that have been keeping partial records of the conditions and melt distribution that existed at ridge crest at the time when the nowadays flank's crust had been formed. One of the examples for this "record-reading" comes from the flanks of Juan de Fuca Ridge. There, Nedimović et al. [2005] discovered presence of frozen melt lenses at the base of the crust (below the Moho discontinuity), ~ 30-100 km away from the ridge axis center. These lenses represent a signature of once molten reservoirs that in the past were sitting at the base of the crust at the tip of a propagating ridge segment.

To different extents this thesis is focused on addressing aspects of all of the above topics related to past and present melt distribution beneath mid-ocean ridges and magmatic processes of crustal formation. In addition, new observations and novel techniques presented in this thesis add more constraints on volcanic eruption processes and volcanic and hydrothermal system segmentation. The work to be described in the following chapters is conducted on geophysical datasets collected during two scientific cruises (MGL0812 and EW0207) sampling two ridge systems: intermediate – the Juan de Fuca Ridge and fast – the East Pacific Rise between 8º20' and 10º10'N. Both regions were extensively sampled and investigated during past decades, as both ridges were locus of focused Ridge Interdisciplinary Global Experiments (RIDGE) Initiative 2000. Combined discoveries from different studies added valuable constrains and allow the results obtained from this thesis to be placed in a broader context.

Chapter 1 "Melt segmentation along the East Pacific Rise (EPR) from 8º20' to 10º10'N at third-order segment scale and its geological implications" uses high-resolution multichannel

seismic dataset collected along multiple ridge-parallel lines, sampling ~ zero age crust formed along the ridge crest of the EPR between 8º20' and 10º10'N. The seismic images obtained from these along axis lines shows presence of prominent seafloor, layer 2a and axial magma lens (AML) events along most of this EPR segment length and presence of weak Moho between 9º10' and 9º30'N. In this study, we examine changes in the geometry, depth, and continuity of the AML reflector. The results show that magmatic system is segmented at all different segment scales and corroborate genetic relationship between tectonic and magmatic segmentation. Furthermore, for the identified higher order tectono-magmatic segments the correlation between depth of the magma sill and seafloor depth is examined. The results show that AML segments delimited by third-order interruptions sit at similar depth below the seafloor, characteristic that is not observed at other segment scales. Interestingly, for the layer 2a and Moho events, segmentation is also observed at the third-order segment scale. The above results, along with observations from other studies [e.g. *Whitehead et al.,* 1984; *Toomey et al.*, 2007], argue that the third-order discontinuities are rooted at the base of the crust or even deeper in the upper mantle and dissect oceanic crust vertically, forming crustal segments with characteristic physical properties. The latter confirms previously suggested view that the third-order segments are the predominant volcanic segments along the fast mid-ocean ridges.

This chapter is intended for submission to Journal of Geophysical Research.

Chapter 2 "Distribution of melt along the East Pacific Rise 9º30' – 10ºN from an amplitude variation with angle of incidence (AVA) technique" uses the axis centered seismic lines from the 2008 multichannel seismic survey to examine melt to mush variations along the EPR. Locally within this region, seismic data organized in common-reflection point gathers show decrease in the amplitude of the P-wave reflection signal off magma sill as a function of

angle of incidence, which implies that within these regions the sill may contain molten material. In oil and gas exploration, techniques known as amplitude variation with angle of incidence (AVA) analysis have been developed to derive reservoir properties from reflection amplitude behavior. One such method, developed recently, uses intercept or A (derived from near-angle of incidence amplitudes), vs. slope or B (derived from mid-angle of incidence amplitudes) as crossplotted seismic attributes to infer reservoir properties. Here, for the first time, this approach is adapted and applied to a reflection signal off a molten rock reservoir to infer variations in melt content within the AML. The AVA behavior suggests the presence of melt within five lens segments (each 5 to 10 km in length) between ~ 9º38' and 9º40'N and ~ 9º42.3'N and 9º56.2'N. Drainage of these lens segments related to the 2005-06 eruption appears to be limited to two narrow areas (~ 600 m in length) centered at 9º50.6' and 9º45.7'N. The AVA crossplotting method tested here thus is found to be a very promising tool for the study of mid-ocean ridge magma systems.

This chapter is in preparation for submission to Geophysical Journal International.

Chapter 3 "Seismic images of magma sills beneath the axial melt lens along the East Pacific Rise 9º20-50'N", presents evidence for presence of multiple melt lenses sitting below the AML (i.e. sub-AML or SAML) north of 9º20'N. First, a careful analysis of the nature of the SAML reflectors is conducted. All possibilities for these events (converted phase, presence of intrabed multiples, side scattering etc.) other than real reflections off the top of sub-axial sills are considered unlikely. Second step included the examination of internal AML characteristics (i.e. presence of melt). By comparison with the character of the AML reflector, these SAML events in some portions are most probably characterized by a low crystalline component, and may be contributing to active crustal accretion. Finally, from the interruption in their extent that spatially

agrees with the drained AML regions identified in Chapter 2, it is suggested that these SAMLs may have had an important role in the 2005-06 volcanic eruption.

This chapter is in preparation for submission to Science.

Chapter 4 “Gravity and seismic study of crustal structure along the Juan de Fuca Ridge axis and across the pseudofaults on the ridge flanks” uses gravity data co-registered with multichannel seismic data from the Juan de Fuca Ridge axis and flanks in order to better understand the origin of crustal structure variations in this area and relate it to present and past distribution of melt within the area. The study shows that thicker crust along the northern and southernmost segments inferred from seismic data alone cannot account for the differences in axial gravity anomalies. Additional low densities/elevated temperatures within and/or below the axial crust are required to explain the remaining axial gravity low at all segments. For pseudofault zones present on the flanks, gravity models suggest the presence of thinner and denser crust within the pseudofault zones, while on the young crust side they indicate presence of a thicker crust. Reflection events interpreted as sub-crustal frozen sills, underlie the zones of thicker crust and are the presumed source for higher densities within the pseudofaults.

This chapter is published in Geochemistry, Geophysics, Geosystems.

Chapter 1

"Melt segmentation along the East Pacific Rise from 8º20' to 10º10' N at third-order segment scale and its geological implications"*

* This manuscript is in preparation for submission to Journal of Geophysical Research with co-authors: Carbotte S.M., H.D. Carton, J. C. Mutter, M. R. Nedimović and J. P. Canales.

ABSTRACT

Multi-channel seismic data acquired along the East Pacific Rise (EPR) extending between 8º20’ and 10º10’N are used to examine variations in geometry, depth, and continuity of axial melt lens (AML) reflector. Axis-centered seismic lines, spanning the entire length of the EPR segment were processed in 2D; for the region north of 9º20’N where two or more ridge parallel seismic lines were acquired data were also processed in 3D. Seafloor, layer 2a and axial magma lens (AML) horizons are imaged and digitized from thus processed seismic sections. Within the region extending between 9º10’ and 9º30’N, a weak Moho reflection event is observed. Visual inspection of the AML reflector and its calculated instantaneous phase seismic attribute (both on 2D lines and 3D) show that this event is disrupted. Moreover, from the along axis 3D dataset it is evident that the AML interruptions are also persistent across the axis, and in some cases extend obliquely to the ridge axis orientation. The most of twenty-six thus mapped interruptions in AML are collocated with previously identified higher (third and fourth) order discontinuities in bathymetry, which corroborate genetic relationship between magmatic and tectonic segmentation. Systematically mapped AML interruptions enable further examination of relationship between AML depth and seafloor depth at all segment scales. The results show that these two variables are mainly uncorrelated. However, for third-order segments prominent clustering of the AML picks around characteristic depth below seafloor for each segment is observed, which suggests that each third-segment behaves as a separate magmatic unit. In addition, presence of disruptions in layer 2a event and Moho reflector (where imaged) appear to be collocated with the limits (i.e. third-order discontinuities) of these magmatic units. The latter

argues that the third-order discontinuities along the ridge axis vertically partition entire oceanic crust. In addition, their spatial correlation with the melt distribution at the base of the crust deducted from an earlier collocated tomography study suggests that processes originating from the uppermost mantle may govern third-order segmentation of the AMLs. Differences in AML depth among third-order segments could reflect long-term differences in melt flux from the base of the crust, with each segment out of phase such that temporal cycle is held constant. Alternatively, integrated magma flux may be the same for each segment on long-time scale, but it may vary on short time-scales with variations being out of phase.

1. Introduction

Mid-ocean ridges are segmented on a range of scales by offsets of the axial zone. Segmentation is observed across different spreading rates and expressed by four hierarchical segmentation orders, each with particular structural characteristics [*Schouten et al.,* 1985; 1987; *Langmuir et al.,* 1986; *Macdonald et al.,* 1988; 1991]. First-order segmentation at fast spreading centers is defined by major transform faults with offsets > 30 km that partition the ridge axis at 600±300 km length intervals [*Schouten et al.,* 1987; *Macdonald et al.,* 1988]. First-order segments can be subdivided into smaller second-order segments present at 140±90 km length intervals, separated by non-transform offsets including overlapping spreading centers (OSC) where two offset (offset zone < 30 km) ridge segments overlap each other [e.g. *Lonsdale*, 1983]. At shorter length scales (50±30 km), a third-order segmentation of the ridge axis is defined by smaller offset (0.5-2 km) OSCs or changes in the ridge axis azimuth [*Schouten et al.,* 1985; *Macdonald et al.,* 1988; 1991]. The finest, fourth-order scale segmentation is present at length intervals of 14±8 km and is expressed by small bends, or steps in the axial fissure zone (in literature also known as DevALs – deviations from axial linearity, *Langmuir et al.,* [1986]).

Along with this morpho-tectonic segmentation, studies of seafloor lavas along the ridge axis show changes in lava chemistry some of which coincide with small tectonic discontinuities indicating that the magmatic system beneath the ridge axis is also segmented [*Langmuir et al.,* 1986]. Along-axis variations in other ridge properties including seafloor depth, cross-sectional area, and gravity are observed with narrowing and deepening of the seafloor, and increase in mantle Bouguer anomalies towards tectonic discontinuities [e.g. *Scheirer and Macdonald,* 1993*;*

Wang and Cochran, 1993; *Cormier et al.,* 1995*; Toomey and Hooft,* 2008]. These observations led to a hypothesis that the along-axis variations arise from focused mantle melt delivery and along-axis redistribution of melt within each segment (e.g 3D diapiric flow within the mantle for largest scales of segmentation and 3D focusing within the crust for the smallest) [e.g. *Whitehead et al.,* 1984; *Schouten et al.,* 1985; *Macdonald et al.,* 1988*; Bell and Buck*, 1992; *Wang et al.,* 1996]. An alternate model is that there are multiple sites of magma injection from the mantle beneath segments [*Whitehead et al.,* 1984; *Langmuir et al.,* 1986]. In both models, magma supply is enhanced beneath segment centers and reduced near the edges [*Whitehead et al.,* 1984; *Macdonald et al.,* 1988]. Distinguishing between these magma supply models has been a subject of numerous studies over the past two decades and remains the topic of ongoing debate.

Seismic techniques enable detection of melt presence in the oceanic crust and mantle and have been widely used to study the present day magmatic system along mid-ocean ridges as well as time-averaged magma supply via indirect proxy of crustal thickness [e.g. *Detrick et al.,* 1987; 1993*; Barth and Mutter,* 1996*; Dunn et al.,* 2000*; Canales et al.,* 2002*; Carbotte et al.,* 2006*; Singh et al.,* 2006*; Toomey et al.,* 2007]. At fast spreading centers multi-channel seismic (MSC) reflection studies show that melt ponds within a relatively narrow and thin intracrustal axial-magma lens (AML)[†] [e.g. *Kent et al.,* 1993a; *Kent et al.,* 1994; *Mutter et al.,* 1995; *Hooft et al.,* 1997; *Babcock et al.,* 1998; *Carbotte et al.,* 2000]. In early studies, this lens was believed to extend continuously between two second-order discontinuities [*Detrick et al.,* 1987] arguing against previously postulated finer-scale segmentation of the magmatic system. However,

[†] Within the mid-ocean community this intracrustal sill imaged in seismic profiles is also called axial magma chamber or AMC. Since geological term "chamber" invokes a large magma body, whereas it has been shown to be a thin narrow, body, here we prefer to use term "lens" (as in e.g. *Nicolas and Boudier*, [2011]).

detailed analysis of MCS data spanning various latitudinal extents and spreading rates along the Southern (between ~13º and 21º S) and Northern (between 9º and 17ºN) East Pacific Rise (EPR), showed presence of AML interruptions [*Babcock et al.,* 1998; *Carbotte et al.,* 2000] and changes in width [*Mutter et al.,* 1988; *Kent et al.,* 1993a], some of which were spatially correlated with previously identified tectonic discontinuities. These findings provided evidence for a relationship between the segmentation of the ridge axis expressed in bathymetry and segmentation of the magma lens present at around 1-2 km below the seafloor. Also noted, was an apparent positive correlation between seafloor depth and depth of the magma lens beneath it and this relationship was proposed as an indicator of magmatic budget [*Scheirer and Macdonald*, 1993]. However, it has to be emphasized that the interpretations in prior reflection studies were based on sparse data coverage and poor navigation. In addition to the mid-crustal magmatic system, seismic tomography [*Dunn et al.,* 2000; *Toomey et al.,* 2007] and seafloor compliance studies [*Crawford et al.*, 1999], showed presence of another, larger magma body (~ 10 km wide and axis centered) at the base of the crust. It has been suggested that this body is also articulated at similar segment scales as seafloor bathymetry [*Dunn et al.*, 2000; *Toomey et al.,* 2007].

At the East Pacific Rise extending between 8º20’ to 10º10’N, early bathymetry data revealed presence of an OSC at 9º03’N as well as a number of third-order discontinuities [*Macdonald et al.,* 1984; 1988] (Figure 1). From side-scan sonar data, a series of smaller-scale fourth-order discontinuities were identified north of 9°10’N [*Haymon et al.,* 1991; *Macdonald et al.,* 1992]. More recently, high-resolution bathymetry permitted detailed mapping of these fine-scale offsets along the entire ridge axis north of the Siqueiros Transform Fault [*White et al.,* 2006; *Carbotte et al.,* submitted]. In 2008 MCS datasets were collected with the primary goal of 3D imaging the EPR from 9°38’ to 9º58’N [*Mutter et al.,* 2010]. One part of the MCS study,

was dedicated to crustal structure imaging along the entire (~ 220 km long) first-order EPR segment (Figure 2). Thus collected seismic dataset offers an excellent opportunity to examine structural variations in the intracrustal AML at all previously defined tectonic segment scales. In the seismic data, these variations are represented by steps in the depth of the AML reflector and/or presence of reflector complexities that we interpret as potential physical interruptions and evidence for existence of discrete magma lenses. Their spatial distribution beneath the modern ridge axis is well correlated with identified segment boundaries in bathymetry. Our results show presence of consistent tectonic-magmatic relationship previously inferred from limited examples in MCS data examined along fast spreading ridges [*Kent et al.,* 1993a; *Babcock et al.,* 1998; *Carbotte et al.*, 2000]. Furthermore, for the first time, we investigate relationship between seafloor and AML depth at different scales of segmentation to test the central magma supply model. Here, we find positive correlation between the two variables to exist only for the northern second-order segment (north of the OSC 9º03'N), whereas for the rest of the segments no correlation (i.e. high scattering) is observed. We also show that, when seafloor-AML data are grouped into third-order segments it becomes evident that magmatic lenses delimited by third-order discontinuities are sitting at characteristic depth beneath the seafloor. Moreover, from vertical alignment of the edges of the third-order tectono-magmatic segments with low velocity regions imaged at the base of the crust [*Toomey et al.,* 2007], we suggest that the third-order segment compartments extend from the seafloor all the way to the uppermost mantle. We speculate that each low velocity zone revealed in tomography represents an individual melt source at the base of the crust that feeds a group of fourth-order intracrustal lenses encompassed by third-order discontinuities.

2. Tectonic setting and prior studies of the axial magmatic system along the EPR 8°20-10º10'N

The EPR extending between the Clipperton and Siquieros Transform Faults (TF) (Figure 1) is one of the most extensively studied regions of the global mid-ocean ridge system. At this portion of the mid-ocean ridge an ~ 6 km thick oceanic crust has been forming [*Barth and Mutter,* 1996*; Canales et al.,* 2002] at the average full spreading rate of 108-109 mm/a [*Carbotte and Macdonald,* 1992]. This first-order segment, delimited by two first-order discontinuities, is further divided into two second-order segments by the OSC 9º03'N. Side-scan sonar data and recent high-resolution bathymetric mapping of the seafloor along the entire segment enables identification of finer scale third- and fourth-order discontinuities within the modern ridge axis [*Haymon et al.,* 1991; *Macdonald et al.,* 1991*; White et al.,* 2002*; White et al.,* 2006; *Carbotte et al.,* submitted]. The identified third-order tectonic discontinuities are centered at: 8º38', 8º52', 9º01', 9º12.5', 9º20', 9º37', 9º51.5' and 9º58'N. Many of them are represented by small overlapping offsets in the axial summit trough (AST), and/or a change in the strike of the AST (Figure 1, and Figure 3A and 3B). In addition, twenty fourth-order tectonic discontinuities are identified from changes in AST width, offsets in the AST and/or small changes in the AST azimuth [*Haymon et al.,* 1991; *White et al.,* 2006].

The first extensive multi-channel seismic (MCS) experiment of a fast spreading mid-ocean ridge system was conducted in 1985 and included coverage of the EPR from 8°50' to 10º10' N [*Detrick et al.,* 1987; *Mutter et al.,* 1988; *Vera et al.,* 1990]. A series of cross and along-axis common mid point (CMP) reflection lines were acquired as well as several expanded spread profiles providing information on velocity structure of the crust at different ages. This

experiment resulted in numerous discoveries related to crustal structure. Presence of a prominent change in velocity gradient in the shallow portion of the crust was resolved, marking the boundary between seismic layer 2a and 2b and interpreted to mark transition in properties between extrusive section (pillow basalts or sheeted flows) and sheeted dike complex [*Vera et al.,* 1990; *Harding et al.,* 1993]. Furthermore, abrupt changes in velocity deeper in the crust within the narrow axial zone (at ~ 1.6 km below seafloor) and at the base of the crust outside of the axial zone, resulted in reflections now known to originate off the axial magma lens and Moho discontinuity, respectively [*Kent et al.,* 1990; *Kent et al.,* 1993a; 1993b; *Vera and Diebold*, 1994; *Barth and Mutter,* 1996]. Detailed forward modeling of the expanding spread profile (ESP) acquired along the axis and centered at 9°34'N [ESP5, *Vera et al.,* 1990], showed that the AML reflection imaged in the CMP lines, coincides with an abrupt decrease in compressional velocity Vp (from 4500 to 3000m/s) and shear velocity Vs (from 2900 to 0 m/s), suggesting that the AML seismically behaves as liquid (i.e. molten rock). Forward modeling of near vertical incidence reflections/diffractions from this low velocity zone argued for significant variations in the width of the AML north of the 9°03'N OSC and segmentation of the magma body at several tectonic discontinuities was inferred [*Kent et al.,* 1993a; 1993b]. These results showed that the AML at ~ 9º35'N is a "pinched-out" reflector (200 m wide) marking a transition between narrow sill (700 m) in the north to wide sill (1200 m) in the south. Spatially, this pinch-out correlates well with the 9º37'N tectonic discontinuity. A more prominent change in AML width of 3 km was inferred from two CMP lines crossing the ridge axis at ~ 9º18'N (sill width 4.15 km) and 9º24'N (sill width 1 km) and was attributed to another tectonic discontinuity at ~ 9°17'N [*Kent et al.,* 1993a]. However, the presence of a very wide melt body to the south and near the 9°03'N OSC called into question the hypothesis that reduced magma supply is associated with tectonic

discontinuities [*Macdonald et al.,* 1988]. In addition, thickness of layer 2a as a proxy for robustness of melt-supply failed to agree with predictions of the melt supply model. Assuming that layer 2a corresponds with the pillow basalt layer, thicker layer 2a was expected at segment centers if these were sites of more abundant magmatic activity, but along the EPR the opposite relationship was found [*Harding et al.,* 1993; *Vera and Diebold,* 1994]. While the layer 2a thickens towards the OSC 9º03'N, elsewhere it is quite continuous and uniform at ~ 100-150 m thick, thus, arguing for no connection between tectono-magmatic signatures and extrusive layer character.

Seismic tomography study conducted in the 9º50'N EPR region revealed narrowing of the axial zone of low velocities in the crust and mantle at small discontinuities at ~ 9°35' and 9°28'N [*Dunn and Toomey,* 1997; *Dunn et al.,* 2000]. Furthermore recent UNDERSHOOT experiment revealed segmentation in the mantle low velocity volume (MLVV) beneath the ridge axis with a series of local maxima in mantle velocities that coincide approximately with the third-order tectonic discontinuities in the region [*Toomey et al.,* 2007]. Both of these studies indicate reduced melt volumes or cooler temperatures in the crust and uppermost mantle associated with small tectonic discontinuities.

3. Data and methods

3.1. Seismic experiment and data processing

In summer 2008, the first 3D multichannel, multistreamer seismic survey of the *R/V M. G. Langseth* was conducted at the EPR (Figure 1). Multichannel seismic (MCS) data were acquired using two tuned air-gun arrays fired in flip-flop mode, each composed of two strings of

nine guns, with a total volume 3300 in^3. The source was deployed at 7.5 m below sea surface and shot on distance at an interval of 37.5 m. The signal was recorded using four solid-state 6 km long streamers, each with 468 channels, electrically coupled at 12.5 m (the first channel ~ 200 m from the source). The streamers were deployed at 10 m below sea surface (except for the along axis lines: axis 1, axis 2, axis 3, axis 2r1 for which the receivers were at 7.5 m).

The survey included a primary 3D box (of 94 lines) and a smaller box (14 lines) shot perpendicularly to the ridge axis spanning 15 km on each ridge flank between ~ 9º38' and 9º58'N (Figure 1). Besides the 3D boxes, the survey also included several along axis lines (axis 1, axis 2, axis 2r1, axis 3, axis 3p2 and axis 4) spanning the entire ridge segment from the Clipperton to Siquieros Transform Faults (three closely spaced parallel lines between 10°10' and 9°41'N, two from 9°41' to 9°20'N and one 2-part line from 9°20' to 8°20'N extending over both limbs of the 9º03'N OSC). Each of these sail lines covered a subsurface swath (262.5 m or more, depending on feathering), providing eight parallel CMP lines spaced 37.5 m apart with an in-line CMP spacing of 6.25 m. Throughout the most of the study area the seismic lines closely follow the location and azimuth changes of the modern ridge axis, except for ~ 30 km along the eastern limb of the 9°03'N OSC where the seismic profile is offset up to 1000 m from the modern axial zone. The along axis lines were processed assuming a 2D geometry (using streamer 2 and combining shots from both air-gun arrays) and in 3D with properly defined 3D geometry for the region north of 9°20'N where multiple parallel lines were shot.

The pre-stack processing sequence for the 2D seismic lines includes geometry definition, minimum phase band-pass filter, spherical divergence correction and amplitude balancing, F-k filtering, data editing, resampling to 4 ms (with anti-aliasing filter applied) and mute below the first water multiple (see Table 1 for processing parameters used). The stacking sequence includes

velocity analysis, normal-move out (NMO) and stacking. From velocity analysis for the AML conducted using semblance and examination of constant velocity stacks, we find that the AML throughout the region is well imaged with a stacking velocity of 2500±50 m/s except for the region within the 9º03'N OSC where a higher stacking velocity (2600 m/s) is required. Results from this analysis are used to modify RMS velocities derived from the ESP5 velocity function [*Vera et al.,* 1990] to create a 2D velocity function, which is hung from the seafloor and used for stacking the seafloor, AML and Moho events (hereinafter referred to as the AML section). Optimal stacking velocities for the layer 2a event are determined from evaluation of constant velocity stacks for a range of velocities from 1530 to 1700 m/s and using the mid-offsets of the streamer of 1500-3000 m. Layer 2a is best stacked using velocities of 1580 m/s for the region south of the OSC 9º03'N, and 1560 m/s for north of the OSC. Higher velocities of 1680 m/s are required to stack the event within the OSC region. Section that is stacked with the above velocities is hereinafter referred to as the layer 2a section. The post-stack processing sequence includes 2D Kirchhoff time migration, applied to both sections (the AML and layer 2a) separately. Migration velocities used for the AML sections are 80% of the modified 2D ESP5 function. For migration of the layer 2a sections, water velocity is used that most efficiently collapsed seafloor diffractions. After migrating layer 2a we apply a surgical mute to extract the event and merge it with the AML section to obtain the final seismic image (Figure 2). All the above processing steps are conducted using *Paradigm's* processing suite *Focus*.

To obtain swath coverage of ridge axis in the regions where two or more ridge parallel lines were collected, along-axis seismic data are also processed in 3D. This includes the following lines north of 9º20'N: axis 2r1, axis 3, axis 3p2, and axis 4. The 3D processing sequence is very similar to that used for the 2D profiles, as described above and outlined in Table

1. The main difference is in pre-processing steps for geometry definition. While for 2D processing, it is sufficient to define X and Y coordinates of the first and last CMP along the line, for swath processing, we need to define geometry boxes (i.e. four X and Y coordinate pairs). For the most efficient use of the data (when considering migration aperture), each box needs to be parallel to the orientation of the seismic lines that contribute to the box. For each change in line orientation (of approximately 1º), a separate box must be defined. Also, due to the change in the number of lines acquired along axis, the widths of the boxes (and thus coordinate pairs) have to be changed accordingly. We define three different boxes (details on geometry definition and shot selection are given in Appendix A and B). Flexible binning is another step that is not present for 2D pre-stack processing. Flexible binning re-organizes the data in common mid-point bins of 37.5 m × 6.25 m (instead of into CMPs for 2D lines) in such way that each CMP bin includes 39 traces (see *Yilmaz,* [2001]). The stacking sequence resembles that used for the 2D profiles. For the seafloor and AML events, NMO correction is applied using RMS velocities from the modified ESP5 velocity function used for 2D processing, arranged in 3D space (the velocity function is hung from the bathymetry grid for each box, hereinafter referred to as V3D), and the data are stacked. Post-stack time migration is applied using a migration velocity function that is 80% of V3D. As for the 2D lines we stack and migrate layer 2a separately. Layer 2a within each box is stacked using a constant NMO velocity of 1560 m/s. The post-stack time migration of the layer 2a stack employs migration with water velocity to collapse seafloor diffractions.

3.2. Mapping crustal reflection events

Along each 2D line, major seismic horizons including seafloor, layer 2a, AML and Moho (where present), are digitized using Paradigm's 2D interpretation tool "*Section*" with a picking

gate of 8 ms/m. Digitized picks are filtered using an anti-causal, finite impulse response, zero phase filter, with 150 m (seafloor), 600 m (layer 2a) and 300 m (AML) averaging distance. For each event we pick the first strong prominent phase of the reflection arrival, which corresponds with the first minimum of the minimum phase wavelet (peak of the first white on stacked seismic section shown in Figure 2, Figure 3A, Figure 3B, Figure 4A) for all events except layer 2a. For layer 2a, we pick the first maximum of the wavelet (first black in Figure 2, Figure 3A and Figure 3B). Two-way travel times (twtts) for all events are converted to depth using crustal velocities appropriate for the axial region: water velocity 1500 m/s, layer 2a velocity 2260 m/s [e.g. *Vera et al.,* 1990*; Canales et al.,* 2005], layer 2b velocity 5500 m/s [*Vera et al.,* 1990] (Figure 5). For depth conversion of Moho within the limited region between 9º10' to 9º30'N where it is imaged, we use the same velocity for layer 3 as for layer 2b [*Vera et al.,* 1990] (Figure 4B and Figure 4C).

Uncertainties associated with the identified horizons arise from a number of sources. Small uncertainties of ± 4ms originate from horizon picking using *Paradigm's* guided picking tool. However, larger uncertainties are associated with choice of velocities used for stacking and depth conversion of the interpreted horizons. The velocity function used for the stacking is derived from the ESP5 velocity function for the ridge axis at 9°34'N [*Vera et al.,* 1990] and additional, but not extensive, velocity analysis (semblance and constant velocity stacking). Using a range of stacking velocities for layer 2a and AML, we estimate stacking errors of ±16 ms and ±8 ms for each event respectively. Combined, picking and stacking errors are estimated to be ±18 ms for layer 2a and ± 11 ms for AML. When depth converted, these combined errors translate to ±20 m for layer 2a and ± 35m for AML. Although Moho event is very weak we give an approximate combined error ± 50 ms, which translates to ± 75 m in depth. Depth conversion of the picked

horizons introduces additional uncertainty, because constant velocity along the ridge axis for each horizon is assumed. If we assume range of velocities and average twtt thickness for layer 2a of 2250-2500 m/s and ~ 150 ms, and for layer 2b of 5100-5500 m/s and ~ 500 ms, the maximum uncertainty in AML depth may be up to 90 m.

Seismic horizons in 3D volumes are digitized using the *Propagator* tool available in *VoxelGeo* (Paradigm's 3D interpretation software). The same phases of the events are picked as for the 2D lines and all events are converted from twtt to depth using the same constant crustal velocities used for the 2D lines. Digitized layer 2a thickness from the swath dataset is shown in Figure 6. In Figures 7 and 8 the digitized AML picks from the swath coverage are shown in both twtt and depth below seafloor respectively. Estimated uncertainties in digitized events are as for the 2D processed data.

3.3. Disruptions in the AML reflection

Along axis seismic data show that the AML reflector, located ~ 1.6 km below the seafloor, is not a continuous horizon, but is rather disrupted. The disruptions vary in character and are present at different length intervals along the ridge. For mapping disruptions in AML we established the following visual criteria: presence of edge diffractions (in stacked section), strongly dipping events, breaks in AML event with step in twtt across the break, and presence of overlapping events (Figure 9). Furthermore, the 3D dataset shows that most of the AML interruptions identified in the 2D lines extend across the swath (Figure 7), in most cases obliquely to the ridge axis orientation (e.g. the interruption at 9º44.6' and 9º51.3'N, Figure 7). Even though the details on structural variations and width of the AML can not be resolved from the available along-axis 3D dataset (due to the very limited aperture of the swath), the locations

of mapped interruptions identified in the these data coincide well with the discontinuities identified in the cross-axis 3D migrated volume [*Carton et al.,* 2010; *Carbotte et al.,* submitted].

In addition to visual identification, disruptions in the instantaneous phase attribute of the AML event calculated from both the 2D lines and along-axis 3D datasets is also used to identify AML interruptions (Figure 10A, Figure 10B and Figure 11). Instantaneous phase is often used within the oil industry to identify discontinuities in horizons [e.g. *Brown,* 1996; *Taner,* 2001]. Theoretical background on instantaneous phase is given by Taner et al. [1979] and is based on a complex (real and imaginary component of seismic signal) trace analysis. First step in calculating instantaneous phase is to generate complex seismic trace by performing Hilbert transform on real seismic trace. Thus obtained complex trace, together with the real trace is then used to obtain instantaneous phase by equation: $\theta(t)=\tan^{-1}[f^*(t)/f(t)]$, where $\theta(t)$ is the phase, $f(t)$ is the real component and $f^*(t)$ is imaginary (or quadrature) component of each seismic trace. The equation above shows that instantaneous phase is independent of signal's amplitude, thus presence of disruptions in the instantaneous phase attribute is considered as representative of a physical discontinuity in a horizon and not an artifact from weakening in reflector's amplitude. This is well illustrated by comparison between Figure 3B and Figure 10B. For instance, while the amplitude of the AML event is diminished between ~ 9º39.8' and 9º41.7'N relative to the adjoining regions, the instantaneous phase remains unchanged. Mapping disruptions in instantaneous phase attribute correlates well with the locations of disruptions picked by visual inspection along the 2D lines and swath (Figure 10A, Figure 10B, and Figure 11), and provides additional confidence in the location of the picked AML disruptions.

4. Results

4.1. Shallow crustal structure - layer 2a

The layer 2a horizon is present along almost the entire length of the modern ridge axis (Figure 3A, Figure 3B and Figure 5) and is imaged as a relatively continuous event providing an average thickness of layer 2a of ~ 150 ± 48 m. Local thinning of layer 2a (thickness < 100 m) is observed around ~ 8º29' (extending for ~ 6 km), ~ 8º53' (~ 3 km), ~ 9º25' (~ 12.5 km), and ~ 9º58'N (~10 km) regions. It is interesting that this thinning is present in regions where seafloor is ~ horizontal.

There are also two regions of prominent layer 2a thickening. One is collocated with the latitudinal extent of the 2005-2006 eruption site [*Soule et al.,* 2007]. Here, layer 2a thickens from ~ 100 m in the north to ~ 200 m over a 3 km distance from 9°55.5' to 9°54'N (Figure 5). Furthermore, in this area within a narrow zone around the AST (available from limited 3D swath) we also observe > 50 m of layer 2a thickening across the axis (Figure 6). Elsewhere within the region of 3D swath coverage north of 9º20'N there is no discernable change in layer 2a thickness across the ridge axis. The other region of pronounced along-axis change in layer 2a thickness is at the 9°03'N OSC. Here layer 2a thickens from ~ 250 m to ~ 400 m towards the ends of both overlapping ridges. It is important to emphasize that our seismic lines within the OSC region are in places more than 1 km off the axis. As shown in previous studies, layer 2a can double in thickness within 1-2 km from the axis [*Harding et al.,* 1993; *Kent et al.,* 1994; *Vera and Diebold*, 1994; *Carbotte et al.,* 1997], which likely contributes to the thick layer 2a observed here along our line.

In the vicinity of many of the third-order bathymetric discontinuities (8º38', 8º51', 9º20', 9º37' and 9º51.5'N) localized complexities in layer 2a horizon are observed. They are expressed by small changes in layer 2a thickness and/or presence of dipping "reflectors" (e.g. 8º51'N in Figure 3A).

4.2. AML characteristics

A seismic reflection from the AML is imaged along ~ 85% of the ridge axis at ~ 1600 ± 145 m below the seafloor. It is imaged as an event of variable reflection strength (Figure 2), with the brightest reflection north of 9º38'N (for ~ 60 km) and locally around 8°30'N (for ~ 5 km) and 8°50'N (for ~ 10 km).

4.2.1. Disruptions in the AML

Using a combination of instantaneous phase attribute and visual inspection of the data, twenty-six disruptions in the intracrustal sill reflector are identified along the EPR first-order ridge segment (Figure 3A, Figure 3B, Figure 10A and Figure 10B). As at the seafloor, most of the AML disruptions correspond with zones from 100 m (at 9º37' and 9º51.3'N) up to 3000 m (at 9º06.7'N) long, (Figure 3A and 3B). In addition, for the region of 2D swath coverage (north of 9º20'N), we are able to map the along-axis disruption zones in the across-axis direction (Figure 7). The data show that most of the AML interruptions persist across the 675 m width of the swath, many with an oblique trend with respect to the ridge-axis azimuth. For instance, the interruption at 9º44.6'N along axis 2r1 (Figure 3B) is mapped across the axis extending obliquely to it for ~ 4.2 km between 9º43.4' and 9º45.7'N (Figure 7). Similarly, the interruption at ~ 9º51.3'N corresponds with a 3.2 km long disruption zone with an ~ N4°E orientation. It is

interesting to note that the 9º56.2' and 9º58.4'N disruptions in axis 2r1 (Figure 3B), appear to be south and north delimiting points of one interruption zone (~ 5.7 km long) evident in the 2D swath dataset (Figure 7). This zone underlies the 9°58 third-order seafloor discontinuity which extends over a longer region from 9º56.2' to 9º58.2'N.

4.2.2. AML depth vs. seafloor depth within segments

Early studies at fast spreading mid-ocean ridges showed that the ridge crest typically shallows near the middle of tectonically defined segments and deepens toward their edges [*Macdonald et al.,* 1984; *Lonsdale,* 1989]. In addition, it was noticed that the ridge axis is broader and flat-topped in cross-sectional area when shallower in depth [e.g. *Macdonald and Fox*, 1988; *Scheirer and Macdonald,* 1993]. These morphological variations in the ridge crest have been attributed to differences in magmatic budget along segments. Furthermore, the apparent correlation between presence of shallow mid-crust magma lens and shallow portion of the ridge [e.g. *Detrick et al.,* 1987; *Kent et al.,* 1993a; *Scheirer and Macdonald,* 1993] supported the magma supply model and suggested AML depth as a proxy for magmatic budget. While some regional scale studies of intermediate and fast spreading centers [e.g. *Mutter et al.,* 1995; *Carbotte et al.,* 2000; *Baran et al.,* 2005; *Carbotte et al.,* 2008] provide evidence consistent with the above view, others have found little relationship between ridge crest depth and depth of the AML [e.g. *Harding et al.,* 1993; *Collier and Sinha,* 1992; *Hooft et al.,* 1997]. It is worth noting that all the studies that argue for absence of positive linear relationship between axial depth and depth to the AML make use of data collected prior to year of full operational capacity of Global Positioning System (GPS). The latter may have resulted in poor navigation of the seismic lines

that perhaps did not sample the apex of the AML. Also, the resolution of data and pick density were comparatively low, which may have contributed to the observed high scatter and inconsistent results.

We use our GPS navigated seismic data with densely picked horizons to examine the seafloor depth vs. AML depth relationship as a function of the AML segmentation at all segment scales for the EPR region (Figure 12, Figure 13, Figure 14 and Figure 15).

Second-order segmentation

Depth of the AML beneath the northern second order segment varies from 1440 to 2290 m below seafloor (bsf) with a mean depth of 1600±110 m. For this segment, the AML depth shows a positive linear relationship with depth to the seafloor (Figure 12B). In contrast, for the southern second-order segment a linear relationship is not observed (Figure 12A). Instead, the AML depth data group into two clusters (a shallow cluster at ~ 1350 m and a deeper cluster at ~ 1700 m). On average, the AML beneath the southern segment is deeper than along the northern segment (average depth 1680±185 m, range 1260 to 1970 m bsf). However, the shallowest AML events observed along the entire EPR region are along the southern segment, centered at ~ 8º53'N (~ 1310 m bsf) and ~ 8º30'N (~ 1380 m bsf). The shallow event at 8º53'N extends for only 0.6 km beneath the axis and coincides with a small volcanic cone (~ 300 m in width and 20 m in high) found within the wide axial summit through (AST) present in this region. Interestingly this shallow AML was also detected in the seismic data acquired in 1985 [*Detrick et al.,* 1987; *Kent et al.,* 1993a]. At ~ 8º30'N the shallow AML extends for ~ 4 km at ~ 1350 m below seafloor. The event is not continuous, with a prominent AML disruption at 8º30.02'N (Figure 3A). This shallow event also varies in strength, with the strongest AML patch north of

the inferred interruption. Interestingly, ridge crest morphology in this region (in particular between 8º30' and 8º35'N) is very similar to that of the 2005-2006 eruption site at 9°50'N. Both regions have shallow (~ 2525 m), inflated axial highs with nearby off axis seamounts or volcanic ridges indicative of locally enhanced magma supply. By analogy with the well studied 9º50'N eruption site, we speculate that the 8º50'N area might be an area of active volcanism along the southern segment. Unfortunately, data from the region are limited (to high resolution bathymetry from White et al. [2006] and sparse geochemistry Langmuir et al. [1986]), and thus more extensive comparison is not possible.

Third-order segmentation

Beneath the northern second-order segment, five third-order AML segments are identified nested within it (Figure 13, Figure 14B) ranging from ~ 8-34 km long. Average AML depth for each segment varies from 1510 to 1770 m (Figure 14B, Table 2) with differences in average depth of up to 100 m for adjacent segments. In most segments, AML depth varies over a small range about the mean depth for the segment. Differences in average seafloor depth for adjacent segments are small and in all cases are less than 40 m. For instance, the segment extending between 9º37.8 and 9º51.3'N has average seafloor depth of 2525 m and the shallowest AML at an average depth of 1510±40 m. This segment is surrounded by segments (south and north of it) with seafloor depth of 2550-2560 m and average AML depth of 1580-1590 m. Average AML depth beneath the two AML segments identified south of 9º20'N, differ by 100 m (although there is a wide range in AML depth at the southernmost segment over the eastern limb of the 9º03'N OSC) but average seafloor depth is very similar (Table 2).

Beneath the southern second-order segment, three third-order segments are identified (Figure 14A). Their length varies from 16 to 30 km and as to the north the mean AML depth varies from segment to segment. Here, the average depth of the shallowest AML segment is 1340±30 m below seafloor (seafloor depth ~ 2520 m), whereas the deepest is at 1750±80 m (seafloor depth ~ 2540 m). Compared with the AML beneath the northern segment it is apparent that for the same change in seafloor depth along the northern segment (~ 40 m), the third-order segments beneath the southern segment show much larger AML depth variations (up to 400 m). Also of note, the two shallowest third-order segments throughout the study have similar seafloor depth (~ 2520 m) but ~ 170 m difference in mean AML depth.

Comparison of the AML depth data by scale of segmentation shows lower variance in in AML depth within the third-order segments than the second-order segments (standard deviations (STD) of ± (25 to 200) m for the third order segments, compared with ± (110 to 200) m the second order segments, Table 2) and much of the variation in AML depth present at the second order scale appears to be explained by the third order segmentation. Correlation coefficients calculated for each segment (Table 2) show a weak linear relationship between seafloor and AML depth for some third-order segments. From these observations two main conclusions are reached: within the third-order segments, there is no consistent relationship between AML depth and seafloor depth, and third order segments are each associated with a distinct mean AML depth, with in the most cases, larger variations in AML depth between third order segments than within them.

Fourth-order segmentation

Along the length of the first-order EPR segment from 8°20 to 10°10'N, twenty-seven 2.8 to 14 km long fourth-order AML segments are identified. The number of these highest-order segments nested within a single third-order segment varies from two to up to five (Figure 15). Changes in AML depth from segment to segment at the fourth order scale are smaller than for the third order segments (Table 2). Most fourth-order segments have similar AML depth as that of their enclosing third-order segment.

4.2.3. Moho

Between 9º10' and 9º30'N, a low-amplitude Moho reflection is imaged in along-axis lines axis 2r1 and axis 3 (Figure 1 and 4). Between 9º10' to 9º20'N these lines are offset 600-1000 m to the east of the modern axial zone but the Moho is imaged only along the axis 2r1 line. For most of the region where Moho is imaged, an AML event is detected in the crust (Figure 4B). Although weak, Moho shows a distinct pattern of ~ 20 km long sections that deepen southward with steps of ~ 200 to 400 m between the adjacent Moho "shingles" (Figure 4C). The steps in depth to Moho coincide with the third-order AML discontinuities at ~ 9º10'N and 9º21.5'N and associated tectonic discontinuities of the axis (Figure 4A, 16). Although we do not image Moho south of 9º10'N in our data set (low signal to noise ratio due to rough seafloor topography), a Moho reflection is well imaged in the previously acquired ARAD 3D seismic volume that covers the entire OSC 9º03'N to ~ 9°10'N [*Singh et al.,* 2006]. In the ARAD volume, Moho exhibits the same southward deepening pattern as we observe north of 9°10'N.

5. Discussion

5.1. Relationship between third-order AML segmentation and shallow crustal structure

In Iceland, central volcanoes and their corresponding rift zone fissures and dikes are referred to as a volcanic system, all of which are believed to share the same volcanic plumbing system [*Gudmundsson,* 1995]. From a study of variations in volcanic morphology along the EPR 9°-10°N, White et al. [2002] inferred that third-order tectonic segmentation of the ridge axis corresponds with analogous volcanic units characterized by a common volcanic plumbing system. Near-bottom acoustic and visual data from this region as well as from the Southern EPR and Juan de Fuca Ridge reveal systematic variations in lava flow morphology and volcanic structures along the ridge axis [*Embley and Chadwick,* 1994; *Embley et al.,* 2000; *White et al.,* 2000; *White et al.,* 2002] that correlate with the third-order tectonic segmentation of the axis. Whereas axial lava domes and pillow lava flows are concentrated at the ends of third-order segments, sheet flows dominate at segment centers. White et al. [2002] attributed these differences in lava morphology to segment-scale variations in lava effusion rate and lava viscosity [*Gregg and Fink,* 1995]. These observations resulted in two main implications for the spatial and physical characteristics of each volcanic unit (i.e. segment): 1) volcanic segmentation is congruent with third order tectonic segmentation, and a common volcanic plumbing system underlies these segments and 2) lava effusion rates are lower at third-order discontinuities. Using the seismic data of Kent et al. [1993a], White et al. [2002] inferred segmentation of the magma

lens coincident with third-order tectonic segmentation and attributed the lower effusion rate eruptions to this segmentation.

Detailed mapping of the AML from our 2008 seismic data set shows that there are disruptions in the AML collocated with both third- and fourth-order discontinuities in bathymetry (Figure 3A and 3B). Why then are pillow lava flows observed at third- and not at fourth-order discontinuities? White et al. [2002] suggest that higher magma viscosities and lower effusion rates reflect lower geothermal gradient or higher magma overpressures associated with deepening of the AML near discontinuities. Changes in overpressure within the magma lens due to the change in AML depth at third order discontinuities are small (0.1 MPa for 100 m change in AML depth, [*White et al.,* 2002]), and are probably not sufficient, but even if they were, deeper third-order segments would be expected to erupt pillow flows along their entire length, which is not observed. We speculate that the change in temperature field associated with the AML disruptions is more likely to contribute to the inferred higher magma viscosities and lower effusion rate. At the third-order discontinuities, magma lenses beneath two ridge segments are offset both in depth and also across the axis in plan view [*Kent et al.,* 1993a] and thus come into contact with colder crustal rocks that may lower their temperature and increase crystalline component within the lens' edges. Partial crystallization leads to increased magma viscosity, which results in eruption of pillow flows. In contrast, across the fourth-order discontinuities magma lens depth changes may be too small to have an impact on thermal structure sufficient to result in eruption of pillow lavas onto the seafloor.

White et al. [2002] proposed two models for the volcanic plumbing system between the magma lens and seafloor: dikes that propagate the full length of third-order segments versus multiple short dikes. In the first model, low effusion rate eruptions are common near the

segment end as a propagating dike narrows and driving pressures decrease. In the second model, smaller and cooler magma sources expected near volcanic segment ends result in narrower dikes, lower magma driving pressures, and higher magma viscosities. The presence of the fourth-order lenses mapped in our study strongly argues against the first model, suggesting that the melt is propagating through the upper crust as dikes that are at least at the same length scales.

5.2. Relationship between third-order AML segmentation and deeper structure

Causal relationship between third-order tectonic discontinuities and magma distribution beneath the crust was suggested (but not further discussed) from results of tomography study conducted along the EPR ridge segment [*Toomey et al.,* 1990]. This study shows that the location and number of the third-order bathymetric segments roughly correlates with the spacing and number of closed-contour lows in the mantle low velocity volume (MLVV) imaged beneath the ridge axis (< 7.5 km/s; Figure 16). In our study, where Moho is observed beneath the axial zone, changes in Moho structure are observed in the vicinity of two third-order discontinuities. These observations suggest that the magmatic system present at the base of the crust is also segmented at third-order scales (Figure 4 and 16). This vertical alignment of discontinuities throughout the crust argues that third-order tectonic discontinuities originate from melt distribution in the shallow mantle.

Further evidence for third-order segmentation in mantle melting beneath ridges comes from field studies in the Oman ophiolite, which is believed to have formed at a fast spreading ridge. Measurements of spinel Cr# in samples taken beneath paleo-Moho from the mantle section indicate long wavelength variations in extent of partial melting of the mantle peridotites at scales of ~ 100-160 km on which shorter wavelength ~ 10-20 km scale variations are superimposed [*Le*

Mée et al., 2004; *Monnier et al.,* 2006]. These authors attribute the long wavelength variations in geochemical signatures to large domes of mantle upwelling equivalent to second-order segmentation, with higher inferred extents of melting within segment centers and lower at segment ends. The shorter wavelength variations in partial melt tracers are attributed to shallower mantle diapirs beneath the crust, equivalent to third and fourth-order segmentation.

5.3. Geological significance of variations in magma lens depth

The mechanisms that control the depth of the AML are not well understood. Early studies of magmatic systems suggested that the level of neutral buoyancy (LNB) at which density of melt is equal to that of surrounding rocks, controls the depth of magma ponding within shallow crustal levels [*Walker,* 1989; *Ryan,* 1993]. However, calculations of Hooft and Detrick [1993] and Hooft et al. [1997] showed that the LNB predicted for basaltic melt compositions is too shallow (100-400 m below seafloor) compared to the average depth at which the AML is imaged at fast spreading ridges (1-2 km below seafloor). They argue that the presence of a thermally controlled permeability boundary, as proposed by Phipps Morgan and Chen [1993], controls the depth of the AML.

Our results suggest that the magma lens is located at a characteristic depth beneath each third-order segment, but that this depth varies from segment to segment, indicating a different thermal structure within each. If this third-order segmentation arises from variable melt distribution in the upper mantle (Section 5.2.) it is plausible that the main factor governing the permeability boundary that controls AML depth will be melt flux from each independent third-order scale magma reservoir at the base of the crust [*Crawford et al.,* 1999; *Dunn et al.,* 2000; *Toomey et al.,* 2007]. This flux may be constant for long time periods, corresponding with the

life time of third-order segments, which is believed to be several 100,000 years [*Macdonald et al.,* 1988*; White et al.,* 2002]. Over this time period the AML would then reside at a similar depth (steady-state model, Figure 17A).

Alternately, magmatic flux to all segments may be the same when integrated over long time intervals but may vary within each segment on shorter time scales [e.g. *Perfit and Chadwick,* 1998] with fluctuations out of phase from segment to segment (Figure 17B). In this magmatic cycle model, AML depth observed in 2008 is a snapshot, with the AML moving up and down in the crust with changes in magma supplied from below (i.e. depth of each third-order lens fluctuates through time and the seismic data capture only their current position). In the Phipps Morgan and Chen [1993] model, the balance between heat addition from below due to mantle magma supply and heat removal from above by hydrothermal circulation controls the depth of the crustal magma body. However, a primary role for hydrothermal circulation in controlling the regional-scale depth of the AML is not supported by the observations from our data. For instance, within the site of recent volcanic eruption at 9º50'N where currently numerous, active hydrothermal vents are identified, one would expect the highest cooling rate from above to occur, and a deeper AML is predicted. In contrast we observe the shallowest AML within this area.

These two models (Figure 17) have different predictions for long-term crustal production that can be tested with studies of crustal thickness. The steady-state model (Figure 17A) predicts that each third-order segment will be associated with an approximately uniform crustal thickness that differs from segment to segment. In contrast, the magmatic cycle model (Figure 17B) predicts that while crustal thickness may differ from segment to segment at any one time, the longer term average crustal thickness within each segment will be similar. The available crustal

thickness data for our study area are sparse but lend support to the steady-state model and indicate larger changes in crustal thickness along the axis than across axis [*Barth and Mutter,* 1996*; Canales et al.,* 2002]. Further studies using the 2008 MCS data are underway and can be used to further examine these predictions [*Aghaei et al.,* 2011]. We note that hybrid models between these two end members may be most likely; the new data will some provide information on crustal thickness variations within 2 third order segmentations to test these models.

Regardless of whether magma flux is uniform or variable through time, our results argue that each third-order segment behaves as an independent unit that encompasses a group of the fourth-order segments and also governs their depth. In the along the axis direction one third-order segment could be visually compared to a *boudinage* structure found in sedimentary rocks, where each "*boudin*" is composed of smaller fourth-order melt lenses. The fourth-order lens segments correspond with the finest-scale tectonic segmentation of the eruptive fissure zone and are associated with differences in composition of lavas erupted onto the seafloor [*Carbotte et al.,* submitted]. Segmentation of the AML at these fine scales may result from melt focusing within the lower crust or shallow level processes linked to, for example, hydrothermal cooling [*Fontaine et al.,* 2011] or crustal assimilation at the roof of the magma lens [e.g. *Coogan,* 2003 and *Coogan et al.,* 2003].

6. Summary

Seismic data collected along the EPR 8°20' to 10°10'N show that the intracrustal magma sill that sits at ~ 1.6 km below seafloor is segmented at all segment scales defined in bathymetry [*Macdonald et al.,* 1991; *White et al.,* 2006; *Carbotte et al.,* submitted]. For a group of fourth-order segments delimited by two third-order disruptions we find that the depth of the AML in

adjacent fourth-order segments is located at a similar average depth. In contrast, AML depth varies significantly between two adjacent third-order segments and each third-order segment appears to be associated with a characteristic AML depth. The above strongly supports the idea that each third-order segment behaves as an independent magmatic unit, sharing a common volcanic plumbing [*White et al.,* 2000 and *White et al.,* 2002]. Along-axis variations in lava morphology within third-order segments and their absence at the fourth-order [*White et al.,* 2002], may result from the AML depth changes across disruptions that affects geothermal gradient, leads to great cooling at edges of two adjacent sills and correspondingly lower effusion rate eruptions.

Location of disruptions in Moho imaged along the axis, and local regions of lower melt inferred within the mantle low velocity volume at the base of the crust [*Toomey et al.,* 2007], project through the crust, coincident with disruptions in the AML and layer 2a horizon, to the third-order tectonic disruptions of the axis at the seafloor. This vertical alignment argues that magmatic and tectonic segmentation at this scale may originate from the base of the crust in response to variations in melt accumulation within the upper mantle. Melt (heat) flux from the sub-crustal magma reservoir may play the primary role in the base-level AML depth within each segment. From each of the local mantle low velocity volume minima different amounts of magma ascends upward (i.e. magma flux) and ponds at the base of the dike section giving rise to a characteristic third-order intracrustal sill segment depth. If magma flux is constant, this depth could be preserved over the lifetime of each third-order segment. Alternately, magma flux from the upper mantle may vary over time giving rise to fluctuations of AML depth within third-order segment over shorter time scales.

Acknowledgments

We thank Captain M. Landow, crew, technical staff for their effort for succesful data collection durin the MGL0812 cruise. We thank Roger Buck for helpful discussion. This research was supported by US NSF grant.

References:

Aghaei O., M. R. Nedimović, J. P. Canales, Carton, S. M. Carbotte, J. C. Mutter, (2011), Crustal thickness from 3D MCS data collected over the fast-spreading East Pacific Rise at 9º50'N, Abstract OS11B-1498, *presented at 2011 Fall Meeting, AGU*, San Francisco, Calif., 5-9 Dec.

Babcock, J. M., A. J. Harding, G. M. Kent, and J. A. Orcutt (1998), An examination of along-axis variation of magma chamber width and crustal structure on the East Pacific Rise between 13º30'N and 12º20'N, *J. Geophys. Res.,* 103(B12), 30,451-30,467, doi:10.1029/98JB01979.

Baran, J. M., J. R. Cochran, S. M. Carbotte, and M. R. Nedimović, (2005), Variations in upper crustal structure due to variable mantle temperature along the Southeast Indian Ridge, *Geochem. Geophys. Geosyst.,* 6, Q11002, doi:10.1029/2005GC000943.

Barth, G. A., and J. C. Mutter, (1996), Variability in oceanic crustal thickness and structure: Multichannel seismic reflection results from the northern East Pacific Rise, *J. Geophys. Res.*, 101(B8), 17,951-17,975, doi:10.1029/96JB00814.

Bell R. E. and W. R. Buck, (1992), Crustal control of ridge segmentation inferred from observation of the Reykjanes Ridge, *Nature* 357, 583-586.

Boudier F., and A. Nicolas, (2011), Axial melt lenses at oceanic ridges - A case study in the Oman ophiolite, *Earth and Planetary Sci. Lett.* 304, 313-325, doi:10.1016/j.epsl2011.01.029.

Brown, A.R. (1996), Seismic attribute and their classification, *The Leading Edge*, October, pp 1090.

Canales, J.P., G. Ito, R.S. Detrick, and J. Sinton, (2002), Crustal thickness along the western Galapagos Spreading Center and the compensation of the Galapagos hotspot swell, *Earth Planet. Sci. Lett.,* 203 (1), 311-327.

Canales, J. P., R. S. Detrick, S. M. Carbotte, G. M. Kent, J. B. Diebold, A. J. Harding, J. Babcock, M. R. Nedimović, and van Ark, E, (2005), Upper crustal structure and axial

topography at intermediate-spreading ridges: seismic constraints from the Southern Juan de Fuca Ridge, *J. Geophys. Res.,* 110, doi:12110.11029/12005JB003630.

Carbotte, S., and K. Macdonald (1992), East Pacific Rise 8º-10º30'N: Evolution of Ridge Segments and Discontinuities From SeaMARC II and Three-Dimensional Magnetic Studies, *J. Geophys. Res.,* 97(B5), 6959-6982, doi:10.1029/91JB03065.

Carbotte, S.M., J. C. Mutter and L. Xu, (1997), Contribution of tectonism and volcanism to axial and flank morphology of the southern EPR from a study of Layer 2A geometry, *J. Geophys. Res.,* 102, 10,165-10,184.

Carbotte, S.M., G. Ponce-Correa, and A. Solomon, (2000), Evaluation of morphological indicators of magma supply and segmentation from a seismic reflection study of the EPR 15°30'-17°N, *J. Geophys. Res.,* 105, 2737-2759.

Carbotte, S. M., R. S. Detrick, A. Harding, J. P. Canales, J. Babcock, G. Kent, E. Van Ark, M. Nedimović, J. Diebold, (2006), Rift topography linked to magmatism at the intermediate spreading Juan de Fuca Ridge, *Geology*, 34, 209-212, doi:10.113/G21969.

Carbotte, S. M., M. R. Nedimović, J. P. Canales, G. M. Kent, A. J. Harding, and M. Marjanović (2008), Variable crustal structure along the Juan de Fuca Ridge: Influence of on-axis hot spots and absolute plate motions, *Geochem. Geophys. Geosyst.,* 9, Q08001, doi:10.1029/2007GC001922.

Carbotte S. M., M. Marjanović, Carton, H. D., J. C. Mutter, M. R. Nedimović, J. P. Canales, Xu M., Aghaei O., M. Perfit, S. Han, Fine-scale segmentation of the crustal magma reservoir beneath the modern eruptive zone of the East Pacific Rise, (submitted).

Carton, H. D., S. M. Carbotte, J. C. Mutter, J. P. Canales, M. R. Nedimovi_, O. Aghaei, M. Marjanović, and K. R. Newman, (2010), Three-dimensional seismic reflection images of axial melt lens and seismic layer 2A between 9¡42'N and 9¡57_N on the East Pacific Rise, Abstract OS21C-1514, *Presented at 2010 Fall Meeting, AGU*, San Francisco, California.

Collier, J. S. and M. C. Sinha, (1992), Seismic mapping of a magma chamber beneath the Valu Fa Ridge, Lau Basin, *J. Geophys. Res.,* 97(B10), 14,031-14,053, doi:10.1029/91JB02751.

Coogan, L. A., N. C. Mitchell, and M. J. O'Hara, (2003), Roof assimilation at fast spreading ridges: An investigation combining geophysical, geochemical, and field evidence, *J. Geophys. Res.,* 108, 2002, doi:10.1029/2001JB001171.

Coogan, L.A., (2003), Contaminating the lower crust in the Oman Ophiolite, *Geology*, 31, 1065-1068.

Cormier, M.-H., K. C. Macdonald, and D. S. Wilson (1995), A three-dimensional gravity

analysis of the East Pacific Rise from 18º to 21º30'S, *J. Geophys. Res.*, 100(B5), 8063-8082, doi:10.1029/95JB00243.

Crawford, W. C., S. C. Webb, and J. A. Hildebrand, (1999), Constraints on melt in the lower crust and Moho at the East Pacific Rise, 9º48'N, using seafloor compliance measurements, *J. Geophys. Res*., 104(B2), 2923-2939, doi:10.1029/1998JB900087.

Detrick R. S., P. Buhl, E. Vera, J. Mutter, J. Orcutt, J. Madsen and T. Brocher, (1987), Multi-channel seismic imaging of a crustal magma chamber along the East Pacific Rise, *Nature* 326, 35 - 41, doi:10.1038/326035a0.

Detrick, R. S., A. J. Harding, G. M. Kent, J. A. Orcutt, J. C. Mutter, and P. Buhl (1993), Seismic Structure of the Southern East Pacific Rise, *Science*, 259, 499-503.

Dunn R. A. and D. R. Toomey, (1997), Seismological evidence for three-dimensional melt migration beneath the East Pacific Rise, *Nature*, 338, 259-262.

Dunn, R. A., D. R. Toomey, and S. C. Solomon (2000), Three-dimensional seismic structure and physical properties of the crust and shallow mantle beneath the East Pacific Rise at 9º30'N, *J. Geophys. Res.*, 105(B10), 23,537-23,555.

Embley, R. W., and W. W. Chadwick Jr. (1994), Volcanic and hydrothermal processes associated with a recent phase of seafloor spreading at the northern Cleft segment: Juan de Fuca Ridge, *J. Geophys. Res.,* 99(B3), 4741-4760, doi:10.1029/93JB02038.

Embley, R. W., W. W. Chadwick, M. R. Perfit, M. C. Smith, and J. R. Delaney (2000), Recent eruptions on the CoAxial segment of the Juan de Fuca Ridge: Implications for mid-ocean ridge accretion processes, *J. Geophys. Res.,* 105(B7), 16,501-16,525, doi:10.1029/2000JB900030.

Fontaine, F. J., J.-A. Olive, M. Cannat, J. Escartín, & Perol, T. (2011), Hydrothermally-induced melt lens cooling and segmentation along the axis of fast- and intermediate-spreading centers. *Geophys. Res. Lett.* **38**, L14307.

Gregg, T. K. P., and J. H. Fink, (1995), Quantification of submarine lava-flow morphology through analog experiments, *Geology*, 23, 73- 76.

Gudmundsson, A., (1995), Infrastructure and mechanics of volcanic system in Iceland, J. *Volcanol. Geotherm. Res.,* 64, 1-22.

Han S., H. D. Carton, S. M. Carbotte, J. C. Mutter, J. P. Canales, M. R. Nedimović, (2011), 3D seismic reflection images of an off-axis melt lens and its association with the upper crust around 9¼39'N, East Pacific Rise, Abstract OS22A-02 *presented at 2011 Fall Meeting, AGU*, San Francisco, Calif., 5-9 Dec.

Harding, A. J., G. M. Kent, and John. A. Orcutt (1993), A Multichannel Seismic Investigation

of Upper Crustal Structure at 9ºN on the East Pacific Rise: Implications for Crustal Accretion, *J. Geophys. Res.,* 98(B8), 13,925-13,944.

Haymon, R.M., D.J. Fornari, M.H. Edwards, S. Carbotte, D. Wright, and K.C. Macdonald, (1991), Hydrothermal vent distribution along the East Pacific Rise crest (9º09'-9º54'N) and its relationship to magmatic and tectonic processes on fast spreading mid-ocean ridges, *Earth Planet. Sci. Lett.* , 104, 513-534.

Hooft, E. E. and R. S. Detrick (1993), The role of density in the accumulation of basaltic melts at mid-ocean ridges, *Geophys. Res. Lett.,* 20(6), 423-426, doi:10.1029/93GL00295.

Hooft, E. E. E., R. S. Detrick, and G. M. Kent (1997), Seismic structure and indicators of magma budget along the Southern East Pacific Rise, *J. Geophys. Res.,* 102(B12), 27,319-27,340, doi:10.1029/97JB02349.

Kent, G. M., A. J. Harding, and J. A. Orcutt (1993a), Distribution of Magma Beneath the East Pacific Rise Between the Clipperton Transform and the 9º17'N Deval From Forward Modeling of Common Depth Point Data, *J. Geophys. Res.,* 98(B8), 13,945-13,969, doi:10.1029/93JB00705.

Kent, G. M., A. J. Harding, and J. A. Orcutt, (1990), Evidence for a smaller magma chamber beneath the East Pacific Rise at 9°30'N, *Nature*, 344, 650-653.

Kent, G. M., A. J. Harding, and J. A. Orcutt (1993b), Distribution of Magma Beneath the East Pacific Rise Near the 9º03'N Overlapping Spreading Center From Forward Modeling of Common Depth Point Data, *J. Geophys. Res.,* 98(B8), 13,971-13,995, doi:10.1029/93JB00706.

Kent, G. M., A. J. Harding, J. A. Orcutt, R. S. Detrick, J. C. Mutter, and P. Buhl (1994), Uniform accretion of oceanic crust south of the Garrett transform at 14º15'S on the East Pacific Rise, *J. Geophys. Res.,* 99(B5), 9097-9116, doi:10.1029/93JB02872.

Langmuir, C. H., J. F. Bender, and R. Batiza, (1986), Petrological and tectonic segmentation of the East Pacific Rise, 5º30'-14º30'N, *Nature*, 322, 422-429.

Le Mée L., J. Girardeu and C. Monnier, (2004), Mantle segmentation along the Oman ophiolite fossil mid-ocean ridge, *Nature* 432, 167-172.

Lonsdale P., (1983), Overlapping rift zones at the 5º5'S offset of the East Pacific Rise, *J. Geophys. Res.*, 88, B11, 9393-9406.

Lonsdale, P. (1989), Segmentation of the Pacific-Nazca Spreading Center, 1°N–20°S, *J. Geophys. Res.*, *94*(B9), 12,197–12,225, doi:10.1029/JB094iB09p12197.

Macdonald, K.C., J.-C. Sempere and P.J. Fox, (1984), East Pacific Rise from Siqueiros to Orozco fracture zones: Along-strike continuity of axial neovolcanic zone and structure and

evolution of overlapping spreading centers, *J. Geophys. Res.* 89:6049-6069 and 6301-6306.

Macdonald, K.C. and P.J. Fox, (1988), The axial summit graben and cross-sectional shape of the East Pacific Rise as indicators of axial magma chambers and recent volcanic eruptions, *Earth. Planet. Sci. Lett.* 88:119-131.

Macdonald, K.C., P.J. Fox, L.J. Perram, M. F. Eisen, R.M. Haymon, S.P. Miller, S.M. Carbotte, M. H. Cormier and A.N. Shor, (1988), A new view of the mid-ocean ridge from the behaviour of ridge axis discontinuities, *Nature* 335:217-225.

Macdonald, K.C., D.S. Scheirer and S.M. Carbotte, (1991), Mid-ocean ridges: Discontinuities, segments and giant cracks, *Science* 253:986-994.

Macdonald, K.C., P.J. Fox, S. Miller, S. Carbotte, M.H. Edwards, M. Eisen, D.J. Fornari, L. Perram, R. Pockalny, D. Scheirer, S. Tighe, C. Weiland and D. Wilson, (1992), The East Pacific Rise and its flanks 8-18ºN: History of segmentation, propagation and spreading direction based on SeaMARC II and Sea Beam studies, *Mar. Geophys. Res.* 14:299-344.

Monnier, C., J. Girardeau, L. Le Mée, and M. Polvé (2006), Along-ridge petrological segmentation of the mantle in the Oman ophiolite, *Geochem. Geophys. Geosyst.,* 7, Q11008, doi:10.1029/2006GC001320.

Mutter, J.C., G.A. Barth, P. Buhl, R.S. Detrick, J. Orcutt and A. Harding, (1988), Magma Distribution across Ridge-Axis Discontinuities on the East Pacific Rise from Multichannel Seismic Images, *Nature*, Vol. 336, No. 9195, p. 156-158.

Mutter, J. C., S. C. Carbotte, W. Su, L. Xu, P. Buhl, R. S. Detrick, G.M. Kent, J. A. Orcutt, A. J. Harding, (1995), Seismic images of active magma systems beneath the East Pacific Rise between 17º05' and 17º35'S, *Science*, vol. 268, 391-395.

Mutter, J.C., H. Carton, M. Marjanović, S. Carbotte, J.P. Canales, and M.R. Nedimović, (2010), Eruption-related changes in magma chamber structure at 9°50'N on the EPR from coincident reflection images, 1985 and 2008. *Eos, Transactions, American Geophysical Union*, Abstract OS24A-01.

Nicolas, A., and F. Boudier, (2011), Structure and dynamics of ridge axial melt lenses in the Oman ophiolite, *J. Geophys. Res.,* 116, B03103, doi:10.1029/2010JB007934.

Perfit, M.R., and Chadwick, W.W. Jr., (1998), Magmatism at mid-ocean ridges: Constraints from volcanological and geochemical investigations. in Faulting and Magmatism at Mid-Ocean Ridges, ed. W.R. Buck, P. Delaney, and J.A. Karson. *Geophys Monograph* 92., Amer. Geophys Union, Washington D.C.

Phipps Morgan, J. and Y. J. Chen (1993), The genesis of oceanic crust: Magma injection, hydrothermal circulation, and crustal flow, *J. Geophys. Res.*, *98*(B4), 6283–6297,

doi:10.1029/92JB02650

Ryan, M. P. (1993), Neutral Buoyancy and the Structure of Mid-Ocean Ridge Magma Reservoirs, *J. Geophys. Res.,* 98(B12), 22,321-22,338, doi:10.1029/93JB02394.

Scheirer, D. S. and K. C. Macdonald (1993), Variation in cross-sectional area of the axial ridge along the East Pacific Rise: Evidence for the magmatic budget of a fast spreading center, *J. Geophys. Res.,* 98(B5), 7871-7885, doi:10.1029/93JB00015.

Schouten H., K. D. Klitgord, J. A. Whitehead, (1985), Segmentation of mid-ocean ridges, *Nature*, 317, 225-229.

Schouten H., H. J. B. Dick, K. D. Klitgord, (1987), Migration of mid-ocean-ridge volcanic segments, *Nature*, 326, 835- 839.

Singh S. C., Harding A. J., Kent G. M., Sinha M. C., Combier V., Nazin S., Tong C. H., Pye J. W., Barton P. J. Hobbs R. W., White R. S., Orcutt J. A., (2006), Seismic reflection images of the Moho underlying melt sill at the East Pacific Rise, *Nature* 422, 287-290, doi:10.1038/nature04939.

Soule, S. A., D. J. Fornari, M. R. Perfit, and K. Rubin (2007), New insights into mid-ocean ridge volcanic processes from the 2005–2006 eruption of the East Pacific Rise, 9°46′N– 9°56′N, *Geology*, 35(12), 1079–1082, doi:10.1130/ G23924A.1.

Taner M. T., F. Koehler, R. E. Sheriff, (1979), Complex seismic trace analysis, *Geophysics*, 44(6), 1041-1063.

Taner M. T., (2001), Seismic attributes, *CSEG Recorder*, pg 48-56.

Toomey, D. R., G. M. Purdy, S. C. Solomon and W. S. D. Wilcock, (1990), The three-dimensional seismic velocity structure of the East Pacific Rise near latitude 9° 30'N, *Nature, 347*, 639-645.

Toomey D. R., D. Jousselin, R. A. Dunn, W. S. D. Wilcock, and R. S. Detrick, (2007), Skew of mantle upwelling beneath the East Pacific Rise governs segmentation, *Nature* 446, 409-414.

Toomey D. R. and E. E. Hooft, (2008), Mantle uwelling magmatic differentiation and the meaning of axial depth at fast-spreading ridges, *Geology*, 36, 679-682.

Vera, E. E., J. C. Mutter, P. Buhl, J. A. Orcutt, A. J. Harding, M. E. Kappus, R. S. Detrick, and T. M. Brocher (1990), The Structure of 0- to 0.2-m.y.-Old Oceanic Crust at 9ºN on the East Pacific Rise From Expanded Spread Profiles, *J. Geophys. Res.*, 95(B10), 15,529-15,556.

Vera, E. E., and J. B. Diebold (1994), Seismic imaging of oceanic layer 2A between 9º30’N and 10ºN on the East Pacific Rise from two-ship wide-aperture profiles, *J. Geophys. Res.,* 99(B2), 3031-3041, doi:10.1029/93JB02107.

Walker, G. P. L., (1989), Gravitational (density) controls on volcanism, magma chambers and intrusion, *Austr. J. Earth Sci.,* 36, 149-165.

Wang, X., and J. R. Cochran (1993), Gravity Anomalies, Isostasy, and Mantle Flow at the East Pacific Rise Crest, *J. Geophys. Res.,* 98(B11), 19,505-19,531, doi: 10.1029/93JB01551.

Wang, X., J. R. Cochran, and G. A. Barth (1996), Gravity anomalies, crustal thickness, and the pattern of mantle flow at the fast spreading East Pacific Rise, 9º-10ºN: Evidence for three-dimensional upwelling, *J. Geophys. Res.,* 101(B8), 17,927-17,940, doi:10.1029/96JB00194.

White, S. M., Macdonald, K. C., & Haymon, R. M., (2000), Basaltic lava domes, lava lakes, and volcanic segmentation on the southern East Pacific Rise, *Journal of Geophysical Research*, 105 (B10), 23519-23536.

White, S. M., R. M. Haymon, D. J. Fornari, M. R. Perfit, and K. C. Macdonald (2002), Correlation between volcanic and tectonic segmentation of fast-spreading ridges: Evidence from volcanic structures and lava flow morphology on the East Pacific Rise at 9º-10ºN, *J. Geophys. Res.,* 107(B8), 2173, doi:10.1029/2001JB000571.

White, S. M., R. M. Haymon, and S. Carbotte (2006), A new view of ridge segmentation and near-axis volcanism at the East Pacific Rise, 8-12ºN, from EM300 multibeam bathymetry, *Geochem. Geophys. Geosyst.,* 7, Q12O05.

Whitehead Jr J. A., H. J. B. Dick, H. Schouten, (1984), A mechanism for magmatic accretion under spreading centres, *Nature*, 312, 146-148.

Yilmaz O., (2001), Seismic data analysis, Processing, Inversion, and Interpretation of Seismic Data, *Society of Exploration Geophysicists*.

Processing sequence	2D line (CBL#2)	3D swath
Geometry definition	2D geometry	3D geometry (see Appendix A)
Editing	_	_
Pre-stack	1. Band-pass filtering (2-7-220-250 Hz) 2. Spherical divergence correction 3. Surface consistent amplitude correction 4. Resampling to 4 ms (with applied anti-aliasing filter) and 8 [s] trace length 5. F-k filter and edits applied 6. Mute right above the first water multiple	1. Bandpass filtering: 2-7-220-250 [Hz] 2. Suppress swell noise and spherical divergence correction 4. FK -filter 5. Resample at 4 [ms] (with anti-aliasing filter applied) and 8 s trace length 6. Edits applied 7. Flexible binning (bins=6.25×37.5 m) with maximum fold=39 8. Amplitude balancing 9. Mute right above the first water multiple
Satcking	7.Defining stacking velocity 8. NMO and stacking	10. Defining 3D velocity function for stacking (V3D) 11. NMO and stack CMP gathers using V3D velocity
Post-stack	9a. For layer 2a: 2D Kirchhoff post-stack time migration using water velocity 9b. For AMC: 2D Kirchhoff post-stack time migration using ~ 80% of the ESP5 velocity function	15a. For l2a: 2D Kirchhoff post-stack time migration using water velocity 15b. For amc: 2D Kirchhoff post-stack time migration using ~80% of the ESP5 velocity function
Display	10. Top mute above the seafloor 11. Apply surgical mute to the layer 2a section and merge it with the AMC section 12. Scaling composite seismic section	16. Top mute above the seafloor 17. Scaling entire 2D swath

Table 1. Summary of 2D and 3D swath processing steps.

	seafloor depth [m]	AML depth [m]	STD in AML [m]	correlation coefficient
second-order segments				
southern segment	2550	1690	±200	0.4
northern segment	2560	1600	±110	0.66
third-order segments				
segment 1	2521	1340	±30	0.035
segment 2	2540	1770	±80	0.37
segment 3	2618	1710	±40	0.6
segment 4	2610	1770	±200	0.36
segment 5	2590	1671	±80	-0.62
segment 6	2560	1580	±30	0.78
segment 7	2520	1510	±40	0.06
segment 8	2550	1590	±25	0.42
fourth-order segments				
segment 1.1	2550	1850	±50	-0.4
segment 1.2	2525	1400	±75	-0.7
segment 1.3	2520	1360	±40	0.5
segment 1.4	2555	1620	±130	0.6
segment 2.1	2540	1910	±160	0.075
segment 2.2	2530	1490	±240	0.63
segment 3.1	2545	1730	±50	0.42
segment 3.2	2580	1900	±45	-0.53
segment 3.3	2620	1720	±45	0.2
segment 4.1	2635	2100	±140	0.33
segment 4.2	2615	1550	±20	-0.87
segment 4.3	2600	1715	±65	-0.37
segment 4.4	2595	1830	±15	0.39
segment 5.1	2595	1595	±60	0.07
segment 5.2	2580	1720	±50	-0.33
segment 6.1	2570	1600	±25	0.77
segment 6.2	2555	1560	±5	-0.14
segment 6.3	2545	1550	±20	0.3
segment 7.1	2535	1580	±20	-0.6
segment 7.2	2535	1510	±20	-0.041
segment 7.3	2540	1490	±10	-0.4
segment 7.4	2520	1470	±20	0.75
segment 7.5	2510	1530	±25	-0.74
segment *	2550	1550	±50	0.64
segment 8.1	2565	1560	±15	0.13
segment 8.2	2560	1600	±20	-0.13
segment 8.3	2550	1570	±10	-0.73

Table 2. Seafloor depth, depth to the AML and its standard deviation (STD), and correlation coefficients for second-, third- and fourth-order segments. Nomenclature for segments from Figure 14 (for the third-order segments) and Figure 15 (for the fourth-order segments). Appendix

A: Defining 3D swath geometry

Defining an initial 3D geometry or 3D swath box[‡] for seismic data acquired along a mid-ocean ridge axis can be challenging due to the fact that mid-ocean ridges can exhibit abrupt and frequent, although relatively small, changes in the orientation of the ridge axis. When defining the geometry of the box required for 3D processing one needs to consider both the best geometry orientation from the subsurface imaging point of view (i.e. the goal is to image the subsurface along the ridge with the same quality) and the most efficient way to do it. At this initial stage, it is also very important to come up with the scheme for numbering inlines and crosslines[§] within the geometry boxes to enable the smooth transition between boxes at the interpretation stage.

Here we describe how the geometry of the two boxes used for processing the swath data set was defined for the region from 9°20'N to ~10°10'N. Within this region, the along-axis lines change orientation to accommodate a change in ridge axis trend at ~ 9°55'N, which is expressed as an azimuth[**] change of ~ 3.9°, i.e. from ν_1=351.7° to ν_2=347.8°. Thus we define two boxes with different geometries, the first one will encompass the ridge axis data south of the bending point and the other north of it. In Figure A.1.A the latter is represented by a green rectangle. The former includes two sub boxes, shown in brown and blue rectangles that have the same orientation (the split into two boxes south of the bending point is to accommodate change in width due to different number of seismic lines included in each swath). Here, we discuss the

‡ The final geometry box with migrated seismic data has different origin and size, but the same orientation as the initial processing geometry box

§ Within a geometry box an inline (also called subline) is oriented parallel to the survey navigation and a crossline is perpendicular to it.

** Here, azimuth is the angle measured from the geographic north in clockwise sense.

definition of the "brown" box (hereinafter southern box) and "green" box (hereinafter northern box).

We first define the southern swath box, choosing the location for its southwest (SW) corner (shown with a purple dot in Figure A.1.B) at some arbitrary, but reasonable distance (some 1000 m) from the ridge axis. In our case the chosen origin of the southern box in UTM coordinates is X=581738.6 m and Y=1053295 m. Then, we define the survey angle of rotation (or orientation of the inlines), such that the longer side of the box is parallel to the ridge axis. This angle has a different definition than the azimuth and is measured counterclockwise from the east, as shown in Figure A.1.C. For our southern box, the azimuth of ν_1= 351.7° corresponds with a survey angle of 98.3° and northern box azimuth of ν_2= 347.8° gives a survey angle of 102.2°. The next step is to define the inline and crossline spacing and the number of inlines and crosslines within this box. For our dataset the inline spacing, as defined by our source and receiver geometry, is 37.5 m, and the crossline spacing is 6.25 m, which gives a nominal CMP bin size of 37.5 × 6.25 m. For our case of an along axis box with origin at its SW corner, the inline spacing has to be defined as a negative distance increment to obtain the box oriented as shown in Figure A.1.B (hence spacing is -37.5 m). For the first box defined, the inline and crossline numbering scheme is arbitrary. However, to ensure that the inline/crossline numbering is consistent across adjacent boxes, geometry definition for the second (here northern) box is more complex. For our northern box we first define what we call the "pivot point" or common point for both boxes (marked by a black dot in Figure A.1.B). This point bears the same inline and crossline numbers[††] in both boxes. It is obtained at the intersection between the ~ 400th

[††] Since *Focus* requires numbering of inlines and crosslines to be less than 10000, for our northern box crosslines we established a relationship for which: pivoting point crossline from northern box#=pivoting point crossline from southern box# – 6000 (in our case for the pivoting point instead of the crossline #=7991 that is in the northern box, in the southern box we have crossline#=1991).

crossline[‡‡] from the northern side of the southern box (in Figure A.1.B shown in red line) and one of its central inlines (shown in thick black line in Figure A.1.B). Once the location of the pivot point is established, we can define the central inline for the northern box (thick white line in Figure A.1.B) with the angle required by the orientation of the ridge axis. The southernmost crossline central point (green dot in Figure A.1.B) of the second box is then defined along this central inline at ~ 2500 m (400 crosslines) distance from the pivoting point. The orientation of the crossline is perpendicular to the central inline. The inline of the origin of the second box can then be determined moving along the southernmost crossline of the northern box (in our case toward SW) for as many inlines as necessary to encompass the geographical extent of the collected data within the region of interest. Origin of the northern box is shown in blue dot in Figure A.1. The rest is the same as for the southern box.

---

‡‡ According to our calculations ~ 400 crosslines (~ 2500 m) sufficient to account for the migration aperture. It is important to mention that for defining the optimal width of the box for picking in VoxelGeo number of crosslines should be larger (~ 500). Since we used 400, we have some gaps for the picks between the boxes.

Appendix B: Definition of shots within each box for processing the 3D swath dataset

Another important challenge when processing 3D swath seismic data sets within a survey that requires definition of two or more geometry boxes, is to determine which shot numbers are contributing to each of the defined boxes.

Here we describe a simple way for determining the range of shots that sample the subsurface delimited by the box geometry and with reflected signals captured by receivers within the same geometry limits. Since the streamers are towed behind the ship, the definition of the shots to include in each box will be different for the two cases of the ship entering and exiting the box.

Case 1: Ship entering a box

When entering a box, although a shot may be geographically within the box, the signal reflected from the seafloor and subsurface may sample a region out of the box (Figure B.1.B). Furthermore, some shots may sample the subsurface within the box for near and mid source-receiver offsets, but not at far offsets so that far offset traces would not belong to the delimited box. Thus, the first shot to include for processing is the first to produce reflections located only within the defined box geometry (Figure B.1.B). The general formula is:

S_{in}=CL/2 +RD/2;

where: S_{in} is the distance from the first crossline within the box to the first included shot (hereafter referred to as shot-in distance); CL is the cable length and RD is the distance of the first receiver from the source. In our case, CL=6000 m, RD is ~ 200 m, and the first included shot-in distance S_{in} is ~3100 m. Then, for the shot spacing of 37.5 m, the first shot number that we include for further processing is 83 shots from the geographically first shot in the box.

Case 2: Ship exiting a box

When the ship is exiting a box all the receivers are still geographically within the box (receivers are behind the ship), but also due to the distance between the ship and first receiver of ~200 m there are a few shots located out of the box that still contribute to sampling the subsurface within the box limits (Figure B.2). The distance of the last included shot from the last crossline (S_{out}) is:

$$S_{out}=RD/2;$$

For our shot spacing (37.5 m), the last shot included for processing the box would be two shots after the last shot that is geographically located within the box.

Figure 1. Track lines of along-axis multi-channel seismic data collected during expedition MGL0812 and used for 2D data processing. The lines are labeled and color-coded (axis 1 - red, axis 2r1 - purple and axis 3 - black); dots show location of every 300 common-mid points along each line. Track lines are superimposed on bathymetric data of the East Pacific Rise (EPR) collected during our survey (EM120 gridded at 50 m) with the major (first- and second-order) discontinuities of the ridge axis labeled (Siquieros and Clipperton transform Faults (TF) and Overlapping Spreading Center – OSC at 9º03'N). White rectangles outline the extent of the fully migrated 3D volumes obtained as part of the larger MGL0812 study [*Carton et al.,* 2010*; Han et al.,* 2011]. Blue asterisks and circles indicate location of the third- and fourth-order discontinuities, whereas thick, ridge parallel blue lines mark bathymetry discontinuity zones of the modern ridge axis mapped using high resolution EM300 data [*White et al.*, 2006; *Carbotte et al.,* submitted].

Figure 2. Along axis, stacked 2D seismic lines along the EPR segment with the most prominent reflectors identified (seafloor, layer 2a and axial magma lens - AML). Axis 2r1 shows the image of the oceanic crust along the northern second-order segment, extending from Clipperton TF to the OSC 9º03'N and over its eastern limb (Figure 1). Axis 1 and axis 3 image the southern second-order segment extending over the western limb of the OSC to the Siquieros TF in the south. Grey zones without data show zones of low fold that were not included in seismic data processing.

Figure 3A. Migrated seismic sections (axis 1 and axis 3) along the southern second-order segment with two-way travel time (twtt) picks superimposed for the seafloor (yellow), layer 2a

(green) and AML (red). All picks are shifted ~ 10 ms above the corresponding event for better visibility of the seismic data. Dashed red line with question marks denotes possible AML. Locations of mapped AML interruptions are shown by black arrows with latitude labeled and black bars showing the extent of the AML interruption zone. Grey area without seismic data represents location of low fold, which we exclude from further data analysis. White asterisks and circles denote third- and fourth-order discontinuities in bathymetry, whereas white bars show the extent of the discontinuity zone.

Figure 3B. Migrated seismic section, axis 2r1, along the northern second-order segment with digitized seafloor, layer 2a and AML picks superimposed. Color code, symbols, bars and arrows are the same as in Figure 3A. Blue arrows represent along axis extent of 3D boxes shown in Figure 1. Asterisk next to the 10º04.2'N AML interruption label is to mark that this interruption and interruption zone is mapped along axis 3p2 (line parallel and west of the line axis 2r1).

Figure 4. A) Close up of Moho event imaged along the ridge axis for a portion of axis 2r1 (orange) and axis 3 (green) marked by arrows. The Moho picks are shifted ~ 100 ms upward for better visibility of the event. The AML discontinuities at 9º10' and 9º21.5' are shown in red squares with latitude labeled. B) Depth converted composite profile (axis 2r1 and axis 3) of seafloor (brown), layer 2a (blue), AML (red) and Moho (orange from axis 2r1 and green from axis3) for region shown in A). For depth conversion we use: seafloor v=1500 m/s, layer 2a v=2260 m/s [*Canales et al.,* 2006], layer 2b and layer 3 v=5500 m/s [*Vera et al.*, 1990]. C) Thickness of layer 3 calculated from depth converted picks shown in B). The color code is the same as in A).

Figure 5. Depth to seafloor, layer 2a and AML events along the axis of the EPR from 8°20' to 10°10'N identified from 2D seismic lines located closest to modern axial zone (Figure 1). A) Digitized horizons along southern second-order segment from axis1 (brown) and axis 3 (green). The question marks denote possible AML. B) Digitized horizons along northern second-order segment from axis 2r1 (red) and axis 3p2 (violet). Crustal velocities used to convert digitized horizons from twtt to depth are the same as in Figure 4B. Vertical lines represent AML interruptions identified from the seismic data (the bold ones indicate interruptions in the vicinity of the third-order bathymetric discontinuities). Around the interruptions, the along-axis extent of AML disruption zones is indicated with transparent rectangle (see text). Grey dashed lines show locations of changes in azimuth of the survey line (> 10º) and grey rectangles represent data gaps.

Figure 6. Plan view of twtt and depth below seafloor to the layer 2a horizon digitized from the 3D swath dataset north of 9°20'N and superimposed on grey-shaded regional bathymetry. Twtt-to-depth conversion uses a uniform layer 2a velocity of 2260 m/s. Grey rectangles represent gaps in layer 2a picks introduced by migration aperture. Blue asterisks, dots and bars as in Figure 1.

Figure 7. Plan view of twtt below seafloor to the AML reflection digitized from the 3D swath dataset north of 9º20'N and superimposed on grey shaded regional bathymetry. Open circles show AML interruptions identified from instantaneous phase seismic attribute along each inline within the 3D swath (an example shown in Figure 11B). Open squares represent point locations of AML disruptions picked from 2D axis 2r1 seismic line with latitudes labeled (Figure 3B). Remaining symbols as in Figure 6.

Figure 8. Plan view of depth converted AML picks shown in Figure 7 (depth below seafloor). For depth conversion of the AML horizon, thickness of layer 2b is calculated and added to thickness of layer 2a shown in Figure 6 using same crustal velocities as in Figure 4B. Open circles as in Figure 7, the rest of symbols as in Figure 6.

Figure 9. Examples of AML interruptions: A) strongly dipping event (example from axis 2r1) from adjacent spatially overlapping lens; B) break in AML event with two reflection events overlapping in twtt within zone of weak reflection (example from axis 2r1); C) edge diffraction event (example from axis 1) and D) abrupt change in depth (example from axis 3). Location of each interruption is marked in black arrow with latitude labeled.

Figure 10A. Instantaneous phase seismic attribute section (from -180º to +180º) calculated for AML event for lines axis1 and axis 3 along the southern second-order segment. Locations of visually mapped AML interruptions are shown by black arrows with latitude labeled (as in Figure 3A). Grey rectangle shows location of low fold in the data.

Figure 10B. Instantaneous phase seismic attribute for the AML event along the axis 2r1. The arrows and grey rectangles are the same as in Figure 3B.

Figure 11. A) Close up for AML from migrated inline (#570 in our numbering scheme) extracted from the 3D swath dataset for ~ 9º41’ to 9º54’N. White arrow to mark AML interruptions identified along axis 2r1 line processed in 2D with latitude labeled. B) Instantaneous phase

seismic attribute section (from -180º to +180º) for the AML event along the inline 570 shown in A). Black dots show location of AML interruption identified from the instantaneous phase seismic attribute.

Figure 12. Scatter plots of AML depth below seafloor versus seafloor depth for: A) the southern second-order segment from Siqueiros TF to the 9°03'N OSC and B) the northern second-order segment from the 9°03'N OSC to Clipperton TF. The AML/seafloor picks are from 2D seismic lines shown in Figure 3A and Figure 3B, converted to depth using same velocities as in Figure 4B. Circles show mean AML and seafloor depth (with standard deviation); best fit linear relationship is shown in dashed green line. Mean seafloor and AML depth are 2552±32 m and 1683±184 m, respectively for the southern segment and 2560±28 m and 1597±110 m for the northern segment. Vertical exaggeration 1:5.

Figure 13. Depth to AML below seafloor (bsf) along the whole EPR first-order segment. AML disruptions (shown in vertical grey lines with latitude labeled), which correlate with third-order discontinuities in bathymetry shown in blue asterisks. Mean of AML depth for each third-order segment is given in meters and indicated with orange horizontal line (for the southernmost segment AML depth picks immediately adjacent to Siquieros Transform Fault are excluded from mean depth calculation). Numbers at the bottom of the profile mark nomenclature for third-order segments. Grey double arrow shows the extent of the OSC 9º03'N.

Figure 14. Scatter plots of AML depth below seafloor (bsf) versus seafloor depth for each third order segment: A) along the southern second-order segment and B) along the northern second-

order segment. The third-order segments are grouped and numbered as shown in Figure 13. Colored dots with black bars show mean AML/seafloor depth and standard deviation for each third-order segment. Vertical exaggeration 1:5.

Figure 15. Scatter plots of AML depth below seafloor (bsf) versus seafloor depth for each fourth-order segment: A) along the southern second-order segment and B) along the northern second-order segment. Individual fourth-order segments are color coded as in legend; bars delimit to which third-order segment each of them belongs with the nomenclature nested within the identified third-order segments in Figure 14. Asterisk in the legend is to mark wide discontinuity zone. Vertical exaggeration 1:5.

Figure 16. Tomographic image of mantle P-wave velocity from Toomey et al., [2007] on which we superimpose: location of the ridge axis in black line, third-order bathymetric discontinuities (central location in blue asterisks and zones in blue bars), corresponding AML interruptions (grey dots), and two-way-travel-time to Moho detected along lines axis2r1 and axis3 (Figure 4).

Figure 17. Schematic presentation of magma lens depth versus magma flux through time. A) Each third-order segment has a constant magmatic flux over segment lifetime (***t***), resulting in characteristic AML depth below the seafloor. For instance, segment 1 as the deepest AML has the lowest magmatic flux (MFseg1). Notation beneath the figure (in agreement with schematically represented AML depth) states: for all ***t***, magmatic flux of segment 1 (MFseg1) is lower than magmatic flux of segment 2 (MFseg2), which is lower of that of the segment 3 (MFseg3). Thus, according to the above our data collected in t_0=2008 image characteristic AML

depth during a lifetime of each third-order segment. B) Variable magmatic flux over shorter time intervals (shorter than duration of a third-order segment) within each segment governs segment-to-segment differences in AML depth. The notation beneath the illustration states: magmatic flux integrated over third-order segment lifetime (***t***) remains constant. According to this model, our data collected in t_0=2008 represent a snapshot of AML depth within each third-order segment.

Figure A.1 A) Three swath boxes defined north of 9º20'N: green box azimuth 347.8º, brown and purple box azimuth 351.7º. Brown and purple boxes have different widths to accommodate different number of seismic lines contributing to each (brown box includes axis2r1, axis3p2, and axis4; purple box includes axis2r1 and axis3). B) Step-by-step geometry definition for swath boxes to accommodate azimuth change (see text). C) Illustrated terms used to explain geometry definition of the swath boxes (see text).

Figure B.1. Identification of shots to include within each 3D swath box: A) For case of ship entering in same direction wrong and B) correct way (see the text). Red lines with black dots represent location of shots (shot in flip-flop mode at every 37.5 m); four parallel black lines represent location of streamers towed behind the ship, green lines show down-going P-waves and red lines up-going P-waves. Orange rectangle represents location of pre-defined 3D swath box, for which the shots are determined. In B) gradational colors from orange to blue represent fold (high to low, respectively) of the data within defined box obtained from the included shots.

Figure B.2. Defining shots to include for the case when the ship is exiting the swath box. The elements of the graph are the same as in Figure B.1.

Chapter 1: Figures

Figure 1

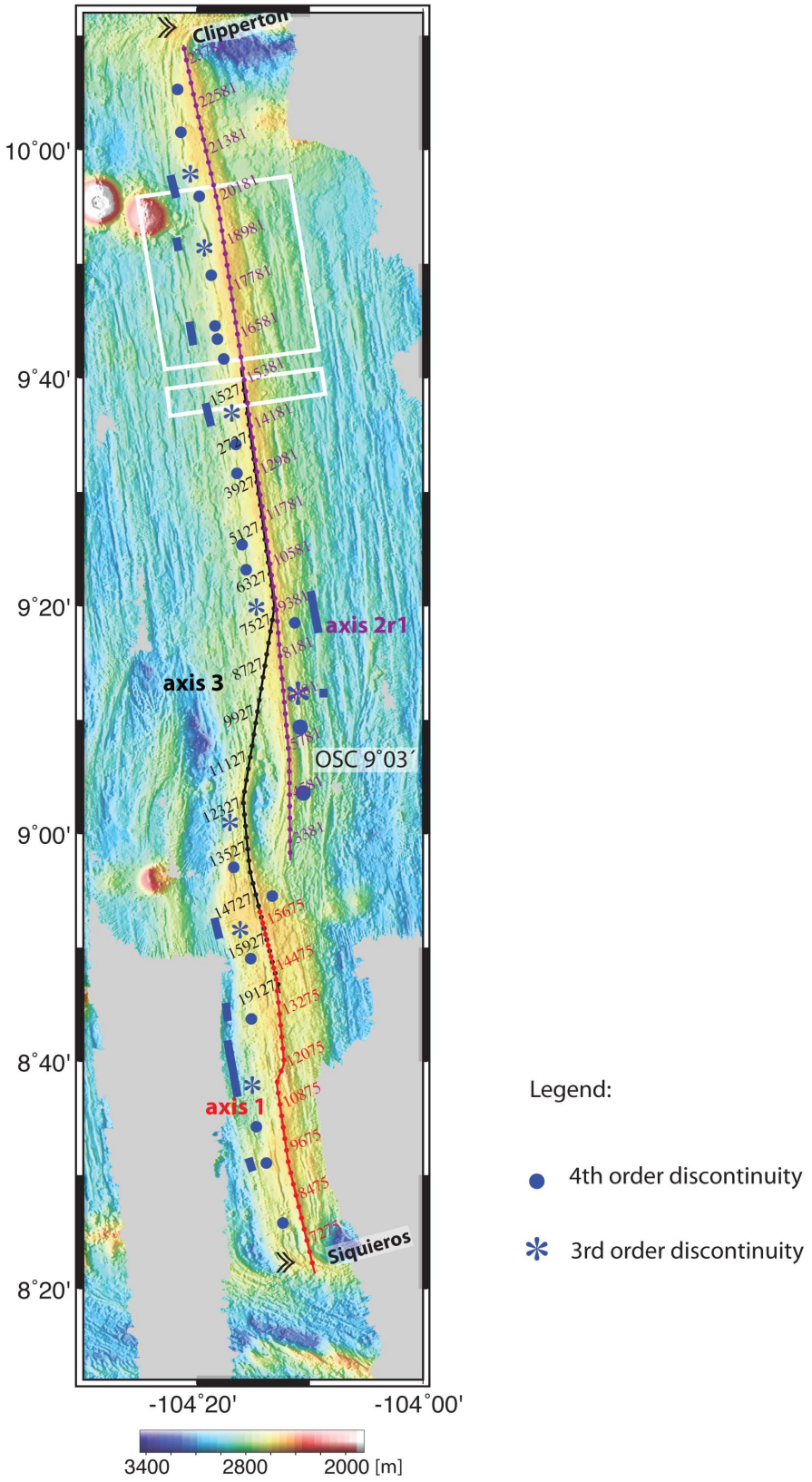
Clipperton
Siquieros
axis 2r1
axis 3
axis 1
OSC 9°03´
10°00'
9°40'
9°20'
9°00'
8°40'
8°20'
-104°20'
-104°00'
3400
2800
2000 [m]
Legend:
4th order discontinuity
3rd order discontinuity

Figure 2

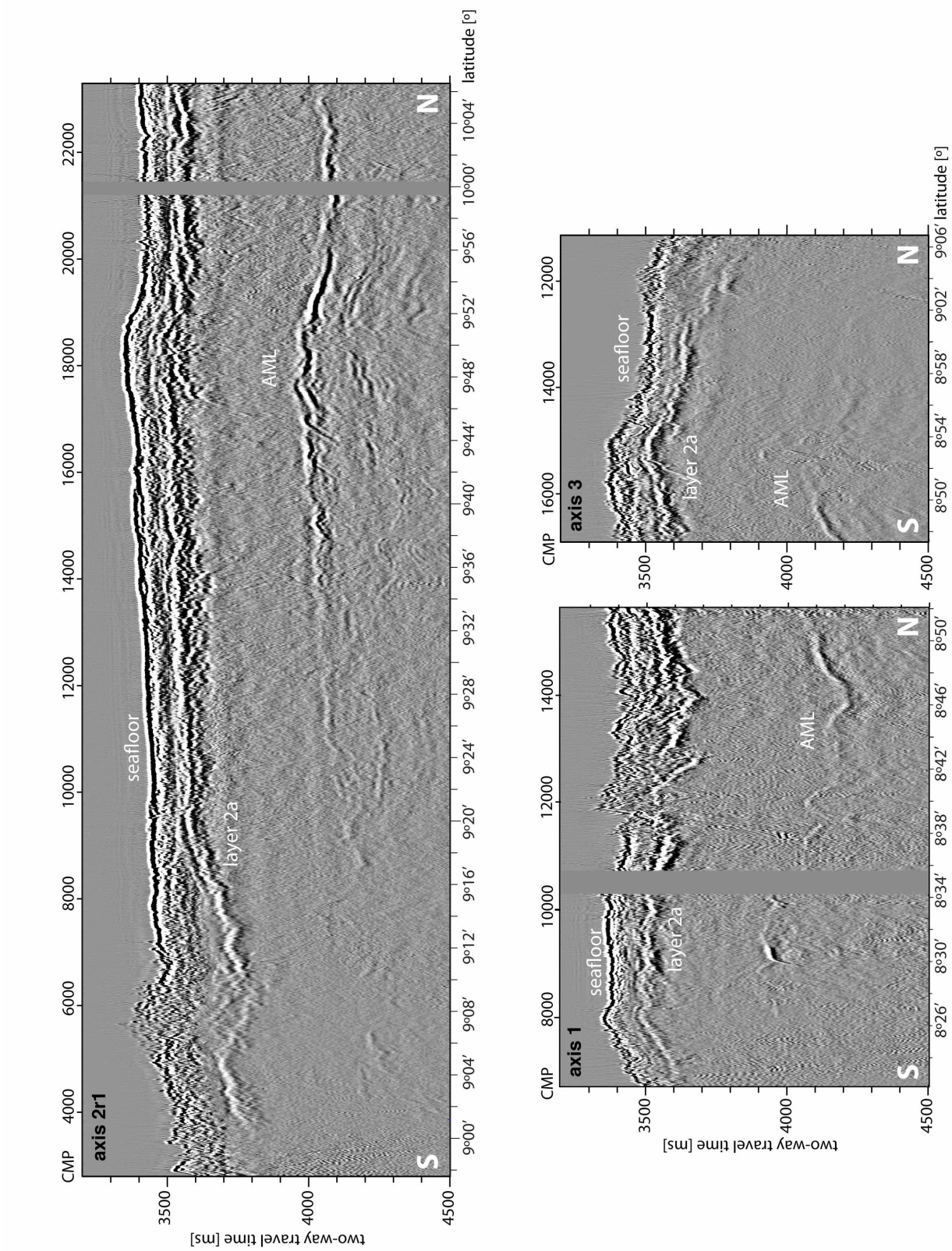
axis 2r1
seafloor
layer 2a
AML
S
N
CMP
two-way travel time [ms]
latitude [°]
axis 1
axis 3

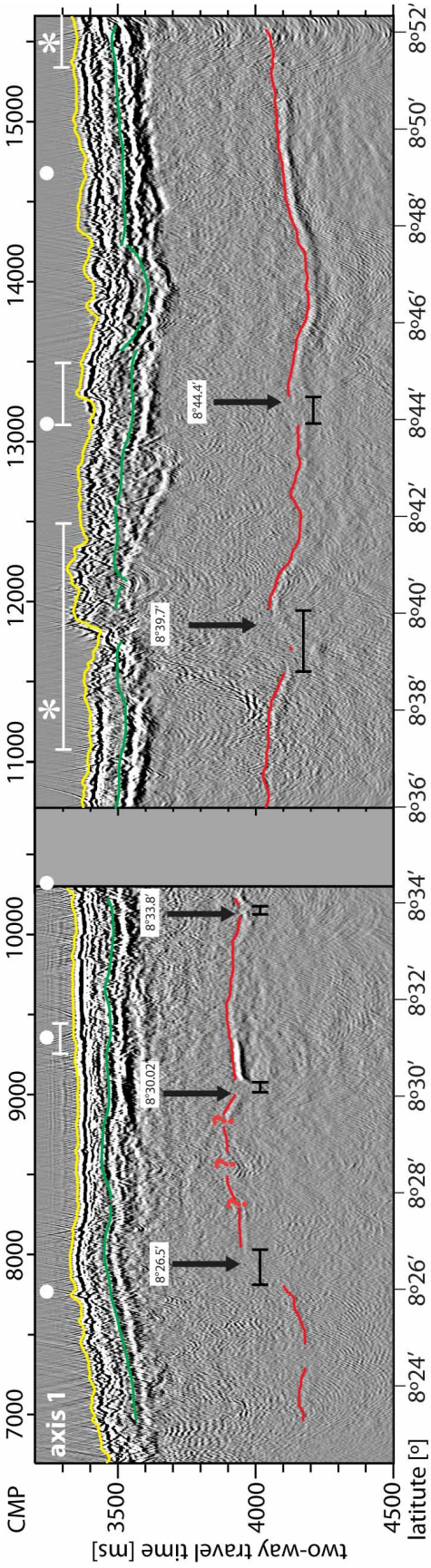
axis 1
CMP
7000
8000
9000
10000
11000
12000
13000
14000
15000
8°24′
8°26′
8°28′
8°30′
8°32′
8°34′
8°36′
8°38′
8°40′
8°42′
8°44′
8°46′
8°48′
8°50′
8°52′
latitute [°]
two-way travel time [ms]
3500
4000
4500
8°26.5′
8°30.02′
8°33.8′
8°39.7′
8°44.4′
H

Figure 3A

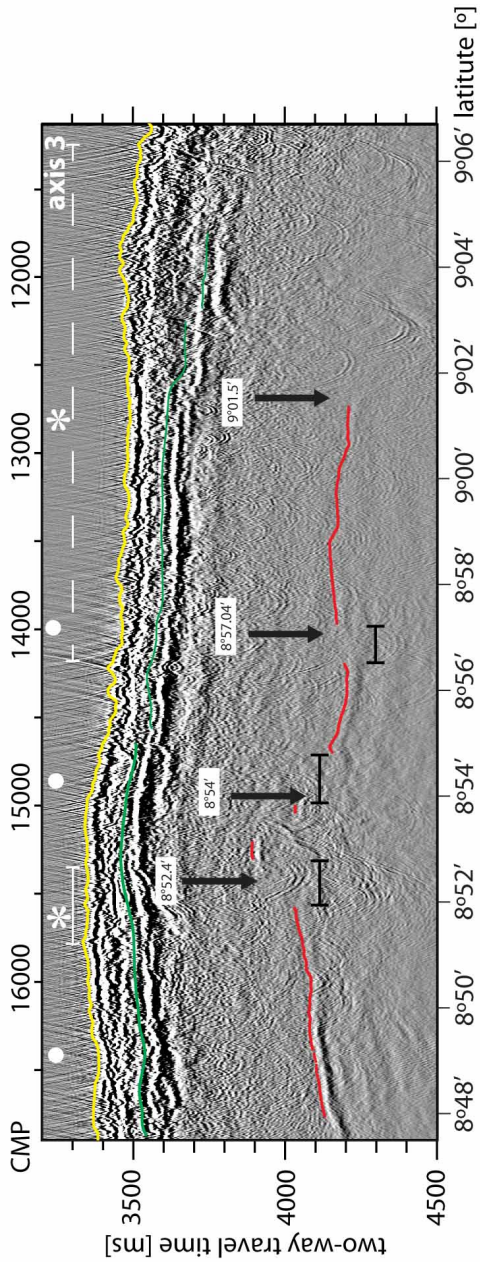
axis 3
CMP
12000
13000
14000
15000
16000
8°48′
8°50′
8°52′
8°54′
8°56′
8°58′
9°00′
9°02′
9°04′
9°06′
latitute [°]
two-way travel time [ms]
3500
4000
4500
8°52.4′
8°54′
8°57.04′
9°01.5′

Figure 3B

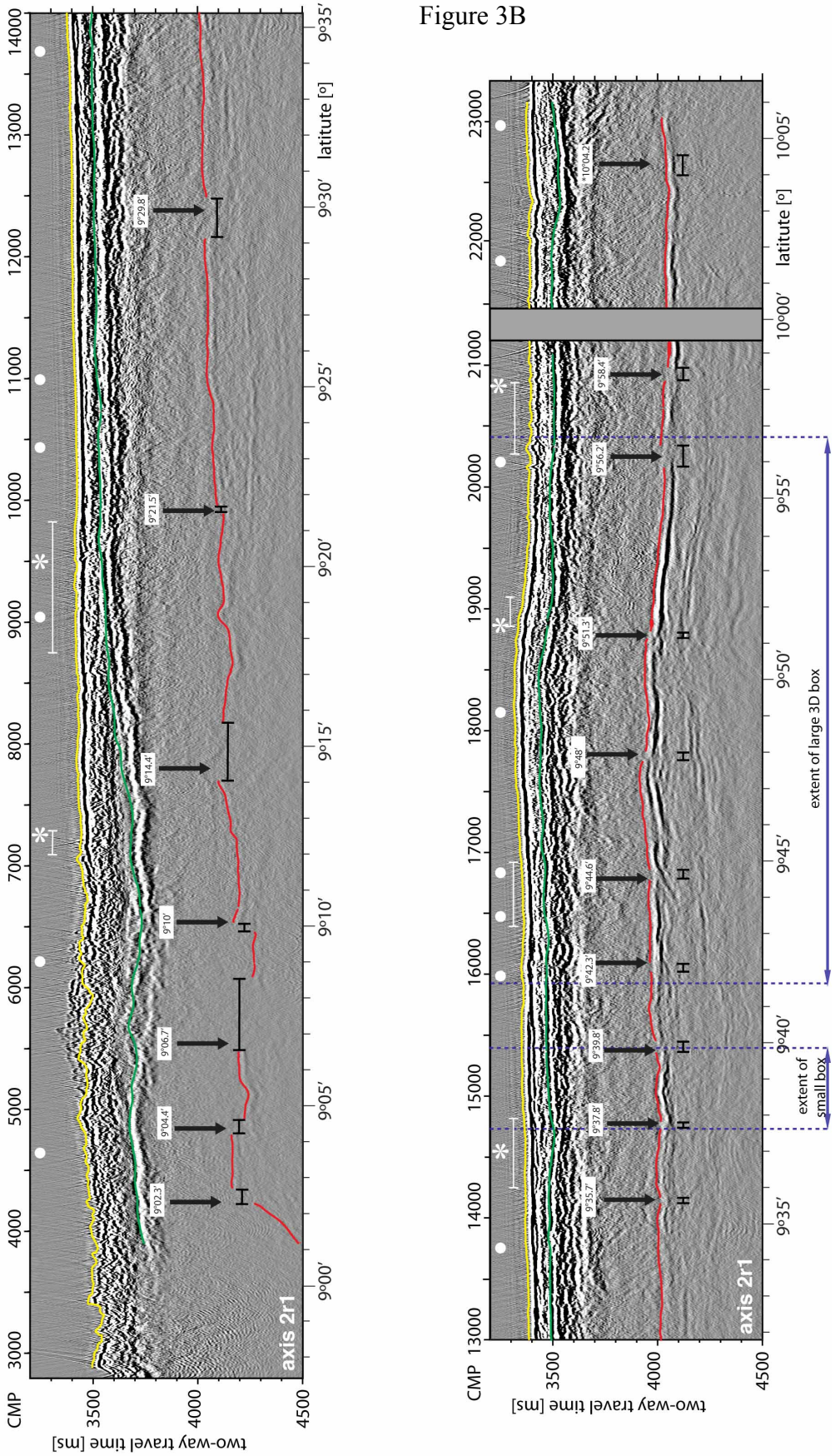
CMP
two-way travel time [ms]
latitute [°]
axis 2r1
extent of large 3D box
extent of small box
9°02.3'
9°04.4'
9°06.7'
9°10'
9°14.4'
9°21.5'
9°29.8'
9°35.7'
9°37.8'
9°39.8'
9°42.3'
9°44.6'
9°48'
9°51.3'
9°56.2'
9°58.4'
10°04.2'

Figure 4

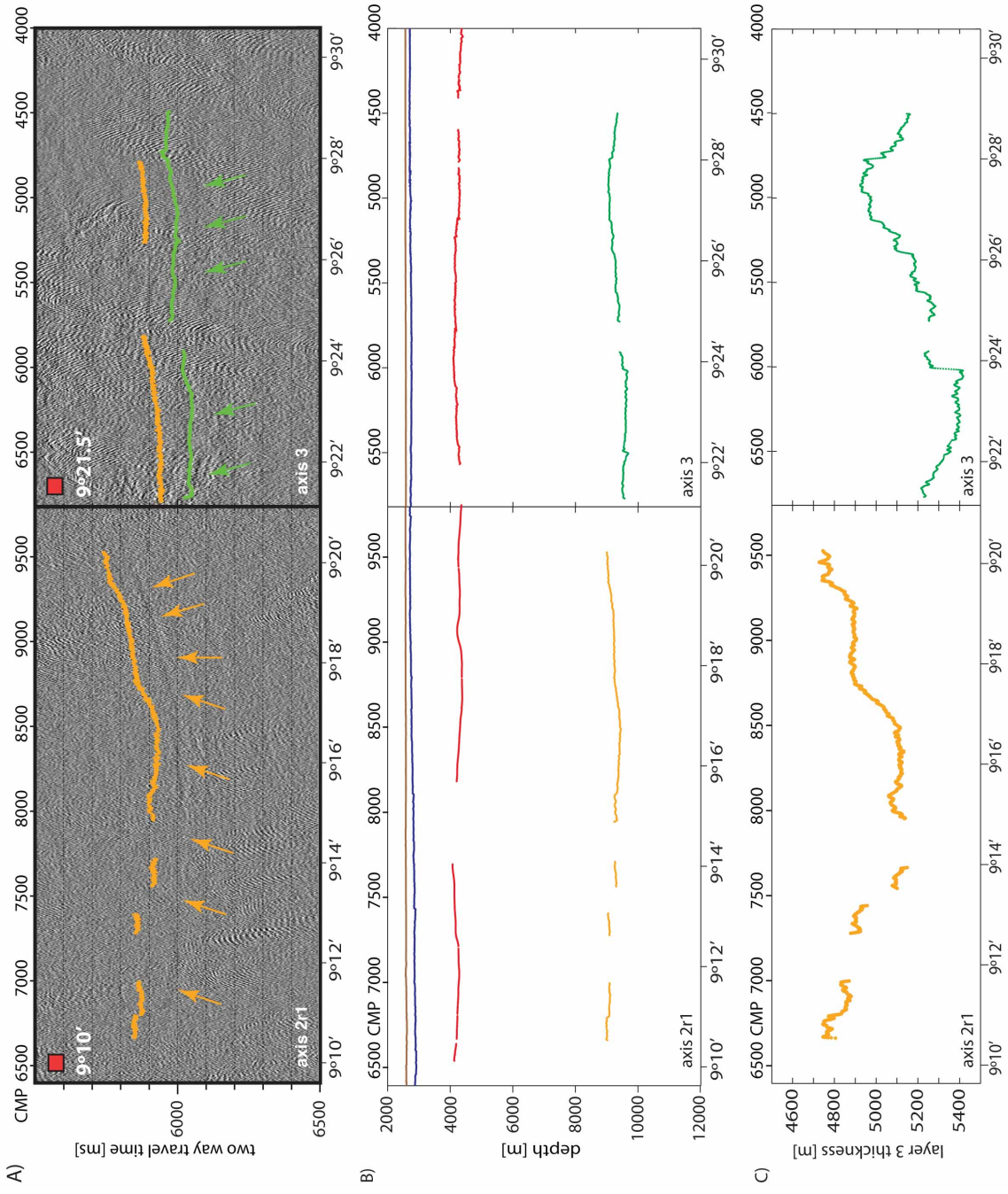
A)
B)
C)
two way travel time [ms]
depth [m]
layer 3 thickness [m]
axis 2r1
axis 3
9°10′
9°21.5′
CMP
9°10′
9°12′
9°14′
9°16′
9°18′
9°20′
9°22′
9°24′
9°26′
9°28′
9°30′

Figure 5

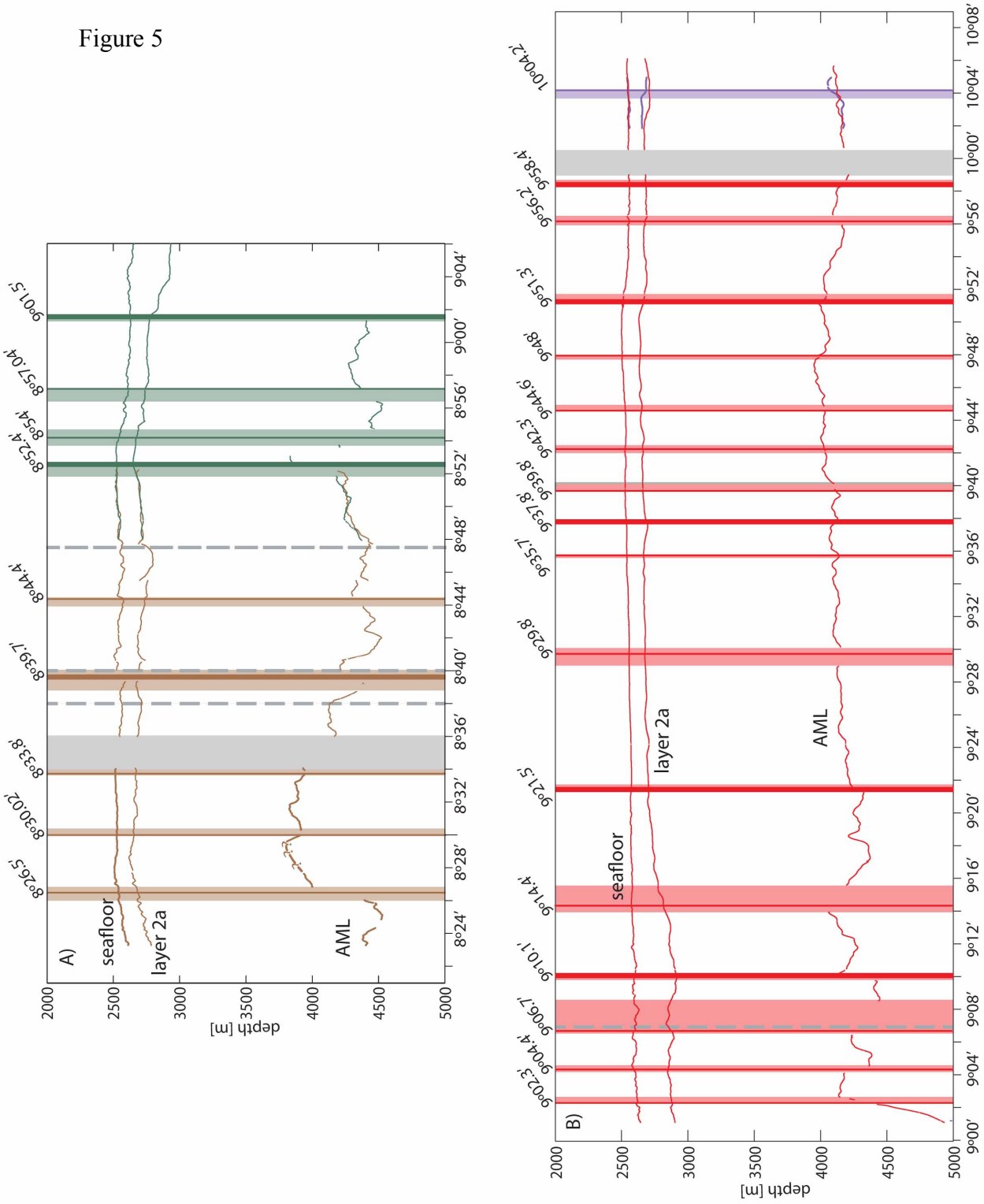
A)
seafloor
layer 2a
AML
depth [m]
2000
2500
3000
3500
4000
4500
5000
8°24′
8°28′
8°32′
8°36′
8°40′
8°44′
8°48′
8°52′
8°56′
9°00′
9°04′
8°26.5′
8°30.02′
8°33.8′
8°39.7′
8°44.4′
8°52.4′
8°54′
8°57.04′
9°01.5′
B)
seafloor
layer 2a
AML
depth [m]
9°00′
9°04′
9°08′
9°12′
9°16′
9°20′
9°24′
9°28′
9°32′
9°36′
9°40′
9°44′
9°48′
9°52′
9°56′
10°00′
10°04′
10°08′
9°02.3′
9°04.4′
9°06.7′
9°10.1′
9°14.4′
9°21.5′
9°29.8′
9°35.7′
9°37.8′
9°39.8′
9°42.3′
9°44.6′
9°48′
9°51.3′
9°56.2′
9°58.4′
10°04.2′

Figure 6

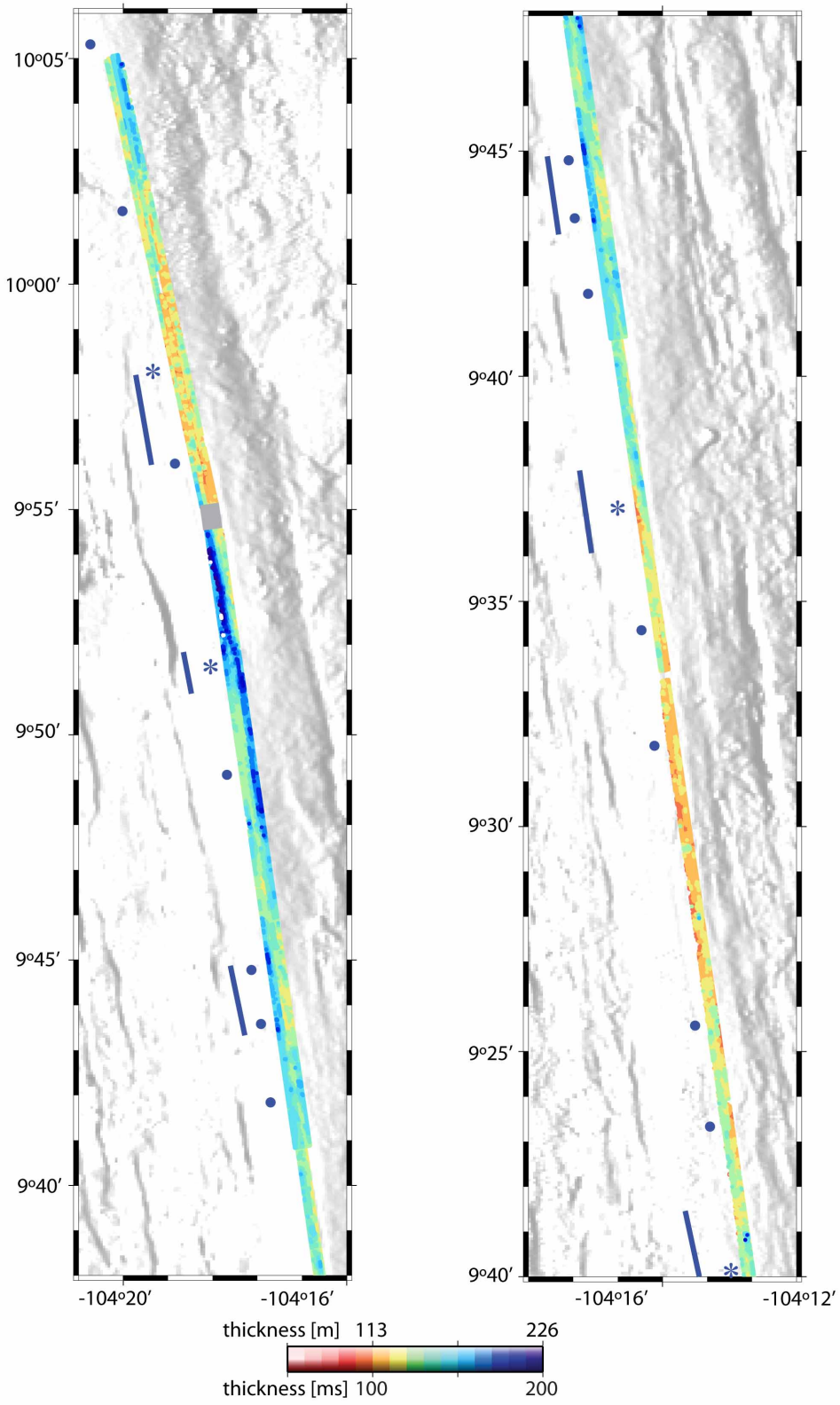
10°05′
10°00′
9°55′
9°50′
9°45′
9°40′
-104°20′
-104°16′
9°45′
9°40′
9°35′
9°30′
9°25′
9°40′
-104°16′
-104°12′
thickness [m] 113 226
thickness [ms] 100 200

Figure 7

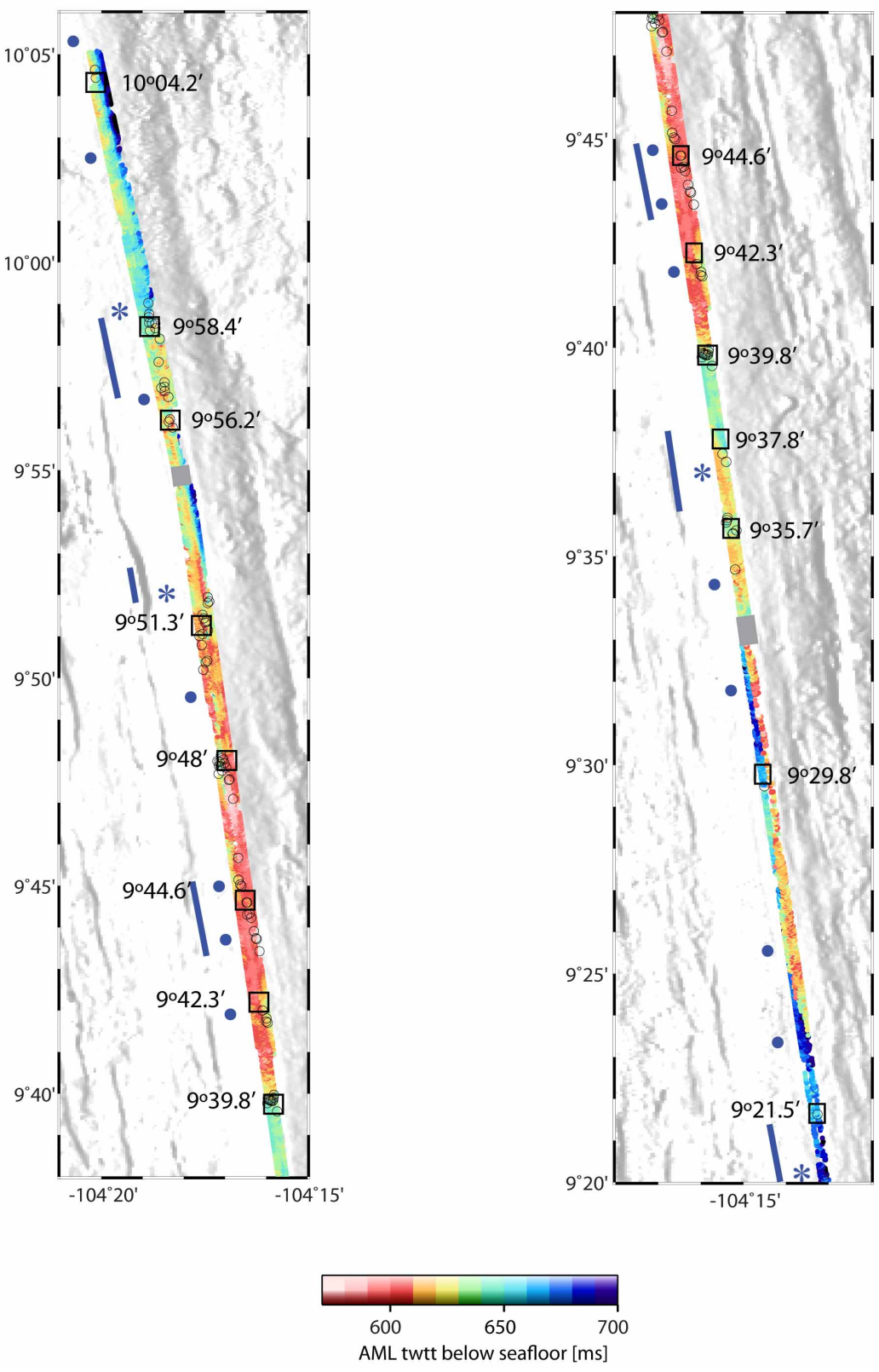
10°05'
10°00'
9°55'
9°50'
9°45'
9°40'
10°04.2′
9°58.4′
9°56.2′
9°51.3′
9°48′
9°44.6′
9°42.3′
9°39.8′
-104°20'
-104°15'
9°45'
9°40'
9°35'
9°30'
9°25'
9°20'
9°44.6′
9°42.3′
9°39.8′
9°37.8′
9°35.7′
9°29.8′
9°21.5′
-104°15'
600
650
700
AML twtt below seafloor [ms]

Figure 8

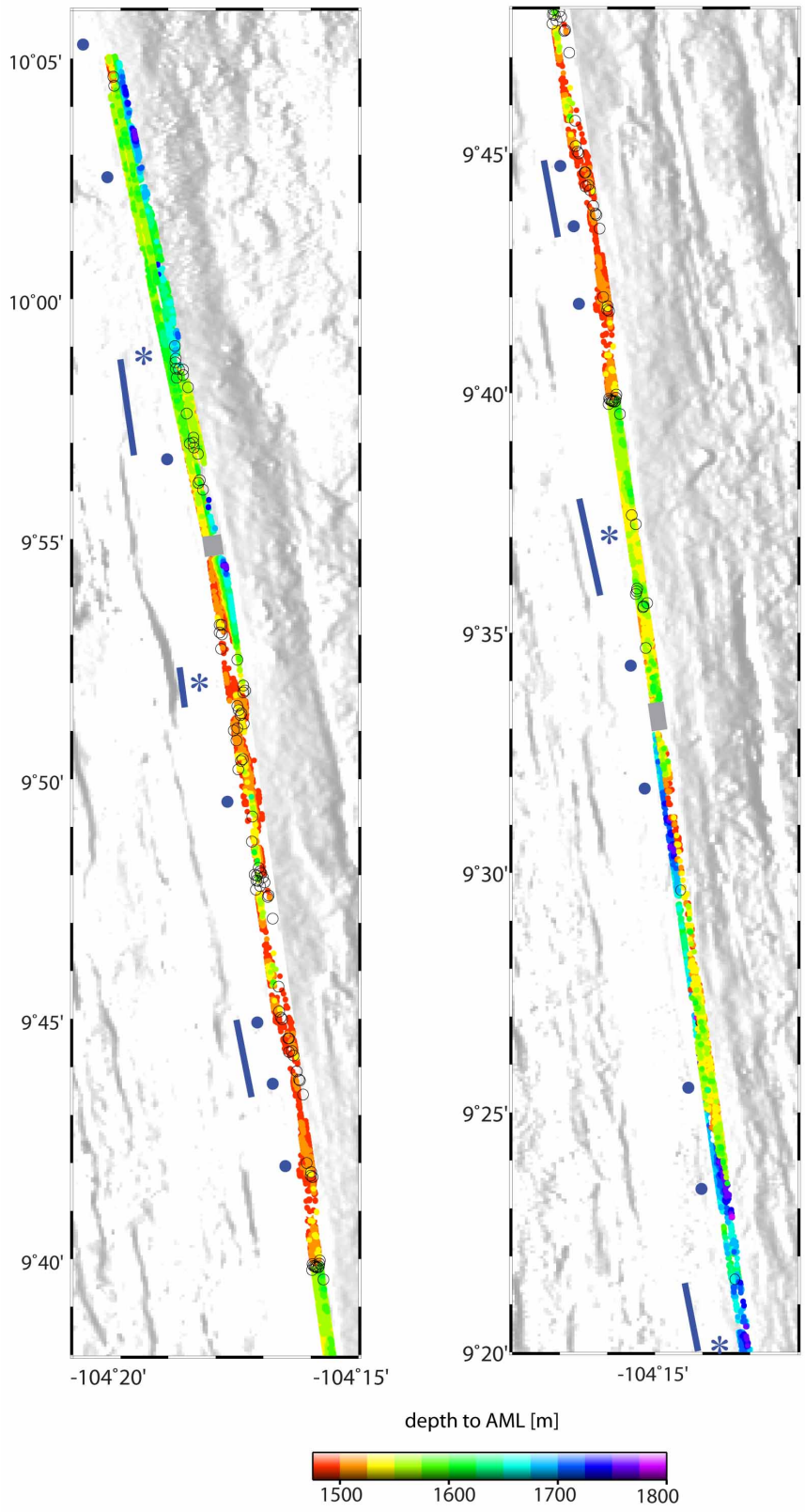
10°05'
10°00'
9°55'
9°50'
9°45'
9°40'
-104°20'
-104°15'
9°45'
9°40'
9°35'
9°30'
9°25'
9°20'
-104°15'
depth to AML [m]
1500
1600
1700
1800

Figure 9

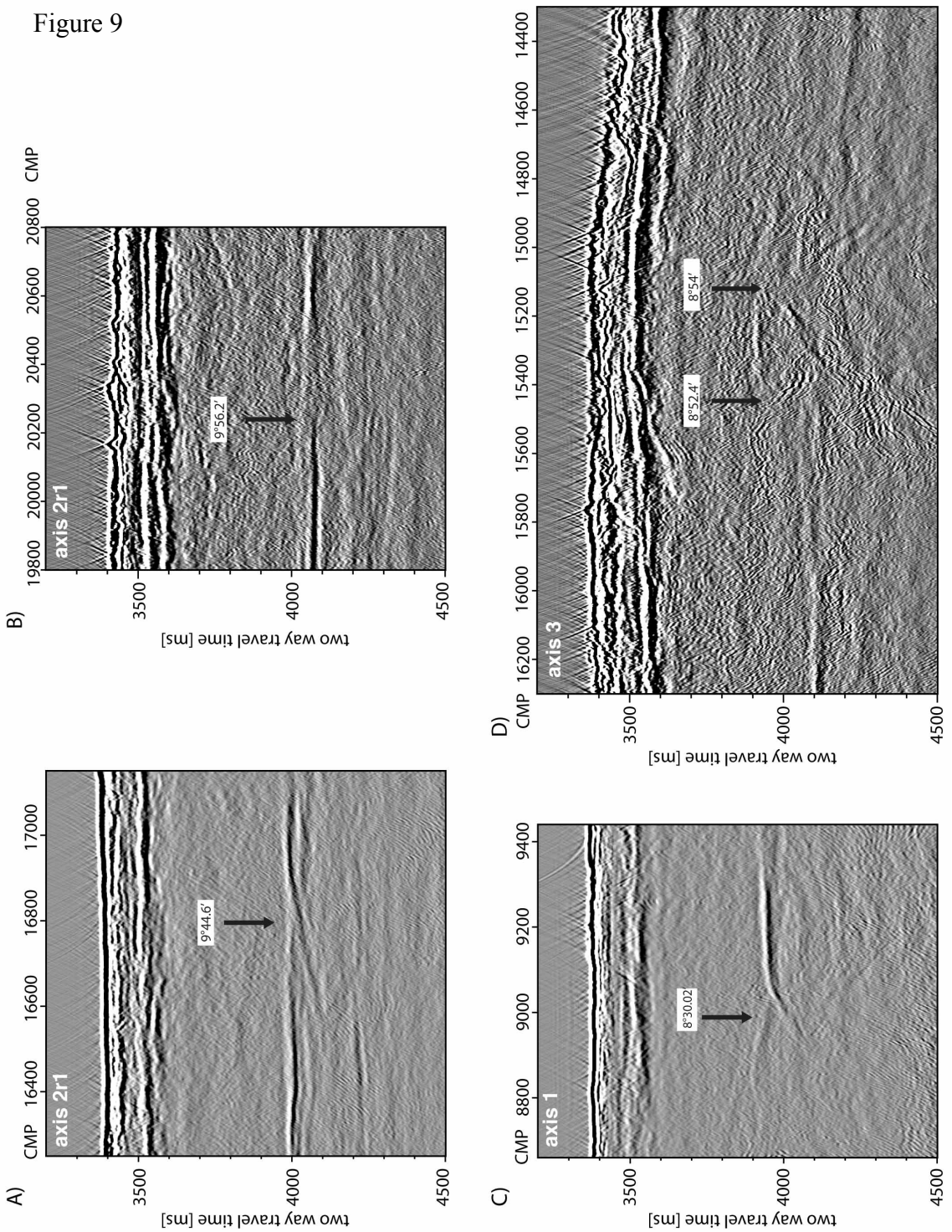
A)
CMP
16400
16600
16800
17000
axis 2r1
9°44.6'
3500
4000
4500
two way travel time [ms]
B)
19800
20000
20200
20400
20600
20800
CMP
axis 2r1
9°56.2'
3500
4000
4500
two way travel time [ms]
C)
CMP
8800
9000
9200
9400
axis 1
8°30.02
3500
4000
4500
two way travel time [ms]
D)
CMP
16200
16000
15800
15600
15400
15200
15000
14800
14600
14400
axis 3
8°52.4'
8°54'
3500
4000
4500
two way travel time [ms]

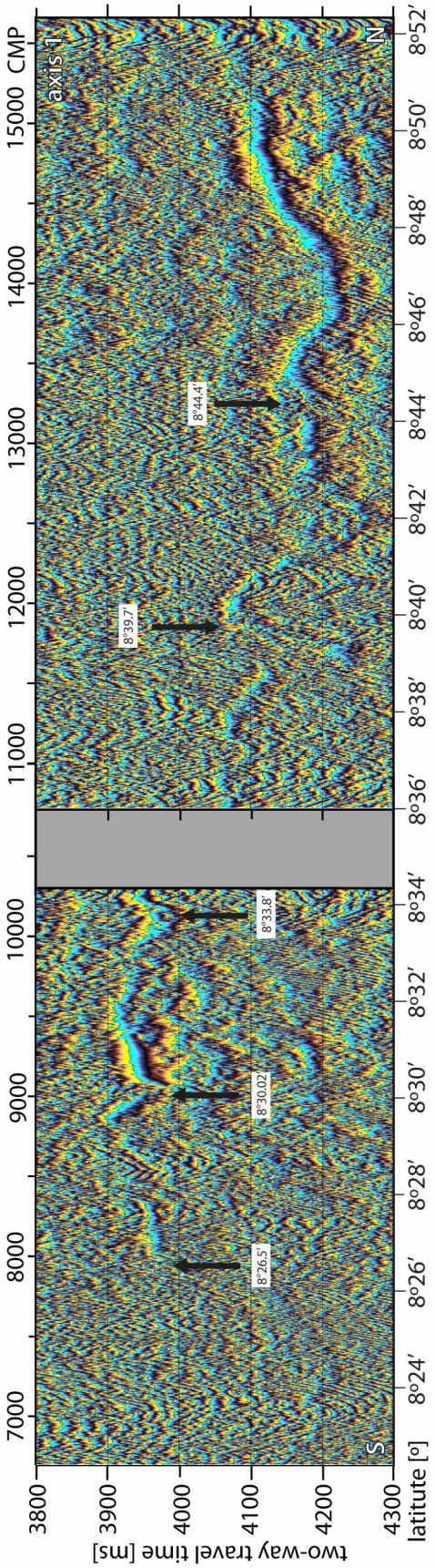
axis 1
CMP
latitude [°]
two-way travel time [ms]
8°26.5'
8°30.02'
8°33.8'
8°39.7'
8°44.4'
S
N

Figure 10A

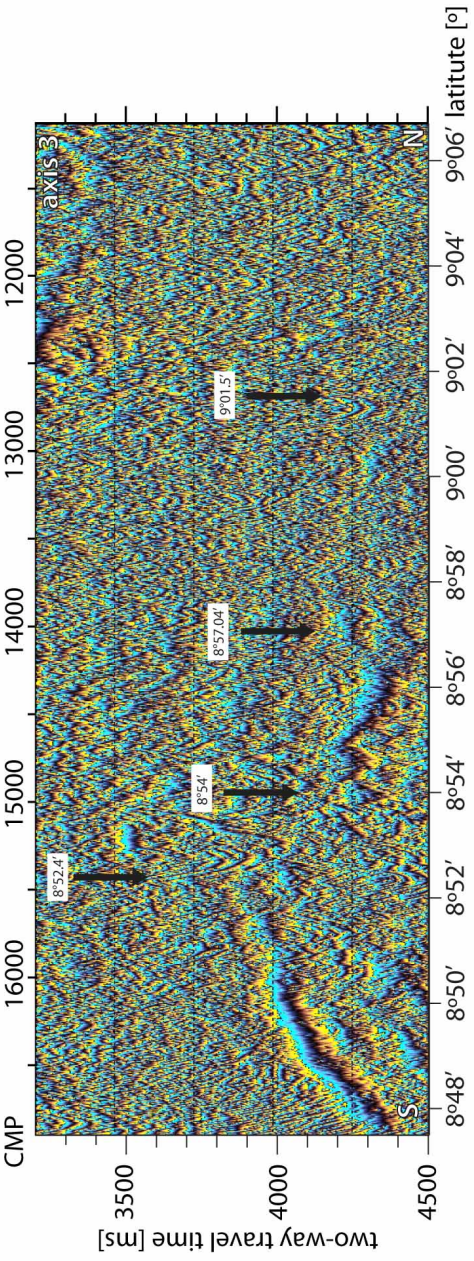
axis 3
CMP
latitude [°]
two-way travel time [ms]
8°52.4'
8°54'
8°57.04'
9°01.5'
S
N

Figure 10B

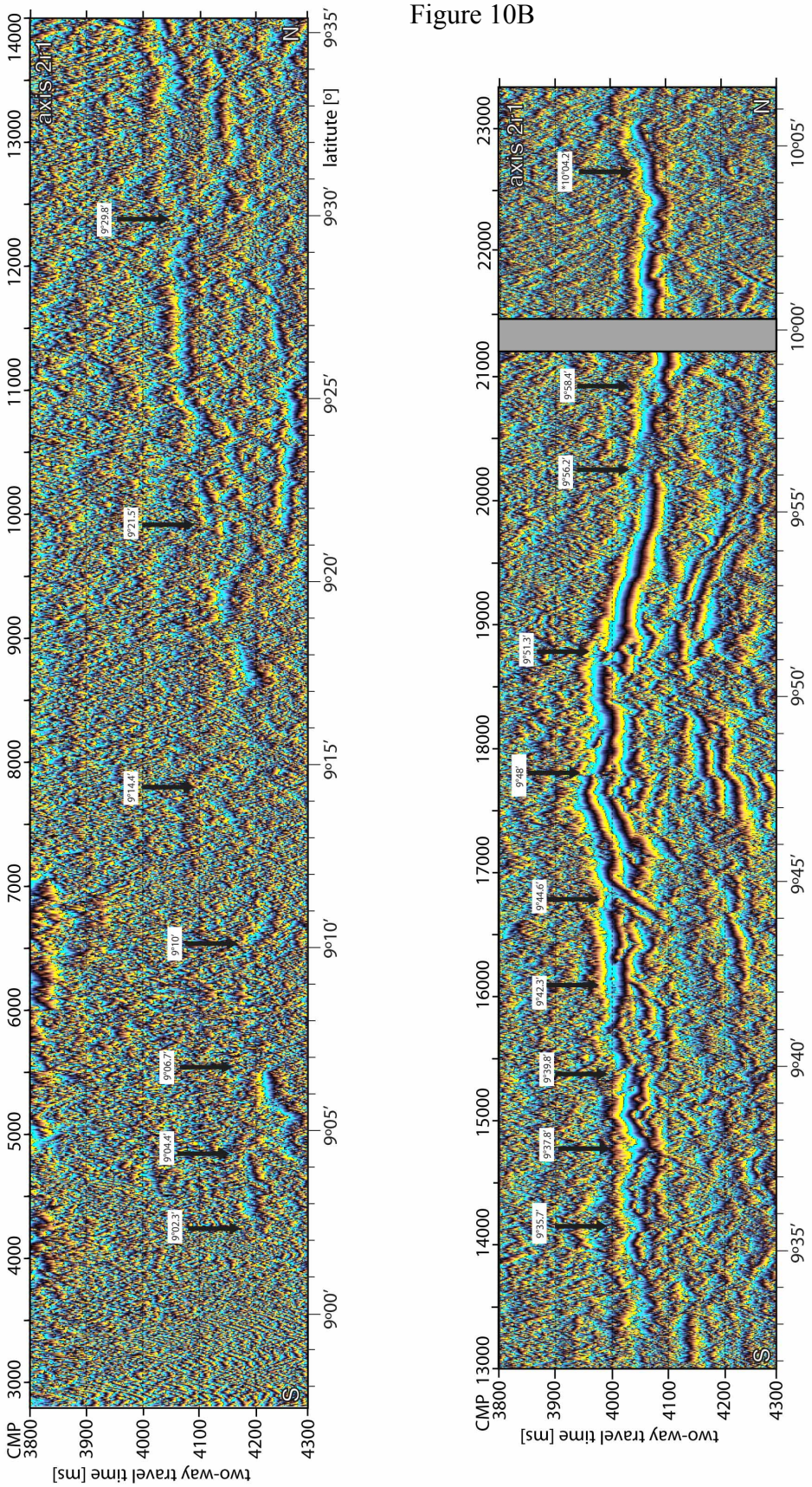
axis 2+1
N
S
CMP
two-way travel time [ms]
latitude [°]
9°02.3'
9°04.4'
9°06.7'
9°10'
9°14.4'
9°21.5'
9°29.8'
9°35.7'
9°37.8'
9°39.8'
9°42.3'
9°44.6'
9°48'
9°51.3'
9°56.2'
9°58.4'
10°04.2'

Figure 11

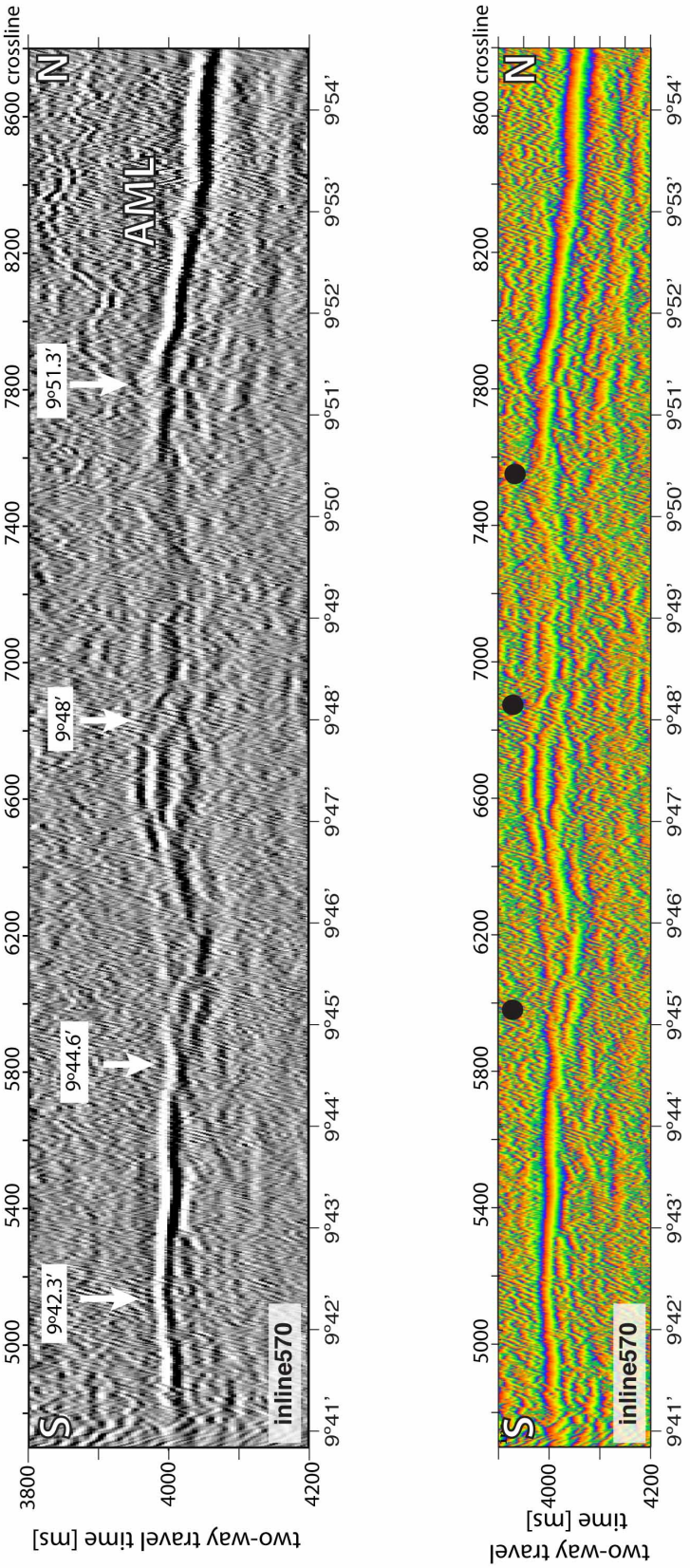
8600 crossline
8200
7800
7400
7000
6600
6200
5800
5400
5000
9°41'
9°42'
9°43'
9°44'
9°45'
9°46'
9°47'
9°48'
9°49'
9°50'
9°51'
9°52'
9°53'
9°54'
S
N
AML
9°42.3'
9°44.6'
9°48'
9°51.3'
inline570
two-way travel time [ms]
3800
4000
4200

Figure 12

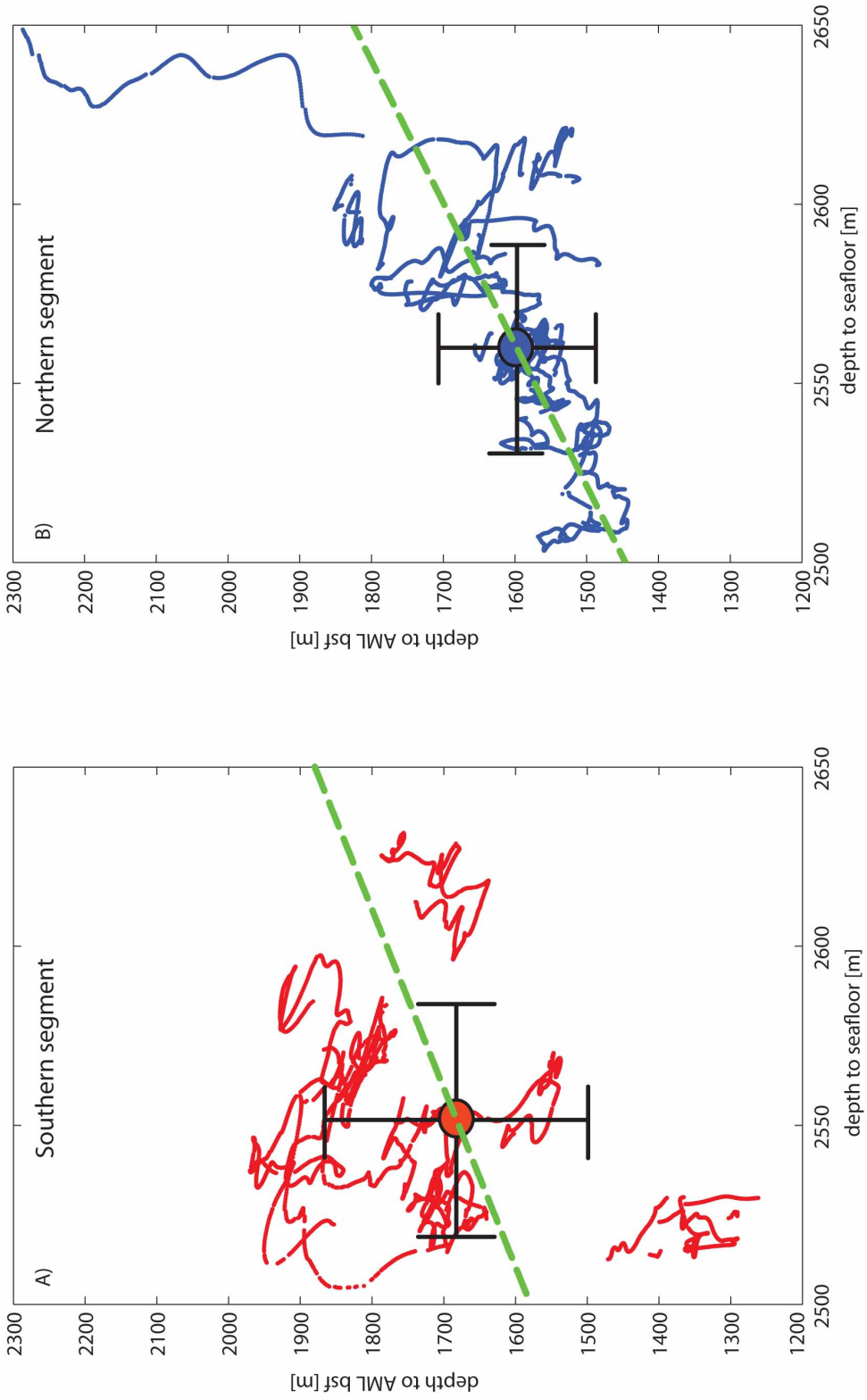
B)
Northern segment
depth to AML bsf [m]
depth to seafloor [m]
2300
2200
2100
2000
1900
1800
1700
1600
1500
1400
1300
1200
2500
2550
2600
2650
A)
Southern segment
depth to AML bsf [m]
depth to seafloor [m]

Figure 13

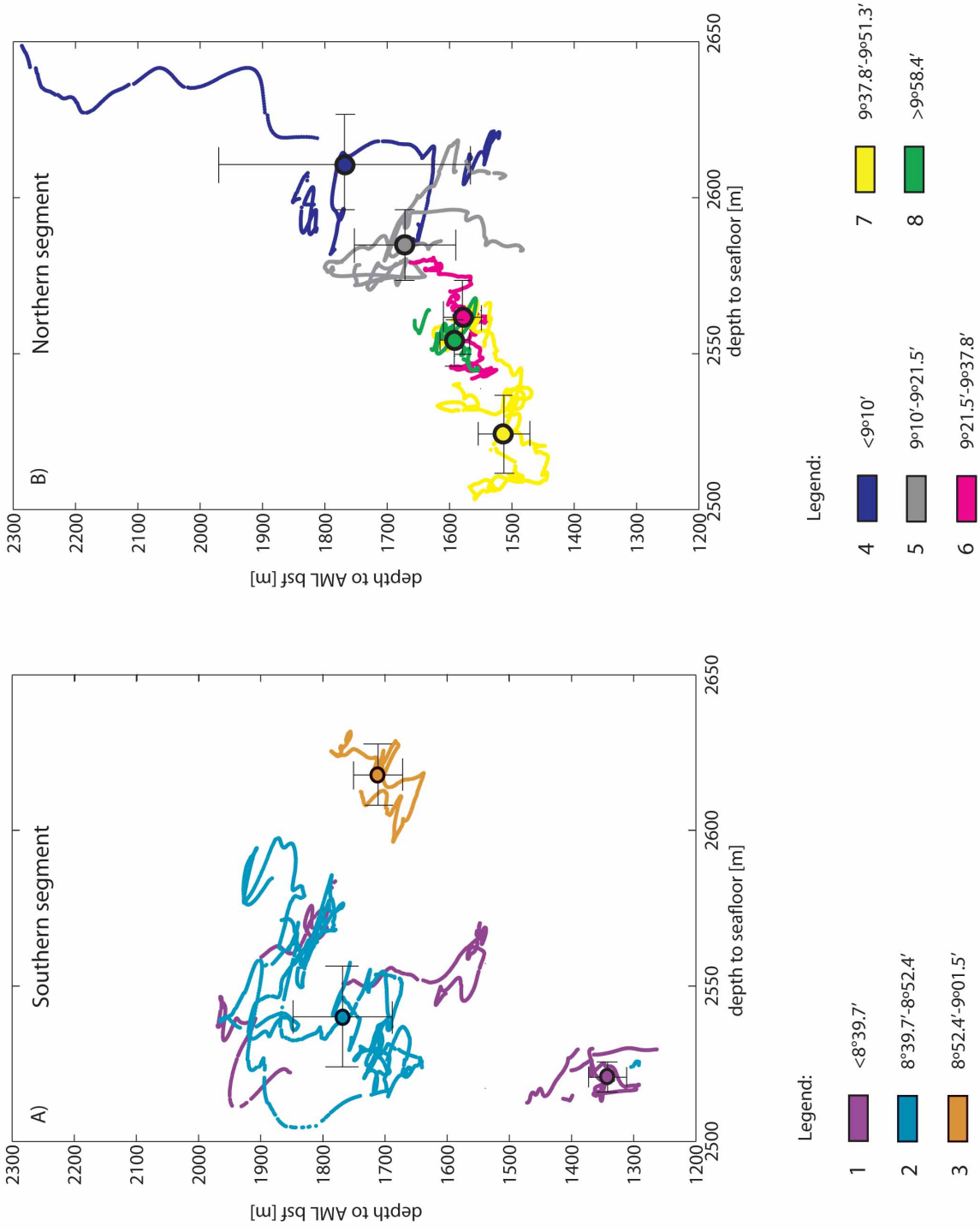
A)
Southern segment
B)
Northern segment
depth to AML bsf [m]
depth to seafloor [m]
2300
2200
2100
2000
1900
1800
1700
1600
1500
1400
1300
1200
2500
2550
2600
2650
Legend:
1 <8°39.7'
2 8°39.7'-8°52.4'
3 8°52.4'-9°01.5'
4 <9°10'
5 9°10'-9°21.5'
6 9°21.5'-9°37.8'
7 9°37.8'-9°51.3'
8 >9°58.4'

Figure 14

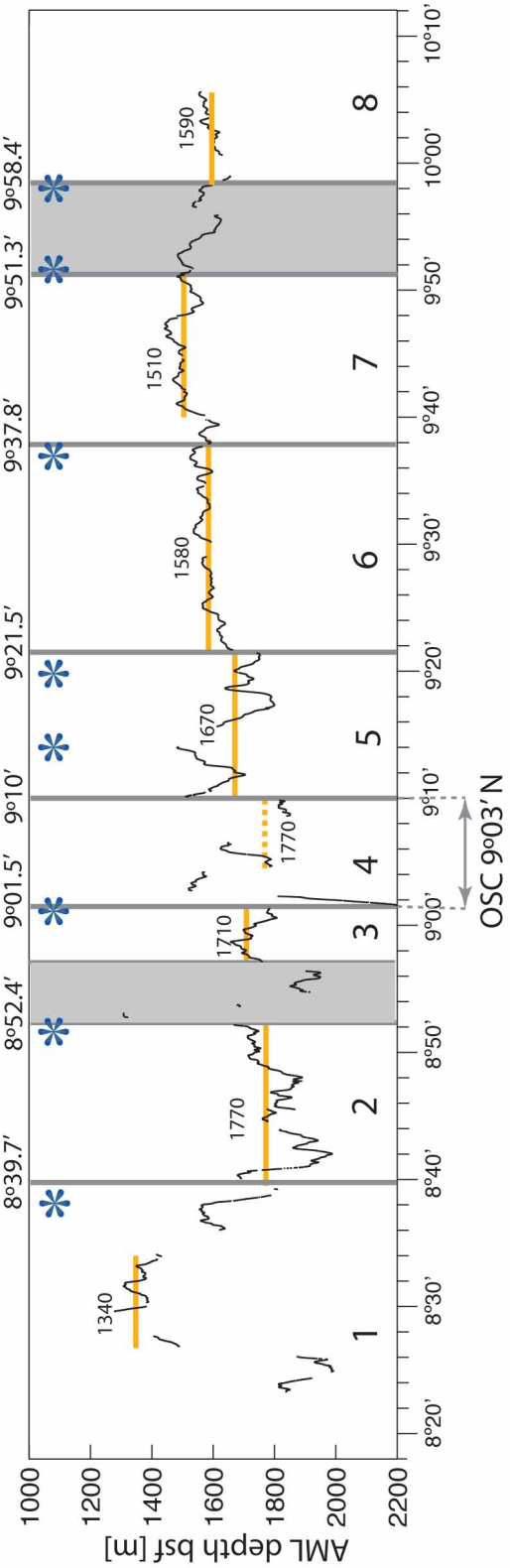
AML depth bsf [m]
1000
1200
1400
1600
1800
2000
2200
8°20′
8°30′
8°39.7′
8°40′
8°50′
8°52.4′
9°00′
9°01.5′
9°10′
9°20′
9°21.5′
9°30′
9°37.8′
9°40′
9°50′
9°51.3′
9°58.4′
10°00′
10°10′
1
2
3
4
5
6
7
8
1340
1770
1710
1770
1670
1580
1510
1590
OSC 9°03′N

Figure 15

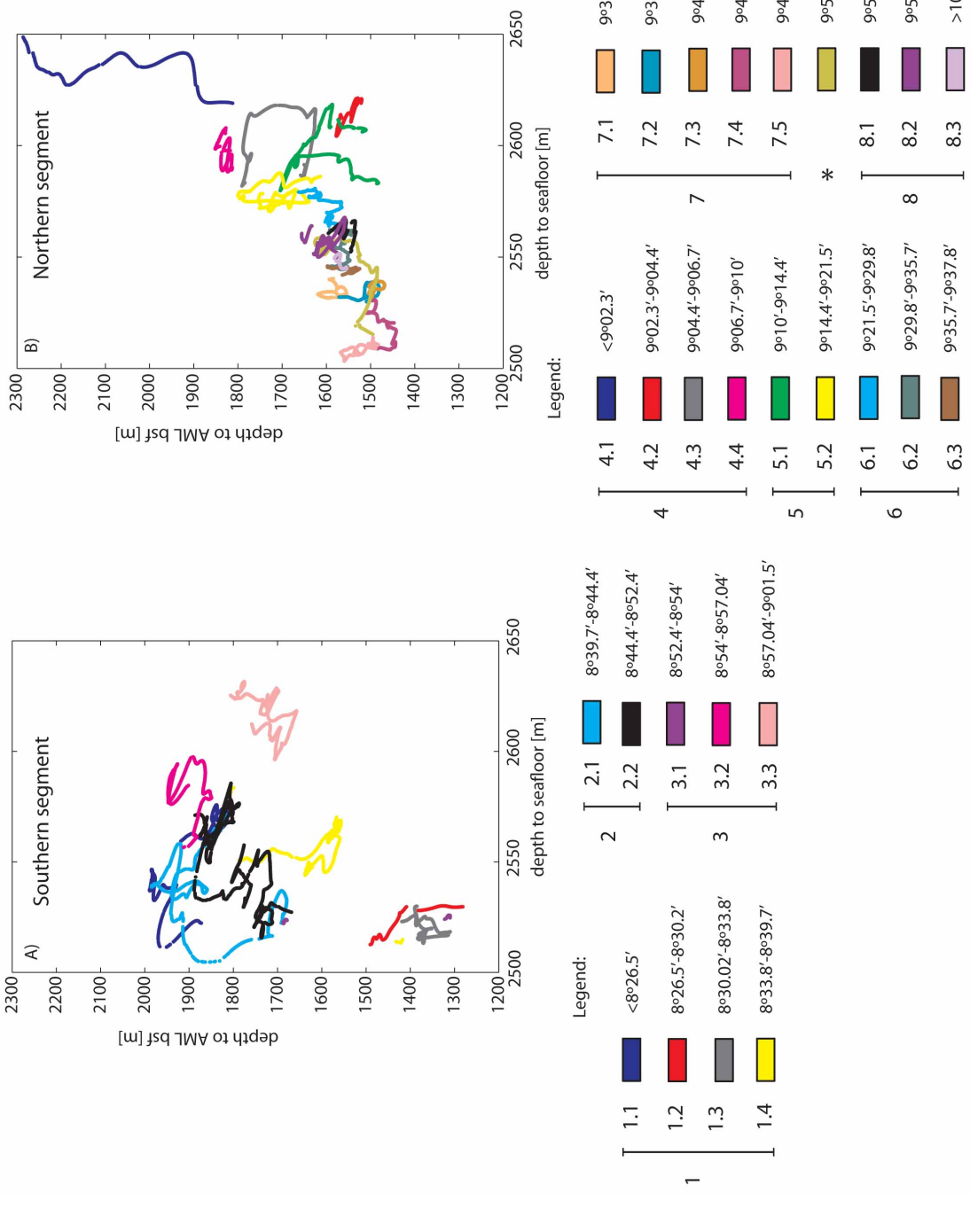
A)
Southern segment
depth to AML bsf [m]
depth to seafloor [m]
B)
Northern segment
depth to AML bsf [m]
depth to seafloor [m]
Legend:
1
1.1 <8°26.5′
1.2 8°26.5′-8°30.2′
1.3 8°30.02′-8°33.8′
1.4 8°33.8′-8°39.7′
2
2.1 8°39.7′-8°44.4′
2.2 8°44.4′-8°52.4′
3
3.1 8°52.4′-8°54′
3.2 8°54′-8°57.04′
3.3 8°57.04′-9°01.5′
4
4.1 <9°02.3′
4.2 9°02.3′-9°04.4′
4.3 9°04.4′-9°06.7′
4.4 9°06.7′-9°10′
5
5.1 9°10′-9°14.4′
5.2 9°14.4′-9°21.5′
6
6.1 9°21.5′-9°29.8′
6.2 9°29.8′-9°35.7′
6.3 9°35.7′-9°37.8′
7
7.1 9°37.8-9°39.8′
7.2 9°39.8′-9°42.3′
7.3 9°42.3′-9°44.6′
7.4 9°44.6′-9°48′
7.5 9°48′-9°51.3′
*
9°51.3-9°56.2′
8
8.1 9°56.2′-9°58.4′
8.2 9°58.4′-10°04.2′
8.3 >10°04.2′

Figure 16

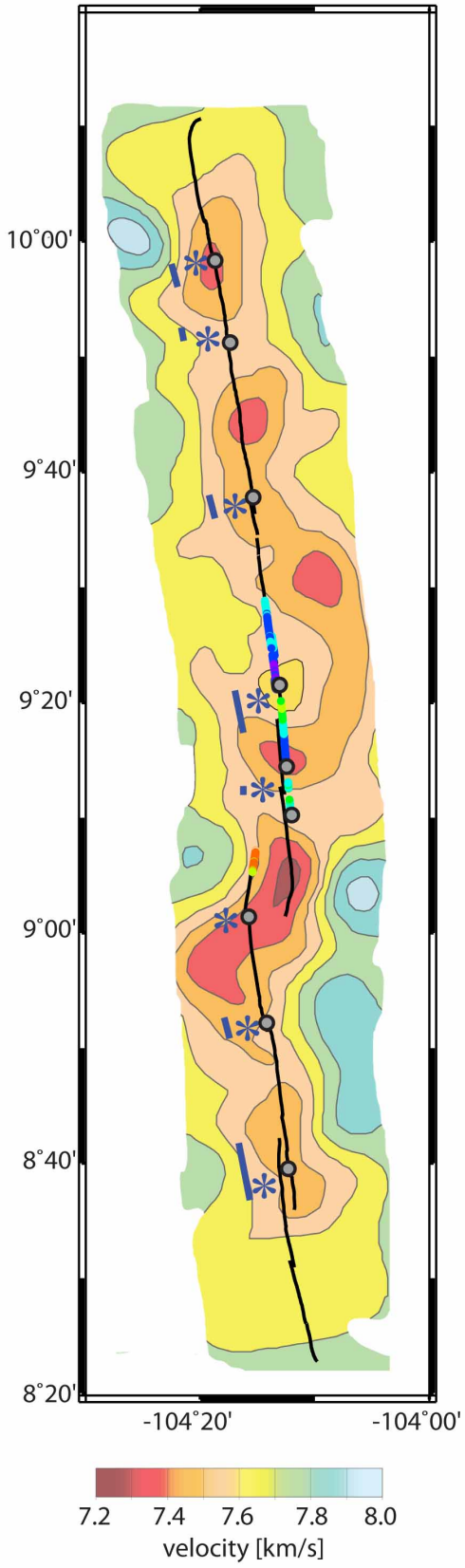
10˚00'
9˚40'
9˚20'
9˚00'
8˚40'
8˚20'
-104˚20'
-104˚00'
7.2
7.4
7.6
7.8
8.0
velocity [km/s]

Figure 17

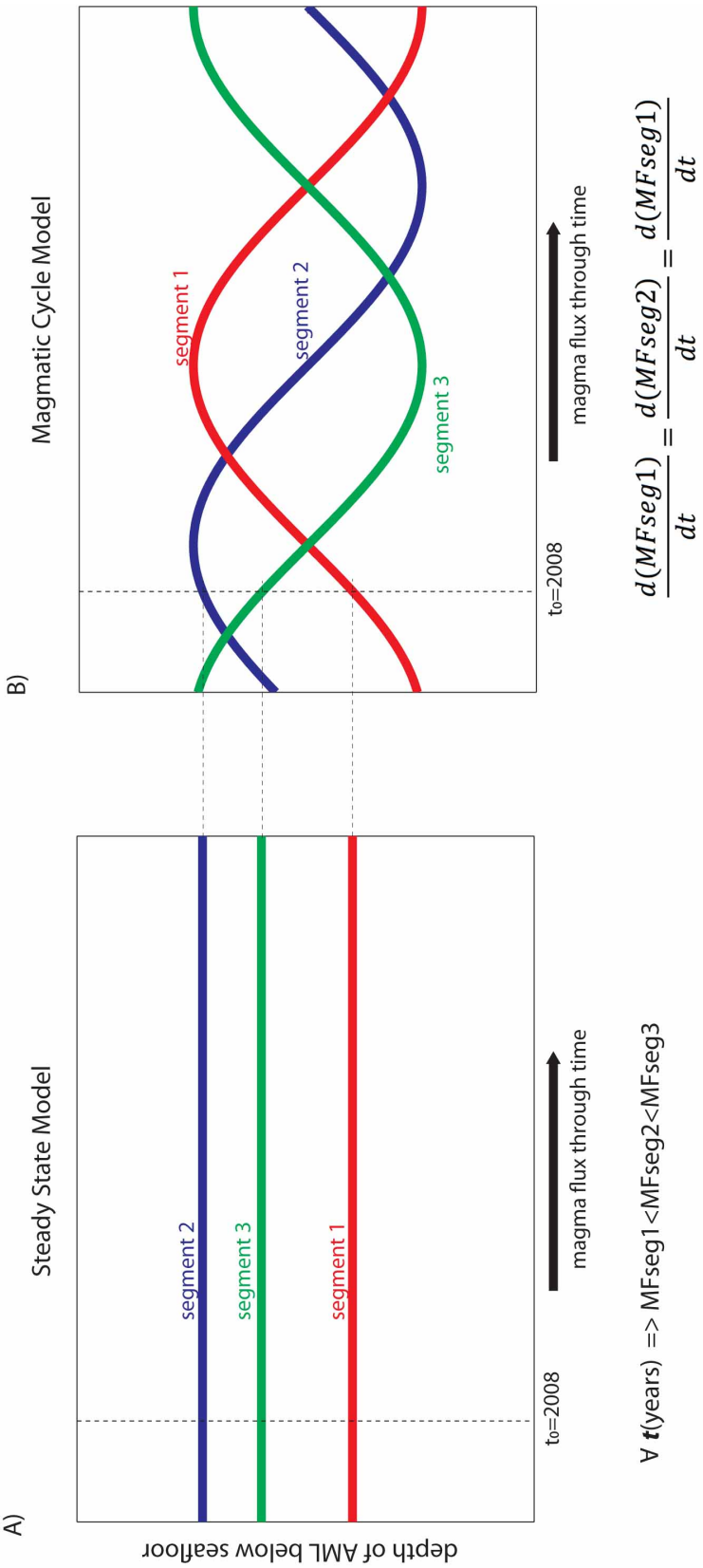
A)
Steady State Model
segment 2
segment 3
segment 1
to=2008
magma flux through time
depth of AML below seafloor
B)
Magmatic Cycle Model
segment 1
segment 2
segment 3
to=2008
magma flux through time
∀ t(years) => MFseg1<MFseg2<MFseg3
$\frac{d(MFseg1)}{dt} = \frac{d(MFseg2)}{dt} = \frac{d(MFseg1)}{dt}$

Appendix Figures from Chapter 1

Figure A.1

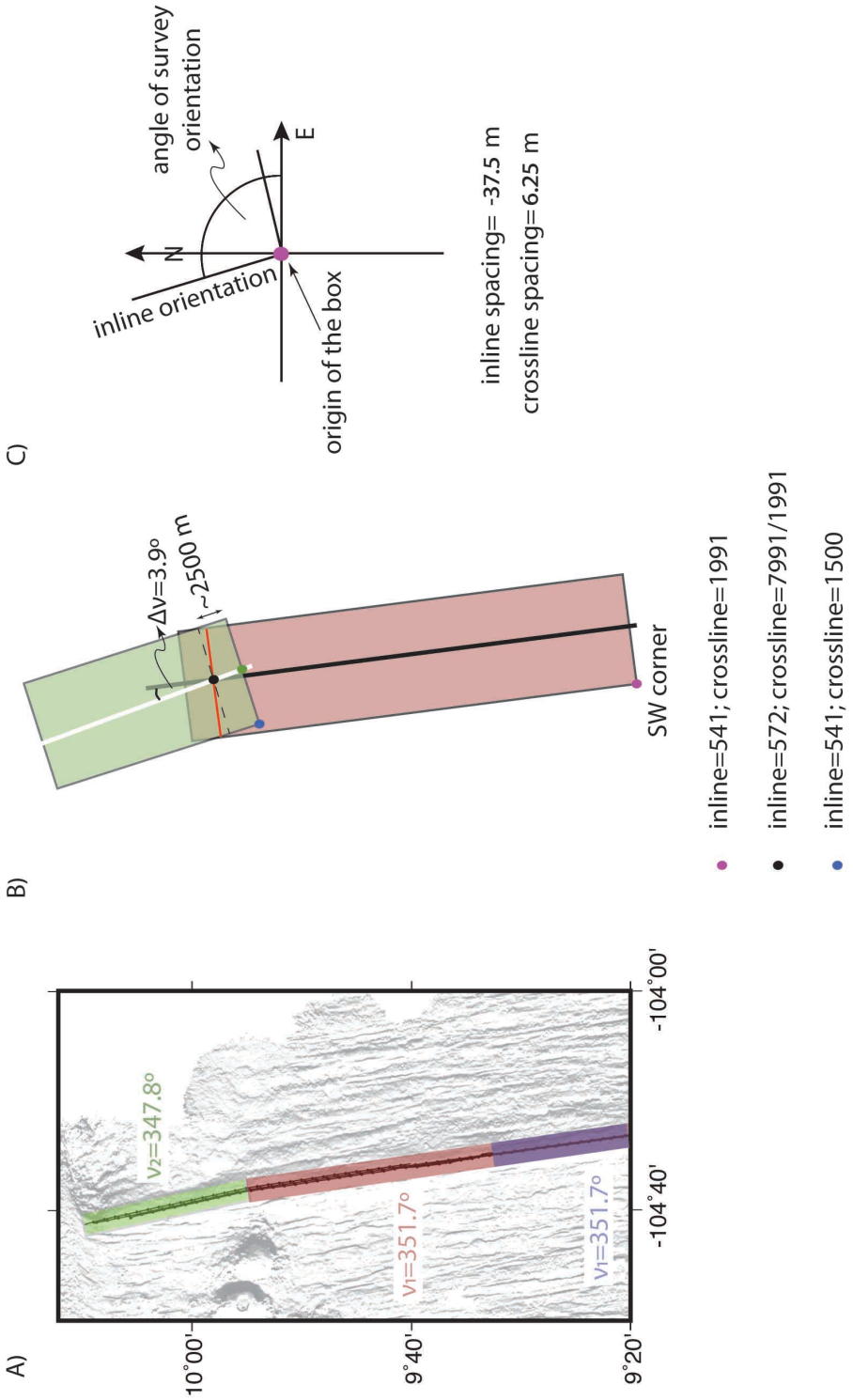
A)
B)
C)
10°00'
9°40'
9°20'
-104°00'
-104°40'
v2=347.8°
v1=351.7°
v1=351.7°
Δv=3.9°
~2500 m
SW corner
angle of survey orientation
N
E
inline orientation
origin of the box
inline spacing= -37.5 m
crossline spacing= 6.25 m
inline=541; crossline=1991
inline=572; crossline=7991/1991
inline=541; crossline=1500

Figure B.1

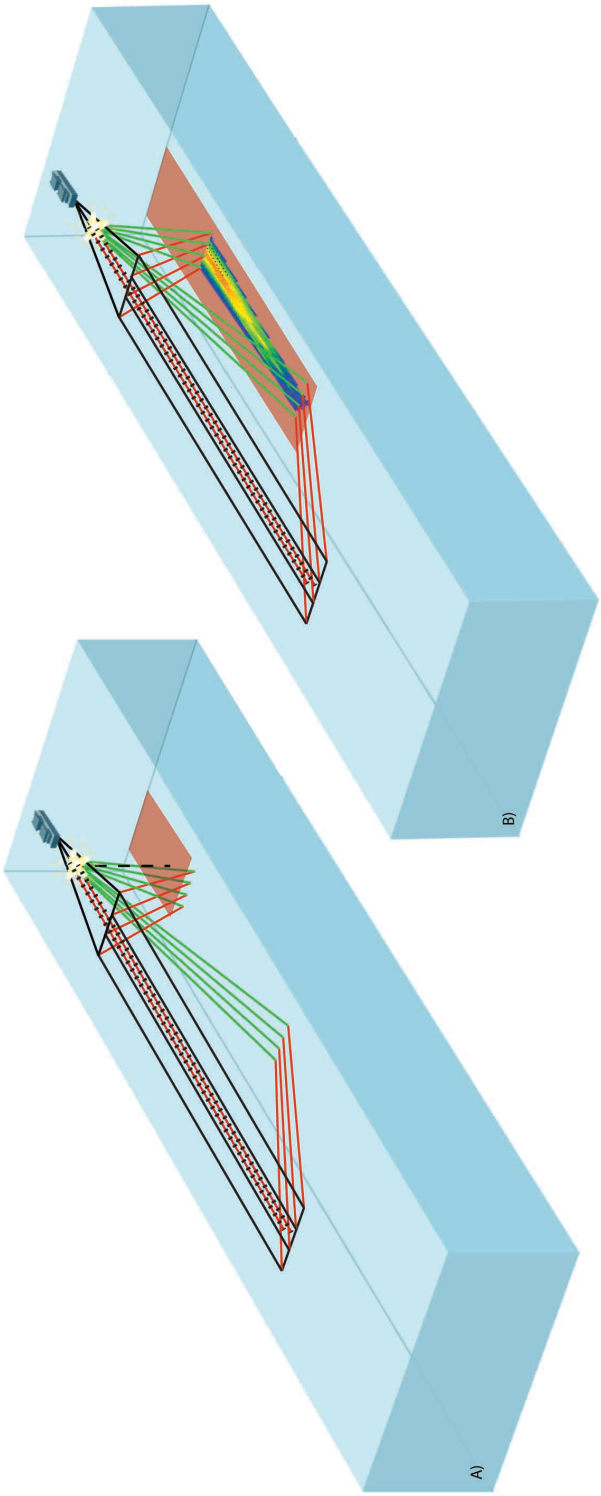

Figure B.2

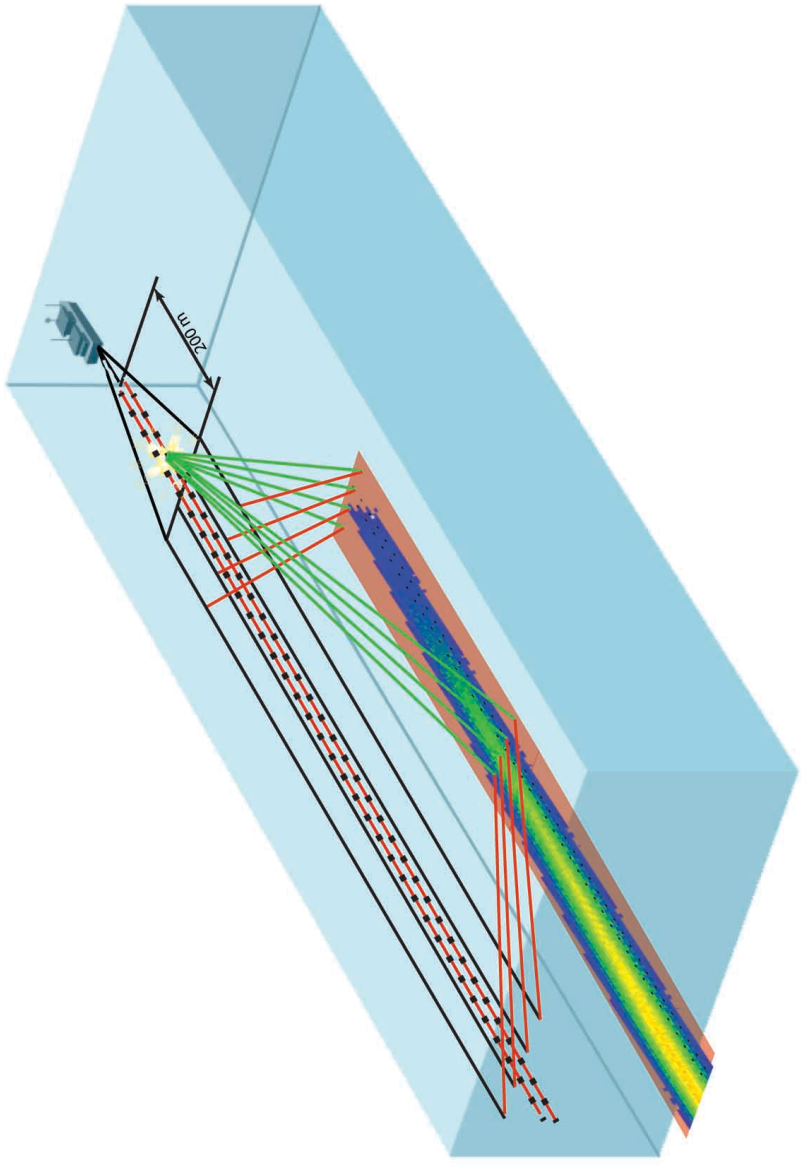

Chapter 2

"Distribution of melt along the East Pacific Rise from 9º30' to 10ºN from an amplitude variation with angle of incidence (AVA) technique"[*]

[*] This manuscript is in preparation for submission to Geophysical Journal International with co-authors: Carton H.D, S. M. Carbotte, J. C. Mutter, M. R. Nedimović and J. P. Canales.

ABSTRACT

Multichannel seismic (MCS) data collected in 2008 along the crest of the East Pacific Rise (EPR) 8º20'-10º10'N offer an excellent opportunity for studying along-axis variations in seismic properties of the mid-crustal magma lens (or sill) imaged at ~ 1.6 km below seafloor and inferred along-axis variations in the physical properties of this melt body. Locally, pre-stack data show decrease in amplitude of P-wave reflection signal off the magma sill as a function of angle of incidence. In oil and gas exploration, a technique known as amplitude variation with angle of incidence (AVA) analysis has been developed to derive reservoir properties from reflection amplitude behavior. One such method, developed recently, uses intercept A (derived from near-angle of incidence amplitudes), vs. slope B (derived from mid-angle of incidence amplitudes) as crossplotted seismic attributes to infer reservoir properties. Here, for the first time, we apply this approach to the mid-ocean ridge environment to infer variations in melt content of the axial magma lens (AML). Using the presence of a converted P- to S- phase at the AML as the first-order proxy for melt, we limit the application of AVA analysis to the region between ~ 9º30' and 10º00'N along the EPR axis. Prior to conducting the AVA analysis, a number of data preparation steps are required (Kirchhoff pre-stack time migration, Radon filtering, velocity analysis of the AML event for its accurate normal move-out correction, conversion of common-mid point gathers from offset domain to angle of incidence domain, and near and mid angle stacking), after which interpretation scheme for the mid-ocean ridge environment is established. The individual regions selected for conducting the AVA analysis were based on previously defined small-scale segmentation of the axial magma sill. The AVA behavior suggests the presence of melt within four lens segments (each 5 to 10 km in length) spanning between ~ 9º42.3'N and 9º56.2'N.

Drainage related to the 2005-06 eruption appears to be limited to two narrow areas (~ 600 m in length) centered at 9º50.6’ and 9º45.7’N. Furthermore, the method shows potential to identify changes in chemical composition of AML: data around 9º53’N area show increased scatter of the crossplotted seismic attributes A and B that may result from the anomalous density/velocity relationship for iron-enriched rocks; within this same region, seafloor lavas show slightly higher iron concentrations. The AVA crossplotting method tested here thus is found to be a very promising tool for the study of mid-ocean ridge magma systems.

1. Introduction

The upper and perhaps some of the lower oceanic crust formed at fast and intermediate spreading centers is thought to originate from a melt body residing within the mid-crust, shaped as a relatively small sill referred to as an axial melt lens (AML) [e.g. *Vera et al.,* 1990; *Kent et al.,* 1990, 1993; *Sinton and Detrick,* 1992]. Although small in size, this sill plays a primary role in the processes of crustal accretion, seafloor volcanism and high-temperature hydrothermal circulation. Its physical properties, and their spatial and temporal variations along the ridge axis are important to better understand these processes at regional scales. The East Pacific Rise (EPR) at 9º50'N (Figure 1), which is characterized by an intense magmatic, hydrothermal and biological activity, represents one of the best studied mid-ocean ridge segments and offers an ideal environment for investigating the physical properties of the AML.

Since the mid '70s, when the first multichannel seismic (MCS) reflection study at the EPR 9°50'N corroborated the existence of an intracrustal sill beneath the ridge axis [*Herron et al.,* 1978 and *Herron et al.,* 1980], numerous geophysical surveys have been conducted in the area. Results from a later, two–ship MCS and wide-aperture survey conducted in 1985 provided extensive information on the geometry (size and shape) of this intracrustal sill. Seismic data collected along the ridge axis imaged the AML as bright reflection that could be followed as a relatively continuous event, sitting at about 1-2 km below the seafloor [*Detrick et al.,* 1987; *Mutter et al.,* 1988; *Kent et al.,* 1993]. From forward modeling of the AML diffraction response recorded on a series of cross-axis common depth point profiles, Kent et al. [1993] were able to determine the width of the lens at seven different locations; their results showed that the AML width varies widely (from 250 m to 4150 m). Due to the absence of evidence for a reflection

from the bottom of the lens, the thickness of the lens has not been well constrained thus far. Results from waveform forward modeling and waveform inversion have estimated that it is relatively thin, only 30-82 m [*Kent et al.,* 1993; *Hussenoeder et al.,* 1996; *Collier and Singh,* 1997].

The internal properties of the magma sill, including melt content, density and composition are still elusive. The phase-reversed waveform of the reflection off the AML (with respect to the seafloor reflection) and the large normal-incidence reflection coefficients [e.g. *Vera et al.,* 1990] have been used as the first-order proxies to argue that the material within the sill should be mostly molten. Compressional and shear wave velocities obtained from waveform modeling of wide angle data at 9º34'N [*Vera et al.,* 1990] and ~ 9º39.3'N [*Kent et al.,* 1993; *Collier and Singh,* 1997] confirmed the presence of low S-wave velocities (Vs) within the AML and showed that Vs within the AML can drop to 0 m/s, indicating presence of molten material. These studies were limited to single point locations along the ridge crest, and the variations in intrinsic properties of the AML along the bulk of the EPR in the 9-10ºN area has remained unknown.

In 2008, a 3D MCS survey, cruise MGL0812, was conducted in the region spanning the ridge axis from 9º38' to 9º57'N. In addition to the main ridge-perpendicular survey acquired for 3D imaging [*Mutter et al.,* 2008; *Canales et al.,* 2012; *Carton et al.,* 2010; *Han et al.,* 2011], a multi-swath along-axis survey [*Mutter et al.,* 2010; *Marjanović et al.,* 2010; *Carbotte et al.,* 2012] was conducted, designed to facilitate examination of spatial variations in the properties of the magma lens along the ridge axis. A recent one-dimensional waveform inversion study of data from the MGL0812 survey at two axis-centered locations at 9º42.8' and 9º49.1'N showed that at these two locations, the AML is ~ 16-40 m thick [*Xu,* 2012]. At the southern location, Vs within

the magma sill could be less than 500 m/s, which Xu [2012] attributed to the presence of pure (95-100%) melt. In contrast, the northern location exhibits higher Vs (1.5-2 km/s), consistent with only 40-45% of melt. In addition to his waveform modeling study, Xu [2012] obtained more regional but qualitative information about melt distribution along the ridge axis from partial-offset stacking for the P-to-S converted wave at the AML. From this method, Xu identified four limited regions rich in melt (~ 9º42'-9º44', ~ 9º47', 9º51'-9º52' and 9º58'-9º59'N).

The methods of waveform modeling/inversion and partial-offset stacking for the converted phase have been applied elsewhere at fast [*Hussenoeder et al.,* 1996; *Singh et al.,* 1998] and intermediate-spreading ridges [*Canales et al.,* 2006]. Often the two techniques have been applied within the same study area, thus constraining melt distribution along the ridge crest in a quantitative fashion at single point locations (Vp and Vs within the magma sill are used to derive the liquid content), and qualitatively at the regional scale.

Here we use an industry-type amplitude variation with offset (AVO) or amplitude variation with angle of incidence (AVA) technique to obtain regional estimates of liquid content within the intracrustal sill. We use a relatively novel approach based on crossplotting of AVA attributes [e.g. *Castagna et al.,* 1998; *Ross,* 2000; *Pelletier,* 2008; *Foster et al.,* 2010]. This method, known as AVO crossplotting method was developed in the mid '90s and has been successfully used by the oil industry since then. We apply this technique to MCS data recorded by a single streamer, axis-centered 2D line – axis 2r1 of the MGL0812 dataset (Figure 1). Data preparation prior to the method application is extensive and follows standard oil-industry procedures [*Castagna,* 1993; *Resnick,* 1993; *Yilmaz,* 2001]. For the chosen portion of the line, data are analyzed to study the distribution of melt-rich and melt-poor regions. We also show that

the AVO crossplotting (hereinafter AVA crossplotting) method can be used for even more quantitative interpretation, providing not only information on liquid content, but also information related to melt geochemistry.

2. Geological setting

The EPR extending between 8º20' to 10º10'N is a fast spreading center that separates the Pacific and Cocos plates at the full spreading rate of 108-109 mm/a [*Carbotte and Macdonald*, 1992] and represents one of the most extensively studied regions of the global mid-ocean ridge (MOR) system. Our seismic reflection data collected along this entire length of the EPR axis show that the intracrustal magmatic source is segmented on a range of scales that are collocated with previously defined tectonic segments [*Macdonald et al.,* 1991; *White et al.*, 2006] including third-order segments spaced ~ 30 km along the ridge as well as the finer fourth-order segments each around 5-15 km long [*Chapter 1; Carbotte et al.,* submitted].

Within the EPR 9º50'N area, lava flows that were emplaced onto the seafloor during two documented eruptions in 1991-1992 [*Haymon et al.,* 1993] and 2005-06 [*Tolstoy et al.,* 2006*; Soule et al*., 2007] offer a unique opportunity to examine variation in temporal composition of the AML. By comparing geochemical composition of lava samples from these two eruptions, Carbotte et al. [submitted] noticed that three magma lenses that are located directly below the seafloor extent of the 2005-06 lava flow (Figure 1; [*Soule et al.,* 2007]) had maintained their distinct chemical composition throughout multiple eruptions. From pinches and swells in the cross-axis of the modern axial zone the authors also argued that this fine scale magma system segmentation is stable and has been maintained for significant time period (1000's of years, [*Carbotte et al*., 2011]).

Besides high magmatic activity, the EPR 9º50'N region is also an area of abundant hydrothermal venting (Figure 1). Several studies at different spreading centers argued for a spatial correlation between the presence of high-temperature vents and melt distribution within the sill [*Singh et al.,* 1998; *Canales et al.,* 2006; *Tolstoy et al.,* 2006]. However, for hydrothermal circulation to develop and persist for decades, as it is observed in the 9°50'N region [*Haymon et al.,* 1991*; Von Damm*, 2004], the presence of a heat source at depth is a necessary but not sufficient condition. Other processes including replenishment of the magma lens, inflation/deflation of the magma lens and stresses in the overlying crustal lid must contribute in ways that remain to be fully understood [e.g. *Tolstoy et al.,* 2008; *Wilcock et al.,* 2009*; Lowell et al.,* 2012].

3. Summary on methods commonly used for estimating melt content

Since the presence of melt within the AML is one of the factors that controls hydrothermal-biological systems at mid-ocean ridges, a number of approaches have been used to estimate its presence either qualitatively or quantitatively. One method that has been used to evaluate regional variations in melt content qualitatively is to examine the presence of P-to-S converted waves off the interface of interest [*Tahtam and Stoffa*, 1976]. Indeed, at a strong reflecting boundary with a negative impedance contrast, mode conversion occurs only when the angle of incidence is non-vertical and reaches its maximum beyond the critical angle, for which no P-wave energy is transmitted (Figures A.1.C3 and A.1.C.4). Reflection coefficients as a function of incidence angle for relevant velocity and density structures suggest that this converted phase should hardly be seen on near-angle stacks (for our environment, incidence angle at the AML less than 10º) and that its strength should be significantly enhanced at mid-

angles where the P phase signal should be weak, where it also exhibits amplitude polarity change. Although strong P-to-S converted phases have been observed in existing studies at several regions along the mid-ocean ridge [*Singh et al.,* 1998; *Canales et al.,* 2006; *Xu,* 2012], all the above characteristics are rarely observed. For instance, at 14ºS on the Southern EPR, Singh et al. [1998] identified localized melt-rich regions based on the detection of strong P-to-S converted phases, although at these locations the P reflection is weak at near source-receiver offsets (where we would expect it to be very strong). It can also be noticed that two out of three interpreted melt-rich regions seem to coincide with disruptions in the AML reflector evident in along-axis seismic profiles of Hooft et al. [1997] and fine-scale morphologic segment boundaries, observed at ~ 14º07.5' and 14º18'S. These results indicate that discontinuity zones that separate two adjacent segments are the regions of enhanced melt supply within the crust, which is contradictory to commonly accepted segment centered melt supply model [e.g. *Macdonald et al.,* 1991].

Waveform modeling and inversion studies provide a powerful way to indirectly, by estimating velocities and comparing with experimental observations or predictions from the Hashin-Shtrikman theory [*Hashin and Shtrikman*, 1963], estimate melt content within the sill [*Hussenoeder et al.,* 1996; *Collier and Singh,* 1997; *Singh et al.,* 1998; *Canales et al.,* 2006; *Xu,* 2012]. This method is computationally demanding and with one exception [*Shipp and Singh,* 2002] has been limited to one-dimensional analysis of data from single point locations, and no regional scale analysis has been published.

4. Data preparation and AVA analysis

4.1. Processing sequence

Since preservation of relative amplitudes is a fundamental requirement for application of AVO analysis, the processing flow for data preparation has to be designed with special care. Here, data preparation flow was established in close collaboration with members of the *ConocoPhillips subsurface imaging team* and is tailored to deep water, mid-ocean ridge environment. All processing steps (except trace editing which was done using Focus from *Paradigm*) are conducted using *Landmark'* SeisSpace. Pre-migration data processing steps include trace editing, filtering and noise suppression, and spherical divergence correction (Table 1). The common mid-point (CMP) data are pre-stack time migrated after binning into seventy-eight 75 m - long bins in the offset domain. An 1-D velocity function derived from expanded spread profile results at ~ 9º34'N [ESP5, *Vera et al.,* 1990] is used as a starting velocity function for migration velocity analysis. The final velocity field for pre-stack time migration is obtained by performing velocity analyses at sparse common-mid point (CMP) intervals (every ~ 400 CMPs). After pre-stack time migration, a Radon filter [e.g. *Foster and Mosher,* 1992; *Sacchi and Ulrych,* 1995] is applied to remove undesired noise: the data is transformed into the τ-p domain where a mute is picked to attenuate energy with different move-out from the primary reflections (here, the AML event). For the AVO analysis to be successful, it is important to have the event of interest flattened at all source-receiver offsets included in the analysis. We therefore conducted a second pass velocity analysis on Super-CMP gathers obtained by vertically stacking 24 adjacent CMPs located at approximately 625 m intervals along the profile. This final velocity field is used for the final residual normal move-out (RNMO) correction. The final velocity field is also used to convert the data from source-receiver offset/two-way travel time (twtt) domain to

angle of incidence/twtt (even though the data are recorded in the offset domain, reflectivity at an interface is a function of the angle of incidence at that interface). Thus, although the method is most commonly known as AVO analysis, a term used whether the conversion to the angle of incidence is performed or not, for our data analysis we prefer to use the accurate name of amplitude variation with angle (hereinafter AVA) analysis. An example of flattened Super-common reflection point (CRP) is given in Figure 2. The CRP-sorted data are then stacked. For the specific AVA analysis method used here, near-angle and mid-angle stacks are required. We carefully examined angle stacks formed for different ranges of incidence angles, and decided to use 5-20º as the near-angle stack and 20-30º for the mid-angle stack. These sets of ranges are commonly used when doing AVA crossplotting [e.g. *Foster et al.,* 2010]. In Figure 3 we show selected CRP gathers that display the entire range of angles we use for the AVA analysis, 5º-30º, with 5º marked by thick line, 20º by dashed line and 30º by dotted line; for convenience we include the corresponding offsets as well. The resulting near- and far-angle stacks are shown in Figure 4. A summary of the processing sequence is given in Table 1, with the main points being the preservation of relative amplitudes at all steps, enhancement of signal-to-noise ratio, and flattening of the AML event at all offsets of interest.

4.2. Amplitude variation with angle of incidence (AVA) analysis: AVA crossplotting

The main objective of seismic studies is to relate observed seismic reflections to subsurface structure and rock properties. Ostrander [1984] was one of the first to show how AVA analysis can be used for distinguishing between signals reflected off gas-saturated sand and that of reflected off basalt. Since then the development of techniques for qualitative interpretation of amplitude variations has rapidly advanced. A common approach proceeds as an

inversion method, by fitting amplitudes as a function of source-receiver offset/angle of incidence in a CRP gather to either Zoeppritz equation or Aki and Richards' approximation [e.g. *Demirbag et al.,* 1993; *Carazzone and Srnka,* 1993]. However, this process of matching amplitude variations as a function of angle of incidence with the theoretical curves has proved challenging [*Douglas J. Foster*, personal communication], and significant efforts conducted in the past two decades have aimed to design techniques to facilitate AVA analysis. A as result an AVA crossplotting technique has been developed. It is based on two-term Shuey's approximation of the Zoeppritz equation: $R(\theta) = A + B\sin^2\theta$, where R – reflection coefficient as a function of θ, which is angle of incidence; A – intercept; B – slope (Appendix A). This method relates the angular dependence of the P-wave reflection coefficient from the equation to two parameters: A - near vertical incidence reflection coefficient (i.e. near angle amplitudes) and B – reflection coefficient for mid-angles (i.e. mid angle amplitudes). Information on the intercept A (i.e. its amplitudes) is extracted from the near-angle stack (in our case 5-20º), whereas the information on the slope B (i.e. its amplitudes) is extracted from the mid-angle stack (in our case 20-30º).

Castagna and Swan [1997] laid out the main principles of the crossplotting method and expanded the work of Rutherford and Williams [1989] on classification of AVA behavior for oil and gas exploration. In an A vs. B crossplot obtained by plotting amplitudes from near-angle stacks versus amplitudes from mid-angle stacks, two main elements are typically defined: a background trend (or fluid line) and a scattered anomaly as shown in Figure 5A [*Ross,* 2000; *Foster et al.,* 2010]. The background trend is derived from A and B attributes across reservoir-seal rock interface (e.g. across interface between porous sandstone and clay) devoid of hydrocarbons (Figure 5B.1); its slope depends solely on the ratio between the average Vp and Vs across the interface [*Foster et al.,* 2010]. When pores of the same reservoir rock are filled in with

hydrocarbons instead of air (Figure 5B.1), a cluster of A and B values plot away from the background trend in the A versus B crossplotting domain. This cluster of points represents an anomaly. Case studies have amply documented associations between where scattered anomalies plot in the direction orthogonal to the background trend and the presence and nature of hydrocarbons. In Figure 5A, AVA anomaly trend responses for brine (blue line), oil (green line) and gas (red line) are shown (which may or may not be parallel to the inferred background trend, depending on Vp and Vs of the hydrocarbon bearing rock), for the top of reservoir sands below the background trend line, and the base of reservoir sands above the background trend line. Depending on how much the anomaly is displaced with respect to the background trend and in which quadrant it plots, it is possible to distinguish between different types of pore fluid (e.g. between gas sand and wet sand) and between different classes of AVA behavior (for the first negative amplitude peak: class I – amplitude decreases with angle of incidence with change in sign and plots in the IV quadrant; class II – amplitude increases with angle of incidence in absolute value and may change sign and plot in the III or IV quadrant; class III – amplitude increases in angle of incidence and plots in the III quadrant; class IV – amplitude decreases with angle of incidence in absolute value with no change in sign and plots in the II quadrant). Furthermore, Foster et al. [2010] showed that the AVA crossplotting method can be used to estimate fluid compressibility (as a measure of distance from the background trend), reservoir porosity (as a measure of distribution of the anomaly along its trend), and shale content (Figure 5A), which they confirmed with results from well logs.

It is important to note that in crossplot domain trends are obtained from the reflection signal present in the data. However, along the wavelet that is examined there may be presence of

noise, which can be also crossplotted; noise it is normally represented by a cloud of low A and B values (close to AB coordinate system origin) [*Ross et al.,* 2000].

4.3. AVA crossplotting for mid-ocean ridges

The lithology and structural setting at fast to intermediate oceanic spreading centers are very different from that of typical hydrocarbon environment. At the ridge axis the source of the AML reflection is magma (with different percentage of crystals within) that ponds between gabbro (below) and dikes (above). When the melt is absent, as it is the case on the ridge flanks there is no reflection signal related to the gabbro/dike boundary. The above is illustrated in Figure 5B.2. As a result the background trend analogous to that defined for potential hydrocarbon reservoir rock (i.e. where pores are filled in with air) cannot be defined. Thus it is necessary to define an interpretation approach for the A vs. B crossplots interpretation that is appropriate for this setting. Here, instead of using background trend *per se*, the crossplotting approach applied to examine distribution of melt along the ridge axis, defines a reference anomaly trend in A vs. B crossplot domain with average compressional-to-shear velocity ratio across the reflection interface: $Vp/Vs \sim 2$ (ratio that is valid for mushy rock).

Since the contrasts in seismic velocities at the AML may be large it has to mention that Foster et al. [2010] tested the AVA crossplotting method for arbitrarily large contrasts and showed that the method does not rely on small-perturbation assumptions (i.e. $Vp/Vs \approx 2$). This is

achieved by referring to equation that gives a relationship between exact intercept and slope with the only assumption that density contrasts are negligible[†] at the interface:

$$B = (1 - 8\gamma^2)A - 4\gamma\Delta\gamma(1 - \Delta\gamma) + (1 - 2\gamma)O(A^2) \qquad (1)$$

where $\gamma = \frac{V_{S1}+V_{S2}}{V_{P1}+V_{P2}}$ and $\Delta\gamma = \frac{V_{S2}}{V_{P2}} - \frac{V_{S1}}{V_{P1}}$. In this equation, the first term $(1 - 8\gamma^2)A$ represents a linear relationship between A and B, the second $-4\gamma\Delta\gamma(1 - \Delta\gamma)$ represents the displacement perpendicular to this trend (illustrated in Figure 5), and the third term is $(1 - 2\gamma)O(A^2)$, which is second-order in A^2.

Besides the above, the AML is likely to be a thin sill only a several 10's of meters thick [*Kent et al.,* 1990; *Xu,* 2012]. Appendix A summarizes findings on thin-bed AVA, which suggest that for the range of plausible AML thicknesses, AVA crossploting method will give reliable results.

4.4.Set up for the East Pacific Rise data

At the EPR we focus our AVA analysis on the portion between 9º29.8'N and 9º58.4'N. This is based on the observation that the primary P reflection from the AML is brightest north of 9º38'N (see Figure 2 in *Chapter 1*) and that the P-to-S converted phase from the AML is brightest north of 9º38'N and almost absent south of it (Figure 6). Hence we expect the AML in this region to be melt rich with a detectable AVA response. The extent from 9º30' to 9º38'N is used for comparison purposes as an example of AVA behavior when there is no melt. Moreover,

---

[†] This assumption is reasonable for the AML given the small density difference between solid and molten basaltic rocks of ~ 0.1 g/cm^3 determined in laboratory tests [*Murase and McBiney*, 1973].

the bathymetry of the EPR axis south of 9º10'N exhibits significant short wavelength roughness that may contribute to lower amplitude AML reflections, which makes this region less suitable for the AVA analysis, due to the lower signal-to-noise ratio of the AML reflection amplitudes irrespective of angle of incidence.

With the extent of analysis windows defined in along-axis direction by the AML lens segmentation (Chapter 1; Figure 4), the AVA crossplotting analysis is used to examine differences in melt content between segments, assuming that melt is relatively uniformly distributed within an individual lens (excluding its edges). In the region between 9º30' and 10º00'N region, AML segments vary in length between 2.8 and 10 km. The actual window length used for the analysis in *GeoCraft*© (AVA crossplotting analysis software developed by ConocoPhillips) is shorter than the segment length because we exclude the region proximal to the AML disruptions. Thus, the total number of CRP included for each segment, going from south to north is: 1500, 400, 500, 500, 500, 800, 700, 900, 400. These numbers exclude on average 200 CRPs (maximum 800 for the wide 9º56.2'N AML disruption zone) from each segment's total length. The software also needs to be fed by information on the vertical extent of the analysis window, i.e. it is necessary to define a time window that represents the vertical extent of the region for which the AVA analysis is done. For each segment the analysis time window was defined to be 150-180 ms centered at the first break of the AML reflection at the central CRP of each segment (Figure 4).

It has to be mentioned that the method can be conducted on windows that are as long as ~ 25 CRPs (~ 150 m) along the axis. For regions smaller than that the number of points is too small to define meaningful trend.

As a result an AVA crossplot displays a cloud of data points, each point corresponding to two (A, B) pairs, one for the positive and one for each negative amplitude peak (including noise) within predefined window for wavelet at each CRP location, with A extracted from near and B extracted from far-angle stacks, respectively. Thus, for each CRP, for each positive-negative amplitude pair, in the crossplot domain we obtain two points that are symmetric with respect to the origin of the B= f(A) coordinate system. For instance, one point for a reflection off a top of molten sill and in agreement with Equation A.2, will plot as A<0 and B>0 (i.e. it will lie in quadrant IV of the graph). By symmetry, the other point will plot with the similar absolute value of A and B but opposite in sign (i.e. A>0 and B<0), and hence will lie in quadrant II. For the noise signal, the values of A and B will plot close to coordinate origin. In Figure 5C a random wavelet to represent reflection signal at near angles of incidence (left) within a limited time window is used to illustrate where in the crossplot domain each peak and trough may plot.

5. Results and discussion

5.1. Interpretation template

To facilitate the interpretation of the crossplots, A vs. B trends ($\frac{V_{P1}+V_{P2}}{V_{S1}+V_{S2}}$ or Vp/Vs trends) across the AML interface are calculated (Figure 7) following Castagna and Swan [1997]. Here, the Vp/Vs trends range from 1.55 to 2.5 at increments of 0.15 or 0.2. The calculated trends rotate counterclockwise around the origin as Vp/Vs increases. Looking at the $\frac{V_{P1}+V_{P2}}{V_{S1}+V_{S2}}$ it becomes clear that decrease in Vs_2 and slight decrease in Vp_2, as expected for a high percentage of melt within the AML, would result in a sharp increase in Vp/Vs if velocities above the interface are kept constant. Using reasonable velocities for mid-ocean ridge environment it can be shown that

trends greater than 2 ($Vs_2 < 500$ m/s) are likely to indicate presence of molten material whereas trends equal and lower than 2 ($Vs_2 > 800$ m/s) to represent mushy to solidified material.

Therefore, Figure 7 alone provides a useful template for the interpretation of the crossplots and for inter-segment comparison: melt-rich segments are expected to show a counter-clockwise rotation of the A vs. B trend compared to melt-poor segments, as well as the occurrence of higher values (in absolute value) of the vertical-incidence reflection coefficient A, as well as slope B. The best-fitting A vs. B linear trends are calculated from the ABAVO crossploting software module as the direction of the major axis of the best-fitting ellipse to the cloud of points [*Foster et al.,* 2010] that is governed by the A and B values obtained from the AML reflector. A linear regression using the least squares technique, also available in the module, provides very similar results.

5.2. Comparison of the AVA crossplotting method with other methods for characterization of the physical properties of the AML

The AVA crossplotting method relies on Shuey's approximation of the reflection coefficients, which is valid out to 30º incidence angle. In the case of an AML at ~ 1.6 km below the seafloor this corresponds to a maximum offset of 2.8 km (Figure 3). Even if we were not constrained by this approximation, it may not be straightforward to make use of the reflection response across the entire 6-km offset range recorded by the hydrophone streamer, as the AML event in time-offset domain is crosscut by the seafloor reflection at offsets around 4 km, and the NMO-corrected data at large offsets would be severely affected by NMO stretch (non-stretch stacking could be used to mitigate this issue but the data could not be pre-stack migrated). In the AVA crossplotting approach, only P-wave reflection coefficient at different angles of incidence

is used while that of the $P_{AML}S$ is not. This point warrants careful examination since waveform inversion studies of AML structure have typically argued that results are better constrained when the aperture of the source-receiver array allows proper recording of S-wave information [e.g. *Collier and Singh*, 1997]. A major difference between AVA crossplotting and waveform inversion lies in the fact that in the crossplotting approach there is no attempt to invert for the detailed velocity structure, instead two quantities nearly suffice to describe the crossplots: the average Vp/Vs at the interface (trend) and the maximum absolute value of the vertical incidence reflection coefficient A. Both Vp/Vs and |A| max can be used to characterize each segment or cell individually, as well as inform inter-segment comparisons (Figure 8 clearly illustrates that the method is able to detect variations between segments). The P-wave reflection out to 30º incidence angle contains the information necessary to extract these quantities reliably through stacking over two distinct angle domains. Furthermore, by comparison between crossplots with higher (> 2.10) and lower (≤ 2.06) Vp/Vs it can be noticed that the range of A's and B's over which the crossplotted data extend is less when the sill is inferred to be melt-poor (fit by lower Vp/Vs trend) than when it is melt-rich, i.e. fit by higher Vp/Vs trend (Figure 8). Also, melt-rich segments tend to display more scattering in directions oblique to the trend. The AVA crossplotting thus provides a semi-quantitative approach for evaluating the physical state of the AML, intermediate between partial-offset P-wave stacking followed by visual inspection or graphic rendering of the results [e.g. *Singh et al.,* 2006], which remains essentially qualitative, and waveform inversion which aims to derive the exact $P_{AML}S$ velocity structure at the AML, from which melt fraction can be inferred. An interesting outcome of this study is that this method could be applied, if the signal-to-noise ratio of the data is high enough and the AML sits at a

comparable or shallower depth, to older datasets collected with shorter streamers and that would not have recorded $P_{AML}S$ energy.

5.3. Results and discussion at the fine scales of individual segments

From the series of nine crossplots, we identify five segments - segment 3 (9º37.8' - 9º39.8'N), segment 5 (9º42.3' - 9º44.6'N), segment 6 (9º44.6' - 9º48'N), segment 7 (9º48 - 9º51.3'N) and segment 8 (9º51.3' - 9º56.2'N) - that display the highest Vp/Vs values derived from the best-fit trends, between 2.13 and 2.19, and the strongest scattering around the trend (Figure 8). By comparison with the template trends shown in Figure 7 we interpret these as melt-rich. Among them, segment 5 has the highest Vp/Vs, and is the segment for which a previous 1D waveform inversion study indicated low shear velocities indicative of melt [*Xu,* 2012].

It is interesting to mention that scattering we observe plots within the region of class IV (negative intercept and positive slope in quadrant II; Figure 5A), which indicates a decrease in amplitude with angle of incidence for the event of interest without a change in polarity of the wavelet for angles < 30º [*Castagna and Swan*, 1997]. Our CRP gathers confirm this behavior (Figure 3), and the absence of the expected polarity reversal may be explained either by the velocity structure above and beneath the AML (compare Figure A.1.C2, C3 and C4) or from interference between top and bottom reflections from a thin lens. The effect of a thin bed on the reflection amplitude variation with offset has been demonstrated for gas bearing sand and limestone layers [*Juhlin and Young*, 1993]. The study showed that the effect is significantly smaller (but still present depending on how thin the bed is), when the compressional velocity of the bed is smaller than that of the overburden rock (i.e. $Vp_2<Vp_1$), which is equivalent to our case of a molten sill. We also explore the thin-bed effect by examples given in Figure A.2.4.a

and 4.b, Figure A.2.5.a and 5.b and Figure A.2.6. For the remaining segments, 1, 2, 4 and 9, the trend of the A vs. B crossplotted data matches those calculated for lower Vp/Vs ratios, between 1.9 and 2.06 (Figure 8). We interpret these segments as having a low melt percentage. A schematic interpretation for the series of nine AML segments analyzed is shown in Figure 10A.

From the above results, it is apparent that two years after the last eruption, none of the AML segments beneath the eruption site at 9º51'N is completely drained of melt. There are two possible explanations: either they were drained but then replenished in a very short time period (~ 2 years) or only a portion of their total melt volume erupted onto the seafloor.

To test these hypotheses, we perform AVA crossplotting at finer scales for the lenses located beneath the mapped extent of the 2005-06 lavas (i.e. segments 6, 7 and 8; Figure 4 and Figure 8). For each lens segment, the analysis was conducted within zones ~ 100 CRPs long (i.e. ~ 625 m): segment 6 and segment 7 were subdivided into seven zones, and segment 8 into nine zones (Figure 10B). Although the segment-scale A vs. B trends suggest that each of these three lens segments are mostly melt-rich (Figure 8), the sub-segment trends vary, indicating smaller melt rich and poor regions within each segment. For segment 6, A vs. B trends are similar along most of its length, except between 9º45.5'-9º46'N where we obtain low Vp/Vs < 2 (similar to segment 2), suggesting low melt content (Figure 10B). Similarly, within the segment 7, the southernmost cell and the cell centered at ~ 9º50.6'N also exhibit trends corresponding to low Vp/Vs. We speculate that these regions may have been more fully drained during the 2005-06 eruption. It is interesting to note that the low melt zone at ~ 9º50.6'N identified from the AVA analysis underlies the region inferred from lava flow morphology to be the main source for the 2005-06 eruption [*Fundis et al.,* 2010].

The AVA analysis suggests that the 2005-06 eruption may have drained only limited portions of the AML present beneath the surficial extent of newly erupted lavas. Furthermore, the estimated erupted volume of magma of 22 × 10^6 m^3 [*Soule et al.,* 2007], may be entirely accommodated within these small drained areas rather than by tapping magma from the full length of the magma lens beneath the erupting area, as assumed in *Soule et al* [2007]. To test this idea we compare the erupted volume to the estimated volume of the low melt regions. If we assume that the thickness of the lens is 16-40 m [*Xu,* 2012], cross-axis width between 350 m (obtained from region of diminished AML amplitudes in the 2D swath data – more details on this are given in Chapter 3) and 800 m (width of the sill obtained from 3D data set [*Carton et al.,* 2010]) and along axis length of 600 m (length of sub-cells used for detailed AVA analysis), the range of volumes for the three drained cells (marked in yellow in Figure 10B) is 10.1 × 10^6 to 57.6 × 10^6 m^3. These volumes range from 50% to 250% of the estimated volume of erupted magma, and hence could account for much to all of the eruption. However, we have to note that other sub-segments may have partially participated in the eruption. Without AVA analysis of the 3D dataset, it is difficult to further constrain the volume of the low melt zones although we expect they lie closer to the low end of the range estimated above (using the 350 m wide region of diminished AML amplitudes in the 2D swath data, as width of low melt zone and estimate of 20 m for the thickness for the AML derived from inspection of the AML waveform and comparison with modeled seismic gathers Figure A.2.).

The AVA results for the northernmost of the erupting AML segments are also of interest. The sub-segment zone centered at ~ 9º52.2'N has even higher inferred Vp/Vs ratio than segment 5 and thus the highest melt percentage of anywhere in the study region. This melt rich portion of the lens is collocated with a localized region of seafloor inflation revealed by seabottom pressure

measurements [*Scott Nooner,* personal communication] and of a wider melt lens [*Carton et al.,* 2010] that may be due to local melt influx to the AML from the west. The finer-scale crossplotting reveals that the high scattering observed for segment 8 (Figure 8) arises from the region between 9º52.5' and 9º54'N (Figure 10B). A geochemistry study of samples from lavas erupted in 2005-06 [*Goss et al.,* 2010] found lavas slightly enriched in iron and titanium in this region relative to lavas erupted to the south. Laboratory studies [*Karki and Stixrude,* 1999] on magnesiowüstite (for Fe) and perovskite (for Ti) show that the presence of iron-enriched minerals increases the density of rock, but lowers its Vp and Vs. Thus for iron enrichment (lower Vp_2 and Vs_2), A and B should be higher (in absolute value), consistent with increased scatter along the trend.

The sub-division of every 100 CRP, may not be adequate if changes in the AML are occurring at even shorter length scales (shorter than ~ 600 m). For example, our AVA analysis indicates the sub-segment from 9°49' to 9º49.5'N (segment 7, Figure 10B) is melt rich (high Vp/Vs=2.10). However, 1D waveform inversion for data from 9°49.1'N within this sub-segment show non-zero Vs velocities (1.5-2 km/s) and thus a low melt region is inferred [*Xu,* 2012]. However, when we further divide the sub-segment zones for the AVA analysis to every 50 CRPs (~ 300 m), our method clearly defines two regions with distinct trends: a southern, mush to solid region (Vp/Vs ~ 1.9) that includes 9º49.1'N) and a northern – melt rich region (Vp/Vs > 2.12). Since the mushy region is surrounded by sub-segment zones with quite high A vs. B trends (Vp/Vs ~ 2.15), interpreted as pure melt, we speculate that melt extraction during eruption may drain very narrow parts of this lens.

5.4. Comparison with results from partial offset stacking

On a regional scale, there is good agreement between the results obtained from partial offset stacking (for both P-primary and P converted S phase reflected off the AML, hereinafter $P_{AML}S$) and results from AVA crossploting method. In some regions this correlation is remarkable. For instance, for segment 5, for which the AVA data follow the highest trend (Vp/Vs=2.19; Figure 8) indicative of high melt content, the partial offset stacks show a bright primary P-wave reflection at near source-receiver offsets (Figure 9A), the same phase diminishes (Figure 9B) at mid source-receiver offsets, where $P_{AML}S$ is very prominent (Figure 9C). Based on theory, the above behavior of primary and converted phases is indicative of melt presence. Furthermore, for segment 4, where data crossplot along a trend characteristic for a lens with higher crystallinity, the partial offset stacking agrees and shows a weak primary P in both near- and mid-offset stacks and a weak $P_{AML}S$. However, there are examples for which the results from the two methods are contradictory. For instance, for segment 1 the AVA method shows the lowest trend (Vp/Vs=1.9; Figure 8) and thus indicates the highest crystalline component. For the same segment, the partial offset stacks show presence of $P_{AML}S$, although primary P reflection is weak at all offsets (Figure 9). Similar is true for segment 9.

5.5. Additional implications

In our study area, changes in lava morphology and character of the axial summit through (AST) that marks the region of recent eruptions and hydrothermal venting occur at larger scales (> 30 km) than that of the fine-scale AML segmentation. It has been shown that the changes in lava morphology are well correlated with the third-order tectono-magmatic discontinuities

[*White et al.,* 2002; Chapter 1]. However, changes in the morphology of the axial zone from no AST (south of 9º23'N), to wide AST (9º23'-9º43'N) to narrow AST (9º43'-9º53'N) [*Soule et al.,* 2007] appear to be independent of the third-order segmentation. For instance, an abrupt change in AST width from 50 to 150 m (from narrow to wide) occurs at 9º43'N, ~ 10 km north of the prominent third-order discontinuity at 9º37'N [see Chapter 1]. Soule et al. [2007] argued that this change in width at 9º43'N is due to a difference in frequency of volcanic eruptions in the two regions (higher frequency within narrower AST zone), given that there was no difference in AML structure and melt availability in these regions evident in the seismic data available at the time (inferred from ~ uniform depth of the AML from Kent et al. [1993]). While AML depth below the axial zone in our 2008 data (Chapter 1) also does not change significantly across the wide to narrow AST transition zone, our AVA study indicates significant change in melt content within the AML. Beneath the wide AST region, all segments (except for segment 3 extending between 9º37.8' and 9º39.8'N), exhibit high crystalline component (Figure 10A). Thus, we think that the suggested differences in eruption frequency between the narrow, on the one hand, and wide or no AST, on the other, is closely related to available melt within the mid-crustal sill.

Although several studies have suggested a close spatial correlation between presence of melt-rich AML and hydrothermal venting [e.g. *Singh et al.,* 1998; *Canales et al.,* 2006], this relationship is not very clear in our data. For instance, no hydrothermal vents are observed within segment 5 although this segment has the highest Vp/Vs trend, and thus the highest inferred melt content (Figure 8 and Figure 10A). Also, the majority of modern vents north of 9°10'N [*Haymon et al.,* 1991] concentrate above segments 6 and 7, and none is observed along the segment 8, even if the segment 8 shows very similar Vp/Vs trend (i.e. interpreted melt content) as segment 6

and 7. The above suggests that there must be more complexity to the incidence of hydrothermal vents/melt budget within the crust relationship.

6. Conclusions

Intercept vs. slope seismic attribute crossplotting applied to the AML reflection between 9º30'N and 10ºN on the EPR reveals a melt-rich zone that extends from 9º42.3' to 9º56.2'N, and a smaller one between 9º37.8' and 9º39.8'N (Figure 1 and Figure 10A). The extent of the melt-rich zones show that most of the ridge segment between 9º30'N and 10ºN is involved in current creation of layer 2 (basalts and dikes).

Comparison of AVA trends between the finest scale AML segments provides information on relative melt presence. The highest Vp/Vs is encountered within the segment extending between 9º42.3' and 9º44.6'N and we conclude that this fourth order magma lens segment has the highest melt percentage. This is in agreement with the results from a previous study that included waveform inversion and stacking for the converted $P_{AML}S$ phase [*Xu,* 2012], which found that this zone showed the clearest indications of high melt content. This is also the segment that is located south of the extent of the last eruption; future eruptions may be focused in this high melt region.

The sub-segment analysis shows three narrow regions (~ 600 m) of low melt beneath the eruption site area (at 9º45.7', 9º48.3' and 9º52.2'N) that could be now drained and represent the primary source regions for these eruptions. Elsewhere within the eruption area the AML was only partially tapped by the eruption (Figure 10B). Since our preferred volume estimate of the above drained sub-sill is too small to accommodate the calculated volume of magma erupted in

2005-06, we speculate that there must exist additional magma reservoir(s) within the crust that contribute to the total estimated volume.

A portion of segment 8 centered at ~ 9º53'N displays scattering towards large values of the vertical incidence reflection coefficient, which we speculate reflects higher concentration of Fe and Ti in the AML. From this analysis we conclude that the AVA crossplotting method provides a useful new approach to evaluate variations in both melt % and composition of the crustal magma lens at mid-ocean ridges.

Acknowledgements

Seismic data processing was done in collaboration with the ConocoPhillips' Subsurface Technology Team. We express our sincere gratitude to Jeff Malloy, Mark Wuenscher and Bob Olsen for their effort and time. We thank Douglas Foster (ConocoPhillips), Leon Barens (Total) and Stefan Hussenoeder (ExxonMobil) for insightful information on the AVO/AVA method and interpretation. We are grateful to Douglas Foster and Bill Lucas for providing the ABAVO crossplotting tool within the GeoCraft software developed by ConocoPhillips. We thank Lindsey Doermann, Maya Tolstoy and Spahr Webb for help with extracting the recorded Langseth source signature.

References:

Canales, J. P., S. C. Singh, R. S. Detrick, S. M. Carbotte, A. J. Harding, G. M. Kent, J. B. Diebold, J. Babcock, and M. R. Nedimović (2006), Seismic evidence for variations in axial magma chamber properties along the southern Juan de Fuca Ridge, *Earth and Planet. Sci. Lett.*, *246*, 353-366, doi: 10.1016/j.epsl.2006.04.032.

Canales, J.P., H. Carton, J.C. Mutter, A. Harding, S.M. Carbotte, and M.R. Nedimović (2012), Recent advances in multichannel seismic imaging for academic research in deep oceanic environments. *Oceanography* 25(1):113–115.

Carazzone, J. J., and L. J. Srnka, (1993), Elastic inversion of Gulf of Mexico data, in Castagna J. P. and M. M. Backus, Offset Dependent Reflectivity – Theory and Practice of AVO Analysis, *Society of Exploration Geophysicists*.

Carbotte, S., and K. Macdonald (1992), East Pacific Rise 8°–10°30′N: Evolution of Ridge Segments and Discontinuities From SeaMARC II and Three-Dimensional Magnetic Studies, *J. Geophys. Res.*, *97*(B5), 6959–6982, doi:10.1029/91JB03065.

Carbotte S.M., M. Marjanović, H. D. Carton, J. C. Mutter, J. P. Canales, M. Xu, M. R. Nedimović, O. Aghaei, (2011), The ups and downs of magma in the crust beneath the East Pacific Rise axis 8º20-10º10'N, Abstract OS22A-01 *presented at 2011 Fall Meeting, AGU*, San Francisco, Calif., 5-9 Dec.

Carbotte, S.M., J.P. Canales, M.R. Nedimović, H. Carton, and J.C. Mutter, (2012), Recent seismic studies at the East Pacific Rise 8°20'–10°10'N and Endeavour Segment: Insights into mid-ocean ridge hydrothermal and magmatic processes. *Oceanography* 25(1):100–112.

Carbotte S. M., M. Marjanović, Carton, H. D., J. C. Mutter, M. R. Nedimović, J. P. Canales, Xu M., Aghaei O., M. Perfit, S. Han, Fine-scale segmentation of the crustal magma reservoir beneath the modern eruptive zone of the East Pacific Rise, (submitted).

Castagna, J. P. (1993), AVO analysis – Tutorial and review, in Castagna J. P. and M. M. Backus, Offset Dependent Reflectivity – Theory and Practice of AVO Analysis, Society of Exploration Geophysicists.

Castagna, J. P., and H. W. Swan, (1997), Principles of AVO crossplotting, The leading Edge, Society of Exploration Geophysicists, 17, 337-342.

Castagna, J. P., Swan H. W., D. J. Foster, (1998), Framework for AVO gradient and intercept interpretation, Geophysics, vol. 63, no. 3, 948-956.

Fundis, A. T., S. A. Soule, D. J. Fornari, and M. R. Perfit (2010), Paving the seafloor: Volcanic emplacement processes during the 2005–2006 eruptions at the fast spreading East Pacific Rise, 9°50′N, *Geochem. Geophys. Geosyst.*, *11*, Q08024

Goss, A. R., M. R. Perfit, W. I. Ridley, K. H. Rubin, G. D. Kamenov, S. A. Soule, A. Fundis, and D. J. Fornari (2010), Geochemistry of lavas from the 2005–2006 eruption at the East Pacific Rise, 9°46′N–9°56′N: Implications for ridge crest plumbing and decadal changes in magma chamber compositions, Geochem. Geophys. Geosyst., 11, Q05T09

Hashin, Z., and S. Shtrikman (1963), A variational approach to the theory of the elastic behaviour of multiphase materials, *Journal of the Mechanics and Physics of Solids*, *11*(2), 127-140, doi:10.1016/0022-5096(63)90060-7.

Haymon, R. M., Fornari, D. J., Edwards, M. H., Carbotte, S., Wright, D., Macdonald, K. C., (1991), Hydrothermal vent distribution along the East Pacific Rise Crest (9°09'-54'N) and its relationship to magmatic and tectonic processes on fast-spreading mid-ocean ridges, *Earth Planet. Sci. Lett.* 104, 513-534.

Haymon, R.M., D.J. Fornari, K.L. Von Damm, M.D. Lilley, M.R. Perfit, J.M. Edmond, W.C. Shanks III, R.A. Lutz, J.M. Grebmeier, S. Carbotte, D. Wright, E. McLaughlin, M. Smith, N. Beedle and E. Olson. 1993. Volcanic eruption of the mid-ocean ridge along the East Pacific Rise crest at 9°45-52'N: Direct submersible observations of seafloor phenomena associated with an eruption event in April, 1991. *Earth. Plan. Sci. Lett.* 119:85-101.

Haymon, R. M., and S. M. White, 2004. Fine-scale segmentation of volcanic/hydrothermal systems along fast-spreading ridge crests, *Earth Planet. Sci. Letts.* 226:367-382.

Herron, T. J., P. L. Stoffa, and P. Buhl (1980), Magma chamber and mantle reflections – East Pacific Rise, *Geophys. Res. Lett.*, *7*(11), 989–992, doi:10.1029/GL007i011p00989.

Herron, T. J., W. J. Ludwig, P. L. Stoffa, T. K. Kan, and P. Buhl (1978), Structure of the East Pacific Rise Crest From Multichannel Seismic Reflection Data, *J. Geophys. Res.*, *83*(B2), 798–804, doi:10.1029/JB083iB02p00798.

Hooft, E. E. E., R. S. Detrick, and G. M. Kent (1997), Seismic structure and indicators of magma budget along the Southern East Pacific Rise, *J. Geophys. Res.,* 102(B12), 27,319–27,340, doi:10.1029/97JB02349.

Hussenoeder, S. A., J. A. Collins, G. M. Kent, R. S. Detrick, and the TERA Group (1996), Seismic analysis of the axial magma chamber reflector along the southern East Pacific Rise from conventional reflection profiling, *J. Geophys. Res.*, *101*(B10), 22,087–22,105, doi:10.1029/96JB01907.

Juhlin C. and R., Young, (1993), Implications of thin layers for amplitude variation with offset (AVO) studies, *Geophysics*, vol. 58, no. 8, 1200-1204.

Karki B. B. and L. Stixrude, (1999), Seismic velocities of major silicate and oxide phases of the lower mantle, *J. Geophys. Res.*, vol. 104, no. B6, 13025-13033.

Kent, G. M., A. J. Harding, and J. A. Orcutt (1993), Distribution of Magma Beneath the East Pacific Rise Between the Clipperton Transform and the 9°17′N Deval From Forward Modeling of Common Depth Point Data, *J. Geophys. Res.*, *98*(B8), 13,945–13,969, doi:10.1029/93JB00705.

Kent, G. M., A. J. Harding, and J. A. Orcutt, (1990), Evidence for a smaller magma chamber beneath the East Pacific Rise at 9°30'N, *Nature*, 344, 650-653.

Lowell, R.P., A. Farough, L.N. Germanovich, L.B. Hebert, and R. Horne. (2012). A vent-field-scale model of the East Pacific Rise 9°50'N magma-hydrothermal system, *Oceanography* 25(1):158–167, http://dx.doi.org/10.5670/oceanog.2012.13.

Macdonald, K.C., D.S. Scheirer and S.M. Carbotte, (1991), Mid-ocean ridges: Discontinuities, segments and giant cracks, *Science* 253:986-994.

Marjanović, M., S. M. Carbotte, H. D. Carton, J. C. Mutter, M. R. Nedimović, J. P. Canales, (2010), Axial magma chamber segmentation along the East Pacific Rise from Clipperton to Siqieros Fracture Zone, Abstract OS21C-1511, *Presented at 2010 Fall Meeting*, AGU, San Francisco, California.

Murase, T., and A. R. McBirney, (1973), Properties of some common igneous rocks and their melts at high temperatures, *Geol. Soc. Am. Bull.*, 84, 3563-3592.

Mutter J. C., Carton H. D., Carbotte S. M., J. P. Canales, M. R. Nedimović, K. Newman, M. Marjanović, M. Xu, O. Aghaei, L. Stowe, (2008), Searching for Changes in AMC Characteristics on the EPR Using Comparisons of Reflection Images Obtained in 1985 and 2008, Eos Trans., AGU, 89 (53), Abstract B21A-0321, *Presented at 2008 Fall Meeting*, AGU, San Francisco, California.

Mutter, J. C., G. A. Barth, P. Buhl, R. S. Detrick, J. Orcutt and A. Harding (1988), Magma distribution across ridge-axis discontinuities on the East Pacific Rise from multichannel seismic images, *Nature* 336, 156-158, doi:10.1038/336156a0.

Mutter, J.C., H. Carton, M. Marjanovic, S. Carbotte, J.P. Canales, and M.R. Nedimović, (2010), Eruption-related changes in magma chamber structure at 9°50'N on the EPR from coinci- dent reflection images, 1985 and 2008. *Eos, Transactions, American Geophysical Union*, Abstract OS24A-01.

Ostrander, W. J., (1984), Plane-wave reflection coefficients for gas sands at normal angles of incidence, *Geophysics,* vol. 49, no. 10, 1637-1648.

Pelletier, H., (2008), AVO crossplotting Revisited: A Practitioner's Perspective, *CSEG Resorder*, Focus Article, 40-46.

Resnick, J. R. (1993), Seismic data processing for AVO and AVA analysis, in Castagna J. P. and M. M. Backus, Offset Dependent Reflectivity – Theory and Practice of AVO Analysis *Society of Exploration Geophysicists*.

Ross, C., (2000), Effective AVO crossplot modeling: A tutorial, *Geophysics*, vol. 65, no. 3, 700-711.

Rutherford, S. R. and R. H. Williams, (1989), Amplitude-versus-offset variations in gas sands, *Geophysics*, Society of Exploration Geophysiscists, 54, 680-688.

Sacchi, M.D. and T. J. Ulrych, (1995), High resolution velocity gathers and offset space reconstruction, *Geophysics*, vol. 60, 1169-1177.

Shipp R. M. and S. C. Singh, (2002), Two-dimensional full waveform inversion of wide-aperture marine seismic streamer data, *Geophys. J. Int.,* 151, 325-344.

Singh, S. C., G. M. Kent, J. S. Collier, A. J. Harding and J. A. Orcutt, (1998), Melt to mush variations in crustal magma properties along the ridge crest at the southern East Pacific Rise, *Nature* 394, 874-878, doi:10.1038/29740.

Sinton, J. M. and R. S. Detrick, (1992), Mid-ocean ridge magma chambers, *J. Geophys. Res.*, *97*(B1), 197–216, doi:10.1029/91JB02508.

Soule, S. A., D. J. Fornari, M. R. Perfit, and K. Rubin (2007), New insights into mid-ocean ridge volcanic processes from the 2005–2006 eruption of the East Pacific Rise, 9°46′N– 9°56′N, *Geology*, 35(12), 1079–1082, doi:10.1130/ G23924A.1.
Tahtam, R. and P. Stoffa, (1976), Vp/Vs – A potential hydrocarbon indicator, *Geophysics*, vol. 41, no. 5, 837-849.

Tolstoy, M., F. Waldhauser, D.R. Bohnenstiehl, R.T. Weekly, W. Y. Kim, (2007), Seismic identification of along-axis hydrothermal flow on the East Pacific Rise, *Nature*, doi:10.1038/nature06424.

Vera, E. E., J. C. Mutter, P. Buhl, J. A. Orcutt, A. J. Harding, M. E. Kappus, R. S. Detrick, and T. M. Brocher (1990), The Structure of 0- to 0.2-m.y.-Old Oceanic Crust at 9°N on the East Pacific Rise From Expanded Spread Profiles, *J. Geophys. Res.*, *95*(B10), 15,529–15,556, doi:10.1029/JB095iB10p15529.

Von Damm, K.L., and M.D. Lilley. 2004. Diffuse flow hydrothermal fluids from 9°50'N East Pacific Rise: Origin, evolution and biogeochemical controls. Pp. 245–268 in *The Subseafloor Biosphere at Mid-Ocean Ridges*. W.S.D. Wilcock, E.F. DeLong, D.S. Kelley, J.A. Baross, and S.C. Cary, eds, *Geophysical Monograph Series,* vol. 144, American Geophysical Union, Washington, DC.

White, S. M., R. M. Haymon, and S. Carbotte (2006), A new view of ridge segmentation and near-axis volcanism at the East Pacific Rise, 8-12ºN, from EM300 multibeam bathymetry, *Geochem. Geophys. Geosyst.,* 7, Q12O05.

White, S. M., R. M. Haymon, D. J. Fornari, M. R. Perfit, and K. C. Macdonald (2002), Correlation between volcanic and tectonic segmentation of fast-spreading ridges: Evidence from volcanic structures and lava flow morphology on the East Pacific Rise at 9°–10°N, *J. Geophys. Res.*, *107*(B8), 2173, doi:10.1029/2001JB000571.

Wilcock, W.S.D., E.E.E. Hooft, D.R. Toomey, P.R. McGill, A.H. Barclay, D.S. Stakes, and T.M. Ramirez, (2009), The role of magma injection in localizing black-smoker activity, *Nature Geoscience,* 2:509–513, http://dx.doi.org/10.1038/ngeo550.

Xu M., (2012), Thesis (Ph.D.), Advanced geophysical studies of accretion of oceanic lithosphere in Mid-Ocean Ridges characterized by contrasting tectono-magmatic settings, Massachusetts Institute of Technology, http://hdl.handle.net/1721.1/70780.

Yilmaz O., (2001), Seismic data analysis, Processing, Inversion, and Interpretation of Seismic Data, Society of Exploration Geophysicists.

Table 1

Processing scheme	**Comments**
Trace editing[1]	AXIS 2R1 navigation lines 3 and 4
2D geometry definition	_
Band-pass filtering	Butterworh single, zero phase filter: 10/18-100/72 [(F1 dB/Octave 1)-(F2 dB/Octave 2)]
Noise suppress	Spike and noise burst edit; Trace edits applied
Spherical divergence correction	Gain correction g(t)=t*v(t).
Kirchhoff pre-stack time migration[2]	CMP sorting Prior to migration data were grouped into 78 bins (bin spacing 75 m) required by the KTMIG module. Data are migrated using modified ESP5 velocity function hanged from the seafloor
Radon filtering	Parabolic τ-p transform for p values between -200 and 2000 [m · s] Trace muting
Accurate/residual Normal-MoveOut correction (NMO)	Apply inverse NMO using migration velocities Combining 24 consecutive CMP gathers into super-CMP gathers. Semblance analysis performed to flatten AMC event at every 100 SuperCMP gather. Band-pass Ormsby, single filter: 4-12.5-40-50
Angle-gathers	Angles are calculated using one-dimensional approximation to the input velocity field at each CMP. Near-angle gather for 5-20˚ (maximum average offset ~1800 m - depending on the AMC depth and interval velocity) Far-angle gather fro 20-30˚ (~1800-2800 m)
Stacking	Near-angle (intercept A) stack 5-20˚ and far-angle (slope B) stack 20-30˚

[1]Trace editing was done using Paradigm's processing software; the remaining steps were done using Landmark's processing tool SeisSpace

[2]KTMIG in SeisSpace is very complex but it has very good documentation that explain it in details

Table 1 – Processing sequence for data preparation prior to AVA analysis.

Appendix A: Angular reflection coefficient equations: A historical overview, theory and synthetic examples

At normal incidence, the compressional (P) wave reflection coefficient is defined as the ratio of the amplitude of the reflected P-wave to the amplitude of the incident P-wave. Its sign depends on the velocities across the reflection interface, as illustrated in Figure A.1. In the early 20th century, Knott and Zoeppritz, using the continuity of displacement and stresses at the reflecting interface, developed the equations for P- and S-wave reflection and transmission amplitudes as a function of incidence angle. The equations they developed, nowadays known as the Zoeppritz equations, although robust are not convenient for practical use [*Hilterman,* 2001; *Yilmaz,* 2001]. Bortfeld [1961] was the first to give an approximation of the P-wave reflection coefficient, by linearization of the Zoeppritz equations. Although he separated compressional and shear wave contributions to the P-wave reflection coefficient, which made its expression more usable, it was not until Aki and Richards' approximation in 1980 that the reflection coefficient equations started being used in practice. Aki and Richards [1980] assumed velocity ratio of P and S-wave (Vp/Vs) to be equal to 2 and rearranged the equation by grouping terms that are function of density, Vp and Vs, respectively. In 1985, Shuey, assuming no change in density, presented another approximation, which is commonly written as:

$$R(\theta)=\left[\frac{1}{2}\left(\frac{\Delta Vp}{Vp}+\frac{\Delta\rho}{\rho}\right)\right]+\left[\frac{1}{2}\frac{\Delta Vp}{Vp}-4\frac{Vs^2}{Vp^2}\frac{\Delta Vs}{Vs}-2\frac{Vs^2}{Vp^2}\frac{\Delta\rho}{\rho}\right]\sin^2\theta+\left[\frac{1}{2}\frac{\Delta Vp}{Vp}\right](\tan^2\theta-\sin^2\theta). \qquad (A.1)$$

where: $\Delta Vp=Vp_2-Vp_1$ (Vp_2 and Vp_1 are P-wave velocities below and above the interface, respectively); $Vp=(Vp_2+Vp_1)/2$; $\Delta Vs=Vs_2-Vs_1$ (Vs_2 and Vs_1 are S-wave velocities below and

above the interface, respectively); $Vs=(Vs_2-Vs_1)/2$; $\Delta\rho=\rho_2-\rho_1$ (ρ_2 and ρ_1 are densities below and above the interface, respectively); $\rho=(\rho_2+\rho_1)/2$ and θ is the angle of incidence.

By this rearrangement terms were grouped according to their angle of incidence: the first term is for vertical incidence, the second for near to mid angles and the third one for far angles. The author also observed that for relatively small angles (i.e. less than 30º) the third term in the equation can be neglected and the reflection coefficient can be expressed as:

$$R(\theta) = A + B\sin^2\theta \qquad \text{(A.2)}$$

where:

$$A = \frac{1}{2}\left(\frac{\Delta Vp}{Vp} + \frac{\Delta\rho}{\rho}\right) \qquad \text{and} \qquad B = \frac{1}{2}\frac{\Delta Vp}{Vp} - 4\frac{Vs^2}{Vp^2}\frac{\Delta Vs}{Vs} - 2\frac{Vs^2}{Vp^2}\frac{\Delta\rho}{\rho} \qquad \text{(A.3)}$$

Equation A.2. is known as Shuey's equation and A and B as the intercept and slope attributes, respectively.

In Figure A.1, we compare the reflection coefficients for P- and S- waves calculated using three different approaches: Zoeppritz equations, Aki and Richards' approximation and Shuey's approximation (for the latter we only show the P-wave reflection coefficient that can be readily calculated). For the four different velocity/density settings across the interface displayed here, which use values that match possible velocity/density scenarios at mid-ocean ridge magma bodies, reflection coefficients are similar for incidence angles less than 30º (Figure A.1.C). We also note that when the shear velocity drops to zero below the interface (Vs_2=0 m/s), Shuey's curve is a better approximation to the Zoeppritz curve than is Aki and Richars' curve (Figure A.1.C3 and Figure A.1.C4). This is especially true for the range of incidence angles within which we observe a phase change of the reflected P waveform (i.e. the sign of the reflection coefficient changes from negative to positive). There, the S-wave reflection coefficient reaches its maximum.

This particular angle varies significantly depending on the velocity structure across the interface: for instance, between cases C3 and C4 Vs above the interface changes from 2900 m/s to 2430 m/s and the value of θ at which the phase shift is observed changes from 30 to ~ 37º.

In addition to the velocity change across the interface, reflection coefficients will also depend on structural characteristics of the subsurface, especially on the thickness of the reflecting layer. In Figure A.2 we show synthetic gathers that illustrate both effects, by perturbing ESP 5 velocity function. The tool used for generating the 1D synthetics is *ProMAX*'s "Synthetic CDP Generation" which requires a blocked velocity model and an input wavelet (derivation of a source wavelet used for generation of synthetic gathers is given in Appendix B). Output trace amplitudes are calculated by first finding a ray path connecting the source to the reflecting interface to the receiver. The corresponding reflection amplitude at the interface is then calculated using the full Zoeppritz equations, the input wavelet is scaled accordingly, and added to the data trace at the appropriate time. It is claimed that this process can handle any layer thickness and still treat the arrival times properly. In cases 1 to 3, the AML is associated with a sharp velocity decrease at its top and a gradual velocity increase at its base, and the Zoeppritz curve for a single interface (red curve) provides a very good match to the amplitudes extracted from the synthetics at the two-way time of the top of the AML (dashed blue curve; Figures A.2.1b, 2b, 3b). The effect of changing velocities within the AML is readily seen in amplitudes of the synthetics and calculated reflection coefficients. Note how the phase shift occurs at greater angles as the velocity decreases above the AML (case 2) or increases within the AML (case 3).

The effect of a thin bed on AVO/AVA analysis is well studied in sedimentary environments for oil and gas prospection [*Widess,* 1973; *Kalweit and Woods,* 1982; *Juhlin and Young,* 1993; *Bakke and Ursin,* 1998]. These studies resulted in a commonly accepted view that

for a bed thickness $< \frac{1}{4}\lambda$ (where λ is the source wavelength) the tuning effect is constructive and relative changes in amplitudes with angle of incidence/ offset can still be used as a valid proxy for hydrocarbon prospection. In case 4 (Figure A.2.4), the structure above the AML is unchanged from case 1, but the AML is represented as a sill of thickness ~ 38 m ($\sim \frac{1}{4}\lambda$). The amplitudes extracted from the synthetics at the two way-time of the top of the AML show a good agreement with the Zoeppritz curve for a single interface as well as with the amplitudes extracted from synthetics in case 1 (green curve). As the sill becomes thinner (~ 15 m; case 5) the discrepancy larger, but the relative amplitude variation with angle of incidence/offset is preserved (Figure A.2.5). In the case where the thickness is smaller (~12 m; case 6) the tuning effect is destructive and the event becomes undetectable (Figure A.2.6).

References:

Aki, K. I. and P. G., Richards, (1980), Quantitative seismology, *W. H. Freeman and Co*.

Bakke N. E. and B. Ursin, 1998, Thin-bed AVO effects, *Geophysical Prospecting,* 46, 571-587.

Bortfeld, R., 1961, Approximation to the reflection and transmission coefficients of plane longitudinal and transverse waves, *Geophys. Prosp.,* vol. 9, 485-502.

Hilterman F. J., Seismic Amplitude Interpretation, (2001), Distinguished Instructor Short Course, Distinguished Instructor Series, No. 4, *Society of Exploration Geophysicists and European Association of Geoscientists and Engineers.*

Juhlin C. and R., Young, (1993), Implications of thin layers for amplitude variation with offset (AVO) studies, *Geophysics*, vol. 58, no. 8, 1200-1204.

Kallweit R. S. and L. C. Wood, (1982), The limits of resolution of zero-phase wavelets, *Geophysics* 47, 1035, doi:10.1190/1.1441367.

Shuey, R. T., (1985), A simplification of the Zoeppritz equations, *Geophysics*, 50, 609-614.

Widess M. B., (1973), How thin is a thin bed?, *Geophysics*, vol. 38, no. 6, 1176-1180.

Yilmaz O., (2001), Seismic data analysis, Processing, Inversion, and Interpretation of Seismic Data, *Society of Exploration Geophysicists*.

Appendix B: Source wavelet for generation of synthetic gathers

The 2008 East Pacific Rise survey (MGL0812) aboard *R/V M. Langseth* used a tuned 3300 in^3 airgun array deployed at 7.5 m depth (Figure B.1). The array consisted of two identical gun strings, each with nine active guns and one spare. Tuning of the source signal is achieved using airgun chambers of different volumes, such that the bubble pulses from each gun signal are destructively superimposed producing a tuned signal with relatively little reverberations (http://www.ldeo.columbia.edu/~johnd/). Modeling of both the far-field signature (signal received at large distance beneath the center of the array) and notional signatures (individual gun signals taking into account airgun interactions) was done with PGS's *Nucleus* MASOMO software using the array geometry and tow depth of the MGL0812 survey (Figure B.2).

To investigate how similar the modeled far-field signature is to the actual array output, we examined hydrophone recordings from the *R/V M. Langseth* calibration survey that took place in late 2007-early 2008 (cruises MGL0707 and MGL0802; [*Tolstoy et al.,* 2009; *Diebold et al.,* 2010]). Signals collected in deep water and produced by the two-string airgun array represent the closest approximation to the MGL0812 configuration, with the only difference being array depth (6 m as compared to 7.5 m for MGL0812). The comparison is thus presented between modeled and recorded signals at 6 m depth. Shot gathers were extracted from the calibration hydrophone data for a range of airgun array and buoy positions and the cleanest record, received from shot #2078, is displayed here (Figure B.4.A and Figure B.4.B in black line). The exact location of the (freely-drifting) hydrophone in the plane parallel to the sea surface is unknown, thus for modeling comparison we used its recorded depth and location of the buoy at the sea surface (Figure B.3.B).

The modeled far-field signature was calculated for the source-receiver geometry of shot #2078 using a linear superposition of the notional signals output by *Nucleus*, with time shifting according to time of flight in a constant-velocity water layer, and scaling as the inverse of distance [*Parkes et al.,* 1984; *Fricke et al.,* 1985]:

$$S = \sum_{i=1}^{n} \left[\frac{1}{r_i} g_i \left(t - \frac{r_i}{v} \right) - \frac{1}{s_i} g_i \left(t - \frac{s_i}{v} \right) \right];$$

$$s_i = \sqrt{(x - x_i)^2 + (y - y_i)^2 + (z + h)^2} \quad \text{and} \quad r_i = \sqrt{(x - x_i)^2 + (y - y_i)^2 + (z - h)^2}.$$

where: S – is the far-field source signal; n=18 and is the number of guns in the array; r_i is the distance between hydrophone and the i^{th} gun, s_i is the distance between hydrophone and the mirror image of the i^{th} gun with respect to the sea surface, g_i - is the notional signal of i^{th} gun; v=1521 m/s (water velocity at ~20ºC); x (937 m), y (692 m) and z (7.5 m) are the coordinates of the hydrophone (measured from the central point of the air-gun array) and x_i, y_i and h (500 m) are the coordinates of the i^{th} gun.

The resulting modeled far-field signal for the source-receiver geometry of shot #2078 compares very well with the recorded signal (Figure B.4.B). The high frequency reverberations observed after the primary signal pulse might be related to the fact that the hydrophone at the deep site is not fixed and/or by the presence of noise.

Given the close match between the modeled and measured signals at 6 m depth, and the fact no measured signal is available for 7.5 m depth, we used a modeled far-field source signature computed for 7.5 m depth to generate synthetic gathers (Figure A.2).

Refernces:

Diebold, J. B., M. Tolstoy, L. Doermann, S. L. Nooner, S. C. Webb and T. J. Crone (2010), R/V Marcus G. Langseth seismic source: Modeling and calibration, *Geochem. Geophys. Geosusy*. 11 Q12012, doi: 10.1029/2010GC003216.

Fricke J. R., J. M. Davis, and D. H. Reed, (1985), A standard quantitative calibration procedure for marine seismic sources, *Geophysics*, vol. 50, no. 10, 1525-1532.

Parkes, G. E., A. Ziolkowski, L. Hatton, and T. Haugland, (1984), The signature of an air gun array: Computation from near-field measurements including interactions – Practical considerations; *Geophysics*, vol. 48, no. 2, 105-111.

Tolstoy, M., J. Diebold, L. Doermann, S. Nooner and S. C. Webb, (2009), Broadband calibration of the R/V Marcus Langseth four-string seismic sources, *Geochem. Geophys. Geosyst*., 10, Q08011, doi: 10.1029/2009GC002451

Figure 1. Location map for the amplitude variation with angle (AVA) analysis study of the East Pacific Rise (EPR) from 9º28' to 10ºN. The location of seismic line axis 2r1/cable 2 used for the analysis is shown in black. Black dots along the line indicate locations of interruptions in the axial-magma lens [*Carbotte et al.,* submitted.]. Numbers are the common-reflection-points (CRPs) for each identified interruption. White stars are locations of hydrothermal vents [*Haymon et al.,* 2004] and grey contour shows the spatial extent of lava flows from the 2005–06 eruption as determined from Alvin observations and TowCam photographic images [*Soule et al.,* 2007]. Bathymetry is from the EM120 grid collected during the MGL0812 cruise.

Figure 2. An example of correctly flattened AML event. The example is a 24 fold Super-common reflection point (SuperCRP) gather centered on CRP 16400 along line axis 2r1 with the semblance panel (on the left) and traces at offsets ranging from 200 to ~2800 m (on the right). The AML event is indicated with red double arrow.

Figure 3. Selected CRP gathers after pre-stack migration and final/residual NMO correction to flatten the AML. Data is shown for angles of incidence between 5º (in black line), 20º (dashed line) and 30º (dotted line) with the angle of incidence indicated near the AML interface (marked with a double red arrow). The conversion from offset to angle of incidence is calculated using the final velocity function used for the final NMO. Offset is shown along x axis for convenience.

Figure 4. Angle stacks: A) for the entire range of incidence angles at the AML interface used in this study (5º to 30º) which is equivalent to offsets of ~ 350 to 2800 m. Dashed lines labeled with CRP number, represent locations of the CRP gathers shown in Figure 3. Superimposed

rectangles show windows used for AVA analysis. Colors are used to distinguish AML segments: segment 1 in orange (9º29.8'-9º35.7'), segment 2 in violet (9º35.7'-9º37.8'), segment 3 in yellow (9º37.8'-9º40.1'), segment 4 in light blue (9º40.1'-9º42.3'), segment 5 in pink (9º42.3'-9º44.6'), segment 6 in dark blue (9º44.6'-9º48'), segment 7 in bright red (9º48'-9º51.2'), segment 8 in green (9º51.2'-9º56.2') and segment 9 in brown (9º56.2'-9º58.4'). B) For 5º to 20º incidence angle at the AML interface (near-angle, corresponds with offsets of ~ 350 to 1800 m, as shown in Figure 3). This angle stack is used to extract the intercept attribute A for crossplotting. C) For 20º to 30º incidence angles at the AML interface (mid-angle, corresponds with offsets of ~ 1800 to 2800 m, as shown in Figure 3). This angle stack is used to extract the slope attribute B for crossplotting. Black arrows in all panels indicate interruptions in the AML reflection [Chapter 1] with corresponding CRP numbers labeled.

Figure 5. A - Schematic illustration of intercept versus slope crossplot modified from Foster et al. [2010]. See text for details. B – Schematic illustration of: 1) the lithology case for which anomaly is obtained in crossplot domain (hydrocarbon filled in pores) and for which background trend is obtained (air filled in pores of a reservoir sedimentary rock); 2) the lithology at the mid-ocean ridges for the anomaly (AML on axis) and no reflection (on flanks). See text for description.

Figure 5C - Illustration of a near angle incidence waveform (left) showing where negative (colored dots) and positive (colored open circles) peaks plot in A versus B crossplotting domain.

Figure 6. $P_{AML}S$ stacks. Close up of seismic sections stacked for mid-offsets (1500-4000 m) using stacking velocity (v=2400 m/s) appropriate for the P to S converted phase off the AML or $P_{AML}S$. Seismic sections span entire EPR segment from 8º20' to 10º10' and include along-axis seismic lines axis 1, axis 3 and axis 2r1. Location of these along axis lines is shown in Figure 1 Chapter 1. Expected twtt of the $P_{AML}S$ reflection (some 200 ms below the AML event) is indicated with blue arrows; observed $P_{AML}S$ is marked by red arrows.

Figure 7. A vs. B crossplot template for calculated trend lines for different constant ratios of compressional and shear velocity. Note the counterclockwise rotation of the trend as Vp/Vs ratios (labeled) increases.

Figure 8. AVA crossplots obtained from ABAVO software for the nine AML segments highlighted in Figure 4A (identical color code is used). For each segment, the scattered anomaly is plotted as colored dots, each dot representing the A, B pair calculated from one CRP gather. The best-fit trend determined as the major axis of the ellipse enclosing all data points is also plotted with colored solid line with the corresponding Vp/Vs value indicated in the bottom left corner of the crossplot. The series of black lines plotted on top represent the template trends for the suite of Vp/Vs ratios as shown in Figure 7.

Figure 9. Partial offset stacked seismic sections for the P and $P_{AML}S$ events. A) near offset (200-1500 m) stack with stacking velocity optimal for the AML event (v=2600 m/s); B) mid offset (1500-4000 m) stack using the same stacking velocity v=2600 m/s ; C) mid offset (1500-4000 m) stack using lower velocity optimal for P-to-S converted phase (v=2400 m/s); $P_{AML}S$ event is

indicated with red arrows. Blue lines highlight boundaries of AML segments with each segment labeled (as shown in Figure 4) and red arrows indicate presence of $P_{AML}S$ event. For comparison purposes, A and B are plotted with the same gain.

Figure 10. Schematic summary of along-axis variations in melt content of the AML obtained from AVA analysis. A) for the entire stretch of the EPR included in this study (Figure 1); B) at a finer scale for the three lens segments that are located beneath the zone of recent documented eruptions. Black arrows indicate the AML interruptions with latitude labeled. Double blue arrows show locations of 1D waveform inversion study of Xu, [2012].

Figure A.1. – A theoretical overview on: A) vertical incidence P-wave for the case when $Vp_1<Vp_2$ (left side) and $Vp_1>Vp_2$ and $Vs_2=0$ (right side) with a schematic zero-phase wavelet reflected from the interface (´P – up-going P-wave, `P –down-going P-wave); B) for incident P-wave at non-vertical incidence angle for the case when $Vp_1<Vp_2$ (left side) and $Vp_1>Vp_2$ and $Vs_2=0$ (right side), with all reflected and transmitted phases (´S- up-going S-wave, `S – down-going S-wave, P-wave the same as in A); C) reflection coefficients as a function of angle of incidence calculated using Zoeppritz equations for reflected P- (thick red line) and S-wave (red dashed line), Aki and Richard's approximation for reflected P- (thick green) and S-wave (dashed green line), and Shuey's approximation for reflected P-wave (blue line). The reflection coefficients are calculated for four cases: 1) solid to solid, 2) solid to mush and 3) and 4) solid to melt with parameters given in the figure and representing possible velocity scenarios at the mid-ocean ridges. Grey shading highlights angles of incidence >30º.

Figure A.2. – Synthetic common-mid-point (CMP) gathers, generated using modeled source wavelet from *R/V M. Langseth* (see Appendixes A and B), for different Vp and Vs velocity functions are shown (part a, right hand panel). Graph below each synthetic gather (part b) compares P-wave reflection coefficients calculated using Zoeppritz equation (red line) and Shuey's approximation (thick blue line) with reflection amplitudes picked from the synthetic gathers (dashed blue line). The ESP 5 velocity function (shown in 1a, from *Vera et al.,* [1990]) was used as a starting velocity structure for Vp and Vs. We further modified it by imposing: in 2a), a decrease in Vs above the AML from 2900 m/s to 2430 m/s; in 3a), an increase in Vs within the AML from 0 m/s to 1800 m/s; in 4a) the gradient zone below the AML is eliminated and the AML is represented as a thin bed with constant Vp and Vs and a thickness of ~ 1/4λ (where λ is the dominant wavelength of the source signal), 38 m; in 5a) the thickness of the sill is decreased to 15 m and 6a) to 12 m. Note that for case 4, the reflection coefficient picked from the synthetic gather varies with angle of incidence (blue dashed line) in very similar as for case 1 (thick green line).

Figure B.1 – Top: schematic profile view (not to scale) of an airgun string with individual airgun chamber volumes listed. Bottom: plan view of the geometry of the two-string array as used for modeling in *Nucleus* MASOMO. Circles are scaled according to volume, and red circles represent two-gun clusters.

Figure B.2 – Notional signatures modeled in *Nucleus* for each airgun of the two-string array towed at 6 m depth (thick blue line is for string 1 and red for string 2). The signals from airguns 4 and 14 are not included since these guns are the inactive, spare ones.

Figure B.3 – A) Source signatures modeled at ~ 500 m below the central point of the two-string airgun array (in blue) and at the location of the field hydrophone for shot #2078 during the calibration of the two-string array in deep water (in red). B) A schematic view of the geometry used for the calculation of these two signatures. The blue circle indicates the theoretical (i.e., here 500 m beneath the center of the array) position of a hydrophone for far-field signature recording. The red circle shows the estimated position of the hydrophone for shot #2078. The dashed arrows represent an average direct path (in black) from airguns to hydrophone and an average source ghost path (in orange).

Figure B.4 – A) Survey map for the deep-water site during calibration cruise MGL0802. The ship track is shown in blue and the track of the drifting hydrophone buoy at the water surface is shown in red. In the enlarged window, the blue star shows the location of shot #2078 and the red star the location of the buoy. B) Comparison between received source signal for shot #2078 from the calibration cruise (in black) and modeled source signal (in green) for the source-receiver geometry of shot #2078, assuming that the hydrophone is located vertically beneath the buoy.

Chapter 2: Figures

Figure 1

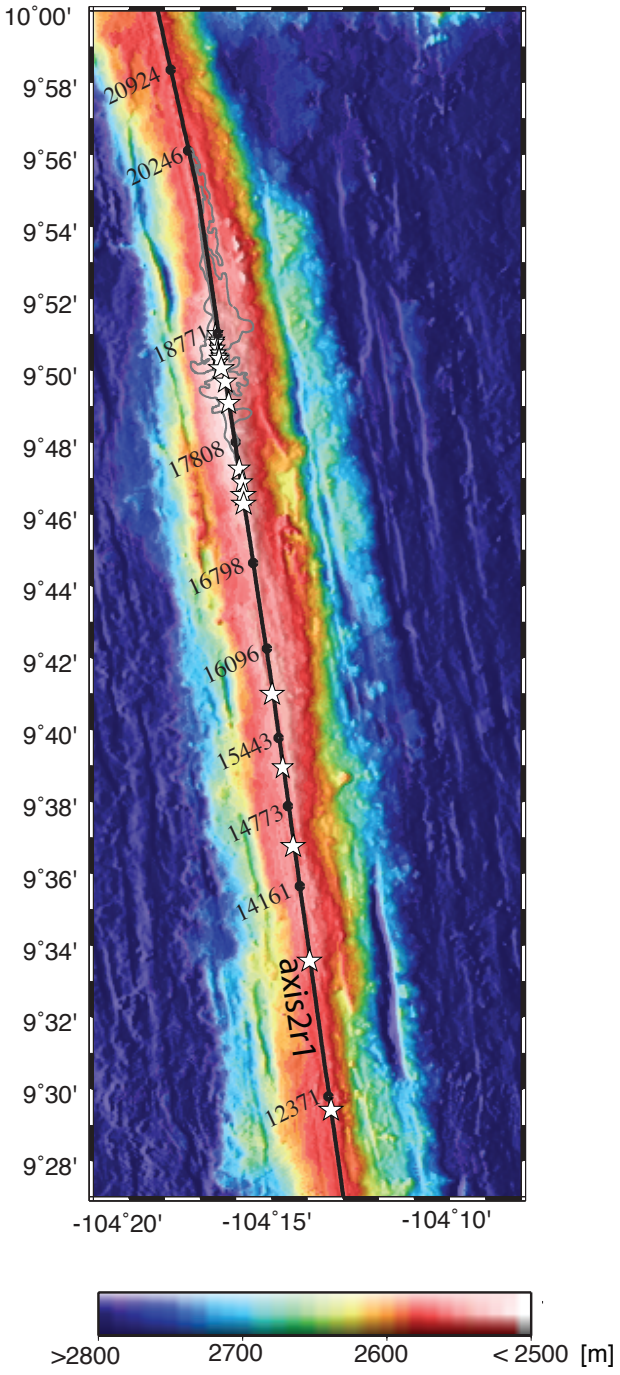
10˚00'
9˚58'
9˚56'
9˚54'
9˚52'
9˚50'
9˚48'
9˚46'
9˚44'
9˚42'
9˚40'
9˚38'
9˚36'
9˚34'
9˚32'
9˚30'
9˚28'
-104˚20'
-104˚15'
-104˚10'
20924
20246
18771
17808
16798
16096
15443
14773
14161
12371
axis2r1
>2800
2700
2600
< 2500 [m]

Figure 2

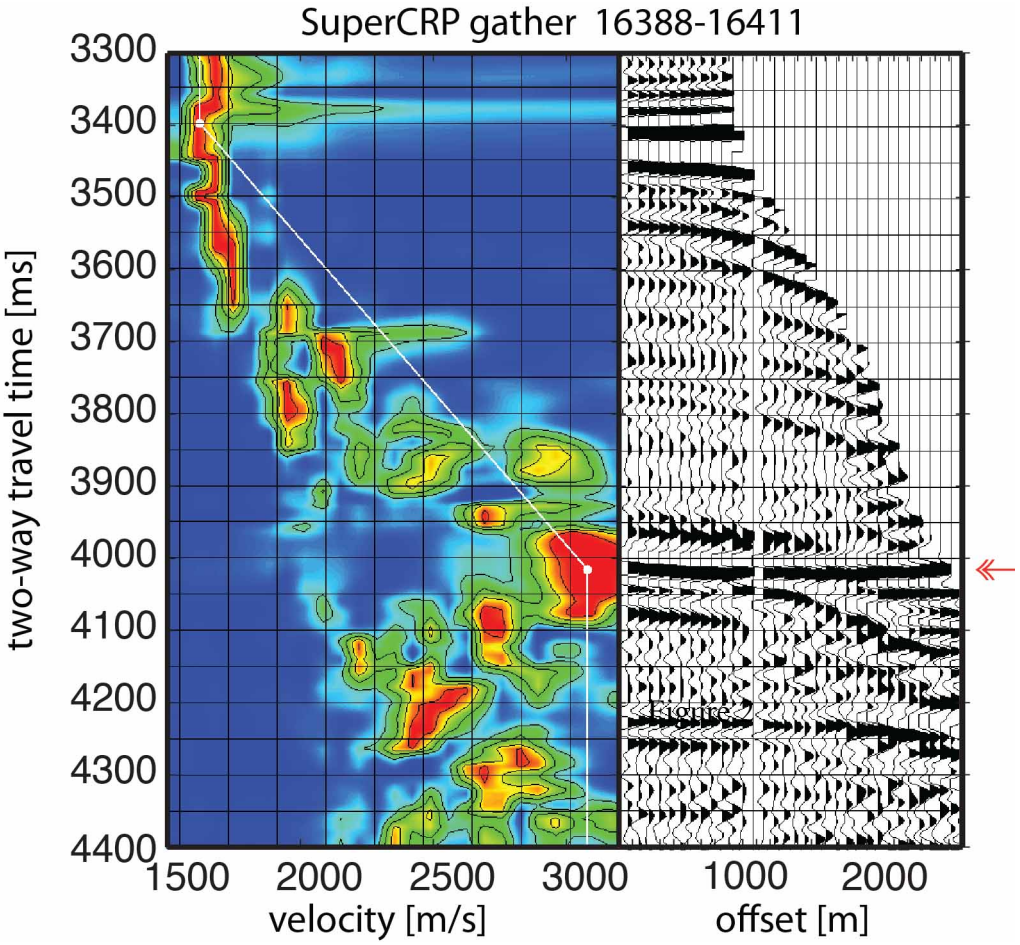
SuperCRP gather 16388-16411
two-way travel time [ms]
3300
3400
3500
3600
3700
3800
3900
4000
4100
4200
4300
4400
1500
2000
2500
3000
velocity [m/s]
1000
2000
offset [m]

Figure 3

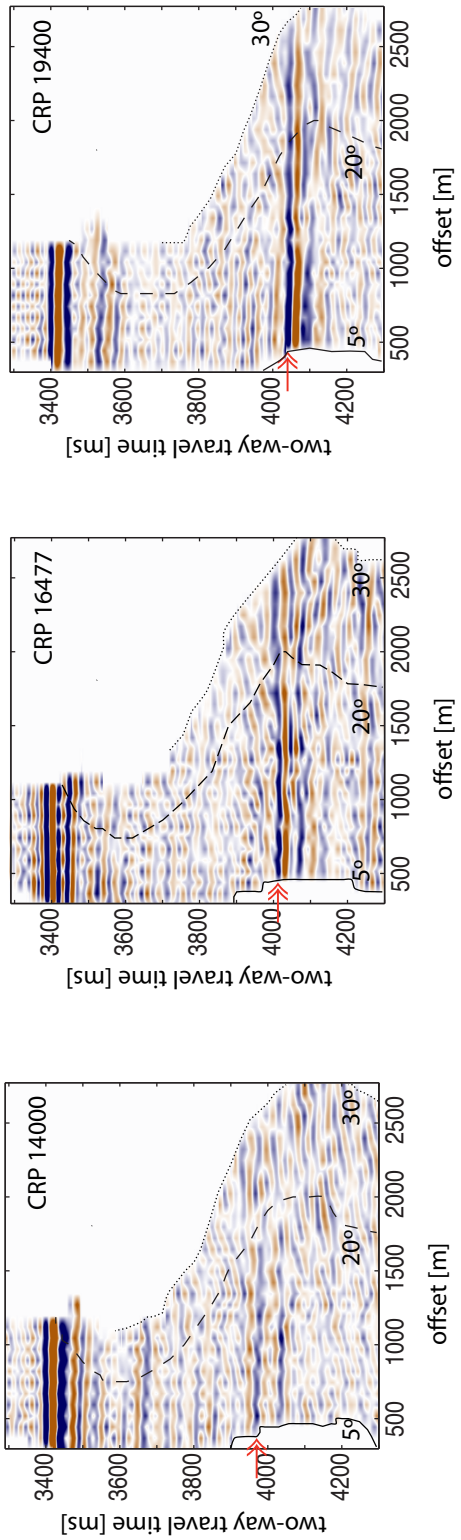
CRP 19400
CRP 16477
CRP 14000
5°
20°
30°
offset [m]
two-way travel time [ms]
500
1000
1500
2000
2500
3400
3600
3800
4000
4200

Figure 4

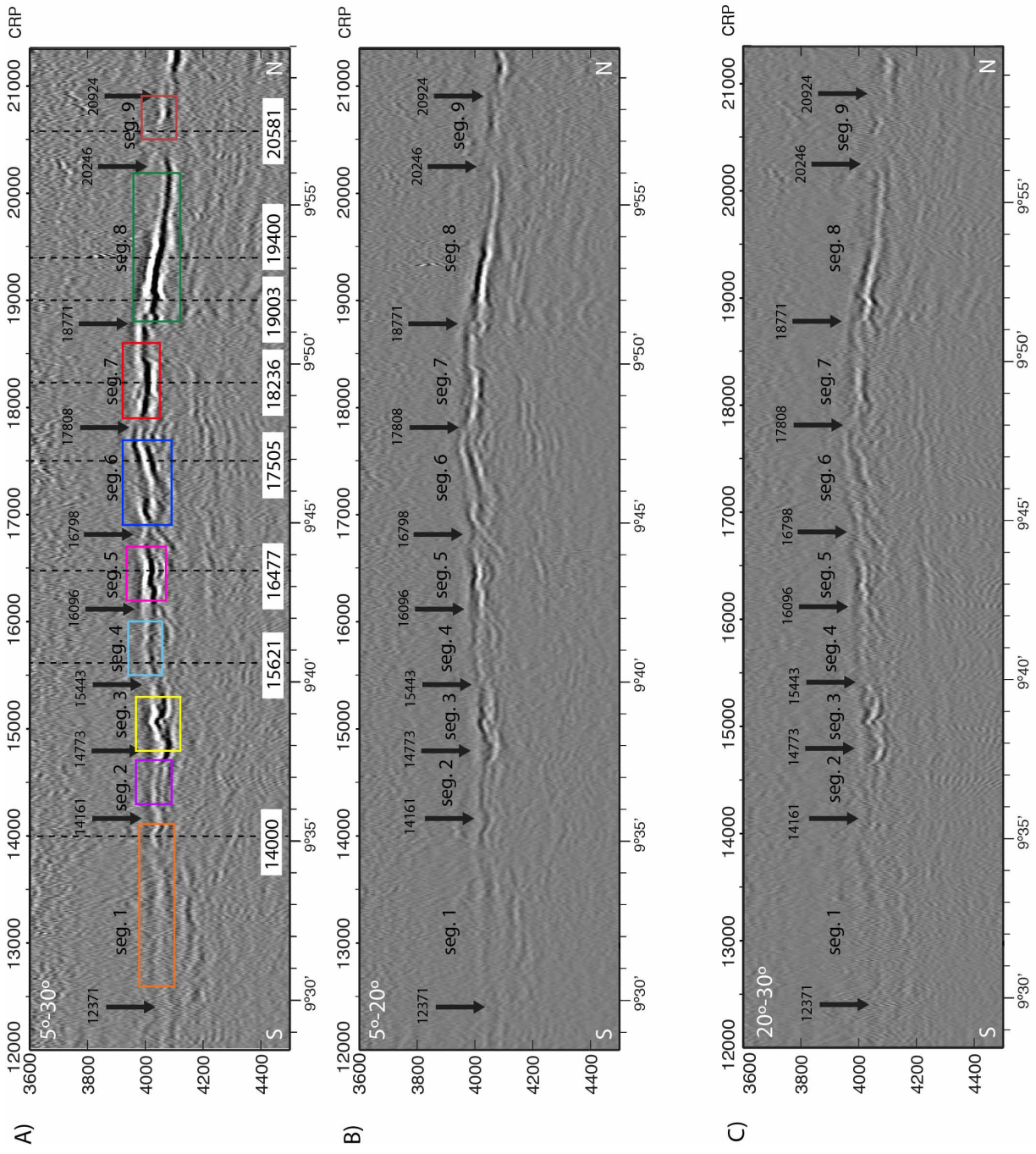
A)
B)
C)
CRP
5°–30°
5°–20°
20°–30°
seg. 1
seg. 2
seg. 3
seg. 4
seg. 5
seg. 6
seg. 7
seg. 8
seg. 9
12371
14161
14773
15443
16096
16798
17808
18771
20246
20924
14000
15621
16477
17505
18236
19003
19400
20581
S
N
9°30'
9°35'
9°40'
9°45'
9°50'
9°55'

Figure 5

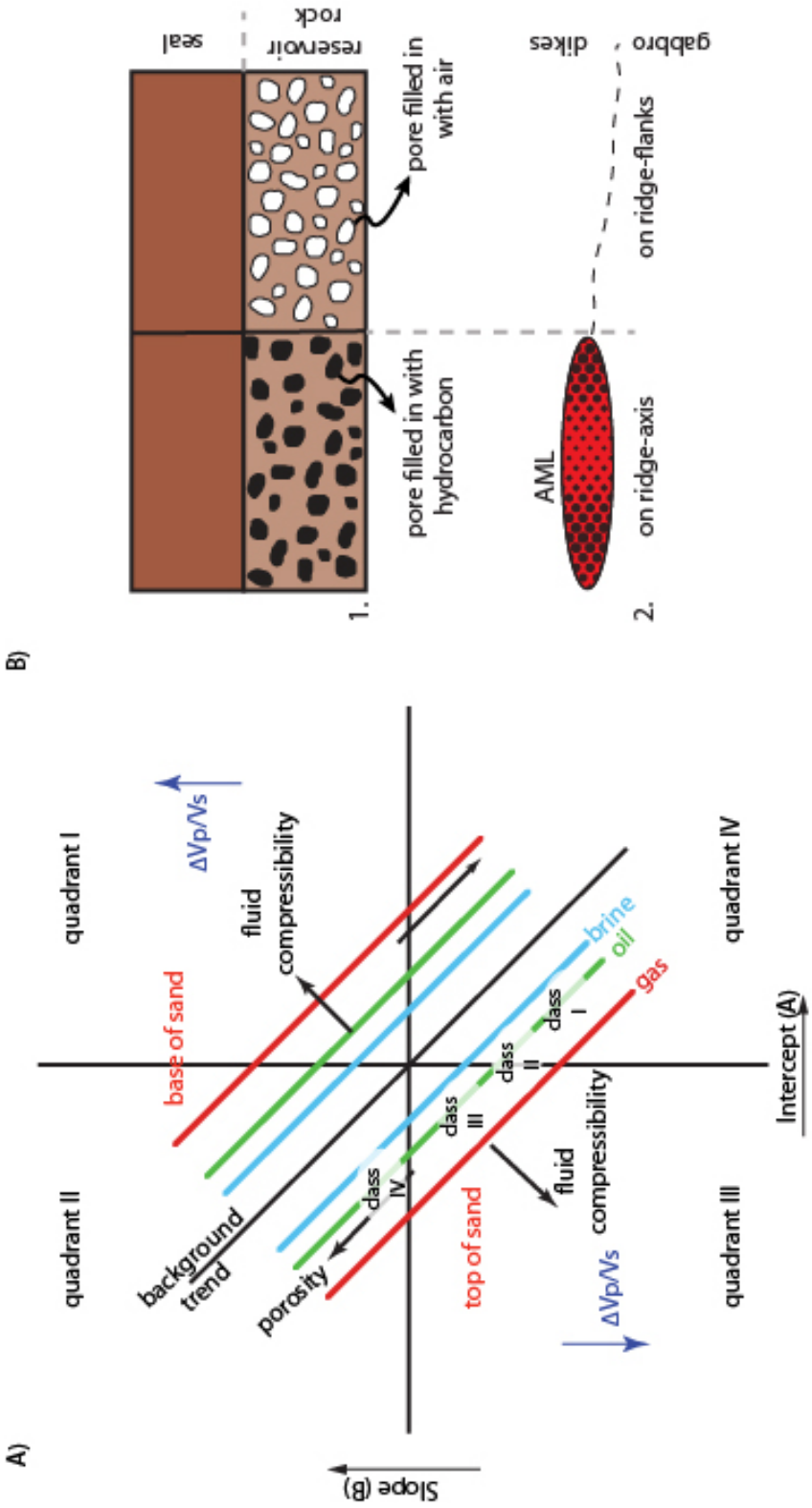
B)
seal
reservoir rock
pore filled in with air
pore filled in with hydrocarbon
1.
dikes
gabbro
on ridge-flanks
AML
on ridge-axis
2.
A)
quadrant I
quadrant II
quadrant III
quadrant IV
ΔVp/Vs
fluid compressibility
base of sand
background trend
porosity
top of sand
brine
oil
gas
class I
class II
class III
class IV
Intercept (A)
Slope (B)

Figure 5.C)

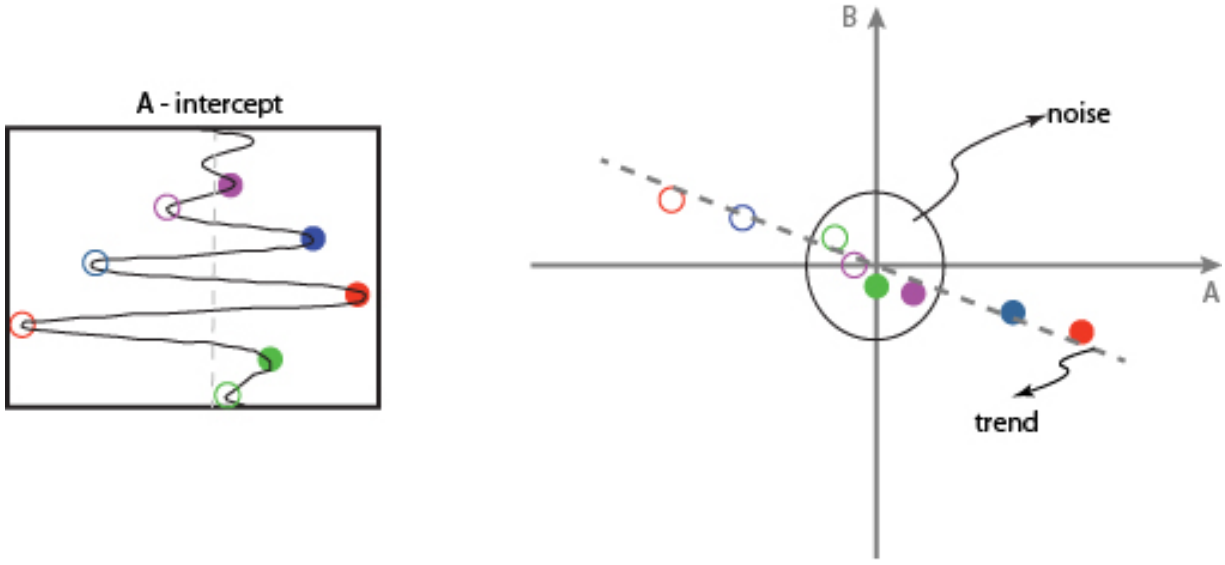

Figure 6

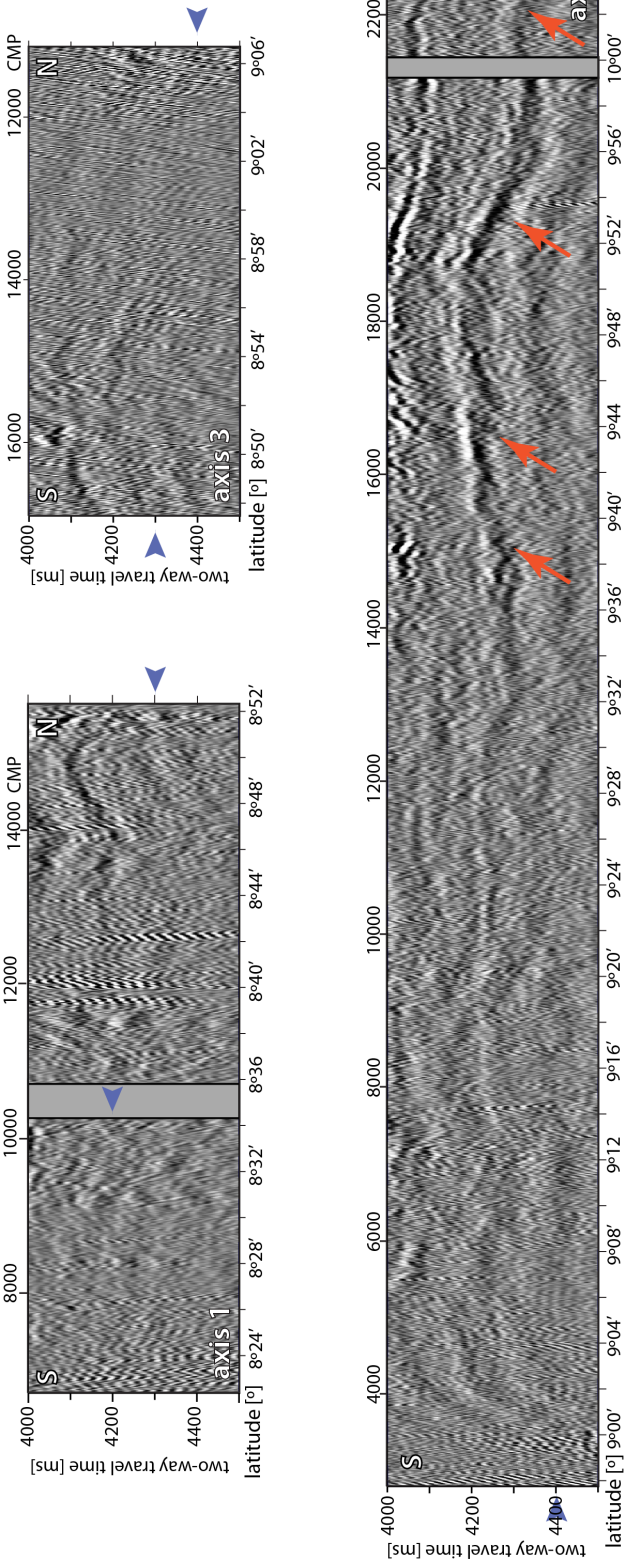
axis 1
axis 3
axis 2r1
S
N
CMP
latitude [°]
two-way travel time [ms]
4000
4200
4400
8000
10000
12000
14000
16000
18000
20000
22000
8°24′
8°28′
8°32′
8°36′
8°40′
8°44′
8°48′
8°52′
8°54′
8°58′
9°02′
9°06′
9°00′
9°04′
9°08′
9°12
9°16′
9°20′
9°24′
9°28′
9°32′
9°36′
9°40′
9°44
9°48′
9°52′
9°56′
10°00′
10°04′

Figure 7

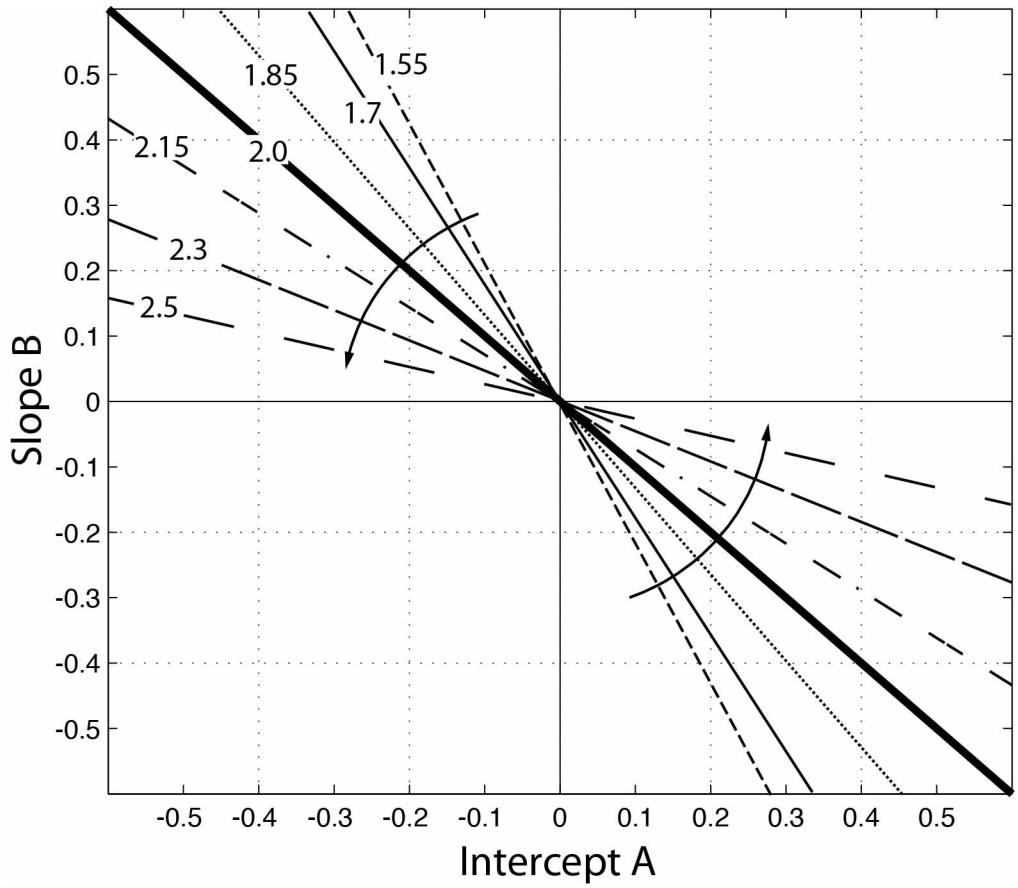
1.85
1.55
1.7
2.15
2.0
2.3
2.5
Slope B
Intercept A
0.5
0.4
0.3
0.2
0.1
0
-0.1
-0.2
-0.3
-0.4
-0.5
-0.5 -0.4 -0.3 -0.2 -0.1 0 0.1 0.2 0.3 0.4 0.5

Figure 8

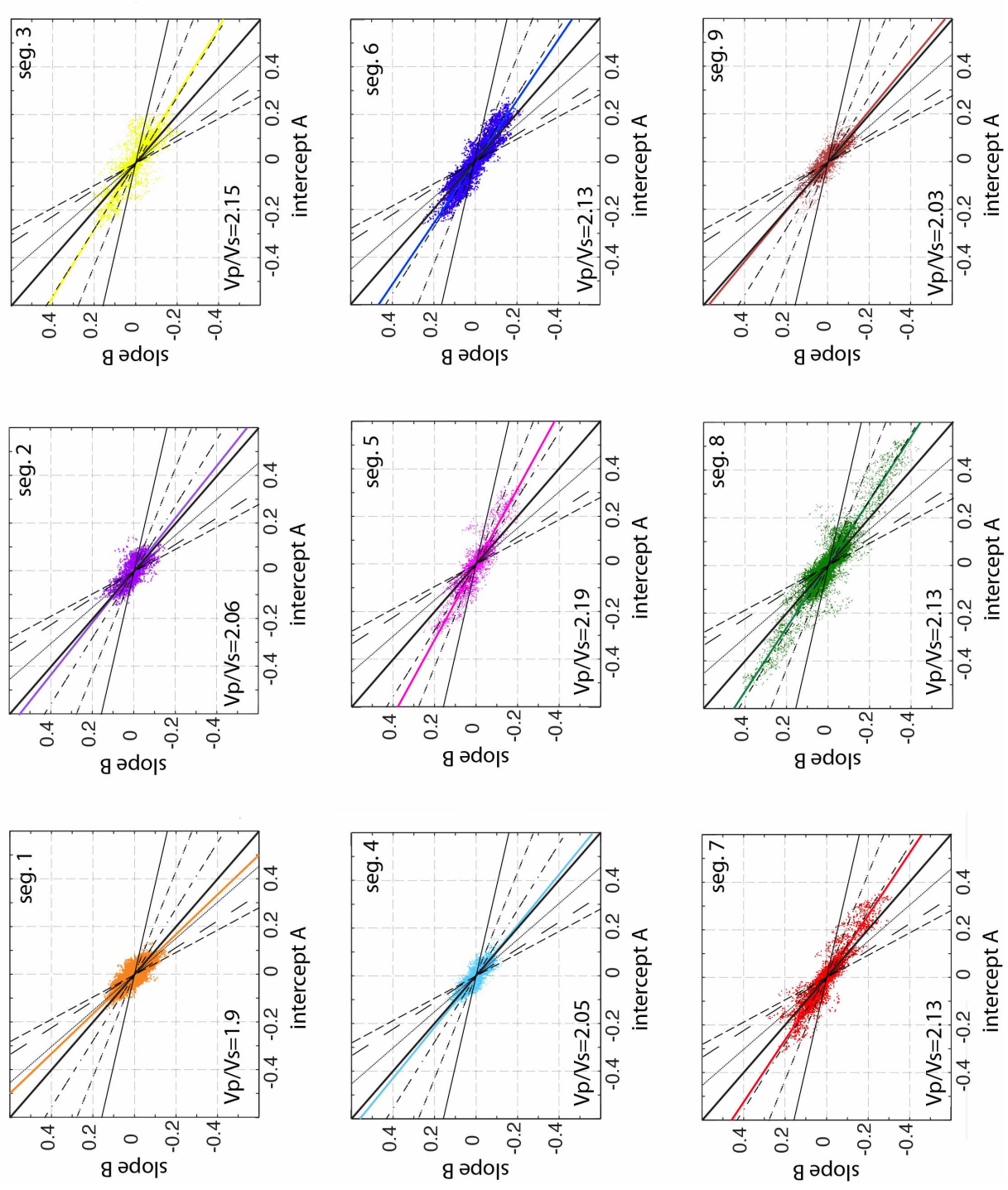
seg. 1
Vp/Vs=1.9
seg. 2
Vp/Vs=2.06
seg. 3
Vp/Vs=2.15
seg. 4
Vp/Vs=2.05
seg. 5
Vp/Vs=2.19
seg. 6
Vp/Vs=2.13
seg. 7
Vp/Vs=2.13
seg. 8
Vp/Vs=2.13
seg. 9
Vp/Vs=2.03
slope B
intercept A
0.4
0.2
0
-0.2
-0.4

Figure 9

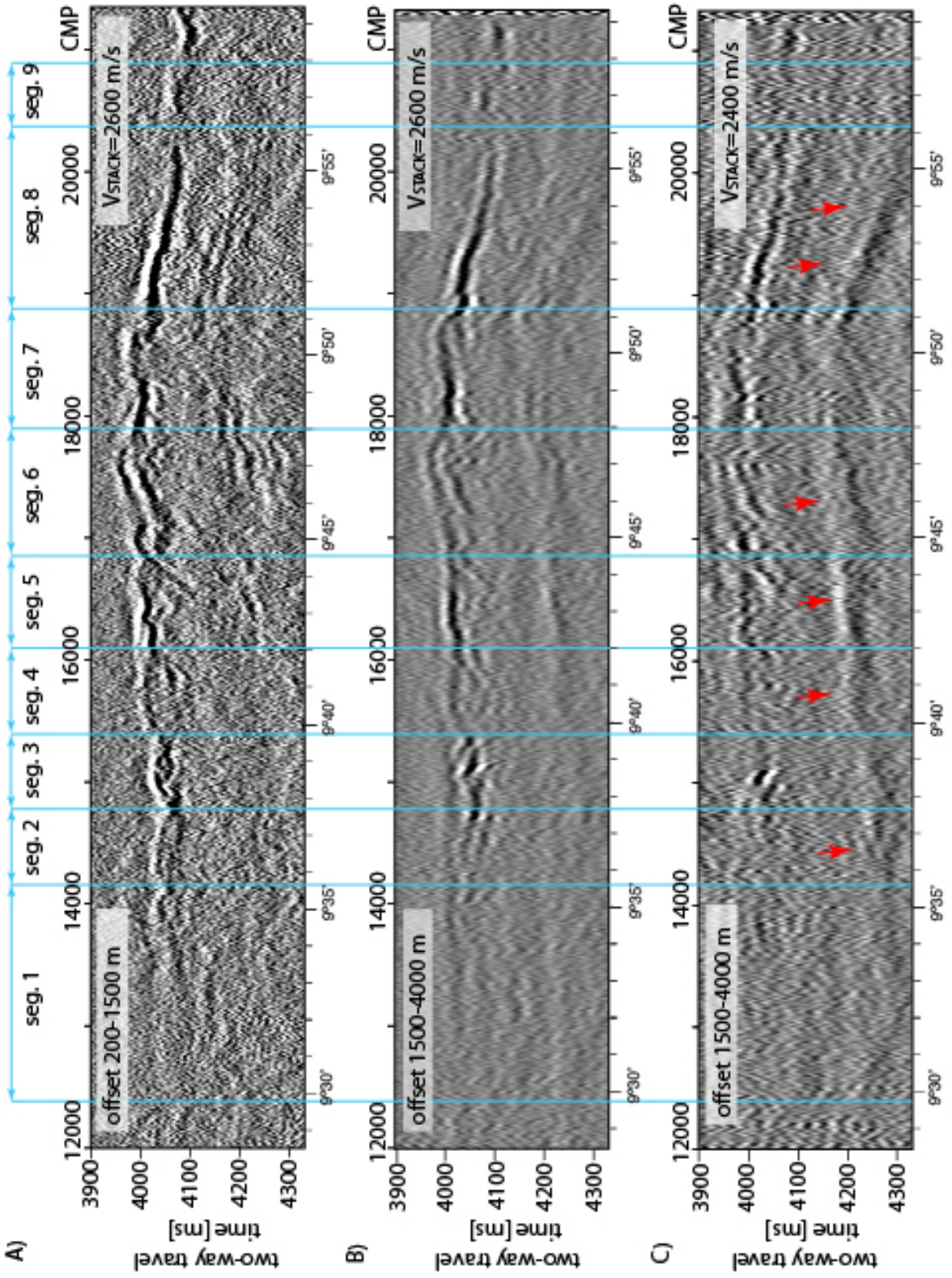
A)
B)
C)
seg. 1
seg. 2
seg. 3
seg. 4
seg. 5
seg. 6
seg. 7
seg. 8
seg. 9
CMP
12000
14000
16000
18000
20000
offset 200-1500 m
offset 1500-4000 m
VSTACK=2600 m/s
VSTACK=2400 m/s
two-way travel time [ms]
3900
4000
4100
4200
4300
9°30'
9°35'
9°40'
9°45'
9°50'
9°55'

Figure 10

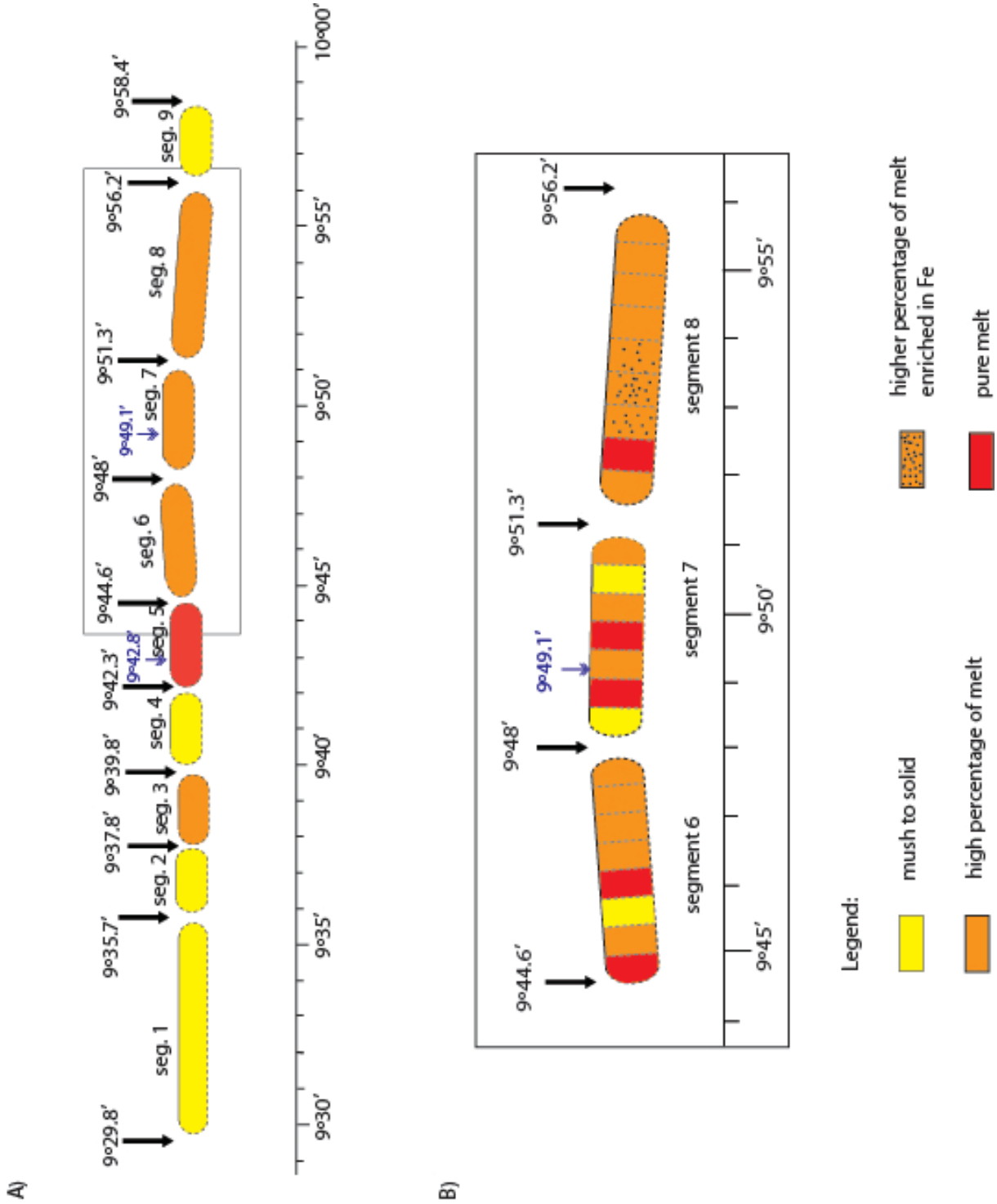
A)
9°29.8′
9°35.7′
9°37.8′
9°39.8′
9°42.3′
9°44.6′
9°48′
9°51.3′
9°56.2′
9°58.4′
seg. 1
seg. 2
seg. 3
seg. 4
seg. 5
seg. 6
seg. 7
seg. 8
seg. 9
9°42.8′
9°49.1′
9°30′
9°35′
9°40′
9°45′
9°50′
9°55′
10°00′
B)
9°44.6′
9°48′
9°51.3′
9°56.2′
9°49.1′
segment 6
segment 7
segment 8
9°45′
9°50′
9°55′
Legend:
mush to solid
high percentage of melt
higher percentage of melt enriched in Fe
pure melt

Appendix Figures: Chapter 2

Figure A.1

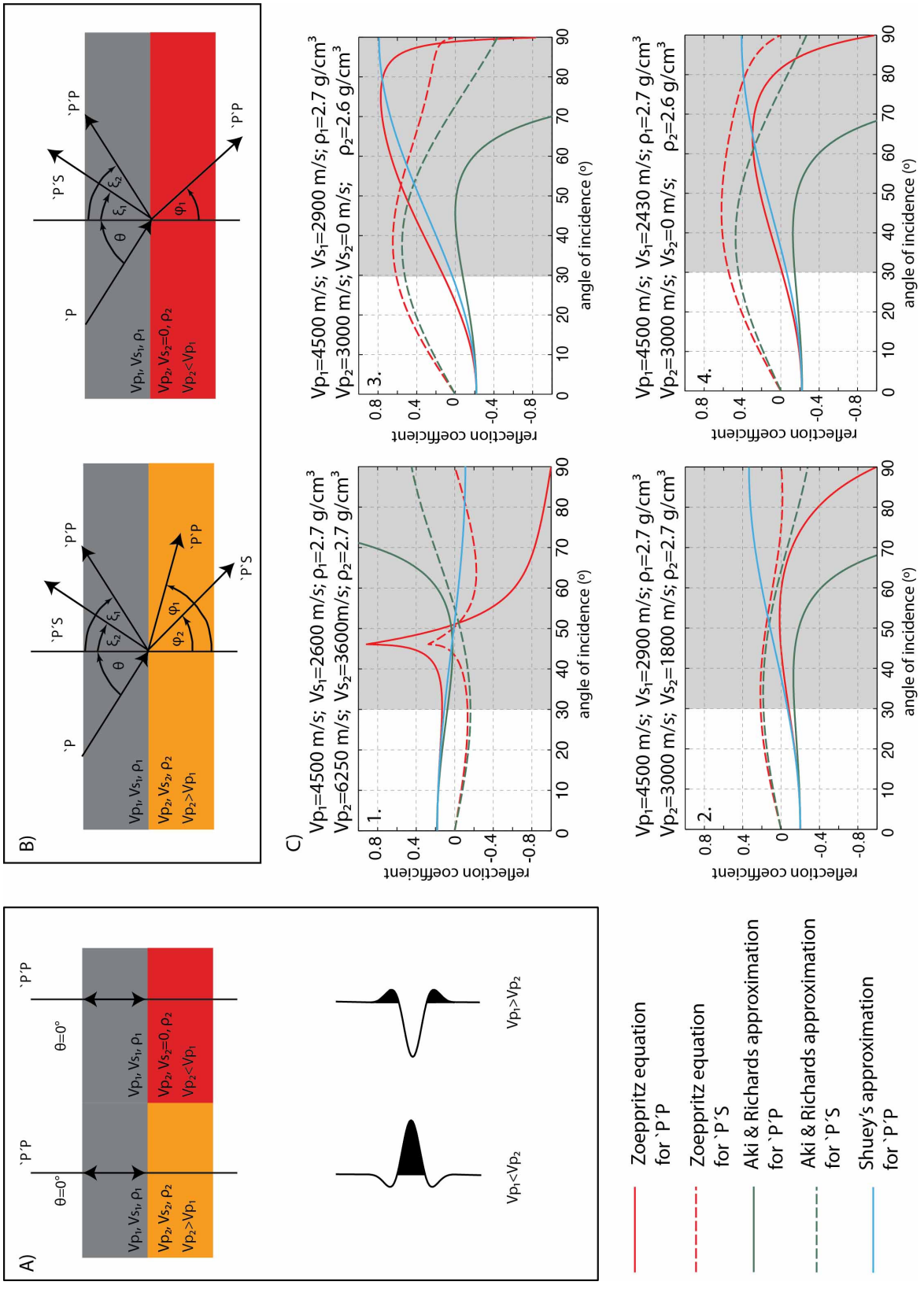
A)
θ=0°
`P´P
Vp1, Vs1, ρ1
Vp2, Vs2, ρ2
Vp2>Vp1
Vp2, Vs2=0, ρ2
Vp2<Vp1
Vp1<Vp2
Vp1>Vp2
B)
`P
`P´S
`P´P
`S´S
`S´P
Vp1, Vs1, ρ1
Vp2, Vs2, ρ2
Vp2>Vp1
Vp2, Vs2=0, ρ2
Vp2<Vp1
θ
ξ1
ξ2
φ1
φ2
C)
1.
Vp1=4500 m/s; Vs1=2600 m/s; ρ1=2.7 g/cm3
Vp2=6250 m/s; Vs2=3600m/s; ρ2=2.7 g/cm3
2.
Vp1=4500 m/s; Vs1=2900 m/s; ρ1=2.7 g/cm3
Vp2=3000 m/s; Vs2=1800 m/s; ρ2=2.7 g/cm3
3.
Vp1=4500 m/s; Vs1=2900 m/s; ρ1=2.7 g/cm3
Vp2=3000 m/s; Vs2=0 m/s; ρ2=2.6 g/cm3
4.
Vp1=4500 m/s; Vs1=2430 m/s; ρ1=2.7 g/cm3
Vp2=3000 m/s; Vs2=0 m/s; ρ2=2.6 g/cm3
reflection coefficient
angle of incidence (°)
Zoeppritz equation for `P´P
Zoeppritz equation for `P´S
Aki & Richards approximation for `P´P
Aki & Richards approximation for `P´S
Shuey's approximation for `P´P

Figure A.2

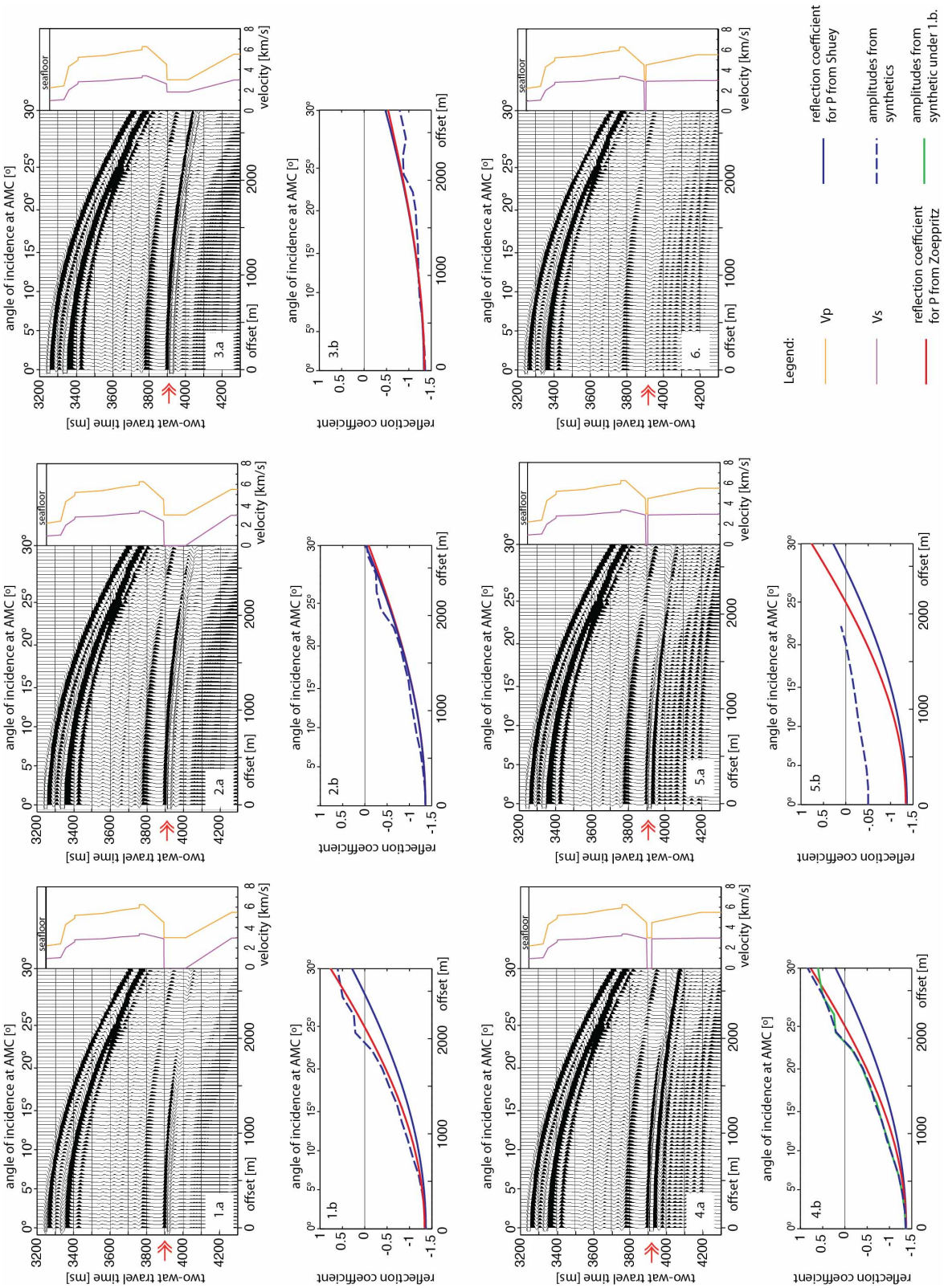
angle of incidence at AMC [°]
two-wat travel time [ms]
velocity [km/s]
offset [m]
reflection coefficient
seafloor
1.a
1.b
2.a
2.b
3.a
3.b
4.a
4.b
5.a
5.b
6.
Legend:
Vp
Vs
reflection coefficient for P from Shuey
reflection coefficient for P from Zoeppritz
amplitudes from synthetics
amplitudes from synthetic under 1.b.

Figure B.1

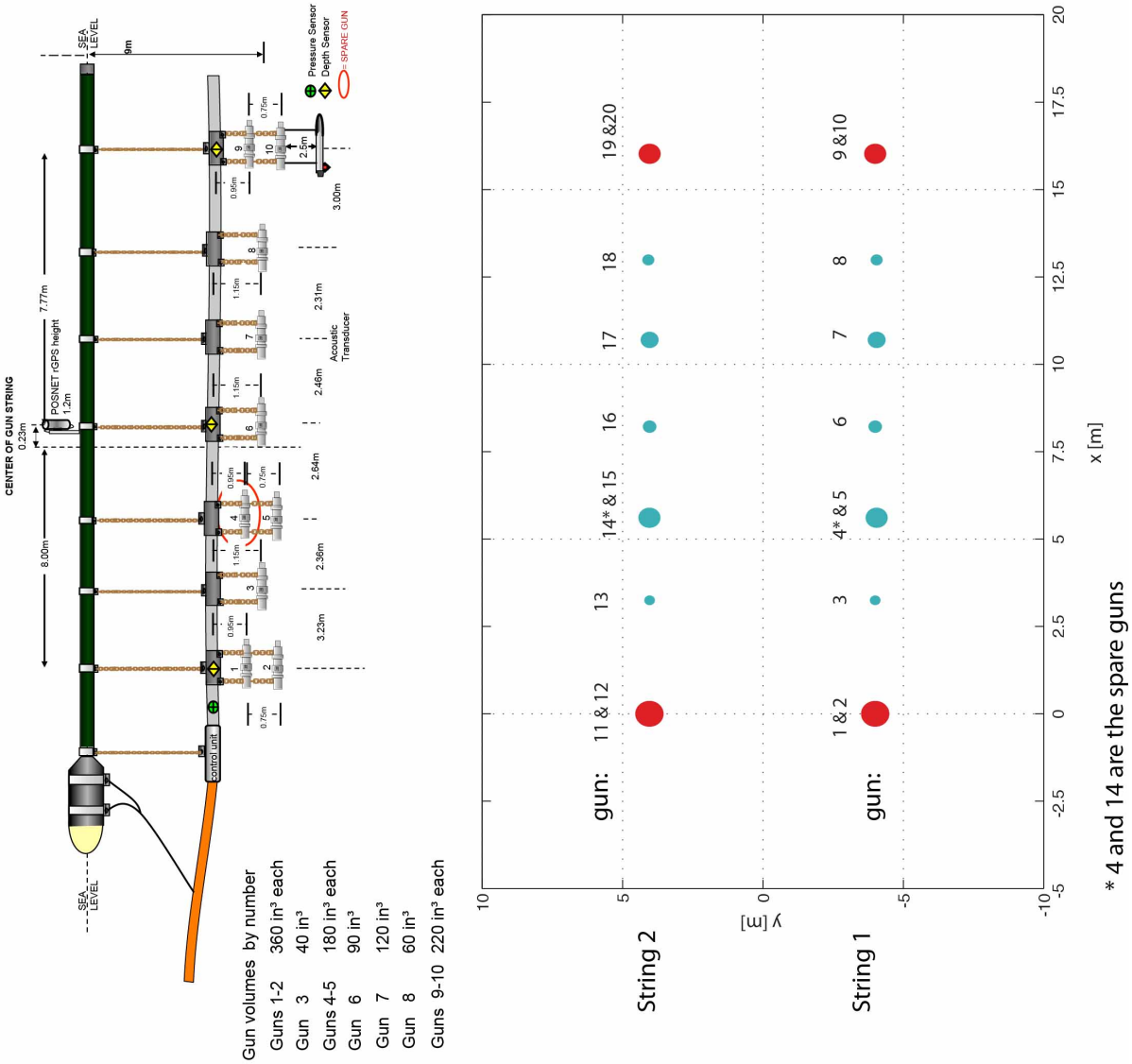
CENTER OF GUN STRING
0.23m
8.00m
7.77m
POSNET rGPS height
1.2m
SEA LEVEL
9m
Control Unit
Pressure Sensor
Depth Sensor
SPARE GUN
Acoustic Transducer
3.00m
2.5m
2.31m
2.46m
2.64m
2.98m
3.23m
Gun volumes by number
Guns 1-2 360 in³ each
Gun 3 40 in³
Guns 4-5 180 in³ each
Gun 6 90 in³
Gun 7 120 in³
Gun 8 60 in³
Guns 9-10 220 in³ each
String 2
String 1
gun:
11 & 12
13
14* & 15
16
17
18
19 &20
1 & 2
3
4* & 5
6
7
8
9 &10
y [m]
x [m]
* 4 and 14 are the spare guns

Figure B.2

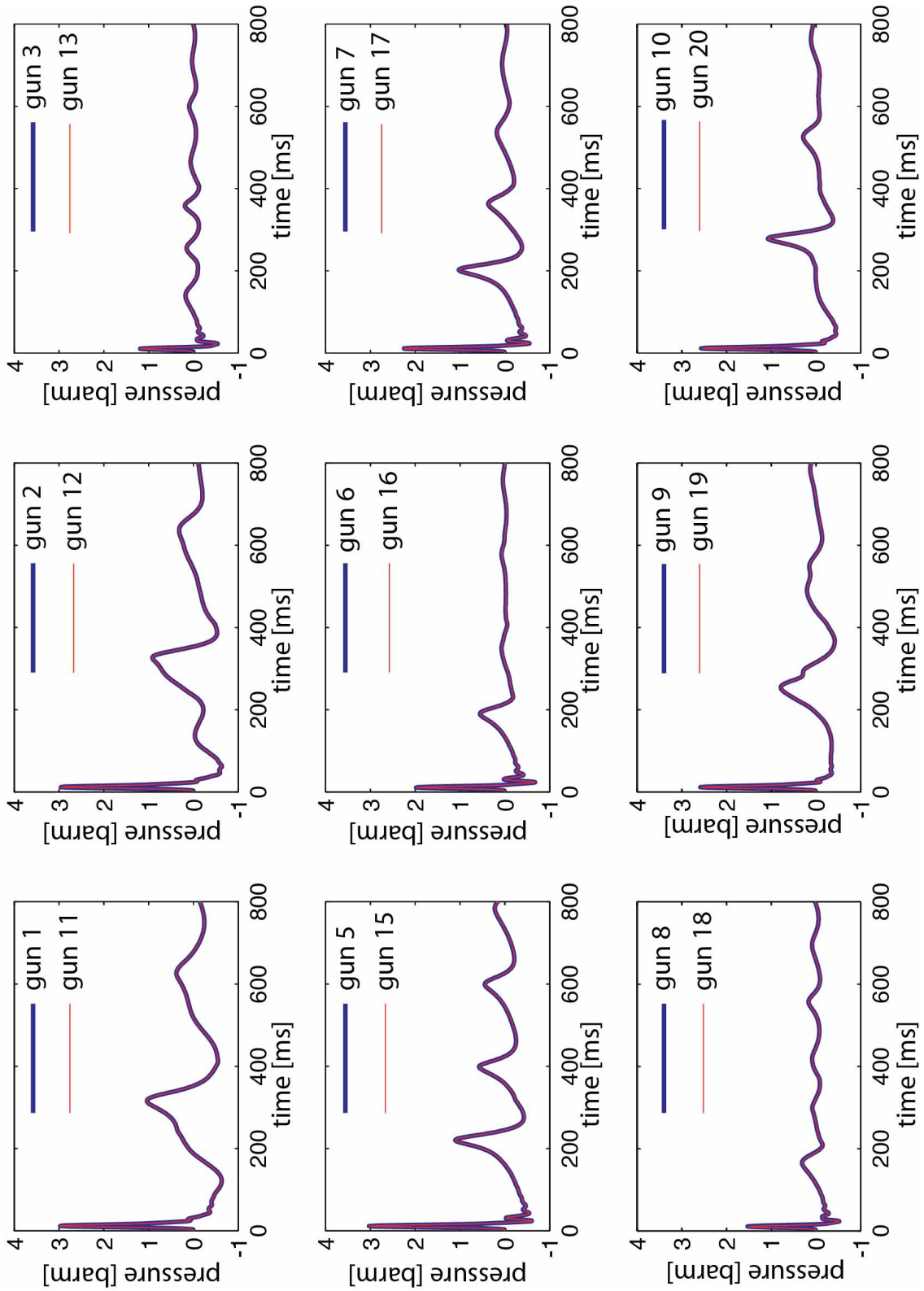
gun 1
gun 11
gun 2
gun 12
gun 3
gun 13
gun 5
gun 15
gun 6
gun 16
gun 7
gun 17
gun 8
gun 18
gun 9
gun 19
gun 10
gun 20
pressure [barm]
time [ms]

Figure B.3

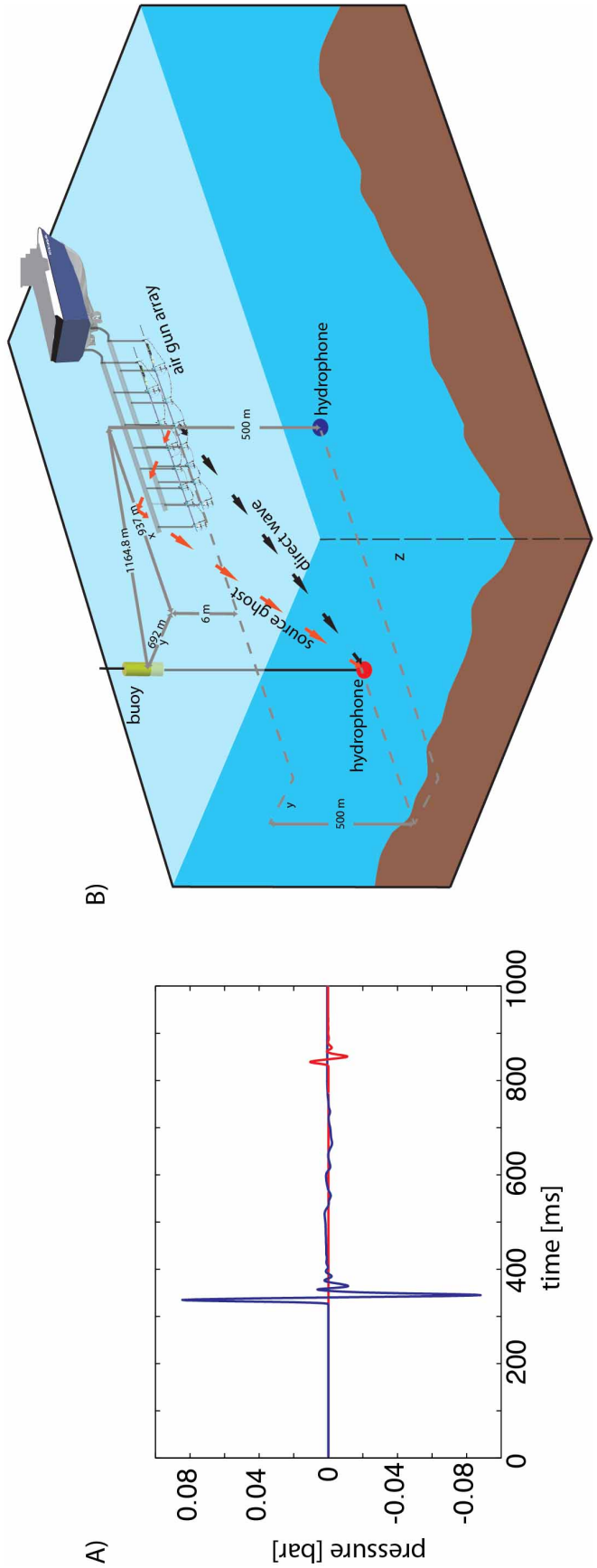
B)
air gun array
hydrophone
500 m
direct wave
source ghost
1164.8 m
937 m
692 m
6 m
buoy
hydrophone
500 m
z
y
x
A)
pressure [bar]
0.08
0.04
0
-0.04
-0.08
0
200
400
600
800
1000
time [ms]

Figure B.4

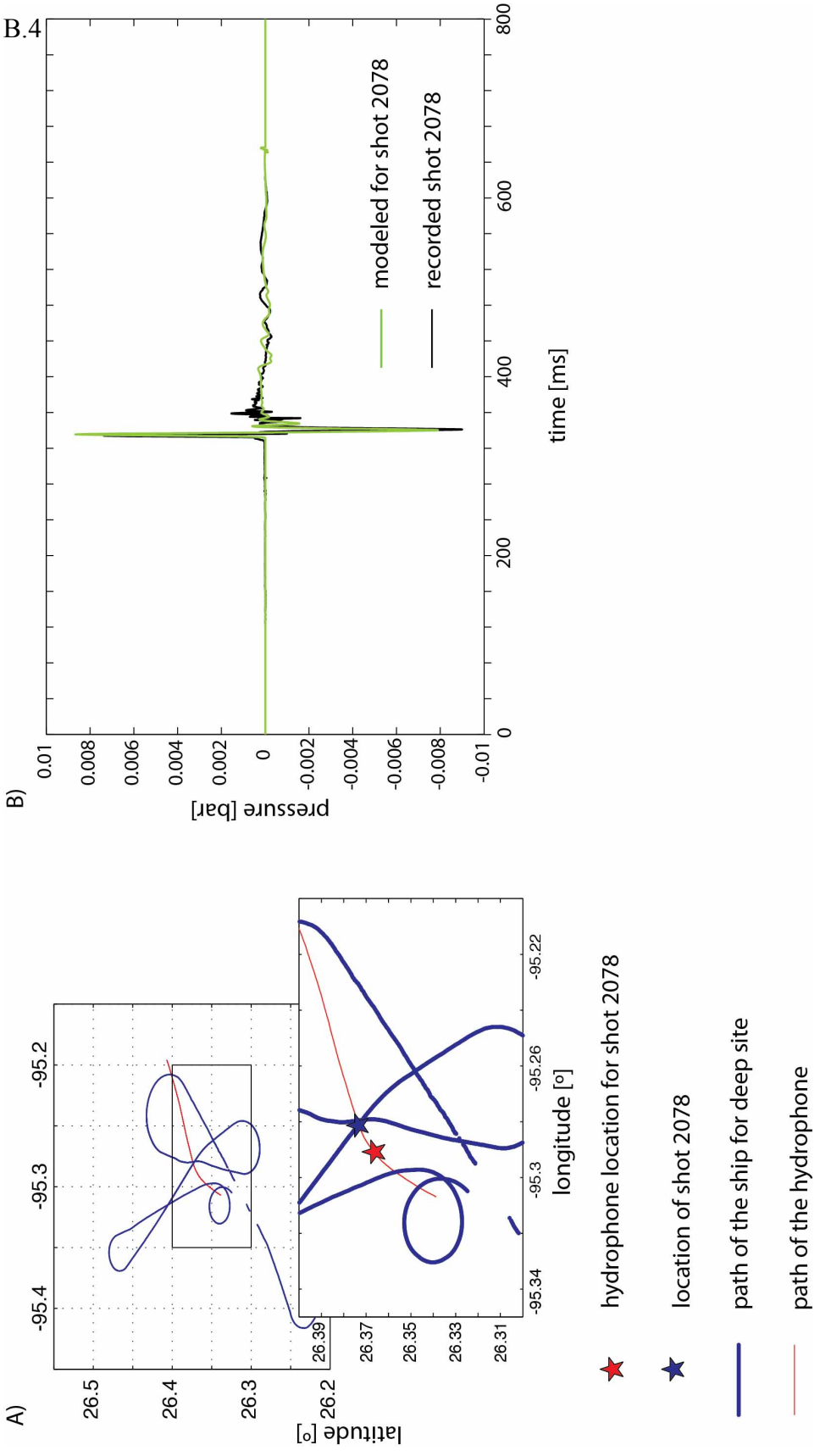
A)
B)
latitude [°]
longitude [°]
pressure [bar]
time [ms]
modeled for shot 2078
recorded shot 2078
hydrophone location for shot 2078
location of shot 2078
path of the ship for deep site
path of the hydrophone

Chapter 3

"Seismic images of magma sills beneath the axial melt lens along the East Pacific Rise 9º20' to 9º50'N"*

* This manuscript is in preparation for submission to Science with co-authors: Carbotte S. M, H. D. Carton, J. C. Mutter, M. R. Nedimović and J. P. Canales.

Existence of a thin and narrow intracrustal magma sill (or axial magma lens – AML) along intermediate and fast spreading centers was first discovered in reflection seismic data collected in the 1970's and 80's [e.g. *Herron et al., 1980; Detrick et al.,* 1987; *Morton et al.,* 1987; *Kent et al.,* 1993]. This discovery led to generally accepted hypothesis that this sill is the primary magma source for the basalt and dike complexes (or seismic layer 2a and layer 2b, respectively) that comprise the upper oceanic crust. However, formation of the lower oceanic crust, inferred from ophiolite observations to be composed of an upper layer of isotropic and vertically foliated gabbros and a lower section of modally layered gabbros, is still actively debated. A number of models have been proposed for the origin of the lower crust, derived primarily from seismic observations at fast to intermediate spreading mid-ocean ridges, and geological mapping and geochemical analyses of ophiolite complexes [*Detrick et al.*, 1987; *Quick and Denlinger*, 1993; *Buck,* 2000; *Boudier et al.,* 1996; *Kelemen and Aharanov,* 1998; *MacLeod and Yaouancq,* 2000]. One end member model, known as the "gabbro glacier" model [e.g. *Nicolas et al.,* 1988; *Phipps-Morgan and Chen,* 1993; *Henstock et al.,* 1993] suggests that most crystal nucleation (and substantial amount of crystal growth) occurs within the AML, which then subsides by ductile flow downward and outward to form the entire gabbro section (or lower crust). In the other end member model, the "sheeted sill" model [*Boudier et al.,* 1996; *Kelemen et al.,* 1997; *Korenaga and Keleman,* 1997; *Keleman and Aharanov*, 1998], crystal nucleation and gabbro formation occurs *in situ* throughout the lower oceanic crust in small magma bodies, with the AML being the shallowest of these. While the gabbro glacier model can explain structure of the upper gabbros (its vertical foliation), it requires large shear strain near the base of the crust to form the lower layered gabbros. However, evidence for extreme shear strains

near the base of the crust is not found in the anisotropic layered gabbros [*Korenaga and Kelemen,* 1997]. While the sheeted sill model better explains ophiolite observations of the layered gabbros, implications of this model for ridge axis thermal structure [*Chen,* 2001] are difficult to reconcile with seismic data observations at the East Pacific Rise (EPR), which indicate presence of not more than 2.5-18% of melt in the lower crust [*Crawford and Webb*, 2002]. In addition, near-axis hydrothermal convection all the way to the base of the crust is required to enable crystallization of lower crustal sills but evidence to support hydrothermal circulation to those depths at the ridge axis has not been found [*Chen,* 2001]. Furthermore, no sills below an AML within the on-axis crust have been reported in seismic reflection data to date. To reconcile these two end member models, intermediate-hybrid models (which combine elements of the two) have been proposed [e.g. *Coogan et al.,* 2003, *Natland and Dick,* 2009]. Defining the most plausible model for the formation of the lower crust would not only place constraints on the above unknowns but also improve our understanding of mechanisms that govern melt delivery to the AML.

During the past two decades, the existence of near-axis and off-axis sills within the Moho transition zone [*Garmany,* 1989; *Dunn et al.,* 2000; *Crawford and Webb,* 2002; *Nedimović et al.,* 2005] and within the lower crust [*Canales et al.,* 2009; *Canales et al.,* 2012] have been inferred from seismic and seafloor compliance studies. Here for the first time, high-fidelity multichannel seismic (MCS) data collected in 2008 along the EPR (Methods 1) show presence of seismic reflectors below the AML (hereinafter referred to as sub-axial magma lens or SAML events). The most prominent SAML events are found beneath the northern EPR between 9º20’ and 9º56’N (Figure 1 and 2, Figure S.1 and Supplementary Discussion 1). Within this region they appear as moderately bright discontinuous reflection events at a range of two-way travel times

(twtts) from ~ 50 to 300 ms below the AML (Figure 1 and 2). It is important to note that they do not show consistent relationship with the presence and reflection intensity of the AML above them with prominent SAML events beneath both strong and weak AML reflections (Figure 3 and S.2). For some regions along the axis, similar events are present at greater twtt, although weaker in amplitude (e.g. 9º22' - 9º29' between 4400 and 4500 ms, and 9º51' - 9º55' between 4300 to 4400 ms; Figure S.2); we focus here on the shallowest, most prominent events beneath the AML.

There are several possible explanations to consider for the origin of the SAML events. These include presence of P-converted S-phase ($P_{AML}S$), "artifacts" due to a variety of sources (seafloor side scattering, out-of-plane imaging of the AML or other crustal horizons, internal multiples), or real events from a reflective horizon in the crust.

The possibility that these reflections correspond with a converted-shear phase from the AML ($P_{AML}S$) is unlikely. Based on theoretical considerations, the $P_{AML}S$ phase is expected at mid source-receiver offsets [*Singh et al.,* 1998; *Canales et al.,* 2006; *Xu,* 2012], and lower stacking velocities than those of the AML (for details see Chapter 2). The $P_{AML}S$ is also expected to be a lower frequency event than the P- wave reflection from the AML or $P_{AML}P$ [e.g. *Xu,* 2012]. Filtered common mid-point (CMP) gathers (Methods 2.a) reveal a prominent $P_{AML}S$ phase present in our data at source-receiver offsets ~ 2000-4000 m (Figure S.3). When normal-move out corrected (here using V_{RMS}≈2400 m/s) and stacked (Methods 2.b) this phase appears at ~ 200 ms below the AML (at ~ 4150-4300 ms, Figure S.1.B), as predicted for the converted shear phase. In contrast, the SAML events are prominent at source-receiver offsets less than 2000 m (Figure S.3), stack at velocities closer to those of the $P_{AML}P$ reflection, and have similar frequency content (Figure 2). In addition, the twtt of the SAML arrivals do not follow that of the $P_{AML}S$ event (Figure S.1.A).

Of the potential artifacts that could contribute to events below the AML, we first consider side scattering from rough seafloor topography. As we show in Figure S.4, side scattered energy arising from prominent fault scarps (Figure S.4.B) closest to the ridge axis is predicted to arrive at a twtt of ~ 5000 ms, which is much greater than the twtt of the observed SAMLs (Figure 2). Moreover, there are arrivals in our seismic sections that match the calculated twtts and can be confidentially attributed to sideswipe from these faults (Figure S.4.C). Next we investigate sideswipe from out-of-plane reflectors present within the crust (here the AML). Some of the most prominent SAML events are imaged within the area for which 3D seismic coverage is available (Figure 2), and hence their 3D geometry can be examined (Figure S.5). The 3D volume shows that the SAML imaged in the along-axis direction are present in cross-axis sections as distinct events below the AML at roughly the same twtt as in the along-axis sections (Figure S.5.A). In addition, the cross-axis profiles show that the SAMLs differ in character from the AML event above (e.g. in shape, complexity, dip of diffraction tails, Figure S.5.B, C and D). For instance, in the cross-axis stacked section shown in Figure S.5.B the AML appears as a complex reflection for which two and possibly three distinct parabolic events can be identified extending over ~ 1800 m in cross-axis direction. In contrast, the SAML in this section is a much narrower (~ 500 m) single parabolic event.

Another possibility to examine is as to whether these events could be multiples. To explore this possibility we calculate predicted paths assuming a 1D model for 1st and 2nd order intrabed multiples within layer 2a (basalt layer), the 1st intrabed multiple within layer 2b (dike layer) and 1st interbed multiple within the upper crust (basalts and dikes) (Figure S.1 and Figure S.2). The predicted layer 2b intrabed and layer 2 interbed multiples arrive at longer twtt (> 4600 ms) than any of the prominent SAMLs (even at longer twtts than for some of the deeper, weaker

events), which eliminates them as plausible candidates for their origin. Although there are regions where the twtt of the SAML events coincides with either the 1st or 2nd order layer 2a intrabed multiple, there is not a consistent match. For instance, while the twtt to the SAML at 9º51-53'N roughly coincides with the predicted twtt of the 1st order intrabed multiple, north of 9º54'N the SAML event deepens to more closely match the predicted path of the 2nd order layer 2a intrabed multiple (Figure S.2). Further evidence that these events are not multiples comes from the source-receiver offset at which the SAML events are present (Figure S.6). Multiples should be observed at source-receiver offsets similar to or greater than the offset range within which the primary events involved in the creation of the multiple are observed. Our data show that the SAMLs stack as prominent events at source-receiver offsets of < 1000 m (Figure S.6.C) whereas the layer 2a event, which is not a true reflection [e.g. *Harding et al.,* 1993], is not present at these near offsets (Figure S.6.a).

Having ruled out the possibility that these events could be artifacts, or a $P_{AML}S$ phase, we suggest that the SAML events are real P-wave reflections from horizons located beneath the AML. One question is whether the SAML and AML events could be reflections off the bottom and top of a thick magmatic sill within oceanic crust. We consider this possibility unlikely. Using a range of geologically plausible velocities for the region below the AML (~ 4000-5500 m/s from Vera et al. [1990] and Dunn et al. [2000]) the depth of the SAMLs beneath the AML is estimated to range from 200-550 m (twtt ~ 100-200 ms). This implies that if these events were bottom reflections, the intracrustal sills would be very thick in places (up to 800 m). Prior waveform modeling of the AML reflection at 9°30'N [*Collier and Singh,* 1997], 9º39' [*Kent et al.,* 1993] and 9º42.8' and 9º49.1'N [*Xu,* 2012] indicated that melt lens is not more than 50 m thick, strongly arguing against the above possibility.

If these events are reflections off a magma body similar to the AML, is the material within them molten? To explore distribution of melt on regional scale within the AML, the method of partial offset stacking is often applied [*Singh et al.,* 1998; *Canales et al.,* 2006]. In Chapter 2, we introduce a new approach for examining melt content within the AML using AVA crossplotting. Results presented in this prior chapter show that both methods can be used to identify melt rich from melt poor portions of the shallowest intracrustal sill, but an important precondition for both methods is the high signal to noise ratio (S/N) for the event of interest. Unfortunately, most of the observed SAML display quite low S/N. To explore the nature of the SAML horizons, we compare the amplitude versus offset behavior of these events on super common-mid point (Super-CMP) gather(s) and with the amplitude behavior of a molten AML, similar to the approach used by Nedimović et al. [2005] and Canales et al. [2009]. Here, this *quasi* forward amplitude variation with offset (AVO) method is applied to one representative Super-CMP gather (Methods 2.c; Figure S.7). The result shows that the AVO response of the SAML event is similar to the AVO response of the AML event above it (Figure S.7.C), with a similar rate of decrease in relative amplitude with increasing source-receiver offset (Figure S.7.D) as expected for presence of liquid (or melt) overlain by solid rock (details in Chapter 2). Moreover, the selected gather is within the region for which the AVA crossplotting method suggests presence of pure melt (Figure 10.B in Chapter 2). In addition, the AVO behavior described above is very different than the AVO response examined for the seafloor and layer 2a reflection (Figure S.7.E). For these events, relative amplitudes increase with offset, as expected for a reflection from an interface for which P-wave velocity in the medium below is greater than velocity in the medium above it. It is worth noting that the polarity of the SAML wavelet is the same as polarity of the AMLs, which also supports similar physical properties (Figure 2).

Based on these arguments, we interpret the SAML as reflections from thin molten sills beneath the AML, which vary in depth and character along the axis. Presence of multiple molten sills within the mid crust has several important implications. For instance, they indicate that permeability barriers (thermal and/or compositional) can form at multiple levels at which melt may accumulate, evolve and fractionate before they reach shallower levels. Geochemical studies of the lavas erupted in 2005-06 [*Goss et al.,* 2010] indicate that they derived from magmas which included more evolved melt from the lower crust and did not form from simple fractionation within the AML, supporting the notion of fractionation at multiple levels within the crust.

Close examination of the SAML reflector reveals regional variations, with a shallower SAML south of 9°34'N than to the north and an intermediate depth SAML beneath the area of recent eruption from ~ 9°45-56'N. Furthermore, it appears that the SAML is segmented consistent with the fine-scale AML segmentation previously identified (Chapter 1), with disruptions in the SAML (represented either by step in twtt or gaps in reflection event) located beneath the AML disruptions (Figure 1 and 2). In addition to these disruptions, two prominent gaps in the SAML events are observed beneath two AML segments. Both are located within the region of the 2005-06 eruption [*Soule et al.,* 2007]: one between 9º45.5' and 9º46.5' and the second between 9º50' and 9º51'N (Figure 2.E). Notably, in both regions of SAML gaps (completely erased reflection signal), locally weakened amplitudes characterize the AML reflection above. Furthermore, the region of the northern SAML gap is believed to be the primary locus of the 2005-06 eruption [*Fundis et al.,* 2010]. Examination of the along-axis 3D seismic swath dataset shows that the SAML gap extends ~ 1500 m along the axis and is persistent in across axis direction, for the entire width of the 3D swath, i.e. ~ 700 m (Figure S.8). The AML reflection is present throughout the same region (Figure S.8.A). However, when we

compare the character of the AML event along the axis-centered (axis 2r1) line with a profile some 300 m shifted to the east (axis 4), we notice significant change in the AML reflection strength above the SAML gap zone (Figure 3). While along axis 2r1 the AML is quite weak, along axis 4 it is significantly stronger, maintaining strength above the SAML gap. When AML amplitudes are examined in the 3D swath volume one can clearly distinguish two zones: an eastern zone ~ 350 m wide with weak AML and a western zone with strong AML signal. Interestingly, AVA crossplotting analysis for axis 2r1 indicates a melt-poor portion of the AML (~ 600 m long) centered at ~ 9º50.6'N (Figure 10.B in Chapter 2). Also of note, geochemical data indicate that magmas erupted within the central eruption region (~ 9º48-51'N) that includes this prominent SAML gap are distinct from lavas erupted to the north and south and have the most primitive (highest MgO wt %) and least fractionated compositions of the erupted lavas indicating a comparatively hotter magma source [*Goss et al.,* 2010]. Within this area Wanless and Shaw [2012] by using volatile contents estimated that more than ~ 25% of the melt inclusions have crystallized at pressures consistent with formation within the lower oceanic crust. Beneath the southern AML segment underlying the eruption site, the same spatial correlation between the SAML gap (between 9º45.5' and 9º46.5'N) and presence of a mushy to solid portion of the AML above is observed (see Figure 10.B in Chapter 2).

The remarkable spatial correlation between two prominent gaps in the SAML horizon and mush-to-solid regions of the overlying AML identified with the AVA crossplotting method within the eruption area may have significant implications for the mechanism behind the last documented eruption. Here, we envision two possible models. In the first, melt draining from the SAML to the AML (perhaps by dike intrusion) may have contributed to over-pressuring the AML above, which then triggered the eruption in this area. Alternatively, eruption may have

been triggered from overpressure within the AML or build up of extensional stresses in the crustal lid above the AML [e.g. Buck et al., 2005] and then magma withdrawal from the AML led to draining of the SAML. In both models, magmas within the SAML contribute to the eruption and need to be considered in estimates of how much of the magma lens may have drained to account for the erupted volume [*Soule et al.,* 2007]. The estimated volume of each AML mush-to-solid region within the eruption site area (Figure 10.B in Chaper 2) is insufficient to accommodate estimated volume of lava flow (~ 22×10^6 m^3) emplaced onto the seafloor [*Soule et al.,* 2007] (Table S.1). The discrepancy is even larger when total estimated evacuated volume (~ 47×10^6 m^3) [*Soule et al.,* 2007] is taken into account (each solid-to-mush AML portion accounts for only 8-18% of the total evacuated volume; Table S.1). However, magma volumes within the SAML may account for the missing melt volume (Table S.1) and it is possible that the source region for the 2005-06 eruption was focused from these two local zones.

Observations from ophiolites have played an important role in our understanding of crustal formation at fast to intermediate spreading centers [e.g. *Kelemen et al.,* 1995; 1997; *Boudier et al.,* 1996; *Maclennan et al.,* 2005; *Boudier and Nicolas,* 2011; *Nicolas et al.,* 1996; 2008]. However, evidence for presence of the solidified AML and its characteristics within ophiolites has been challenging in the field [*MacLeod and Yaouancq,* 2000; *Nicolas et al.,* 2008; 2011]. Field observations and geochemical studies of the Annieopsquitch ophiolite in Newfoundland, reveal presence of multiple 10-30 m thick sills, crosscut by dikes within the upper gabbroic section [*Lissenberg et al.,* 2004]. From presence of cumulates derived from evolved melts in the lower crust (below the AML) and presence of both primitive and evolved crosscutting dikes, *Lissenberg et al.,* [2004] suggest that the bulk of fractionation processes occurred within these sub-axial sills (not within the AML) while on axis of the ancient fast- to

intermediate-spreading center. According to their geochemical analysis, the role of the top-most sill was mainly to aggregate melt delivered from deeper sills. After delivery to the AML, this melt was then expelled from it to form the upper portion of oceanic crust (i.e. layer 2). In the Oman ophiolite the fossilized AML is recognized as a heterogeneous (or varitextured) gabbro horizon containing fossilized pooled liquids of net basaltic composition and anorthosite lenses [*MacLeod and Yaouancq,* 2000; *Nicolas et al.,* 2008, *Boudier and Nicolas,* 2011]. The SAML events we observe at ~ 200-550 m below the AML, fall within the interval of foliated gabbro below the inferred melt lens trace of Nicolas et al. [2008]. In the core samples of the upper gabbro section from drill hole 1256D [*Wilson et al.,* 2006], alternating dike and gabbroic sections at short length scales (10-40 m) are observed and may indicate preserved signature of multiple sills.

Our data provide evidence for multiple seismic reflections below the AML that may arise from magma lenses at different levels in the crust. Although some weaker events are observed at greater twtt, i.e. up to 4600 ms (which translates to 1200-3300 m below AML, depending on lower crustal velocity assumed) majority of these events and the most prominent ones can be placed within the upper gabbroic layer. However, from our data we cannot rule out the possibility that multiple sills are present throughout the lower crust at the ridge axis, as predicted from ophiolite observations [e.g. *Kelemen et al.,* 1995]. Absence of possible sill reflections from deeper in the crustal column in our seismic sections could be ascribed to imaging limitations (at a given depth, with a given signal frequency, and increasing attenuation with depth within the crystal mush zone, we are probably not able to image bodies < 100 m thick and < 250 m wide).

For the most prominent SAMLs, we speculate that they represent reflections off molten lenses. Furthermore, prominent gaps in the SAML reflector observed beneath the primary

eruption site for the 2005-06 eruption may reflect regions that drained of melt during the eruption and the contribution of these SAML has to be taken into account in estimates of the available melt for eruption.

However, we must emphasize that we have used a strictly deductive approach in this study to identify the seismic events observed beneath the AML as deeper magma lenses. By ruling out a range of possible artifacts including side-scattered energy, converted shear reflection and simplest candidate internal multiples, we conclude the SAML events arise from true crustal horizons. Along with the arguments presented earlier, the seismic image of the SAML gap along and across axis at ~ 9º50'N provides further evidence that these events are not intra-crustal multiples. The prominent SAML gap is present beneath both axis 2r1 and axis 4 even though the AML event is significantly stronger along axis 4 and brighter internal multiples would be expected here (Figure 3). However, it is important to note that we cannot completely exclude the possibility that the SAML events may reflect internal multiples generated from more complex upper crustal structure than modeled here. Future studies using, for example full waveform inversion to determine detailed upper crustal structure, will be needed to further explore the origin and nature of the SAML.

Acknowledgments:

We would like to thank Peter Kelemen, Jill van Tongeren, Donna Schillington and Đorđe Grujić for constructive suggestions that improved our discussion section. We are also very grateful to Jeff Malloy, Douglas Foster and Charles Mosher from ConocoPhillips for comments and suggestions on the technical part of the paper.

METHODS

1. Survey, processing and data description. In summer 2008 a multi-streamer (4 streamers), multi-source (2 air-gun arrays) and multi-channel (468 channels on each streamer) seismic reflection survey was conducted aboard the *R/V Marcus G. Langseth*. One part of the survey was designed to sample oceanic crust in along axis direction spanning the entire EPR segment from 8º20' to 10º10'N. For the portion of the ridge axis north of 9º20'N, two or more ridge parallel closely spaced sail lines were acquired. Due to the use of dual source and four streamer seismic equipment each sail line included eight parallel common-mid point lines spaced 37.5 m apart with an in-line CMP spacing of 6.25 m. The along axis lines were processed assuming a 2D geometry (using streamer 2 and combining shots from both air-gun arrays), and as a 3D swath with properly defined 3D geometry for the region north of 9°20'N where multiple parallel lines were shot.

The processing flows for the 2D seismic lines and 3D swath are quite similar. They both include: data editing, band-pass filter, spherical divergence correction and amplitude balancing, resampling to 4 ms (with anti-aliasing filter applied), mute below the first water multiple, velocity analysis, normal-move out (NMO), stacking and 2D Kirchhoff migration. Details on each processing step, and steps specific to the 3D swath processing are given in Chapter 1.

In the final seismic sections the seafloor and axial magma lens (AML) are imaged at all source-receiver offsets (up to 6 km, which is the length of each streamer) due to prominent change in compressional velocity across the reflection interface. Refracted arrivals from the steep velocity gradient zone at base of layer 2a are observed at source-receiver offsets > 1500 m and can be stacked to provide an image of the base of layer 2a. This is well demonstrated when

the data are organized in CMP gathers, where this event is not a hyperbola with energy at near offsets, but is rather a triplication with two caustic points (see *Harding et al.* [1993] for details).

2. In CMP gathers, the AML, SAML, and $P_{AML}S$ arrivals are severely overprinted at mid to far source-receiver offsets by reflection and refraction events coming from the shallower crust (i.e. seafloor and layer 2a), due to their lower velocity. To improve images of the deeper intracrustal events, additional filtering of the data is needed. Since the shallower events have much larger move-out than the deeper events, and thus are more steeply dipping on CMP gathers, f-k dip filtering can be used to remove them. To avoid spatial aliasing when applying an f-k dip-filter, filtering should be conducted on shot gathers or on interleaved CMP gathers [*Yilmaz,* 2001]. For the latter, the geometry of the reflectors must be uniform (i.e. horizontally layered) with no significant lateral changes in velocity. We assume that these approximations are valid for crustal structure along the ridge axis. Since the along-axis data fulfil the above requirements, f-k filtering is applied on 24 fold CMP gathers.

2.a. SuperCMP gathers – SuperCMP (24-fold) gathers are shown in Figure S3 from two locations chosen after examining the stacked section: SuperCMP centered at 16282 where $P_{AML}P$ (dashed red) $P_{SAML}P$ (dashed green) and converted $P_{AML}S$ (dashed blue) are present and SuperCMP at 19018 where $P_{AML}P$ (dashed red) and $P_{SAML}P$ (dashed green) are present (location shown in Figure 2 and Figure S.1) and are further band-pass filtered (2-7-20-40 Hz). To examine these gathers for the presence of a P- converted S (hereinafter $P_{AML}S$) phase, but also preserve the AML and SAML events (where present), two-step dip filtering process is applied. After number of tests we decide on the following parameters for dip filters. The first dip-filter using a

pass band of -0.9 to 2, removes most of the energy coming from the seafloor and layer 2a events, revealing the $P_{AML}S$ phase. However, after applying the above filter there is still noise (coming from shallower part of the crust – lower velocity) remaining at near offsets that is partially masking the AML and SAML events. To produce a clean, representative Super-CMP gathers, without affecting the primary events of interest, we conduct several tests, and decide to first apply NMO with low velocity 1520 m/s (to flatten noisy events) on the SuperCMP gathers and then a second dip filter with a reject-band -0.2 to -0.2.

2.b. Stacking for $P_{AML}S$ – Pre-stack processing for optimal imaging of the $P_{AML}S$ phase includes band-pass filtering (same parameters as above) and application of a dip filter on NMO corrected gathers (NMO velocity V=1520 m/s) to remove dips between -0.9 and 2 (we apply only the first step of dip filtering process described in (a), because for stacking $P_{AML}S$ phase, we do not use near offsets where the noise removed by the second step resides). Filtering is performed on 24-fold SuperCMP gathers for the entire axis 2r1 2D line (cable 2). After filtering, SuperCMP gathers are split into single fold CMPs, NMO corrected using V_{RMS}=2400 m/s, and stacked for source-receiver offsets of 2000-4000 m. Further details on the theory and methodology for optimal stacking of the $P_{AML}S$ phase (its stacking velocity and offset range) are given in previous chapter (Chapter 2).

2.c. AVO analysis – Due to the low signal-to-noise ratio in pre-stack data (in particular for the SAML events), amplitude variation with offset (AVO) for these events is examined by calculating amplitude envelopes (or instantaneous amplitudes) on SuperCMP gathers. Figure S.7 shows the amplitude envelope for 24-fold SuperCMP 19018 (location shown in Figure 2), where both the AML and SAML events are bright, and can be followed on larger offsets (up to 4000 m). Before calculating the amplitude envelope, this SuperCMP gather was dip-filtered with the

same two-step dip filtering process as in a), and NMO corrected to flatten the AML and SAML events (V_{RMS} ~ 2600 m/s). It is important to emphasize that here we are comparing the AVO behavior of the AML and SAML on the same SuperCMP gather. We also assume that the dip filter has the same effect on both of the events and its application is considered appropriate. Amplitude values are then picked from the amplitude envelopes calculated for the flattened AML and SAML events and plotted as a function of shot-receiver offset (source-receiver offsets from 500-4000 m).

References:

Boudier F., A. Nicolas and B. Ildefonse, (1996), Magma chambers in the Oman ophiolite: fed from the top and the bottom, *Earth and Planet. Sci. Lett.* 144, 239-250.

Boudier F. and A. Nicolas, (2011), Axial melt lenses at mid-ocean ridges – A case study in the Oman ophiolite, *Earth and Planet. Sci. Lett.* 304, 313-325.

Buck, W.R., (2000). Can flow of dense cumulate through mushy upper gabbros produce lower gabbros at a fast-spreading center? In: Dilek, Y., Moores, E., Elthon, D., Nicolas, A. (Eds.), Ophiolites and Oceanic Crust: New Insights from Field Studies and Ocean Drilling. *Special Paper-Geological Society of Americ*a, vol. 349, pp. 121– 128.

Buck, W. R.; Lavier, L. L.; Poliakov, A. N. B. (2005), Modes of faulting at mid-ocean ridges, *Nature*, Apr 7, Volume 434, Issue 7034, p.719-723.

Canales, J. P., S. C. Singh, R. S. Detrick, S. M. Carbotte, A. J. Harding, G. M. Kent, J. B. Diebold, J. Babcock, and M. R. Nedimović, (2006), Seismic evidence for variations in axial magma chamber properties along the southern Juan de Fuca Ridge, *Earth and Planet. Sci. Lett.*, *246*, 353-366, doi: 10.1016/j.epsl.2006.04.032.

Canales, J. P., M. R. Nedimović, Kent G. M., Carbotte S. M., Detrick R. S, (2009), Seismic reflection images of a near-axis melt sill within the lower crust at the Juan de Fuca Ridge, *Nature, vol. 460,* doi:10.1038/nature08095.

Canales J. P., H. Carton, S. M. Carbotte, J. C. Mutter, M. R. Nedimović, M. Xu, O. Aghaei, M. Marjanović and K. Newman, (2012), Network of off-axis melt bodies at the east Pacific Rise, *Nature Geoscience*, vol. 5, doi: 10.1038/NGEO1377.

Chen Y. J. (2001), Thermal effects of gabbro accretion from a deeper second melt lens at the fast spreading East Pacific Rise, *J. Geophy. R.* 106 (B5) 8581-8588.

Collier, J. S., and S. C. Singh (1997), Detailed structure of the top of the melt body beneath the East Pacific Rise at 9°40′N from waveform inversion of seismic reflection data, *J. Geophys. Res.*, *102*(B9), 20,287–20,304, doi:10.1029/97JB01514.

Coogan, L. A., N. C. Mitchell, and M. J. O'Hara, (2003), Roof assimilation at fast spreading ridges: An investigation combining geophysical, geochemical, and field evidence, *J. Geophys. Res.*, *108*, 2002, doi:10.1029/2001JB001171.

Crawford , W.C. and S.C. Webb, (2002), Variations in the distribution of magma in the lower crust and at the Moho beneath the East Pacific Rise at 9º-10ºN, *Earth Planet. Sci. Lett.* 203, 117-130.

Detrick R. S., P. Buhl, J. Mutter, J. Orcutt, J. Madsen and T. Brocher (1987), Multi-channel seismic imaging of a crustal magma chamber along the East Pacific Rise, *Nature,* 326, 35-41, doi:10.1038/326035a0.

Dunn, R. A., D. R. Toomey, and S. C. Solomon, (2000), Three-dimensional seismic structure and physical properties of the crust and shallow mantle beneath the East Pacific Rise at 9°30'N, *J. Geophys. Res.*, *105*(B10), 23,537–23,555, doi:10.1029/2000JB900210.

Fundis, A. T., S. A. Soule, D. J. Fornari, and M. R. Perfit (2010), Paving the seafloor: Volcanic emplacement processes during the 2005–2006 eruptions at the fast spreading East Pacific Rise, 9°50′N, *Geochem. Geophys. Geosyst.*, 11, Q08024, doi:10.1029/2010GC003058.

Garmany, J., (1989), Accumulations of melt at the base of young crust, *Nature*, 340, 628-632.

Goss, A. R., M. R. Perfit, W. I. Ridley, K. H. Rubin, G. D. Kamenov, S. A. Soule, A. Fundis, and D. J. Fornari (2010), Geochemistry of lavas from the 2005–2006 eruption at the East Pacific Rise, 9°46′N–9°56′N: Implications for ridge crest plumbing and decadal changes in magma chamber compositions, *Geochem. Geophys. Geosyst.,* 11, Q05T09, doi:10.1029/2009GC002977.

Harding, A. J., G. M. Kent, and John. A. Orcutt, (1993), A Multichannel Seismic Investigation of Upper Crustal Structure at 9°N on the East Pacific Rise: Implications for Crustal Accretion, *J. Geophys. Res.,* 98(B8), 13,925–13,944, doi:10.1029/93JB00886.

Henstock, T.J., Woods, A.W., White, R.S., (1993), The accretion of oceanic crust by episodic sill intrusion. *J. Geophys. Res.* 98, 4143– 4161.

Herron, T. J., P. L. Stoffa, and P. Buhl (1980), Magma chamber and mantle reflections – East Pacific Rise, *Geophys. Res. Lett.*, *7*(11), 989–992, doi:10.1029/GL007i011p00989.

Kelemen P. B., N. Shimizu, V. J. M. Salters, (1995), Extraction of mid-ocean-ridge basalt from the upwelling mantle by focused flow of melt in dunite channels, *Nature*, 375, 747-753.

Kelemen P. B., K. Kogu, N. Shimizu, (1997), Geochemistry of gabbro sills in the crust – mantle transition zone of the Oman ophiolite: implications for the origin of the oceanic lower crust, *Earth and Planet. Sci. Lett.,* 146, 475-488.

Kelemen, P.B., Aharanov, E., (1998). Periodic formation of magma fractures and generation of layered gabbros in the lower crust beneath oceanic spreading ridges. In: Buck, W.R., Delaney, P.T., Karson, J.A., Lagrabrielle, Y. (Eds.), Faulting and Magmatism at Mid-Ocean Ridges, vol. 106. American Geophysical Union, Washington, pp. 267– 289.

Kent, G. M., A. J. Harding, and J. A. Orcutt (1993), Distribution of Magma Beneath the East Pacific Rise Between the Clipperton Transform and the 9°17′N Deval From Forward Modeling of Common Depth Point Data, *J. Geophys. Res.*, *98*(B8), 13,945–13,969, doi:10.1029/93JB00705.

Kent, G. M., Singh, S. C., Harding, A. J., Sinha, M. C., Orcutt, J. A., Barton, P. J., White, R. S., Bazin, S., Hobbs, R. W., Tong, C. H., and Pye, J. W., (2000), Evidence from three-dimensional seismic reflectivity images for enhanced melt supply beneath mid-ocean-ridge discontinuities, *Nature*, 614-618, 406.

Korenaga, J., and Kelemen, P.B., (1997). Origin of gabbro sills in the Moho transition zone of the Oman ophiolite: Implications for magma transport in the oceanic crust. *J. Geophys. Res.* 102, 27729–27749.

Lissenberg C.J., J.H. Bédard, C.R. van Staal, (2004), The structure and geochemistry of the gabbro zone of the Annieopsquotch ophiolite, Newfoundland: implications for lower crustal accretion at spreading ridges, *Earth and Planet. Sci. Lett.*, 229, 105-123.

Maclennan J., T. Hulme, S. C. Singh, (2005), Cooling of the lower oceanic crust, *Geology*, 33 (5), 357-360.

MacLeod, C.J., and Yaouancq, G., (2000). A fossil melt lens in the Oman ophiolite: implications for magma chamber processes at fast spreading ridges. *Earth Planet. Sci. Lett.* 176, 357– 373.

Morton, J. L., N.H. Sleep, W. R. Normark, and D. H. Tomkins, (1987), Structure of the southern Juan de Fuca Ridge from seismic reflection records, *J. Geophys. R.* 92, 11315-11326.

Natland, J. H.; Dick, H. J. B. (2001): Formation of the lower ocean crust and the crystallization of gabbroic cumulates at a very slowly spreading ridge. *Journal of Volcanology and Geothermal Research,* 110, 3-4, 191-233.

Nedimović M. R., S. M. Carbotte, A. J. Harding, R. S. Detrick, J. P. Canales, J. B. Diebold, G.

M. Kent, M. Tischer, J. M. Babcock, (2005), Frozen melt lenses below the oceanic crust, *Nature* 436, 1149-1152.

Nicolas A., G. Ceuleneer, F. Boudier, and M. Misseri, (1988), Structural mapping in the Oman ophiolites: Mantle diapirism along an oceanic ridge, *Tectonophysics,* 151, 27-56.

Nicolas, A., F. Boudier, J. Koepke, L. France, B. Ildefonse, and C. Mevel (2008), Root zone of the sheeted dike complex in the Oman ophiolite, *Geochem. Geophys. Geosyst.,* 9, Q05001, doi:10.1029/2007GC001918.

Phipps-Morgan, J., Chen, Y.J., (1993), The genesis of oceanic crust magma injection, hydrothermal cooling, and crustal flow, *J. Geophys. Res.* 98, 6283– 6297.

Quick, J.E., Denlinger, R.P., (1993), Ductile deformation and the origin of layered gabbro in ophiolites. *J. Geophys. Res.* 98, 14015– 14027.

Singh, S. C., G. M. Kent, J. S. Collier, A. J. Harding and J. A. Orcutt, (1998), Melt to mush variations in crustal magma properties along the ridge crest at the southern East Pacific Rise, *Nature* 394, 874-878, doi:10.1038/29740.

Singh S. C., Harding A. J., Kent G. M., Sinha M. C., Combier V., Nazin S., Tong C. H., Pye J. W., Barton P. J. Hobbs R. W., White R. S., Orcutt J. A., (2006), Seismic reflection images of the Moho underlying melt sill at the East Pacific Rise, *Nature* 422, 287-290, doi:10.1038/nature04939.

Soule S. A., D. J. Fornari, M. R. Perfit, K. H. Rubin, (2007), New insights into mid-ocean ridge volcanic processes from the 2005-2006 eruption of the East Pacific Rise, 9º46'-9º56'N, *Geology*, 35, 1079-1082.

Vera, E. E., J. C. Mutter, P. Buhl, J. A. Orcutt, A. J. Harding, M. E. Kappus, R. S. Detrick, and T. M. Brocher, (1990), The Structure of 0- to 0.2-m.y.-Old Oceanic Crust at 9°N on the East Pacific Rise From Expanded Spread Profiles, *J. Geophys. Res.*, *95*(B10), 15,529–15,556, doi:10.1029/JB095iB10p15529.

Wanless V. D. and A. M. Shaw, (2012), Lower crustal crystallization and melt evolution at mid-ocean ridges, Nature Geoscience, 5, 651-655.

Wilson D.S. et al., (2006), Drilling to Gabbro in Intact Ocean Crust, *Science*, 312, 1016-1020.

Xu M., (2012), Thesis (Ph.D.), Advanced geophysical studies of accretion of oceanic lithosphere in Mid-Ocean Ridges characterized by contrasting tectono-magmatic settings, Massachusetts Institute of Technology.

Yilmaz O., (2001), Seismic data analysis, Processing, Inversion, and Interpretation of Seismic

Data, *Society of Exploration Geophysicists*.

Table S.1. Calculated volume of the inferred low melt (drained) regions of the AML and SAML compared with volume of the 2005-06 eruption. For the dimensions of drained AML, we assume range of thicknesses (16-40 m) from Xu et al. [2012], width ~350 m estimated from our 3D swath dataset, and an along-axis length of 600 m taken from the amplitude variation with angle of incidence (AVA) study of Chapter 2. The above results in a range of estimated volumes. The last column represents how much of the estimated volume of magma erupted (taken from Soule et al. [2007]) can be accommodated by estimated volume of AML. The first number represents percentage from estimated lava volume emplaced onto the seafloor (i.e. 22×10^6 m^3) and the number in brackets represents percentage from estimated total volume of evacuated magma (i.e. 47×10^6 m^3). The same calculation is done for the gaps in SAMLs at ~ 9º45' and 9º50'N with the width and length of the sill, estimated from 3D swath data set.

Table S.1

	thickness [m]	width [m]	length [m]	volume calculated [m^3]	percentage of emplaced (evacuated) magma
AML	16	350	600	3.4×10^6	16 (8)
	40			8.4×10^6	38 (18)
SAML at 9°50'	16	700	1500	16.8×10^6	76 (36)
	40			42×10^6	190 (90)
SAML at 9°45'	16	400	2000	12.8×10^6	58 (27)
	40			32×10^6	145 (68)

Supplementary discussion

1. Extent of the SAML beneath the northern segment. In addition to the SAML along the axis-centered lines north of 9º20'N, we also observe SAML in the region of the Overlapping Spreading Center (OSC) at 9º03'N. Along the seismic line axis2 (Figure S9A) presence of two prominent intra-crustal reflection events extending between 9º05.6'N and 9º07.4'N is noticed (Figure S9B). In many places, the deeper event is brighter than the shallow one. Furthermore, the topography of the two events differs, with the twtt of the deeper event below the shallower event varying by ~ 200 ms (i.e. it is ~ 200 ms below the shallow event in the north and approaches 0 ms in the south). Events similar in character were observed along the "Omega" seismic line collected during the 3D ARAD survey in 1997 [*Kent et al.,* 2000; *Singh et al.,* 2006] centered at the OSC 9º03'N (*Satish Singh,* personal communication; Figure 9A).

One possible interpretation for these two events is that they are top and bottom reflections of a thick AML sill (up to ~400-600 m, depending on crustal velocity assumed). We consider this possibility unlikely for the same reasons we discussed earlier. The above raises the question of why the SAML are observed beneath some parts of the EPR (i.e. north of 9º20'N and at the eastern limb of the OSC) and are not ubiquitously present along the entire ridge segment? The presence of the SAML may be closely related to the amount of melt available at the base of the crust. Tomography study of the uppermost mantle structure within our study area [*Toomey et al.,* 2007] shows relatively higher velocities below Moho along the segment south of the OSC, suggesting lower melt volumes supply the crustal magmatic system in this region. In contrast, lower uppermost mantle velocities and higher inferred melt volumes are found beneath the OSC region and north of it, which could contribute to presence of multiple sills in these regions.

Refernces:

Carton, H. D., S. M. Carbotte, J. C. Mutter, J. P. Canales, M. R. Nedimović, O. Aghaei, M. Marjanović, and K. R. Newman, (2010), Three-dimensional seismic reflection images of axial melt lens and seismic layer 2A between 9°42'N and 9°57′N on the East Pacific Rise, Abstract OS21C-1514, *Presented at 2010 Fall Meeting, AGU*, San Francisco, California.

Collier, J. S., and S. C. Singh (1997), Detailed structure of the top of the melt body beneath the East Pacific Rise at 9°40′N from waveform inversion of seismic reflection data, *J. Geophys. Res.*, *102*(B9), 20,287–20,304, doi:10.1029/97JB01514.

Hooft, E. E. E., R. S. Detrick, and G. M. Kent (1997), Seismic structure and indicators of magma budget along the Southern East Pacific Rise, *J. Geophys. Res.,* 102(B12), 27,319–27,340, doi:10.1029/97JB02349.

Kent, G. M., S. C. Singh, A. J. Harding, M. C. Sinha, J. A. Orcutt, P. J. Barton, R. S. White, S. Bazin, R. W. Hobbs, C. H. Tong and J. W. Pye, (2000), Evidence from three-dimensional seismic reflectivity images for enhanced melt supply beneath mid-ocean-ridge discontinuities, *Nature*, 614-618, 406.

Toomey, D. R., D. Jousselin, R. A. Dunn, W. S. D. Wilcock and R. S. Detrick, (2007) Skew of mantle upwelling beneath the East Pacific Rise Governs Segmentation, *Nature*, 444, doi:10.1038/nature05679, 409-414.

Figure 1. Location and depth in two-way travel time (twtt) of sub-axial magma lens (SAML) events along the East Pacific Rise (EPR) between 9º15' and 10ºN. Twtt to the SAML events beneath the AML (color scale at bottom) is digitized from along-axis seismic profile axis 2r1 and plotted on profile navigation (black line). Close ups of the most prominent SAML events are shown in Figure 2. White squares show locations of the fine scale interruptions in AML from Chapter 1. All the above is superimposed on grey-scale EPR regional map with isobaths every 100 m.

Figure 2. Ridge-axis centered seismic reflection profile axis2r1. A. Profile from 9°15'N to 9°59'N where prominent SAML events are observed. Black boxes indicate locations of close-up panels in B-E. Vertical black dashed lines show location of SuperCMP gathers (centered at CMP 16282 and 19018) shown in Figure S.3 (19018 is also shown in Figure S.7). Black arrows at bottom of profile show the region with full 3D seismic data coverage. B-E. Grey and red arrowheads indicate AML and SAML events respectively Green arrows in E show the extent of gaps in SAML beneath region of 2005-06 eruption (discussed in text). Description of seismic acquisition and processing sequence is given in Methods 1.

Figure 3. Comparison of two adjacent along-axis seismic sections beneath the central 2005-06 eruption site. A. axis 2r1 and B. axis 4. Layer 2a event (top panel) is indicated with green arrows and SAML events (bottom panel) with red arrows. White arrows indicate location of gap in the SAML (on both top and bottom panels). Location of axis 2r1 is shown in Figure 1; axis 4 is parallel and ~ 300 m to east (navigation shown in Figure S.8). The two lines were acquired in opposite directions (axis 2r1 from south to north and axis 4 from north to south).

Figure S.1. A. Water velocity migrated seismic section as shown in Figure 2.A with digitized picks of primary horizons, predicted multiples and P-converted-S ($P_{AML}S$) phase superimposed. Primary events: seafloor (yellow), layer 2a (green) and AML (red) were picked using Paradigm's interpretation package tool (see Chapter 1). The 1st order layer 2a intrabed multiple (dark blue), 2nd order layer 2a intrabed multiple (light blue), intrabed layer 2b multiple (purple), interbed AML multiple (orange) are calculated using twtt of the primary events and assuming zero source-receiver offset. P-converted-S phase ($P_{AML}S$), shown in dashed pink line, is calculated using the twtt of seafloor and AML reflections and assuming ratio of compressional (V_P) and shear (V_S) velocities $V_P/V_S=\sqrt{3}$. B. Partial offset stack for the $P_{AML}S$ converted phase (source-receiver offsets of 2000-4000 m, stacking velocity V=2400 m/s) with calculated twtt (as in A) superimposed (dashed pink line). Processing steps for the $P_{AML}S$ phase stack are given in Chapter 2. Vertical dashed lines represent locations of SuperCMP gathers shown in Figure S.3 (and Figure S.7). C. Block models of layered oceanic crust showing schematic ray paths for $P_{AML}S$ converted phase and intra/interbed multiples included in A (same numbering and color code). For the second panel from the left: `P – down-going compressional wave, S – up-going shear wave and ´P – up-going compressional wave.

Figure S.2. Close-up sections from seismic line axis 2r1 corresponding to boxes B-E shown in Figure 2. The top panel shows seafloor and layer 2a with digitized horizons superimposed. The second panel shows the AML and SAML with horizon picks and predicted twtt of 1st and 2nd order intrabed multiples within layer 2a, superimposed. In both panels, horizon picks are shifted ~ 10 ms for better visibility of the reflection events. The color code is the same as in Figure S.1. Two lower panels show amplitude envelope seismic attribute calculated for layer 2a (third panel,

using time window between 3500 and 3700 ms to exclude seafloor), and AML and SAML (fourth panel). For the first two sections (from the left), the gain is higher for the AML-SAML panels (due to lower reflection signal). Arrows mark locations of the AML and SAML with the same color code as in Figure 2.

Figure S.3. SuperCMP gathers (24 fold) centered at 16282 (~ 9º43'N) and 19018 CMP (~ 9º52'N). Locations of gathers along the seismic profile are shown in Figure 2.A and Figure S.1.A. SuperCMP gather 16282 shows AML event (dashed red) SAML (dashed green) and $P_{AML}S$ phase (dashed green at offsets between ~ 2000 and 4000 m). The SuperCMP 19018 shows: AML (dashed red) and SAML event (dashed green), Procedure for preparation of the gathers is described in Methods 2a.

Figure S.4. Model results for side scattering from seafloor topography. A. Schematic diagram showing how side-scattered energy from a seafloor fault scarp facing the ridge axis located at distance x away from seismic profile arrives a later twtt than the seafloor vertically beneath the profile (schematic across axis seafloor is shown in brown line). B. Bathymetry map for the EPR 9°48'-10°06'N with prominent seafloor fault scarp closest to the ridge axis marked in red. C. Possible projection of side-scattering trajectory onto axis 2r1 (shown in dark blue line) calculated using depth to the fault scarps and distance from the profile (Figure 1). Axis 2r1 seismic section is stacked with water velocity and is shown for same latitudinal extent as the map in B.

Figure S.5. Presence of the SAMLs events in cross axis profiles. A. Fence diagram displaying along-axis profile axis2r1 and three cross-axis profiles in 2D perspective view (only visible side

of the cross-axis lines is shown). B, C and D show close ups of cross-axis seismic sections (shown in A) intersecting the along axis line at 9º45.5'N, 9º48.9'N and 9º53'N, respectively. Distance scale for cross-axis sections is given at bottom of figure. Red dashed line in the bottom panels shows the locus of intersection with the along-axis line. Black arrows indicate SAML on each of the cross-axis seismic sections. These seismic lines come from two mutually perpendicular surveys: along-axis swath (along-axis inlines) and cross-axis 3D survey (cross-axis seismic inlines) with identical geometries. Processing sequence for the along-axis swath is given in Chapter 1 and for 3D cross-axis survey in Carton et al. [2010].

Figure S.6. Constant velocity, partial source-receiver offset stacks for the seismic section extending between 9º15'N and ~ 10ºN. A. Near source-receiver offset (200-1000 m) stack for stacking velocity V=1560 m/s, appropriate for layer 2a (see Chapter 1). This panel highlights the absence of layer 2a event at near offsets. Yellow and green arrows indicate seafloor bubble pulse arrivals, identified in the modeled source signature (see Appendix B in Chapter 2). B. Mid source-receiver offset stack (1500-3000 m), stacked at same velocity as in A. The layer 2a event (indicated in purple arrows) is imaged at mid offsets at ~100 ms below the seafloor. C. Near source-receiver offset stack (200-1000 m), stacked with AML velocity (V=2600 m/s). In this stack both the AML and the SAML events are well imaged (highlighted by red arrows). Close-up centered at ~ 9º45'N for each panel is shown to the right (close-up area is marked by black rectangle in each seismic section).

Figure S.7. Amplitude variation with offset (AVO) response calculated for SuperCMP gather 19018 (location shown in Figure 2). A. Dip-filtered SuperCMP 19018 gather (Methods 2.c) with

normal move out (NMO) correction applied using velocity V=2600 m/s with the maximum source-receiver offset of 4000 m. B. amplitude envelopes calculated for AML (top) and SAML (bottom) events from the gather shown in A (for the same source-receiver offset range). Red and grey arrows are the same as in Figure 2. C. AVO behavior for AML and SAML events, grey and red lines respectively. Thin, dashed lines are amplitudes picked from the calculated amplitude envelopes at constant twtt, 4024 ms and 4164 ms, for AML and SAML respectively. Thick lines are filtered picks using MATLAB's zero-phase digital filter with order 5. D. Filtered amplitudes of SAML shown in C are scaled so that the SAML amplitude at 500 m source-receiver offset (the nearest offset picked) match the AML amplitude at the same offset (grey is for AML and blue for SAML). D. For comparison, the AVO of seafloor in thin, dashed magenta line (relative amplitudes on ordinate on the left) and layer 2a in thin, dashed green line (relative amplitudes on ordinate on the right) events are shown (amplitudes are picked from calculated amplitude envelope attribute for each of the events). Thick lines represent filtered amplitudes for each reflection event (filter parameters as in C).

Figure S.8. Depth in twtt for the AML and SAML digitized from along-axis swath seismic dataset. A. AML below seafloor and B. SAML below AML (color bar given below each panel). Black line represents outline of 2005-06 lava flow [*Soule et al.,* 2007]. Dotted and dashed lines are the navigation line of cable 2 for axis 2r1 and axis 4 respectively (seismic sections shown in Figure 3). The above content is superimposed on EM300 bathymetry from White et al. [2006] plotted as yellow-grey shaded relief.

Figure S.9. Presence of SAML within the Overlapping Spreading Center (OSC) 9º03'N region. A. Location of seismic lines axis 2r1, axis 3 and axis 2 (thick black line) superimposed on a composite bathymetry map (EM120 and EM300). Red contour represents the outline of AML mapped from 3D ARAD dataset and white line shows location of the 2D Omega line from the same survey [*Singh et al.,* 2006]. B. Portion of axis 2 where SAML event is imaged. Green and orange arrows show AML and SAML event, respectively.

Chapter 3: Figures

Figure 1

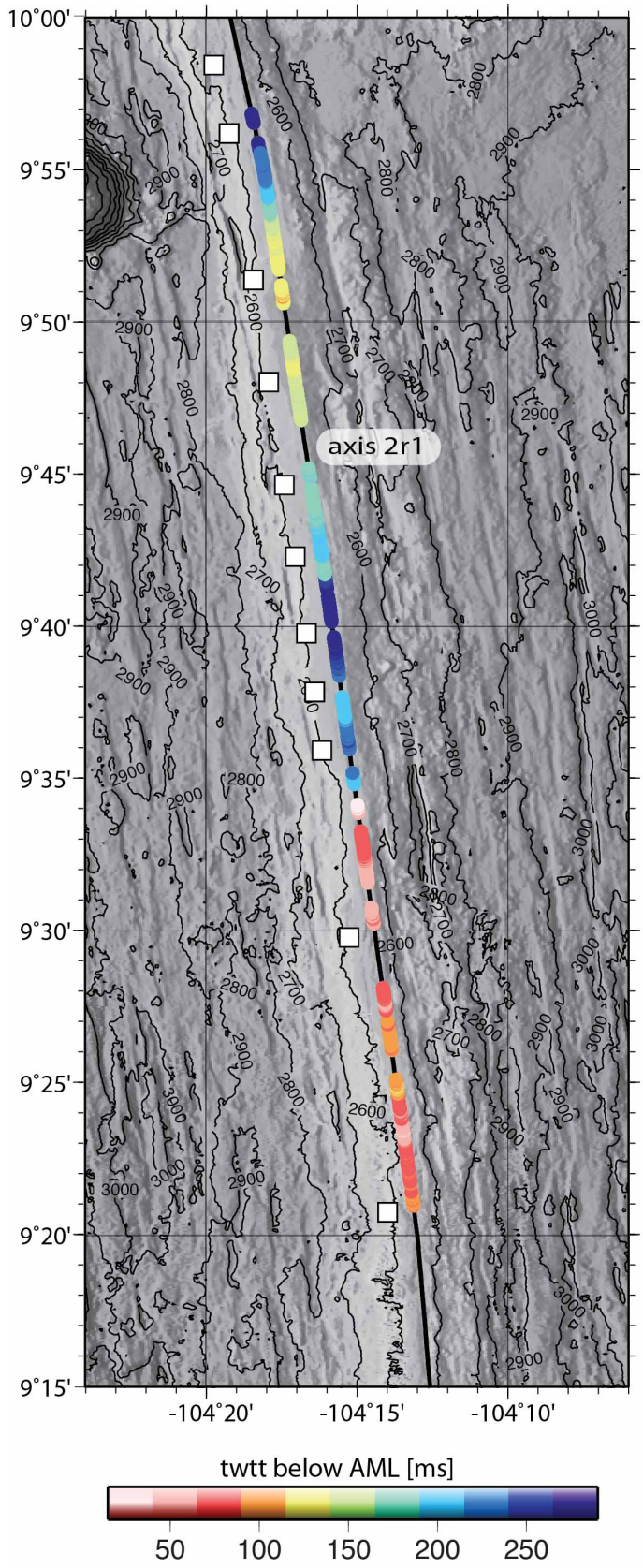
10°00'
9°55'
9°50'
9°45'
9°40'
9°35'
9°30'
9°25'
9°20'
9°15'
-104°20'
-104°15'
-104°10'
axis 2r1
twtt below AML [ms]
50
100
150
200
250

Figure 2

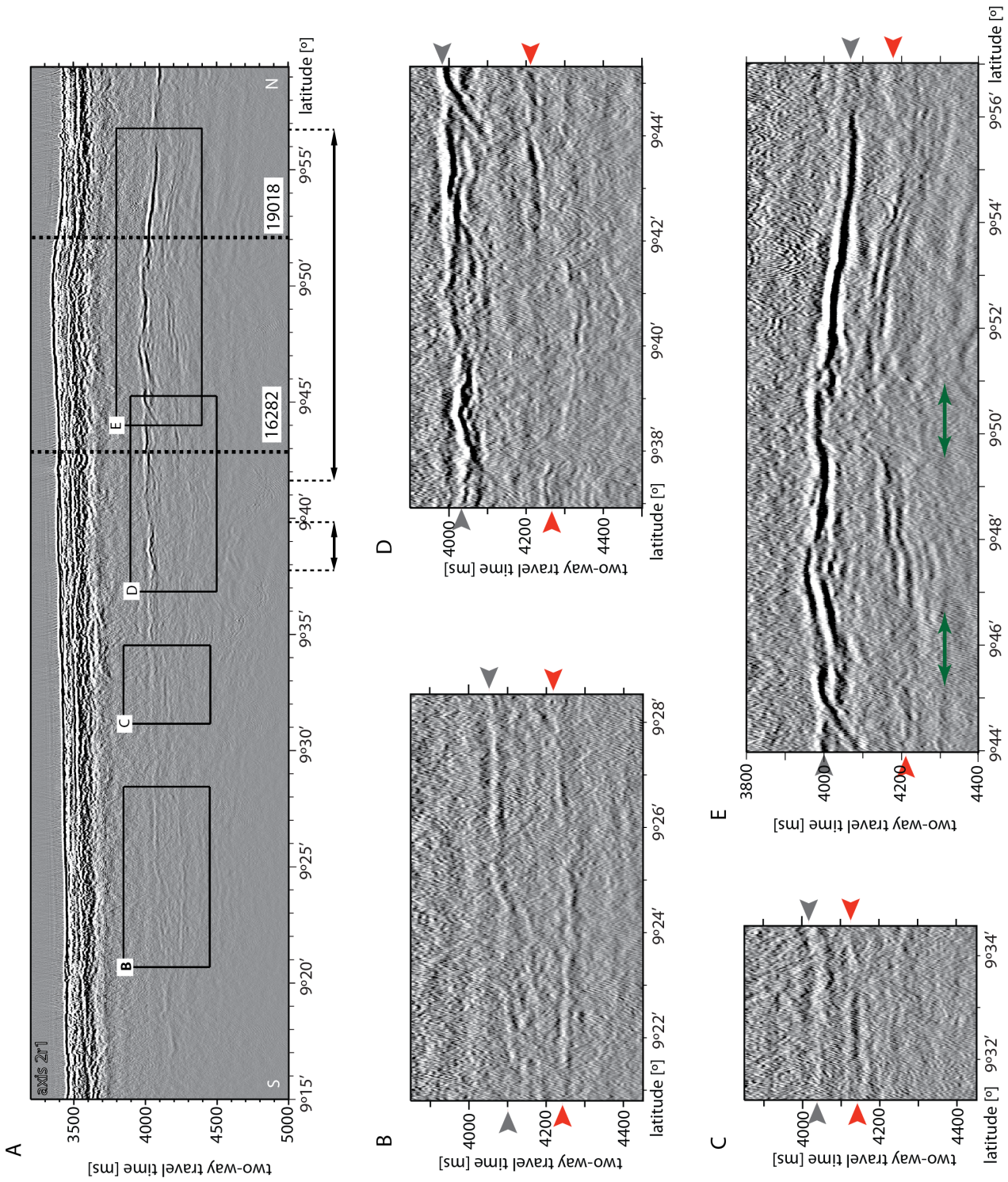
A
axis 2r1
two-way travel time [ms]
3500
4000
4500
5000
9°15′
9°20′
9°25′
9°30′
9°35′
9°40′
9°45′
9°50′
9°55′
latitude [°]
N
S
B
C
D
E
16282
19018
B
two-way travel time [ms]
4000
4200
4400
9°22′
9°24′
9°26′
9°28′
latitude [°]
D
two-way travel time [ms]
4000
4200
4400
9°38′
9°40′
9°42′
9°44′
latitude [°]
C
two-way travel time [ms]
4000
4200
4400
9°32′
9°34′
latitude [°]
E
two-way travel time [ms]
3800
4000
4200
4400
9°44′
9°46′
9°48′
9°50′
9°52′
9°54′
9°56′
latitude [°]

Figure 3

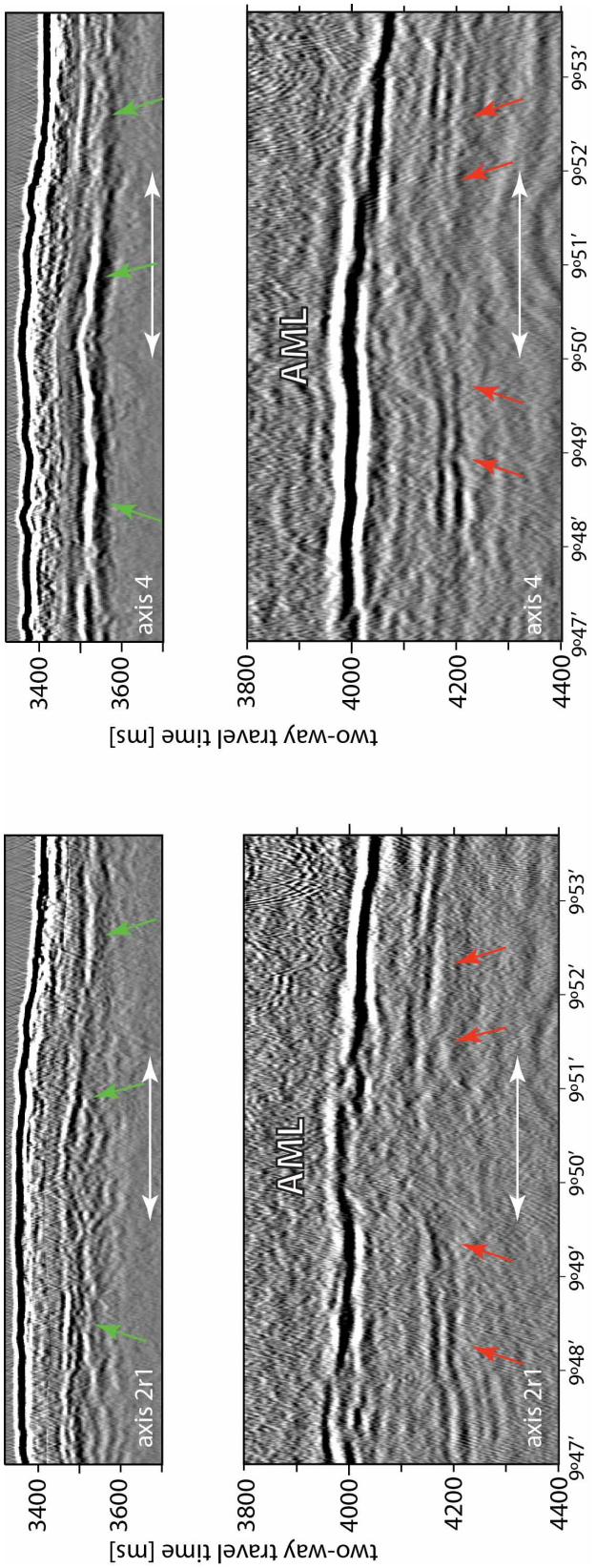
axis 4
AML
axis 4
axis 2r1
AML
axis 2r1
3400
3600
3800
4000
4200
4400
two-way travel time [ms]
9°47′
9°48′
9°49′
9°50′
9°51′
9°52′
9°53′

Figure S.1

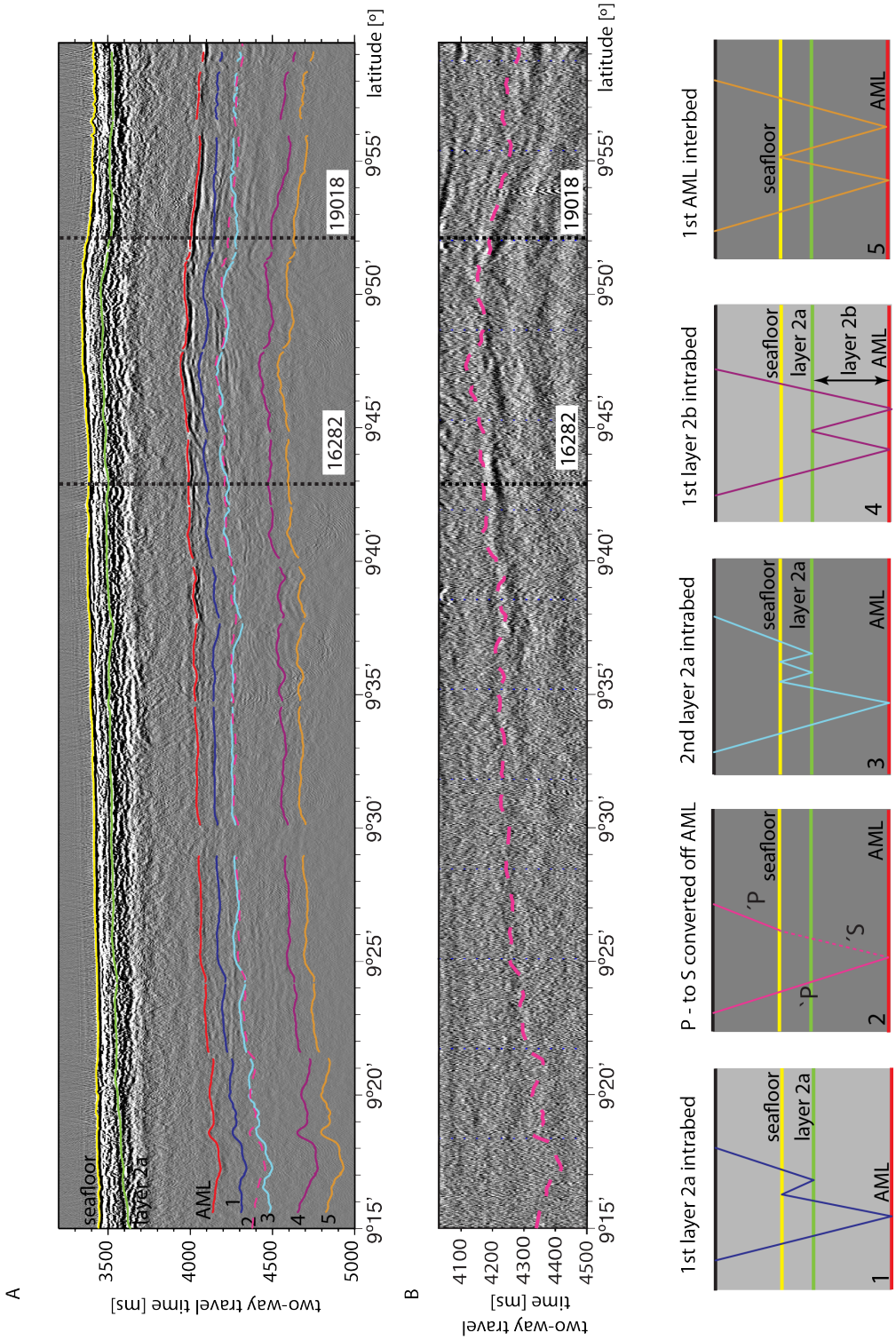
A
B
seafloor
layer 2a
AML
1
2
3
4
5
16282
19018
two-way travel time [ms]
latitude [°]
9°15'
9°20'
9°25'
9°30'
9°35'
9°40'
9°45'
9°50'
9°55'
3500
4000
4500
5000
4100
4200
4300
4400
4500
1st layer 2a intrabed
P - to S converted off AML
2nd layer 2a intrabed
1st layer 2b intrabed
1st AML interbed
layer 2b

Figure S.2

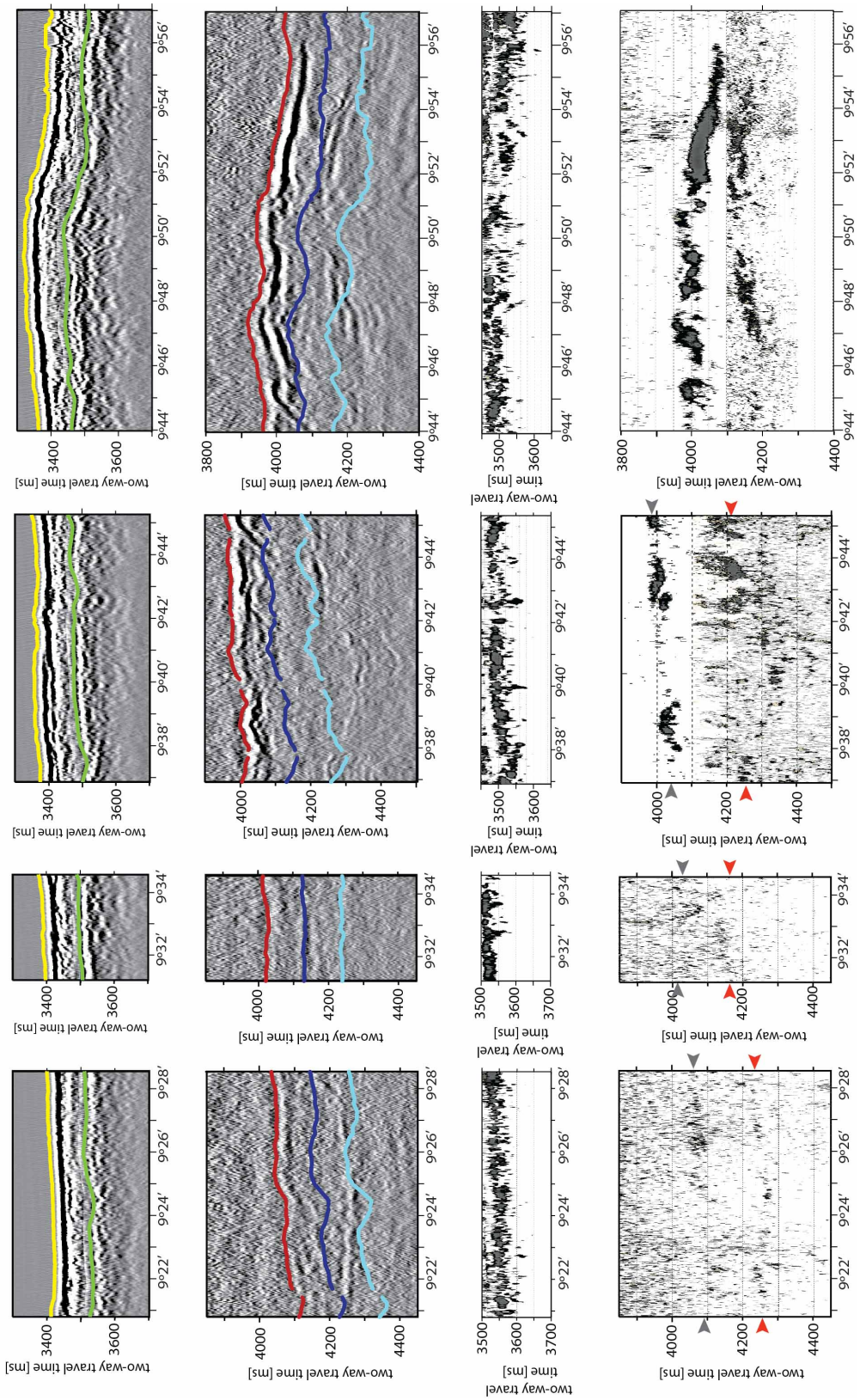
two-way travel time [ms]
3400
3600
9°44′
9°46′
9°48′
9°50′
9°52′
9°54′
9°56′
3800
4000
4200
4400
3500
3700
9°22′
9°24′
9°26′
9°28′
9°32′
9°34′
9°38′
9°40′
9°42′

Figure S.3

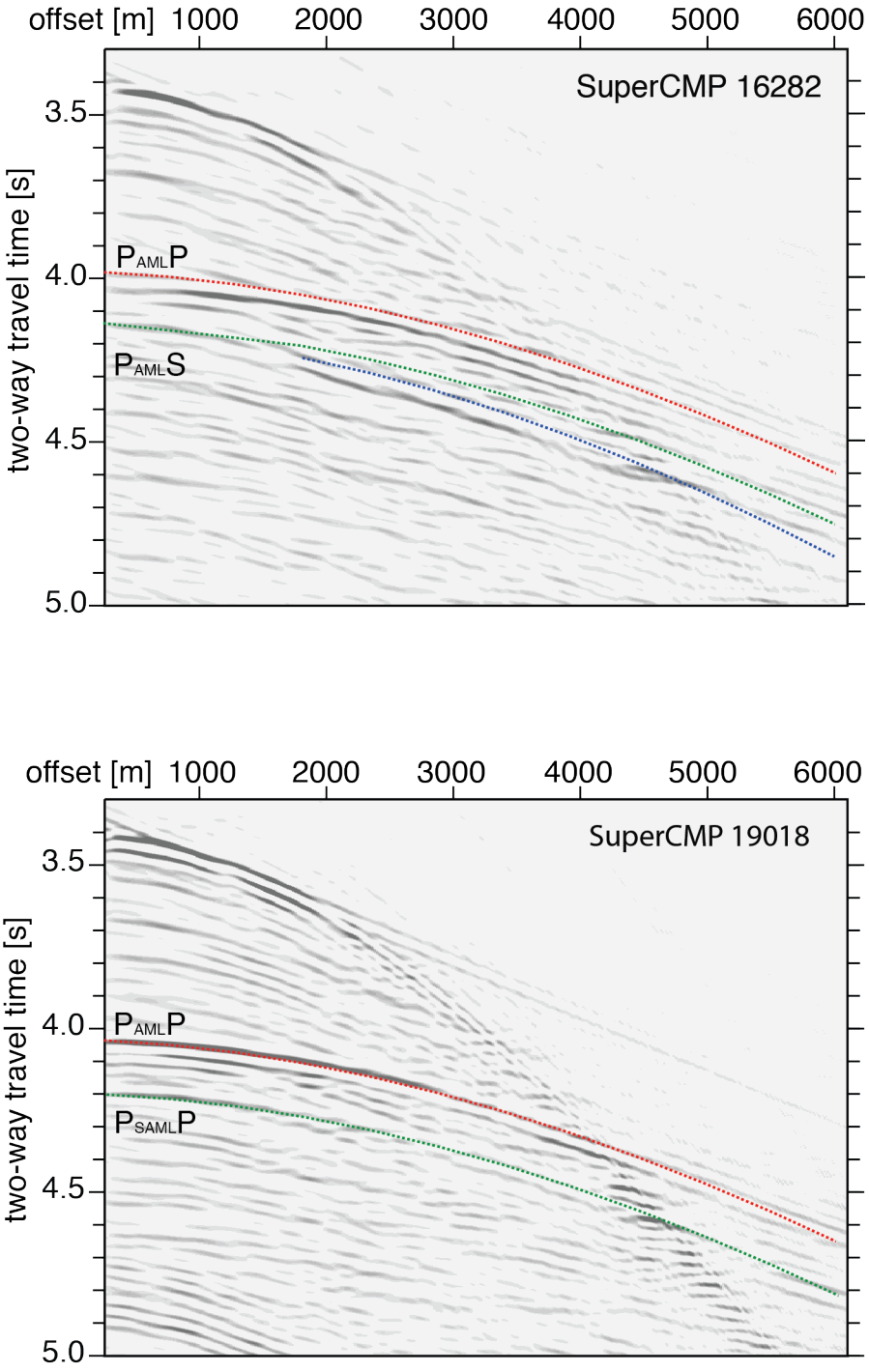
offset [m] 1000 2000 3000 4000 5000 6000
SuperCMP 16282
two-way travel time [s]
3.5
4.0
4.5
5.0
PAMLP
PAMLS
offset [m] 1000 2000 3000 4000 5000 6000
SuperCMP 19018
two-way travel time [s]
3.5
4.0
4.5
5.0
PAMLP
PSAMLP

Figure S.4

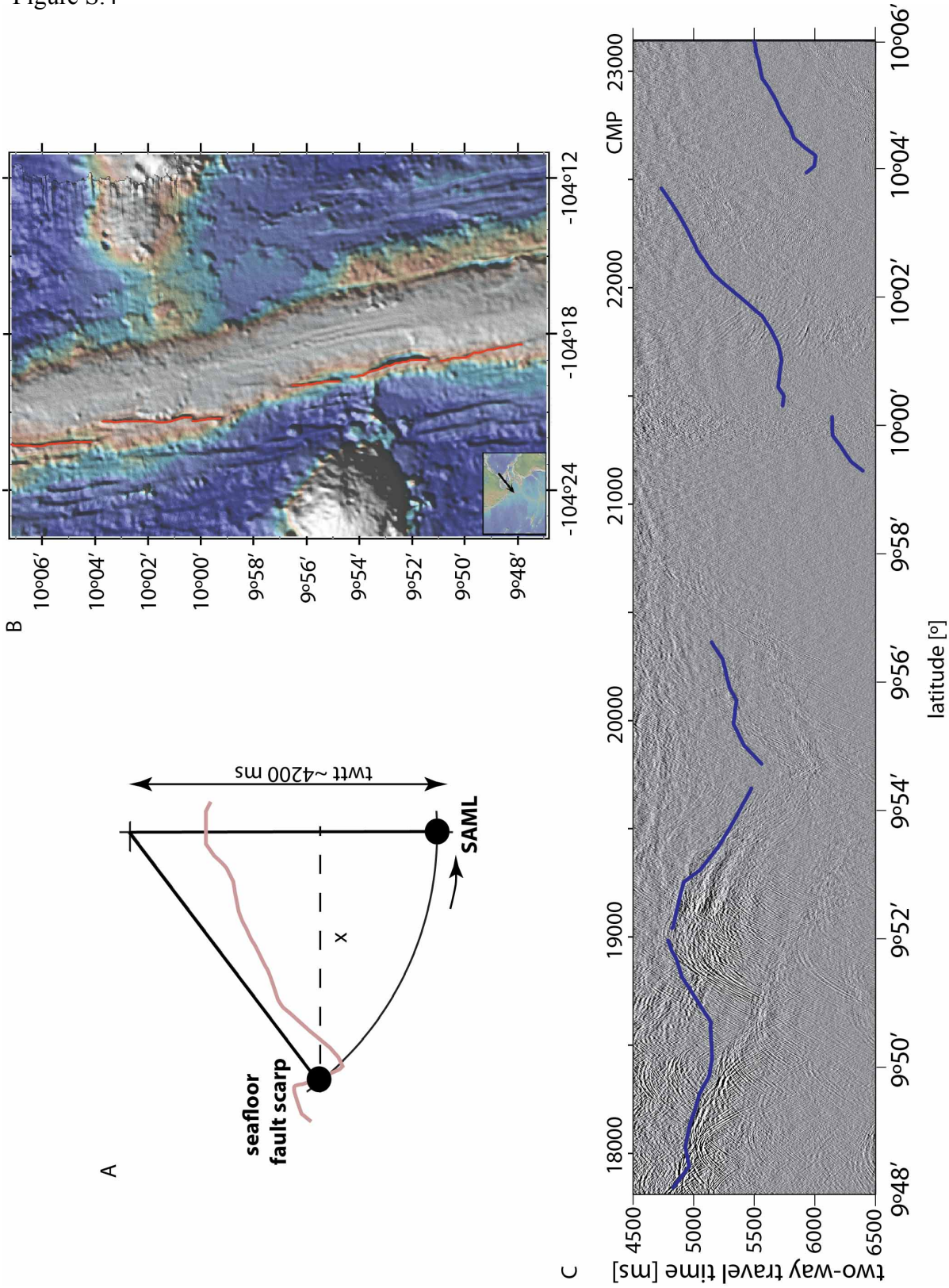
A
seafloor
fault scarp
SAML
x
twtt ~4200 ms
B
10°06′
10°04′
10°02′
10°00′
9°58′
9°56′
9°54′
9°52′
9°50′
9°48′
-104°24
-104°18
-104°12
C
two-way travel time [ms]
4500
5000
5500
6000
6500
18000
19000
20000
21000
22000
23000
CMP
9°48′
9°50′
9°52′
9°54′
9°56′
9°58′
10°00′
10°02′
10°04′
10°06′
latitude [°]

Figure S.5

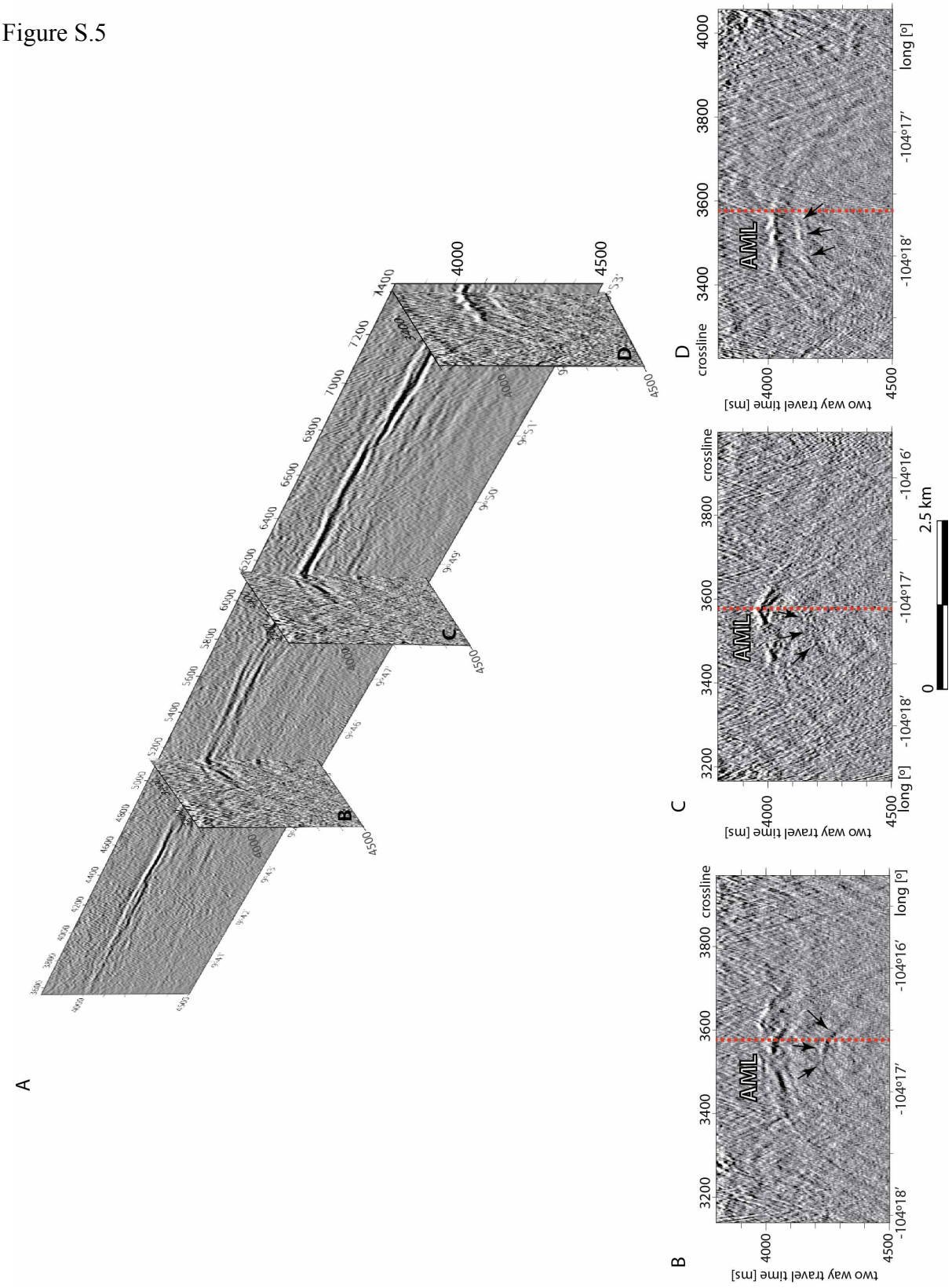
A
B
C
D
AML
AML
AML
two way travel time [ms]
crossline
long [°]
-104°18′
-104°17′
-104°16′
3200
3400
3600
3800
4000
4500
0
2.5 km

Figure S.6

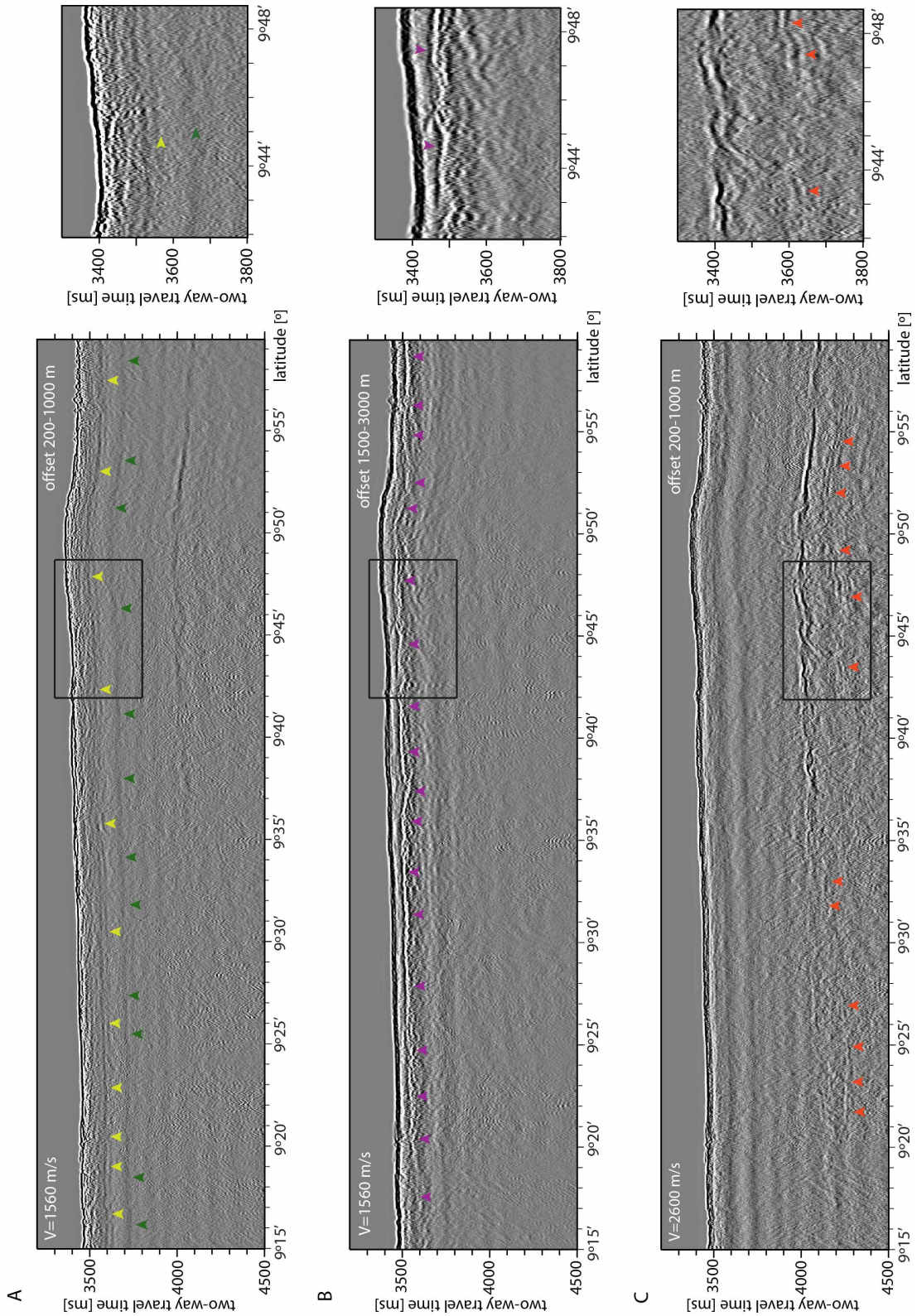
A
B
C
V=1560 m/s
V=1560 m/s
V=2600 m/s
offset 200-1000 m
offset 1500-3000 m
offset 200-1000 m
two-way travel time [ms]
3500
4000
4500
3400
3600
3800
9°15′
9°20′
9°25′
9°30′
9°35′
9°40′
9°45′
9°50′
9°55′
9°44′
9°48′
latitude [°]

Figure S.7

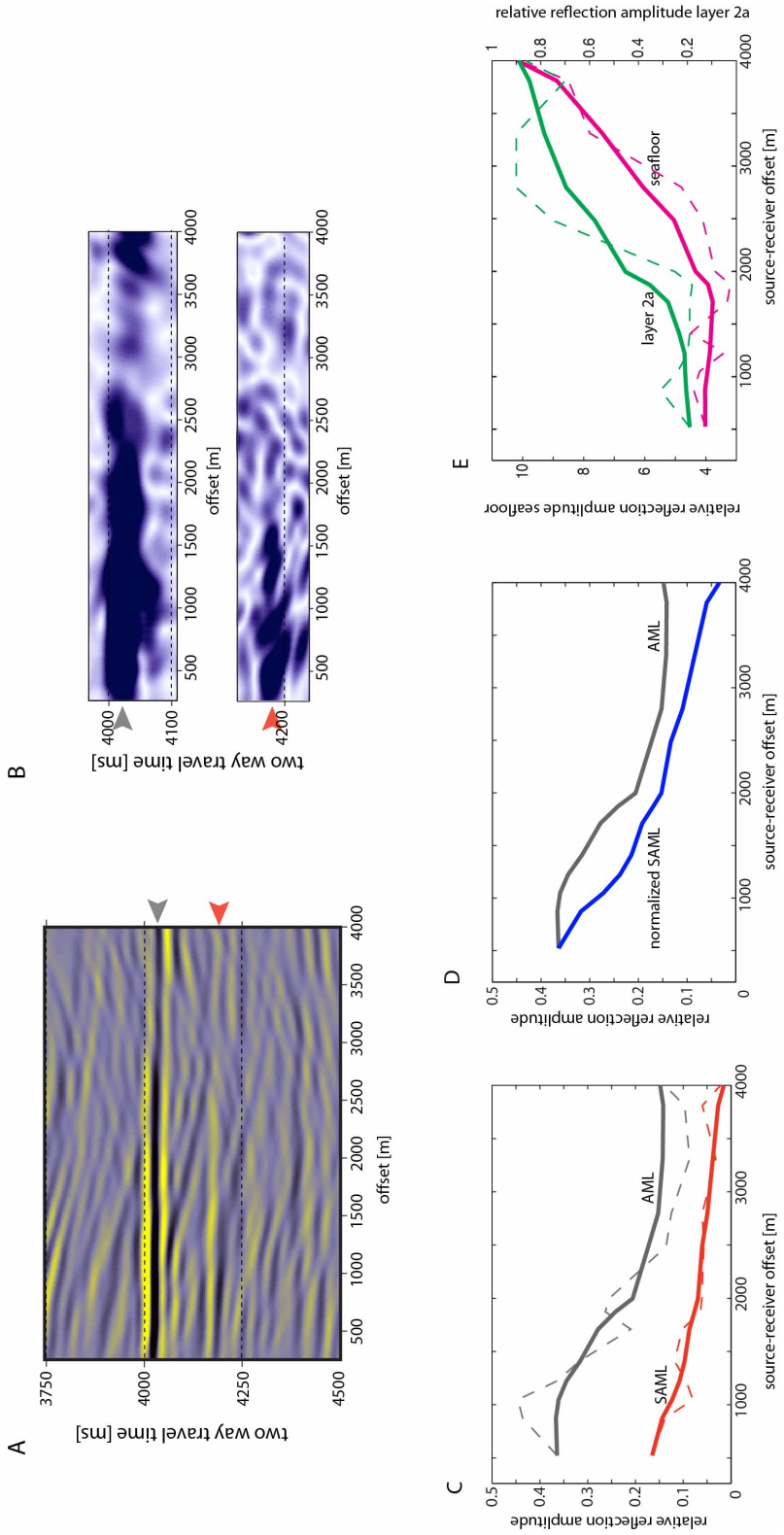
A
two way travel time [ms]
3750
4000
4250
4500
500
1000
1500
2000
2500
3000
3500
4000
offset [m]
B
two way travel time [ms]
4000
4100
4200
offset [m]
C
relative reflection amplitude
AML
SAML
source-receiver offset [m]
D
relative reflection amplitude
AML
normalized SAML
source-receiver offset [m]
E
relative reflection amplitude seafloor
layer 2a
seafloor
relative reflection amplitude layer 2a
source-receiver offset [m]

Figure S.8

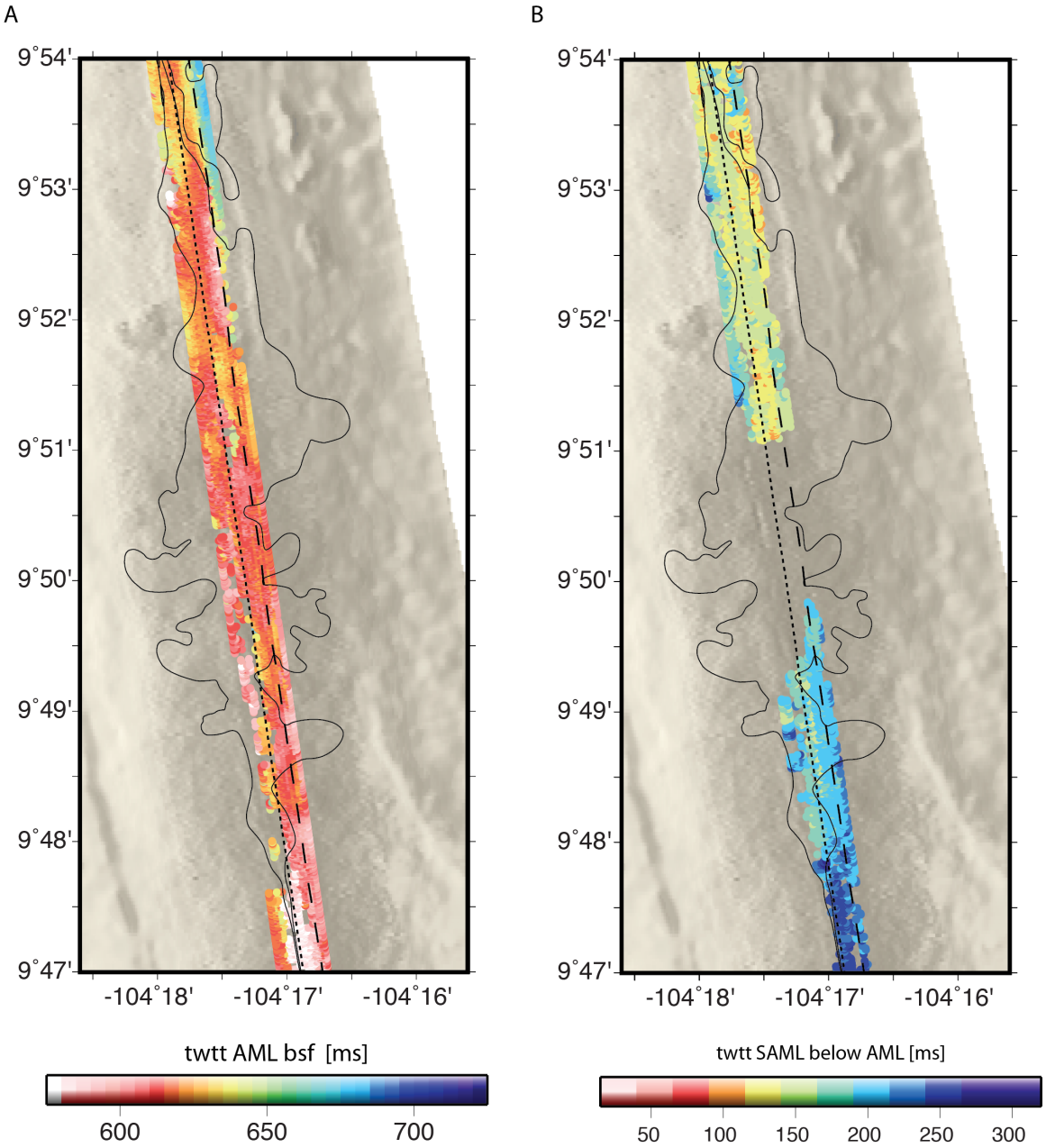
A
B
9°54'
9°53'
9°52'
9°51'
9°50'
9°49'
9°48'
9°47'
-104°18'
-104°17'
-104°16'
twtt AML bsf [ms]
600
650
700
twtt SAML below AML [ms]
50
100
150
200
250
300

Figure S.9

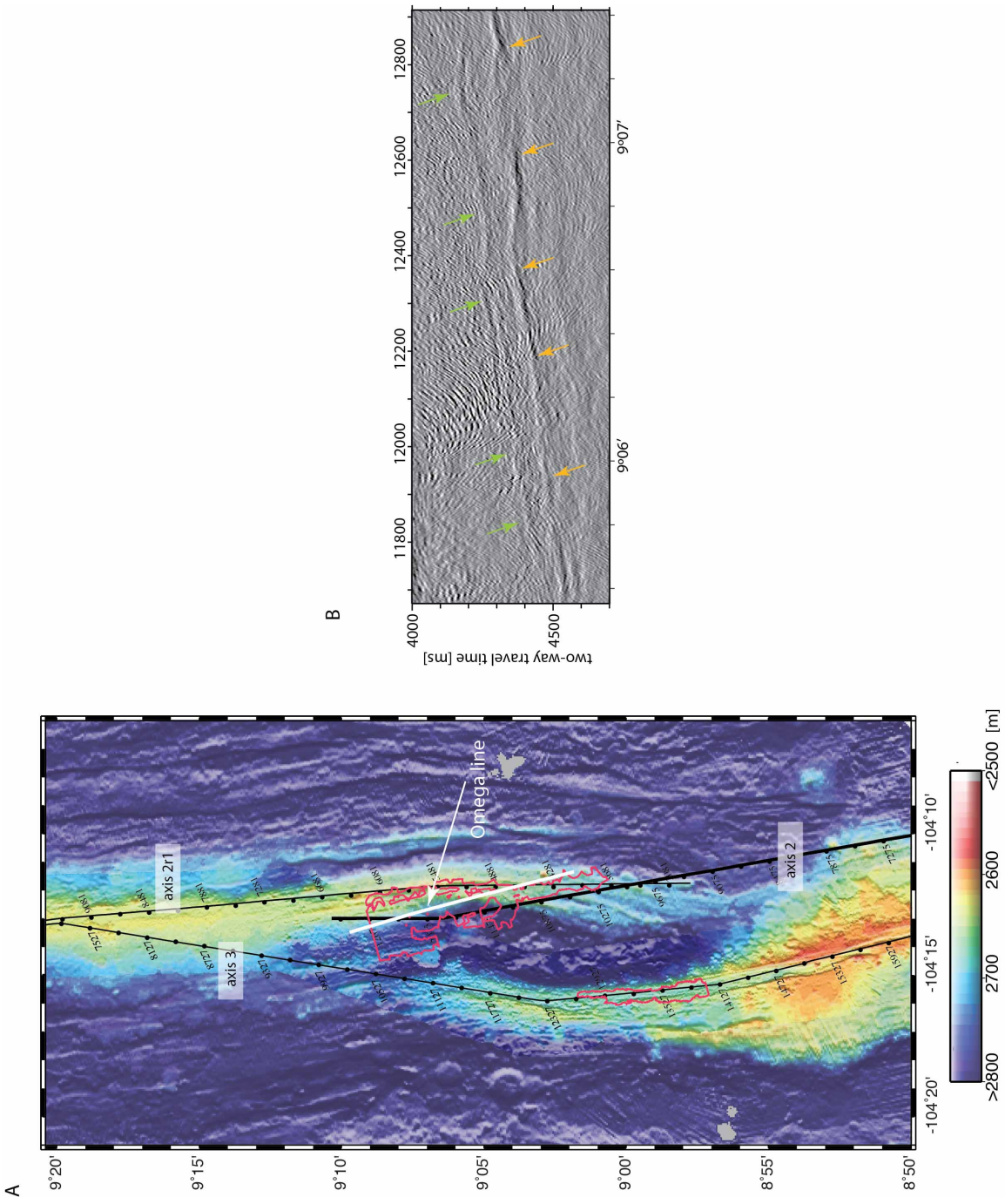
A
B
Omega line
axis 2r1
axis 3
axis 2
9°20'
9°15'
9°10'
9°05'
9°00'
8°55'
8°50'
-104°20'
-104°15'
-104°10'
>2800
2700
2600
<2500 [m]
two-way travel time [ms]
4000
4500
11800
12000
12200
12400
12600
12800
9°06'
9°07'

Chapter 4

"Gravity and seismic study of crustal structure along the Juan de Fuca Ridge axis and across pseudofaults on the ridge flanks"[*]

[*] This manuscript is published in Geochemistry, Geophysics, Geosystems: Marjanović, M., S. M. Carbotte, M. R. Nedimović, and J. P. Canales (2011), Gravity and seismic study of crustal structure along the Juan de Fuca Ridge axis and across pseudofaults on the ridge flanks, Geochem. Geophys. Geosyst., 12, Q05008, doi:10.1029/2010GC003439.

Abstract

Variations in topography and seismic structure are observed along the Juan de Fuca (JdF) Ridge axis and in the vicinity of pseudofaults on the ridge flanks left by former episodes of ridge propagation. Here, we analyze gravity data co-registered with multi-channel seismic data from the JdF Ridge and flanks in order to better understand the origin of crustal structure variations in this area. The data were collected along the ridge axis and along three ridge perpendicular transects at the Endeavour, Northern Symmetric and Cleft segments. Negative Mantle Bouguer Anomalies of -21 to -28 mGal are observed at the axis of the three segments. Thicker crust at the Endeavour and Cleft segments is inferred from seismic data and account for only small differences in axial gravity anomalies. Additional low densities/elevated temperatures within and/or below the axial crust are required to explain the remaining axial MBA low at all segments. Gravity models indicate that the region of low densities is wider beneath the Cleft segment. Gravity models for pseudofaults crossed along the three transects, support the presence of thinner and denser crust within the pseudofault zones that we attribute to iron-enriched crust. On the young crust side of the pseudofaults, a 10-20 km wide zone of thicker crust is found. Reflection events interpreted as sub-crustal sills, underlie the zones of thicker crust and are the presumed source for the iron enrichment.

1. Introduction

Estimates indicate that 15-20% of the total length of the global Mid-Ocean Ridge (MOR) is influenced by the activity of mantle plumes or mantle melt anomalies that are located within ~1000 km from ridge axes [*Ito et al.,* 2003]. The effects of hotspot proximity on MOR are evident in elevated ridge axis bathymetry and low mantle Bouguer gravity anomalies [*Ito and Lin*, 1995*; Canales et al.,* 2002*; Eysteinsson and Gunnarsson,* 1995], thickened crust [*Detrick et al.*, 2002*; Darbyshire et al.,* 2000*; Hooft et al.,* 2006] and compositional anomalies [*Schilling et al.,* 1982*; Sinton et al.,* 1983] observed along the ridge axis. At many hotspot influenced ridges, propagation or lengthening of one (propagating) ridge segment at the expense of the adjacent (dying) segment is observed and a causal link between ridge propagation and hotspot proximity has been proposed [*Hey and Vogt*, 1977*; Phipps Morgan and Parmentier,* 1985]. The Juan de Fuca (JdF) Ridge (Figure 1) is a hotspot influenced, intermediate rate spreading center in the northeast Pacific [*Karsten and Delaney,* 1989*; Embley et al.,* 1990*; West et al.,* 2001]. Motion of the Pacific plate over the Cobb hotspot has resulted in the age-progressive Cobb-Eickelberg seamount chain which extends ~1800 km from the southern JdF Ridge to the Aleutian trench [*Desonie and Duncan,* 1990]. The Cobb hotspot is believed to currently underlie the axis of the JdF Ridge at the Axial Volcano, a prominent dome-shaped volcanic edifice that rises about 1 km above the surrounding seafloor (summit lies at a depth of 1450 m below the sea level) [*Embley et al.,* 1990*; Chadwick et al.,* 2005]. Bathymetry and magnetic anomaly data indicate that volcanism at the Axial Volcano initiated ~0.5 Ma ago with an ~20 km westward jump of the JdF Ridge axis to override the Cobb hotspot [*Tivey and Johnson,* 1990]. In addition to the prominent Cobb-Eickelberg hotspot chain, numerous small seamounts are present in the region, both as

isolated edifices and in small chains, some of which lie close to or intersect the ridge axis. These smaller chains indicate the presence of numerous, shallow, mantle melt anomalies in the region.

Recent observations of crustal structure along the JdF Ridge reveal variations well away from the Axial Volcano, which have been attributed to the influence of the Cobb hotspot and smaller mantle melt anomalies on crustal production at the ridge axis. At the Cleft segment of the JdF Ridge, seismic reflection data reveal Moho two-way travel time (twtt) anomalies that indicate thicker crust (~0.7-1 km) beneath a broad, axis-centered plateau [*Carbotte et al.,* 2008]. Increased crustal production at Cleft for the past 0.5 Ma is inferred, which *Carbotte et al.* [2008] attributed to recent ridge capture of the Cobb hotspot. A similar, axis-centered plateau associated with longer Moho travel times is found at the Endeavour segment. The formation of this plateau is explained by ridge capture of the melt anomaly associated with the Heckle Seamount chain as it is overridden by the ridge axis [*Carbotte et al.,* 2008].

The JdF region has a long history of ridge propagation with 9 major ridge propagating events over the past 18 Ma. These events have been linked to recent changes in JdF plate motion [*Wilson et al.,* 1984*; Wilson,* 1993] and possibly proximity of the Cobb hotspot [*e.g. Karsten and Delaney,* 1989]. Seismic reflection data collected over the discontinuities on the ridge flanks that mark the former location of propagating ridge offsets (commonly referred to as “pseudofaults”, see below), reveal anomalous crustal structure and longer travel times to Moho on the young crust side of these discontinuites [*Calvert et al.,* 1990*; Nedimović et al.,* 2005*; Carbotte et al.,* 2008]. The longer Moho travel times suggest the presence of thicker crust behind propagating ridge tips and that local anomalies in the distribution of melt to the ridge axis may be linked to past events of ridge propagation in this region. However, the crustal velocity information needed

to confidently interpret these seismic reflection observations is sparse for the JdF region and Moho travel time anomalies cannot be unambiguously attributed to crustal thickness variations.

In this study, co-registered gravity and seismic reflection data are used to further investigate the nature of these crustal structure anomalies. Two-dimensional forward gravity modeling is conducted with the following primary goals; 1. To assess whether the axial density distributions inferred from gravity data are consistent with thicker crust beneath the Cleft and Endeavour segments, two ridge segments of proposed melt-anomaly influence, 2. To assess whether additional anomalous densities (i.e. in the mantle) are required to account for axial gravity anomalies, 3. To evaluate constraints from gravity data on crustal structure of pseudofault zones and the origin of Moho travel time anomalies observed adjacent to pseudofaults.

With gravity data, crustal thickness variations cannot be uniquely distinguished from variations in crust and/or mantle densities and the common approach is to evaluate a range of plausible models. With a few exceptions, constraints on crustal thickness from seismic studies are not typically available in prior gravity modeling studies of oceanic crustal structure. Here, the available constraints from seismic data for the structure of uppermost crust (layer 2a) and for reflection Moho are used and a suite of models of varying mid-to-lower crustal structure are constructed. We investigate ridge axis structure using models of constant density and thickness crust, constant density and variable thickness crust from the seismic reflection data, varying densities within the crust due to plate cooling away from the ridge axis, and varying densities within the mantle due to plate cooling. Crustal structure at pseudofaults is investigated using best-fit models of variable crustal densities given the seismic constraints on crustal thickness. The gravity models support the presence of thicker crust at both Cleft and Endeavour segments

and require a broader zone of low densities in the underlying mantle beneath all segments. Preferred models for the ridge flank pseudofaults indicate local zones of thinner and thicker crust and higher densities. The crustal structure models are interpreted in terms of implications for present-day accretion processes along the JdF Ridge and at propagating ridge tips in the past.

2. Regional setting and tectonic history

The JdF Ridge is an intermediate rate spreading center with the full spreading rate of 56 mm/yr [*Wilson,* 1993]. It extends for 480 km from the Blanco Transform Fault (TF) in the south to a triple junction in the north (Figure 1). The ridge is composed of seven morphologically distinct segments (West Valley, Endeavour, Northern Symmetric, CoAxial, Axial, Vance and Cleft), separated by second order non-transform discontinuities. At all segments, a shallow axial graben (50-250 m deep) centered within a <15 km wide axial high, similar to that observed along faster spreading ridges, marks the zone of active magmatism. The width and elevation of the axial high varies along the axis, with the widest axial high at the Cleft and Vance segments (~15 km wide rising 400 m above surrounding seafloor), and the narrowest axial high at the Northern Symmetric and Endeavour segments (5 km wide and 100 m high).

At several of the JdF segments, the axial high is centered on a broader elevated plateau. At the Cleft segment, a 32 km wide plateau bounded by conjugate 300 m high scarps extends along the whole length of the segment, with Moho travel time anomalies relative to older crust suggesting ~1 km thicker crust [*Carbotte et al.,* 2008*; Canales et al.,* 2009]. The age of the plateau estimated from magnetic anomalies is 0.6 Ma, approximately concurrent with westward jump of the JdF Ridge and capture of the Cobb hotspot at ~0.5 Ma. An ~40 km wide axis-centered plateau corresponding to crustal ages of 0.7 Ma is found within the central-southern part

of the Endeavour segment and coincides with the on-axis projection of the west flank of the Heckle seamount chain. Moho travel times indicate that this plateau is associated with 0.7-1 km thicker crust, which *Carbotte et al.* [2008] attribute to the northwesterly migrating JdF Ridge overriding the mantle melt source for the Heckle seamount chain.

Within our study area, dense magnetic anomaly coverage reveals a complicated history of multiple events of ridge propagation beginning ~ 18 Ma ago (Figure 1) [*Wilson et al.,* 1984*; Wilson,* 1993]. Ridge propagation involves the migration of one ridge segment across a ridge-axis discontinuity into older crust formed at the neighboring segment, leading to transfer of lithosphere and cessation of spreading along a portion of the adjacent segment [*Hey et al.,* 1980, *Kleinrock and Hey*, 1989] (Figure 2). A V-shaped pair of structural discontinuities, known as the inner and outer pseudofaults, are left on the ridge flanks in the wake of a propagating ridge and are identified from offset magnetic anomalies and disrupted and rotated seafloor fabric. From the V-shaped wakes of offset magnetic anomalies on the flanks of the JdF Ridge, nine episodes of ridge propagation are identified, including three short-lived southward propagators (propagators 5, 6 and 8 in the nomenclature of *Karsten and Delaney,* [1989]), three long-lived southward propagators (1, 2, 3) and two long-lived northward propagators (4 and 7). A reversal in the propagation direction of the so-called Cobb offset between the Endeavour and Northern Symmetric segments at ~0.8 Ma was recognized by *Johnson et al.* [1983] which we identify here as the propagator 9.

3. Data acquisition and data description

Multichannel seismic (MCS) reflection and gravity data at the JdF Ridge axis and its flanks were collected during R/V *Maurice Ewing* expedition EW0207 in 2002. The survey included long transects onto the ridge flanks across three of the JdF Ridge segments: Endeavour, Northern Symmetric and Cleft, which are the focus of this study (Figure 1). The total length of each transect is ~300 km, spanning 4-8 Ma old crust, on both sides of the ridge. The survey also included along axis lines in total length of 450 km extending from the Blanco TF in the south to the northernmost part of the Endeavour segment in the north (Figure 1). Bathymetry data were also collected along with the gravity and MCS data, and have been merged with other bathymetric data sets available for the region to form the compilation shown in Figure 1.

Inner pseudofaults are crossed on the Northern Symmetric (IP4 and IP6) and Cleft (IP3) transects along with their conjugate outer pseudofault (at Northern Symmetric OP4, at Cleft OP3 and OP2). The Endeavour transect crosses the northern termination of Propagator 4 (P4T) at its northern limit before reversal in propagation direction to the south.

3.1.Seismic data

The MCS data were acquired using a 10 air gun tuned array with a total source volume of 3005 in^3 towed at 7.5 km depth, with shots fired at 37.5 m spacing. For recording, a 6 km long, 480 channel, Syntron digital streamer was used. Detailed description of the data acquisition and processing are given in earlier papers [*Nedimović et al.,* 2005, 2008*; Canales et al.,* 2005*; Carbotte*

et al., 2008]. From the seismic reflection data, seismic arrivals defining the base of oceanic sediments, the base of seismic layer 2a, the Axial Magma Chamber (AMC), and the Mohorovičić discontinuity (Moho) at the base of oceanic crust (Figure 3A) are identified. Moho is imaged discontinuously beneath the ridge flanks at an average twtt of ~2100±100 ms (~7±0.35 km assuming crustal velocity of 6.67 km/s) for all three transects [*Nedimović et al.,* 2005]. Local zones of shorter travel times of 100-200 ms (350-700 m) are found within a number of pseduofaults (Figure 3B). On the young crust side of several pseudofaults, Moho travel times increase by 100-400 ms (350-1300 m) within a 10 km wide region. Within the axial region, Moho is imaged beginning 1-3 km from the ridge axis at each of the segments with differences between segments in Moho twtt within the inner ~20 km. At the Endeavour and Cleft segments, Moho twtts are 200-300 ms (700-1000 m) higher than at Northern Symmetric [*Carbotte et al.*, 2008]. Moreover, the presence of higher twtt to Moho coincides with the plateau regions observed in the bathymetry data at both Cleft and Endeavour (Figure 3B).

3.2.Gravity data

Gravity data were collected using a Bell Aerospace BGM−3 Marine Gravity Meter System. Positioning and speed of the ship during the survey obtained from the Global Positioning System (GPS) are used to calculate the Eötvös correction. The theoretical gravity reference field (calculated using the 1980 International Gravity Formula) together with the Eötvös correction are subtracted from the observed data to derive the Free Air Anomaly (FAA). Crossover errors calculated for the survey are used to estimate uncertainties in the FAA. The standard deviation of the error distribution is σ=1 mGal for 213 track crossings (Figure 4). The FAA for all three transects is filtered using a Savitzky-Golay (a least squares) smoothing filter.

As expected, the FAA broadly mimics seafloor bathymetry along each of the profiles with the highest gravity anomaly at the ridge axis and fluctuations on the ridge flanks associated with pseudofaults along with other intermediate wavelength topographic features (Figure 5). The FAA observed at the axis of the Cleft segment is 25 mGal and at Endeavour, 10 mGal. The smallest axial FAA is observed at Northern Symmetric (8 mGal), which is also the deepest segment. An asymmetric high/low FAA pair is associated with the outer pseudofaults with the anomaly low positioned over the old crust side of the pseudofault (Figure 6A). For the Propagator 4 Termination crossed by the Endeavour transect (P4T), the FAA low is positioned on the young crust side of the pseudofault. The inner pseudofaults are associated with a FAA low roughly centered over the bathymetric depression marking the pseudofault zone (Figures 5 and 6B**).**

4. Gravity modeling

As described previously, the primary goals of our study are to use gravity data to further investigate anomalies in crustal structure inferred from seismic reflection data. Two-dimensional forward gravity modeling along the three ridge flank profiles is conducted. The GM-SYS gravity/magnetic modelling software [*Won and Bevis,* 1987], professional - basic version is used. The GM-SYS package uses the method of *Talwani et al.* [1959] to calculate the gravitational attraction of two-dimensional bodies of arbitrary shape approximated by an n-sided polygon and constant density. All GM-SYS models are extended to ±30,000 kilometers ("infinity") in the X direction to eliminate edge effects. Uniform structure perpendicular to the profile orientation is assumed with the 2D approximation. While this assumption is well justified for the ridge axis

and flanks where profile orientation is perpendicular to the dominant structural trends, it is less appropriate for the pseudofaults, which are oblique to the profile trend.

In our study, model geometry is defined by crustal layers identified from the seismic data. The simplified lithologic sequence includes the sedimentary cover, the extrusive pillow basalt layer (approximated here as seismic layer 2a), sheeted diabase dikes and gabbros (seismic 2b/3 layer), and upper mantle. All layers are characterized by different seismic velocities and densities.

To set the model geometry, seismic velocity information is needed to convert seismic horizons from measured travel times to depth and an initial model density distribution is established. For seawater and sediments, constant velocities of 1.5 km/s and 1.7 km/s, respectively are assumed for depth conversion [*Nedimović et al.,* 2005], and constant densities of 1.03 and 1.9 gm/cm^3. The prior study of *Nedimović et al.* [2008] provides detailed analysis of upper crustal velocities and layer 2a thickness along the three flank transects of our study and is used here to define the geometry and density distribution of layer 2a. For the lower crust, several scenarios for layer geometry and density distribution are tested. Details on the approach for both crustal layers are described below.

4.1.Depth conversion and density distribution for the 2a layer

For all three transects, the thickness of layer 2a is calculated using seismic velocities and travel times obtained by *Nedimović et al.* [2008] from modeling of common mid-point (CMP) supergathers. Velocities for layer 2a are also used to estimate densities for layer 2a using the empirical relations of *Carlson and Herrick* [1990] derived from analyses of borehole log data of the extrusive basalt layer from DSDP Hole 418A (25°02.10´N, 68°03.44´W). First, porosities are

determined according to: Φ_f=(-0.35±0.03)+(2.37±0.15)S, where Φ_f is fractional porosity and S is slowness. The resulting porosity distribution is then used to define the density distribution from the equation: ρ_b=3.0-3.2Φ_f+1.2Φ_f^2, where ρ_b is bulk density (Figure 7). Based on densities for the uppermost crust derived from on-bottom gravity surveys at the East Pacific Rise [e.g. *Cochran et al.,* 1999] and at the Axial Volcano [*Gilbert et al.,* 2007], we adopt the upper bound densities estimated using the *Carlson and Herrick* [1990] relation (black curve in Figure 7). For modeling purposes the resulting layer 2a density function is approximated by series of constant density blocks. Boundaries for the blocks are chosen to roughly coincide with steps in the calculated density distribution along each transect and average density within the bounded region is assigned to the corresponding block. The calculated densities vary from 1.7 to 2.4 g/cm^3.

4.2.Depth conversion and density distribution for layer 2b/3

To assess the contribution of the thickness of the mid-to-lower crust to the FAA along each transect, velocity constraints for layer 2b/3 are needed. Our long-offset streamer seismic data were evaluated for crustal velocity information using semblance analysis on CMP supergathers in areas of smooth basement. However, high confidence velocity picks were only obtained in a few ridge flank locations (from 6.3-7.1 km/s) and no constraints were obtained on velocities within the axial region where Moho twtt anomalies are observed. In the absence of good constraints on crustal velocities along our transects for estimating the thickness of layer 2b/3, gravity modeling was designed to assess both possible thickness and density distributions within this layer, for the axial regions and across the propagator wakes.

4.2.1. Modeling axial properties

To investigate crustal properties in the axial region, four sets of models were considered. For all models, we use variable density within layer 2a, calculated as described in Section 4.1.

The starting model employs constant thickness crust of 6.5 km [e.g. *Wilson,* 1992; *Cormier et al.,* 1995] and constant densities for the water column (ρ_w=1.03 g/cm^3) and all other layers (sediments ρ_s=1.9 g/cm^3, mid-to-lower crust ρ_c=2.75 g/cm^3 and upper mantle ρ_m=3.3 g/cm^3). The calculated gravity signal from this model is subtracted from the FAA to obtain the Mantle Bouguer Anomaly (MBA, Figure 8A).

For model 1, we use constant density crust but variable crustal thickness derived from Moho twtt and an average velocity for the mid-to-lower crust of v=6.67 km/s, derived from a nearby seismic refraction study [*Christeson et al.,* 2010, personal communication]. All other parameters are as for the starting model. The resulting Residual Anomaly 1 (RA1) is the gravity signal determined from this model subtracted from the FAA (Figure 8B).

With model 2, we assess the potential contribution of elevated temperatures at the ridge axis associated with crustal accretion. Here, we use a half plate thermal cooling model (taken from *Turcotte and Schubert,* [2002]) with the following equation for determining the depth of crustal isotherms:

$$\frac{T_1 - T}{T_1 - T_0} = \operatorname{erfc} \frac{y}{2\sqrt{kx/u}}$$

where: T_1 initial temperature of half space (here $T_1 \approx$ 1200°C), T_0 temperature at the seafloor (T_0 = 0°C), x distance from the ridge axis, y depth, κ thermal diffusivity (here 1 mm^2/s, taken from *Turcotte and Schubert*), u half spreading rate.

Minor modifications to this model are made to account for the thermal effects of the thick

sediment cover, which blankets the eastern flank of the JdF Ridge and is expected to thermally insulate the underlying igneous crust. Temperature measurements from ODP boreholes at the base of the sedimentary cover on the east flank of the Endeavour segment are ~ 60°C [*Davis et al.*, 1997], which we use as T_0 in the equation above to calculate the asymmetric thermal cooling model (Figure 9A). This asymmetric thermal cooling model is used to define density variations within the mid-to-lower crust at temperature steps (dT) of 200°C using equation $d\rho = -\rho_0\alpha_v dT$ (where: ρ_0, starting density, is 2.7 g/cm^3, and α_v, volumetric coefficient of thermal expansion, is 3 $\times$ 10^{-5} K^{-1}, [*Turcotte and Schubert,* 2002]). For the eastern flank of the JdF Ridge, calculated gravity values using this asymmetric thermal cooling model 2 (Figure 9B) differ by up to 8 mGal from gravity models that do not include the thermally insulating effects of the local sediment cover.

In model 3, we calculate the effects of variable densities within the upper mantle as well as within the crust due to half-space cooling (Figure 10A). The mantle density distribution is determined using the same formula as for the crust ($d\rho = -\rho_0\alpha_v dT$) with starting density, ρ_0 = 3.2 g/cm^3. Calculated gravity from model 3 subtracted from the observed FAA gives Residual Anomaly 3 (RA3 – Figure 10B).

4.2.2. Modeling pseudofault zones

Pseudofault zones are identified on the ridge flanks from offsets in magnetic isochrons (Figure 1) and local disruptions in seafloor bathymetry, with 200-400 m deep troughs at the inner pseudofaults and steps in bathymetry (deeper seafloor on the older plate side) at outer pseudofaults (Figures 3). To model gravity anomalies associated with the pseudofault zones, we adopt model 1 of constant crustal density but seismically inferred crustal thickness as the starting

model. Pseudofaults are located beyond the expected region of most rapidly varying densities in the upper mantle due to plate cooling (Figures 3 and 10B) and we adopt uniform density for the upper mantle. From the starting model, densities within vertical crustal blocks coincident with the pesudofaults and adjoining crust are varied until a good match between calculated and observed gravity signal over the pseudofaults is obtained (Figures 11 and 12). The width of the bathymetric anomalies and zone of disturbed magnetic anomalies are used to set the width of model pseudofault zones, which varies from ~3 km for OP4 at Northern Symmetric transect to ~55 km for IP3 at Cleft transect. Coherent, obliquely trending magnetic anomalies are identified within IP3, indicating the presence of rotated crustal blocks within this inner pseudofault (Figure 1). To examine the possibility that crustal thickness variations could account for the gravity anomalies over the pseudofaults, we also ran models where the thickness of constant density crust is varied until a satisfactory fit between the calculated and observed data is reached.

5. Results

5.1.Axial region

The MBA along all three transects is characterized by a broad axial low centered at the ridge axis which differs in magnitude and width at the three transects (Figure 8A). Lower axial MBA are observed at the Cleft and Endeavour segments (-28 and -25 mGal respectively), compared with the Northern Symmetric segment (-21 mGal). The width of the axial MBA low, defined qualitatively by change in slope of the MBA from high to low gradient, is narrower (~40 km) at Northern Symmetric than at Cleft or Endeavour (~70 km).

The differences between transects in the axial MBA are largely account for model 1 of constant crustal density and seismically inferred crustal thickness (Figure 8B). At the ridge axis, residual gravity values are -20 ±1 mGal, at all three transects. This result supports the inference from the Moho twtt anomalies, of thicker crust within the axial region at the Cleft and Endeavour segments.

The remaining axial anomaly in RA1 requires additional sources of low densities in the axial region at all three segments. Model 2 (RA2) tests the contribution of lower densities in the axial region due to elevated temperatures in the mid-to-lower crust (Figures 9A). This model accounts for 48% of the axial MBA at the Endeavour segment and 38-39% at Cleft and Northern Symmetric (Figure 9B, Table 1). With the addition of lower densities in the upper mantle due to half plate cooling (Figure 10A), the calculated anomalies (RA3) account for ~50-76% of the MBA (Figure 10B, Table 1).

At the edge of the axial anomaly, residual anomalies calculated for the half plate cooling models (RA2, RA3) are reduced to near zero on the eastern flank of the Endeavour and Northern Symmetric segments, whereas a broad anomaly low remains on the western flank at both segments. At the Cleft segment, low residual anomalies persist on both flanks, roughly symmetric about the axis (Figures 9B, 10B).

5.2.Propagator pseudofaults

Along all three transects, the gravity signal from constant thickness and density crust (i.e. the MBA) is inadequate to explain the observed gravity anomalies over the pseudofaults (Figures 11 and 12, panel C) and variations in crustal thickness and/or density are required to fully account for the FAA. At the two inner pseudofaults crossed along the Northern Symmetric

transect, thinner crust within the pseudofault zones inferred from the seismic data (~350-700 m), with little variation in density (<0.02 g/cm^3) are sufficient to explain the observed gravity signal (Figures 11C and 11D). Significant variations in density are only needed at the broad inner pseudofault IP3 crossed along the Cleft transect, where crustal blocks of higher density than adjoining crust are required**.** These higher density blocks correlate with a region of thicker crust inferred from Moho travel times, and rotated crust as inferred from magnetic isochrons. Local zones of sheared and fractured crust presumably accompany this crustal rotation, and crustal velocities may be lower than assumed

At the outer pseudofaults, variable crustal thickness inferred from the seismic data does not fully account for the gravity anomalies and variable densities are also needed (Figure 12). Best fit models require a zone of higher densities (0.02-0.14 g/cm^3) within all outer pseudofaults compared with the adjacent crust. Moreover, seismic data indicate locally thicker crust (0.35-1.3 km) on the young crust side of the pseudofaults and best-fit models require slightly higher density crust extending part way into the younger crust zones. These young, thick crust regions are located beyond the zone of possible reduced crustal velocity caused by enhanced crustal shearing and fracturing in the pseudofault and hence overestimated crustal thicknesses are not expected. In all cases, higher density crust is inferred on the old crust side of the pseudofaults compared with the young crust side, which is consistent with an age contrast across the discontinuity (Figure 12, panel D).

Given the uncertainties in crustal thicknesses, due to both the lack of detailed crustal velocity information and intermittent Moho imaging, we also determine models of constant density crust but variable crustal thickness that give the best fit to the FAA. The results show that much thinner crust (by ~1.8 km for total crustal thickness of ~4.7 km) within the outer

pseudofaults would be needed. To match the observed travel times to Moho for this crustal thickness, very slow seismic velocities (4.5 km/s) would be required to extend throughout the mid-to-lower crust. Evidence for such low seismic velocities are found only in the upper crust even at fracture zones [e.g. Van Avendonk et al., 1998] and we favor a model of higher density and moderately thinner crust (~0.5 km) within the outer pseudofaults as the more plausible source of the observed gravity anomalies.

6. Along-axis models and comparison with earlier study

Hooft and Detrick [1995] conducted 2D forward gravity modeling along the JdF Ridge axis using data available at the time from the historical archives of the National Geophysical Data Center (NGDC). In conflict with our results from the ridge perpendicular transects, their analysis indicated comparable crustal thickness and/or mantle densities beneath the Cleft and Northern Symmetric segments (their Figure 5). To better understand the origin of the discrepancy with our results, we modeled along axis gravity data collected during our EW0207 survey using the same model parameters as *Hooft and Detrick* [1995] (Figure 13): constant crustal thickness d=6 km, constant density for seawater ρ_w=1.03 g/cm^3, crust ρ_c=2.7 g/cm^3 and upper mantle ρ_m=3.3 g/cm^3. With the exception of the Axial Volcano and the north end of Northern Symmetric, the along-axis MBA defined by these model parameters (Figure 13C – green line), accounts for the observed along axis gravity signal. Furthermore, the MBA indicates little difference in axial density structure at the Northern Symmetric and Cleft segments, which is consistent with the results of *Hooft and Detrick* [1995], but contradictory to the results from our study at the ridge perpendicular transects (Figure 8A). We attribute this discrepancy to the inherent limitations of the 2D assumption for an along axis geometry. Uniform seafloor depths

and crustal structure perpendicular to the ridge are assumed in the 2D model geometry, which are clearly invalid assumptions given the pronounced axial high topography and rapid subsidence of the crust, along with presence of local near axis seamounts. These results highlight the limitations of 2D along-axis gravity studies of along-axis profiles and the need for significant caution in interpretation of the resulting along axis MBA.

To facilitate direct comparison between the axial MBA from our study with *Hooft and Detrick* [1995], we recalculate the FAA anomaly from our study (Figure 13B - green line) using the 1967 Gravity International Formula (IGF) used in the earlier study (Figure 13B - red line). Even after accounting for the differences due to the gravity reference field used, the observed axial gravity anomaly for these two studies differ. The FAA from the *Hooft and Detrick* [1995] study show short wavelength variations that are not present in the modern data as well as significantly lower values (up to 25 mGal) from the Axial segment up to the southern end of the Endeavour segment (Figure 13B). Discrepancies are also observed in the bathymetry data with deeper seafloor depths for much of the ridge axis in the *Hooft and Detrick* profile (Figure 13A*)*. We attribute these differences to a poorly sampled and mislocated ridge axis in the earlier study due to the sparse gravity data coverage and large navigation uncertainties associated with the largely pre-GPS data available. These differences in the observed FAA and seafloor depth for the two studies account for the discrepancies in calculated along-axis MBA values (Figure 13C).

7. Discussion

7.1. Variations in Axial Structure

Modeling results indicates that the differences in axial gravity anomalies at the Cleft, Endeavour and Northern Symmetric segments can be explained by the differences in crustal

thickness obtained from the reflection data (Figure 8B), with thicker crust in the near axis region at Cleft and Endeavour. The modeling results also indicate that thermally reduced densities in the crust and upper mantle, expected in the axial region due to elevated temperatures, only account for part of the remaining MBA (76% at the Endeavour segment to 50% at the Cleft segment, Figure 10B, Table 1). The remaining anomaly requires the presence of additional low densities at all three segments, presumably related to the presence of melt. These results are similar to those obtained in the earlier study of *Wilson* [1992] from gravity modeling of a composite cross-axis profile for the Cleft segment, where he found that reduced densities due to thermal expansion within the crust and upper mantle account for 60% of the axial MBA. *Wilson* [1992] attributed the remaining anomaly to an additional lower density body that extends 20 km into the upper mantle and that corresponds to ~3% melt.

After accounting for thermally reduced densities, axial gravity models reveal residual anomaly lows that are markedly asymmetric about the axis of the Northern Symmetric and Endeavour segments, with broad lows extending beneath the western flank of the ridge (Figure 9B, 10B). As noted earlier, the JdF region is characterized by numerous near-axis seamounts, predominantly found on the Pacific flank of the ridge. *Davis and Karsten* [1986] attribute this asymmetric distribution to small upper mantle melt anomalies that are tapped by the northwesterly advancing JdF Ridge. The asymmetric gravity anomalies at the Endeavour and Northern Symmetric transects suggest warmer temperatures or presence of higher percent of melt beneath the Pacific plate, consistent with the inference of *Davis and Karsten* [1986].

In contrast to the Endeavour and Northern Symmetric transects, the residual gravity anomaly low extends beneath both flanks of the Cleft segment, and is more pronounced on the eastern flank, persisting up to 70 km to the east of the axis. Regional scale south-to-north

gradients in a number of properties along the JdF Ridge, including axial depth and presence and depth of the mid-crust magma lens, indicate a warmer axial regime at the Cleft segment than elsewhere along the JdF Ridge (with the exception of the Axial Volcano, [*Carbotte et al.,* 2006]). Furthermore, within the Cleft segment, the shallowest magma lens and thickest crust [*Canales et al.,* 2009] is found at the southern end of this segment adjacent to the Blanco TF, in spite of the large age offset and expected cold edge effect associated with this transform fault. *Carbotte et al.* [2008] attribute enhanced magma supply/thicker crust at the Cleft segment to damming of southward directed subaxial, asthenospheric flow from Cobb by the Blanco TF. Interestingly, *Gregg et al.* [2007] in their analysis of fast and intermediate rate transform faults, find a pronounced MBA low associated with the Blanco TF, with the largest density deficit located along the northwesterly portion that is closest to the Cleft segment. The origin of these low densities within the transform domain are presumably also linked to the low-density mantle inferred from our data beneath the east flank of the Cleft segment (located ~50 km to the north from the Blanco TF).

7.2. Crustal structure of pseudofault zones

Modeling of gravity and seismic data from the pseudofault zones indicates the presence of thinner and/or denser crust within these discontinuities. Evidence for thinner crust within pseudofaults is seen elsewhere [*West et al.,* 1999*; Kruse et al.,* 2000] and is attributed to low melt supply at propagating ridge tips as spreading rate gradually decreases from full rates to zero behind the tip [*Hey et al.,* 1992; *West et al.,* 1999*; Kruse et al.,* 2000]. Extensive shearing and rotation of preexisting crust is expected between propagating and dying ridge segments (Figure 2), and could also contribute to thinner crust [*Kleinrock and Hey,* 1989*; Martinez et al.,* 1991;

Hooft et al., 1995]. Our best fit models show that crust is on the order of 0.5 km thinner within the inner pseudofaults compared with adjacent crust. Even greater crustal thinning (by ~1.8 km for total crustal thickness of ~4.7 km) is required to fully account for the gravity anomaly at the outer pseudofaults assuming constant crustal densities. However, to match the measured Moho twtts at the pseudofaults for this crustal thickness, seismic velocities of ~4.5 km/s would be required throughout the mid-to-lower crust, which is much slower than average crustal velocities observed at fracture zones, and we consider such low velocities unlikely. Instead, we favor the presence of a local zone of higher density crust within the outer pseudofaults.

Higher density crust is consistent with the presence of FeTi basalts that are commonly sampled at modern propagating ridges [*Hey et al.,* 1992; *Carbotte and Macdonald,* 1992; *Klein et al.,* 1991). In the JdF region, FeTi basalts are sampled along the ridge axis at the intersection of Cleft segment with the Blanco TF and at the northern end of the Northern Symmetric segment. In both locations these compositions were attributed to ridge propagation [*Sinton et al.,* 1983]. ODP drilling along the Endeavour FlankFlux transect, which is coincident with our profile, sampled fractured ferrobasalts at two sites on the ridge flanks (1025 and 1029, Figure 12D, Endeavour) located nearby the propagator wake PT4 [*Davis et al.,* 1997*; Marescotti et al.,* 2000]. Our calculations indicate that a 2.5-3 km thick layer of FeTi basalts assuming a density of ~3.1-3.2 g/cm^3 [from *Karato and Becker,* 1983; *Iturrino et al.,* 1991] and no variation in crustal thickness, would completely account for the observed FAA over the outer pseudofaults (with the rest of the crust at constant density). However, iron enrichment is also expected to be associated with slower seismic compressional wave velocities of ~5.5 km/s [e.g. *Iturrino et al.,* 1991], which can explain only up to 850 m thinning of the crust. Based on these results and the presence of FeTi basalts near the pseudofault zone at Endeavour, we favor contributions from

both higher density iron enriched crustal rocks and moderately thinner crust (equivalent to the thinning at the inner pseudofaults) to account for the gravity anomalies associated with the outer pseudofaults.

The presence of wehrlite within the crust, with its high density (~3.3 g/cm^3) and high P-wave velocity (8.2 km/s, *Karson et al.,* 1984), could also contribute to the observed gravity anomalies at the outer pseudofaults. Wehrlite bodies less than 250 m thick have been documented within the Moho Transition Zone of the Oman ophiolite massif [*e.g. Benn and Laurent,* 1987*; Boudier and Nicolas,* 1995*; Koga et al.,* 2001]. At the JdF propagator-ridge tips a much thicker wehrlite layer (>1km thick) with the same lateral extent as the pseudofaults would be necessary to explain both the higher density crust inferred from the gravity modeling as well as the shorter Moho twtt.

7.3. Crustal thickness anomalies adjacent to pseudofaults

Seismic data indicate the presence of a 10-20 km wide zone of thicker crust (by 350-1300 m, Figure 11 and Figure 12) located up to 10 km from several of the pseudofault crossings and present only on the young crust side of the pseudofaults. Gravity modeling suggests this crust is of possibly higher density (although the inferred density anomalies are small and we can not rule out overestimated crustal thicknesses). Observations of modern propagating ridges indicate that seafloor volcanism initiates at comparable distances behind the propagator tip (~10 km) [e.g. *Kleinrock and Hey*, 1989] as the crustal thickness anomaly, and from this coincidence the presence of a local mantle melt excess beneath the magmatic rift tip at propagating ridges is inferred.

Beneath these zones, *Nedimović et al.* [2005] identified bright ridge-ward dipping sub-

Moho reflection events (locations shown in Figure 12), which they interpreted as frozen melt sills at the base of the crust emplaced behind the propagating ridge tips. In a 1980's era seismic reflection study located nearby, similar subcrustal reflectors are identified beneath the young crust side of outer pseudofaults OP4 and OP7 [*Calvert et al.,* 1990*; Hasselgren et al.,* 1992]. We interpret the sub-crustal events imaged in these regions as the now frozen source magma bodies for the denser, iron-enriched crustal rocks within the pseudofault zones. The formation of highly differentiated FeTi magmas requires presence of magma bodies with low magma replenishment rates and moderate cooling rates to allow closed-system fractionation to occur; such conditions may be common at propagating ridges, as spreading breaks into older and cooler lithosphere [*Sinton et al.,* 1983]. If these melt sills are the source of the more differentiated iron-rich rocks at the propagating ridge tips, lateral melt transport over distances of 10-20 km is required (Figure 14). Lateral transport could occur at sub-Moho depths or by lateral dike intrusion from mid-crust lenses that are fed by sub-crust lenses below and is presumably enhanced by the local gradients in topography and crustal thickness in the propagating ridge environment.

The best constraints on crustal structure at any propagating offset along the global Mid-Ocean Ridge are from the southward propagating 9°03'N Overlapping Spreading Center (OSC). At this offset, remarkably similar relationships are observed as at the JdF psuedofaults, including an ~20 km wide band of crust that is both thicker and denser, located behind the V-shaped discordant zone left by OSC propagation [*Canales et al.,* 2003*; Singh et al.*, 2006; *Toomey and Hooft,* 2008]. A broad swath of higher crustal magnetizations encompasses the region of thicker and denser crust as well as the bounding V-shaped discordant zone of the OSC [*Carbotte and Macdonald,* 1992]. The highest magnetizations are within the discordant zone coincident with the relict OCS ridge tips, and are attributed to presence of FeTi basalts, which are sampled at the

modern overlap ridges [*Sempere,* 1991]. The similarities in crustal properties at the EPR OSC discordant zone with those inferred for the JdF pseudofaults, including presence of thicker and denser crust behind the propagating offset and iron-enriched crust within the discordant/pseudofault zone, suggest a common origin linked to localized excess melt trapped behind propagating ridge tips.

These local melt anomalies could reflect damming and accumulation of melts at the base of the crust due to pronounced lateral gradients in axial thermal structure behind propagating rift tips. The topography of the base of the lithosphere at a propagating ridge tip is expected to be strongly three dimensional, which may result in accumulation of melts behind the narrowing V-shaped wedge of the lithosphere. Many presently active propagating ridges are moving away from mantle hotspots and the influence of hotspots on ridge-axis melt distribution has long been invoked in models for ridge propagation although a direct temporal link has not been established [e.g. *Karsten and Delaney*, 1989; *Wilson*, 1993]. Perhaps mantle melt anomalies at a range of scales (e.g. the Cobb and Heckle) contribute to initiation of propagation, but are not required for propagation to persist, as excess melt accumulations develop behind propagating ridge tips due to the local 3D structure and contribute to further propagation.

8. Conclusions

Gravity models, in combination with MCS data, corroborate the presence of thicker crust underlying the broad axis-centered plateau found at the Endeavour and Cleft segments which *Carbotte et al.* [2008] attribute to the recent ridge capture of nearby seamount melt anomalies. At all three segments, density variations predicted from plate cooling cannot fully account for the broad axial gravity anomalies and the presence of additional low densities/high temperatures in

the mantle below the axis is required. From the width of the axial residual gravity anomaly low, the region of low-density mantle is broader at the Cleft segment and extends beneath both ridge flanks. This is consistent with other indicators of an anomalously warm subaxial regime, compared with elsewhere along the ridge and inconsistent with a significant cold edge effect due to the nearby large age-offset Blanco TF.

Gravity and seismic data support the presence of thinner (~0.5 km) crust at the inner and outer pseudofaults and denser crust at outer pseudofaults. Immediately adjacent to the pseudofaults, thicker and possibly denser crust is present, underlain by bright sub-Moho reflections interpreted as frozen magma lenses by *Nedimović et al.* [2005]. We attribute the higher density of the pseudofault zone crust to iron enrichment, resulting from enhanced differentiation of magmas within these nearby sub-crustal magma lenses. The bands of thicker crust that directly overlie these sub-crust lenses indicate that local melt anomalies are present behind the propagator tips. Excess melt in this region, where stresses resisting propagation will inhibit crack opening, may result in the moderate cooling rates and longer magma residence times needed to generate the more fractionated compositions typical of propagating ridge tips.

Acknowledgements

We thank the reviewers, whose comments greatly improved the manuscript. We are grateful to M. Studinger for his generous help with GMSYS software and J. Cochran for discussions regarding aspects of the gravity data modeling. This work was supported by the National Science Foundation grants OCE-0648303 to Lamont-Doherty Earth Observatory, OCE-0648923 to Woods Hole Oceanographic Institution.

References:

Benn, K. and R. Laurent, (1987), Intrusive suite documented in the Troodos ophiolite plutonic complex, Cyprus, *Geology,* 15, 821–824.

Boudier, F. and A. Nicolas, (1995), Nature of the Moho transition zone in the Oman ophiolite, *J. Petrol*. 36: 777–796.

Calvert A. J., E. A. Hasselgren and R.M. Clowes, (1990), Oceanic rift propagation – a cause of crustal underplating and seamount volcanism, *Geology*, 18, 886-889.

Canales, J. P., G. Ito, R. S. Detrick, and J. Sinton, (2002), Crustal thickness along the western Galápagos Spreading Center and the compensation of the Galápagos hotspot swell, *Earth Planet. Sci. Lett.,* 203 (1), 311-327.

Canales, J. P., R. S. Detrick, D. R. Toomey, and W. S. D. Wilcock (2003), Segment-scale variations in the crustal structure of 150-300 kyr old fast spreading oceanic crust (East Pacific Rise, 8°15'N-10°15'N) from wide-angle seismic refraction profiles, *Geophys. J. Int.*, *152*, 766-794.

Canales, J. P., R. S. Detrick, S. M. Carbotte, G. M. Kent, J. B. Diebold, A. Harding, J. Babcock, M. R. Nedimović, and E. van Ark (2005), Upper crustal structure and axial topography at intermediate spreading ridges: Seismic constraints from the southern Juan de Fuca Ridge, *J. Geophys. Res.,* 110, B12104.

Canales, J. P., M. R. Nedimović, G. M. Kent, S. M. Carbotte, and R. S. Detrick, (2009), Seismic reflection images of a near-axis melt sill within the lower crust at the Juan de Fuca Ridge, *Nature*, 460, 7251, 89-93.

Carbotte S. M. and K. Macdonald, (1992), East Pacific Rise 8°-10°30'N: Evolution of Ridge Segments and Discontinuities From SeaMARK II and Three-Dimensional Magnetic Studies", *J. Geophys. Res.,* 97, 6959-6982.

Carbotte S. M., R. S. Detrick, A. Harding, J. P. Canales, J. Babcock, G. Kent, E. van Ark, M. R. Nedimović, and J. Diebold, (2006), Rift topography linked to magmatism at the intermediate spreading Juan de Fuca Ridge, *Geology,* 34(3), 209-212.

Carbotte, S. M., M. R. Nedimović, J. P. Canales, G. Kent, A. Harding, M. Marjanović, (2008), Variable crustal structure along the Juan de Fuca Ridge; influence of on-axis hot spots and absolute plate motions, *Geochem. Geophys. Geosyst*. 9, 2007GC001922.

Carlson, R. L. and C. N Herrick, (1990), Densities and porosities in the oceanic crust and their variations with depth and age, *J. Geophys. Res.*, 95, 9153-9170.

Chadwick, J., M. Perfit, I. Ridley, I. Jonasson, G. Kamenov, W. Chadwick, R. Embley, P. le Roux, and M. Smith, (2005), Magmatic effects of the Cobb hot spot on the Juan de Fuca Ridge, *J. Geophys. Res*., 110, B03101.

Christeson, G. L., J. A. Karson, and K. D. McIntosh (2010), Mapping of seismic layer 2A/2B boundary above the sheeted dike unit at intermediate spreading crust exposed near the Blanco Transform, *Geochem. Geophys. Geosyst.*, *11*, Q03015.

Cochran J. R., D. J. Fornari, B. J. Coakley, R. Herr and M.A. Tivey, (1999), Continuous near-bottom gravity measurements made with BGM-3 gravimeter in DSV Alvin on the East Pacific Rise crest near 9°31'N and 9°50'N, *J. Geophys. Res*., 104, 4875-4888.

Cormier, M. H., K. Macdonald, and D. Wilson (1995), A three-dimensional gravity analysis of the East Pacific Rise from 18° to 21°30′S, *J. Geophys. Res.,* 100 (B5), 8063-8082.

Darbyshire F. A., R. S. White and K. F. Priestley, (2000), Structure of the crust and uppermost mantle of Iceland from a combined seismic and gravity study, *Earth Planet. Sci. Lett.,* 181, 409-428.

Davis, E. E. and J. L. Karsten, (1986), On the cause of the asymmetric distribution of seamounts about the Juan de Fuca ridge: Ridge-crest migration over a heterogeneous asthenosphere, *Earth Planet. Sci. Lett.,* 79: 385–396.

Davis, E. E., A. T. Fisher, and J. V. Firth, (1997), The Shipboard Scientific Party, Hydrothermal circulation in the oceanic crust: Eastern flank of the Juan de Fuca Ridge, *Proc. Ocean Drill. Program Initial Rep*., 168A, 1–470.

Desonie, D. L., and R.A. Duncan, (1990), The Cobb-Eickelberg seamount chain: hotspot volcanism with mid-ocean ridge basalt affinity, *J. Geophys. Res*., v. 95, p. 12697-12711.

Detrick, R. S., J. M. Sinton, G. Ito, J. P. Canales, M. Behn, T. Blacic, B. Cushman, J. E. Dixon, D.W. Graham, and J. J. Mahoney, (2002), Correlated geophysical, geochemical and volcanological manifestations of plume-ridge interaction along the Galápagos Spreading Center, *Geochem., Geophys., Geosys*., 3 (10), 8501.

Embley, R.W., K. M. Murphy, and C. G. Fox, (1990), High-resolution studies of the summit of Axial Volcano, *J. Geophys. Res.,* 95, 12,785-12,812.

Eysteinsson H., K. Gunnarsson, (1995), Maps of Gravity, Bathymetry and Magnetics for Iceland and Surroundings, Orkustofnun, OS-95055/JHD-07, 39 pp.

Gilbert, L. A., R. E. McDuff, and H. P. Johnson, (2007), Porosity of the Upper Edifice of Axial Seamount, *Geology*, 35(1), 49-52 and 35(4), 384.

Gregg P. M., J. Lin, M. D. Behn, L. G. J. Montési, (2007), Spreading rate dependence of the gravity structure of oceanic transform faults, *Nature*, 448, 183-187.

Hasselgren E., R. M. Clowes, A. J. Calvert, (1992), Propagating rift pseudofaults – zones of crustal underplating imaged by multichannel seismic reflection data, *Geophysic. Res. Lett*, 19, no. 5, 485-488.

Hey R. and P. Vogt, (1977), Spreading centers jumps and sub-axial astenosphere flow near the Galapagos hotspot, *Tectonophysics,* 37, 41-52.

Hey, R., F. K. Duennebier, and W. J. Morgan, (1980), Propagating Rifts on Midocean Ridges, *J. Geophys. Res.*, *85*(B7), 3647–3658.

Hey R. N., J. M. Sinton, M. C. Kleinrock, R. N. Yonover, K. C. Macdonald, S. P. Miller, R. C. Searle, D. M. Christie, T. M. Atwater and N. H. Sleep*, H.P.* Johnson, and C. A. Neal (1992), ALVIN Investigation of an active propagating rift system, Galapagos 95.5°W*, Marine Geophys. Res.*, 14, 207-226.

Hooft E. E. E. and S. R. Detrick, (1995), Relationship between axial morphology, crustal thickness, and mantle temperature along the Juan de Fuca and Gorda Ridges, *J. Geophys. Res*. 100, 22499-22508.

Hooft, E. E. E., M. C. Kleinrock and C. Ruppel, (1995), Rifting of oceanic crust at Endeavor Deep on the Juan Fernandez Microplate, *Mar. Geophys. Res.* 17, 251–273.

Hooft E. E. E., B. Brandsdottir, R. Mjelde, H. Shimamura and Y. Murai, (2006), Asymmetric plume-ridge interaction around Iceland: The Kolbeinsey Ridge Iceland Seismic Experiment, *Geochem., Geophys., Geosys*., 7 (5).

Ito G. and J. Lin, (1995), Mantle temperature anomalies along the past and paleoaxes of the Galpagos spreading center as inferred from gravity analyses, *J. Geophys. Res.*, *100*(B3), 3733–3745.

Ito G., J. Lin and D. Grahma, (2003), Observational and theoretical studies of the dynamics of mantle plume mid-ocean ridge interaction, *Rev. Geophysics*, 41, 1-24.

Iturrino, G. J., Christensen, N. I., Kirby, S., and Salisbury, M. H., (1991), Seismic velocities and elastic properties of oceanic gabbroic rocks from Hole 735B. *In Von Herzen, R., Robinson, P.T., et al., Proc. ODP, Sci. Results, 118: College Station, TX (Ocean Drilling Program)*, 227–244.

Johnson, H. P., J. L. Karsten, J. R. Delaney, E. E. Davis, R. G. Currie, and R. L. Chase (1983), A detailed study of the Cobb offset of the Juan de Fuca Ridge: Evolution of a propagating rift, J. Geophys. Res., 88(B3), 2297–2315.

Karato, S. and K. Becker, (1983), Physical properties of sediments from the Galapagos region and their implications for hydrothermal convection, in J. Honnorez, R. P. Von Herzen et al. (eds.), *Init. Repts. DSDP, vol. 70, U.S. Govt. Printing Office*, Washington, 355–368.

Karson J. A., J. A. Collins and J. F. Casey, (1984), Geologic and seismic velocity structure of the crust/ mantle transition in the Bay of Islands ophiolite complex, *J. Geophys. Res.,* 89, 6126-6138.

Karsten L. J. and R. J., Delaney (1989), Hotspot-Ridge Crest Convergence in the Northeast Pacific, *J. Geophys. Res.,* 94, 700-712.

Klein, E., C. Langmuir, and H. Staudigel (1991), Geochemistry of Basalts From the Southeast Indian Ridge, 115°E–138°E, *J. Geophys. Res.,* 96(B2), 2089-2107.

Kleinrock, M. C., and R. N. Hey, (1989), Detailed Tectonics Near the Tip of the Galapagos 95.5°W Propagator: How the Lithosphere Tears and a Spreading Axis Develops, *J. Geophys. Res.*, 94, 13,801–13,838.

Koga K.T., P. B. Kelemen and N. Shimizu, (2001), Petrogenesis of the crust–mantle transition zone and the origin of lower crustal wehrlite in the Oman ophiolite, *Geochem. Geophys. Geosys.,* 2.

Kruse E. S., S. F. Tebbens, D. F. Naar, Q. Lou, and R. Bird, (2000), Comparisons of gravity anomalies at pseudofaults, fracture zones, and nontransform discontinuities from fast to slow spreading areas, *J. Geophys. Res.*, 105, 28399-28410.

Marescotti, P., D. A. Vanko and R. Cabella, (2000), From oxidizing to reducing alteration: mineralogical variations in pillow basalts from the east flank, Juan de Fuca Ridge. In Fisher, A.T., Davis, E.E., and Escutia, C. (Eds.), *Proc. ODP, Sci. Results, 168: College Station, TX (Ocean Drilling Program)*, 119–136.

Martinez F., D. F. Naar, T. B. Reed and R. N. Hey, (1991), Three-dimensional SeaMARC II, gravity and magnetics study of large offset rift propagation at the Pito Rift, Easter microplate, *Mar. Geophysical Res.,* 101, 13,715-13,730.

Nedimović M. R., S. M. Carbotte, A. J. Harding, R. S. Detrick, J. P. Canales, J. B. Diebold, G. M. Kent, M. Tischer and J. M. Babcock, (2005), Frozen magma lenses below the oceanic crust, *Nature*, 436,1149-1152.

Nedimović M. R., S. M. Carbotte, J. B. Diebold, A. J. Harding, J. P. Canales and G. M. Kent (2008), Upper crustal evolution across the Juan de Fuca ridge flanks, *Geochem. Geophys. Geosys.*, vol. 9.

Phipps Morgan J. and E. M. Parmentier (1985), Causes and rate-limiting mechanism of ridge propagation: A Fracture Mechanism Model, *J. Geophys. Res.* 90, 8603-8612.

Schilling J. G., R. H. Kingsley and J. D. Devine, (1982), Galapagos Hot-spot spreading center system: Spatial petrological and geochemical variations (83°W-101°W), *J. Geophys. Res.,* 87, 5593-5610.

Schouten H., H. J. B. Dick and K. D. Klitgord, (1987), Migration of mid-ocean-ridge volcanic segment, *Nature*, 326, 835-839.

Sempere J. C., (1991), High magnetization zones near spreading center discontinuities, *Earth Planet. Sci. Lett.*,107, 389-405.

Singh S. C., A. J. Harding, G. M. Kent, M. C. Sinha, V. Combier, S. Bazin, C. H. Tong, J. W. Pye, P. J. Barton, R. W. Hobbs, R. S. White and J. A. Orcutt, (2006), Seismic reflection images of the Moho underlying melt sills at the East Pacific Rise, *Nature*, 442, 287-290.

Sinton, J. M., D. S. Wilson, D. M. Christie, R. N. Hey and J. R. Delaney, (1983), Petrologic consequences of rift propagation on oceanic spreading ridges, *Earth Planet. Sci. Lett*, 62, 193-207.

Talwani M., L. J. Worzel, M. Landisman, (1959), Rapid gravity Computations for Two-Dimensional Bodies with Application to the Mendocino Submarine Fracture Zone, *J. Geophys. Res.*, 64, 49-59.

Tivey, M. A. and H. P. Johnson, (1990), The Magnetic Structure of Axial Seamount: Juan de Fuca. Ridge, *J. Geophys. Res.*, 95, 12735-12753.

Toomey, D. R. and E. E. E. Hooft, (2008), Mantle upwelling, magmatic differentiation, and the meaning of axial depth at fast-spreading ridges, *Geology*, 36, 679-682.

Turcotte, D. and J. Schubert (2002), Geodynamics, 2nd ed., *Cambridge Univ. Press*, New York.

Van Avendonk, H. J. A., A. J. Harding, J. A. Orcutt, and J. S. McClain (1998), A two-dimensional tomographic study of the Clipperton transform fault, *J. Geophys. Res.*, *103* (B8), 17,885–17,899.

West, B. P., J. Lin, and D. M. Christie, (1999), Forces driving ridge propagation, *J. Geophys. Res.*, 104, 22,845–22,858.

West M., W. Menke and M. Tolstoy, (2001), Focused magma supply at the intersection of the Cobb hotspot and the Juan de Fuca ridge, *Geophys. Res. Lett*., 30 (14), 1724.

Wilson, D. S., R. N. Hey and C. Nishimura (1984), Propagation as a Mechanism of Reorientation of the Juan de Fuca Ridge, *J. Geophys. Res.*, *89*, 9215–9225.

Wilson D. S., (1992), Focused mantle upwelling beneath mid-ocean ridges: evidence from seamount formation and isostatic compensation of topography, *Earth Planet. Sci. Lett.,* 113, 41-55.

Wilson D. S., (1993), Confidence intervals for motion and deformation of the Juan de Fuca plate, *J. Geophys. Res,* 98, 16053-16071.

Won, I. J., and Bevis, M., (1987), Computing the gravitational and magnetic anomalies due to a polygon: Algorithms and Fortran subroutines, *Geophysics*, 52, 232-238.

Table 1. Gravity anomaly values at the ridge axis calculated from each model along all 3 transects. Grey shaded columns indicate % of MBA accounted for by each residual anomaly (calculated as (RA-MBA)/MBA).

Table 1

Segment	MBA [mGal]	RA1 [mGal]	% MBA	RA2 [mGal]	% MBA	RA3 [mGal]	% MBA
Cleft	-28	-21	25	-17	39	-14	50
NSymm	-21	-20	5	-13	38	-8	62
Endeavour	-25	-20	20	-13	48	-6	76

Figure 1. Bathymetry map of the study area with magnetic isochrons superimposed (numbered thin purple lines and light purple shading). Pseudofaults left by former propagating ridge segments are identified from breaks in magnetic isochrones (corresponding age shown on the bottom scale) and are marked by gray shading (modified from *Wilson* [1993]). Numbering of pseudofaults is after *Karsten and Delaney* [1989], where OP2, OP3 and OP4 are Outer Pseudofaults 2, 3 and 4 respectively, and IP3, IP4 and IP6 refer to Inner Pseudofaults 3, 4 and 6, respectively and P4T is Propagator 4 Termination at its northern limit. White lines perpendicular to the ridge axis and black lines along the ridge axis show locations of seismic and gravity data profiles used in this study.

Figure 2. Schematic model of ridge propagation. Tectonic elements of the system are labeled. Normal lithosphere created at doomed spreading axis is shaded light blue, lithosphere created at the propagating ridge is shaded light violet, and transferred lithosphere is shown in dark violet. Dark purple lines show regularly spaced hypothetical isochrones. V-shaped wake boundaries are delimited with black lines. Propagating ridge segment and dying ridge segment spreading at the full spreading rate are represented by red and orange thick lines, respectively. Active axis with transitional spreading rates and fossil axis are shown in dashed line. After *Hey et al.* [1980], *Kleinrock and Hey* [1989].

Figure 3A. Interpretation of crustal layers from multi-channel seismic (MCS) data for A) Endeavour, B) Northern Symmetric, and C) Cleft transects. Interpreted interfaces include: top of sediments (brown), top of oceanic crust (blue), seismic layer 2a/2b boundary (red), and Moho (green). Gray areas indicate location of pseudofaults defined from bathymetry; the nomenclature

for the pseudofaults as in Figure 1. Yellow shaded regions at the Endeavour and Cleft transects mark the extent of the axis-centered plateaus from *Carbotte et al.,* [2008]. Crustal ages in Ma from *Wilson* [1993] are indicated along each profile at the bottom with labeled black dots. Horizontal-axis is given as distance from the ridge axis in kilometers (bottom) and common mid point (CMPs) number (top) along each transect.

Figure 3B. Thickness of the crust (calculated from top of the oceanic crust to Moho) for A) Endeavour, B) Northern Symmetric and C) Cleft. The thickness is given as two-way travel time [ms] in red (vertical scale on the left) and as thickness [m] (depth converted twtt) in black; depth conversion uses layer 2a thickness from *Nedimović et al.,* [2008] and constant velocity of 6.67 km/s [*Christeson et al.,* 2010, personal communication]. Horizontal axis and shaded rectangles the same as on Figure 3A.

Figure 4. Histograms of crossover errors for A) observed Free-Air gravity Anomaly; standard deviation for 213 track crossings is σ=1 mGal; and B) depth to the sea floor; standard deviation for 213 track crossings is σ=19 m.

Figure 5. Top of oceanic crust and Free-Air gravity Anomaly (FAA) along the A) Endeavour (green), B) Northern Symmetric (red) and C) Cleft (black) transect (the same color code for transects is used in all subsequent figures). Gray shaded rectangles show locations of pseudofaults.

Figure 6. A) Free-air gravity anomaly (FAA) for 50 km sections of each transect centered at the outer pseudofaults. B) Free-air gravity anomaly (FAA) for 70 km sections of each transect centered at the inner pseudofaults. A wider region is shown for the inner pseudofaults due to much wider IP3 pseudofault zone. Thick vertical black line at 0 km marks the pseudofault centers (except for IP3 for which the zero distance is the mid point between the western boundary of the pseudofault and the eastern boundary of the rotated block within the propagator wake); the boundaries of each pseudofault estimated from the bathymetry (see text) are indicated with gray circles. All profile crossings are plotted with younger crust side to the left.

Figure 7. Density distribution for layer 2a along A) Endeavour, B) Northern Symmetric and C) Cleft transects calculated using porosity-velocity and porosity-density relationships of *Carlson and Herrick* [1990] and seismic velocities for layer 2a from *Nedimović et al.* [2008]. The black and red lines for all three transects correspond with upper and lower bound estimates respectively; upper bound estimates are chosen here for gravity modeling (see text). For modeling purposes, the resulting variable density function is approximated as a series of constant density blocks shown with color bar at the bottom of each panel. Gray shaded region shows location of pseudofaults.

Figure 8. A) Mantle Bouguer Anomaly (MBA) for all three transects calculated by subtracting gravity response of the starting model of constant crustal thickness and density (except layer 2a as given in Figure 7) from observed Free-Air Anomaly (FAA). The width of the axial MBA low (indicated with colored dots) is defined qualitatively as the distance between inflection points in long-wavelength (>20 km) anomaly from high-to-lower gradient. Colored arrows show locations

of pseudofaults. Arrows correspond with the center of each pseudofault, except for IP3 for which we show its extent. B) Residual Anomaly 1 (RA1) calculated by subtracting gravity response from model with same density distribution as A) but with seismically inferred crustal thickness (model 1), from the FAA. Arrows and colored dots are as described in Figure 8A.

Figure 9. A) Variable density model assuming half plate thermal cooling (model 2). In this example, calculated isotherms are shown for the Endeavour transect, with the corresponding density distribution estimated from $d\rho=-\rho_0\alpha_v dT$ as indicated with the color-coded polygons. Variable densities are confined to crust with constant density mantle below (ρ_m=3.3 g/cm^3). Depth to sediment-water interface (yellow line), top of oceanic crust (green line), and layer 2a/2b boundary (red line), are from seismic data (see text). Depth to crust/mantle boundary (black line) is calculated assuming constant thickness crust of 6.5 km. Gray shading shows location of pseudofault crossing P4T. Model accounts for thermal effects of sediments, which blanket the eastern flank of the ridge (hereafter referred to as asymmetric thermal model). B) Residual Anomaly 2 (RA2) calculated from model 2 shown in part (A).

Figure 10. A) Asymmetric thermal model with variable densities due to half plate cooling (defined as for Figure 9A) for both crust and upper mantle (model 3). Density distribution is indicated by color-coded polygons (upper mantle shown with shaded pattern polygons). B) Residual Anomaly 3 (RA3) calculated by subtracting gravity signal of model 3 from the FAA.

Figure 11. Gravity models for inner pseudofaults crossed along the Northern Symmetric (IP6 and IP4) and Cleft transects (IP3). For each pseudofault crossing we show, from top to bottom: A)

Top of oceanic crust with location of the pseudofaults defined from topographic troughs and zone of offset magnetic anomalies in grey shading; B) Thickness of the layer 2b/3 inferred from Moho twtt and constant velocity v=6.67 km/s [*Christeson et al.,* 2010, personal communication]; C) Gravity model results with Mantle Bouguer Anomalies (MBA) from Figure 8A in green line, Residual Anomaly (RA1) from Figure 8B in black line and the residual anomaly shown in blue line obtained from the best fit model (part D) subtracted from observed FAA; D) Best fit model assuming seismically inferred crustal thickness. Density distribution as follows: for layer 2A from Figure 7, water column ρ_w=1.03 g/cm^3 (light blue), sediments (brown) ρ_s=1.9g/cm^3, upper mantle (green) ρ_m=3.3 g/cm^3, final best fit density distribution for mid-to-lower crust shown with numbered polygons. Crustal ages from magnetic isochrons are shown in Ma and indicated with black dots. Double sided arrows at bottom of figure indicate younger and older crust side of the pseudofaults.

Figure 12. Gravity models for outer pseudofaults crossed along Northern Symmetric (OP4) and Cleft (OP3) transects and the pseudofault termination crossed along the Endeavour transect (P4T). Locations of ODP drill hole sites along the Endeavour profile are indicated (numbered dots); drill holes where FeTi enriched basalts are sampled are indicated in red. Location of sub-Moho reflections in seismic sections interpreted as frozen sills [*Nedimović et al.*, 2005] are indicated with rectangles at the base of the crust (high amplitude reflections in red, weak reflections in orange); vertical size of rectanglesnot to scale. All other annotations as in Figure 11.

Figure 13. Comparison of along-axis data with earlier study of *Hooft and Detrick* [1995]. A)

Along axis bathymetry data from our study in green and from *Hooft and Detrick* [1995] in blue. Horizontal axis is distance in kilometers calculated from origin at 44°35.688'N and 130° 23.6639'W. B) Free-Air Anomaly (FAA) from *Hooft and Detrick* [1995] in blue. FAA obtained from our study using the Potsdam International Gravity Formula (IGF) from 1980 in green and recalculated using the 1967 IGF shown in red (see text). C) Mantle Bouguer Anomaly (MBA) obtained by subtracting calculated gravity for constant thickness and density crust (see text) from the FAA. MBA from *Hooft and Detrick* in blue, from our study in green, and from our study recalculated using 1967 IGF in red. Cross symbols ("X") show seafloor depth (A) and FAA anomaly (B) recorded at the three cross-axis lines.

Figure 14. Schematic illustration along the axis of a propagating ridge summarizing results from our gravity and seismic data analysis. Higher density crust is found within the propagating ridge tip region and is attributed to presence of FeTi enriched crustal rocks. High extents of fractionation to form FeTi enriched magmas may occur within magma lenses located within the crust (1) and/or beneath the crust (2) with lateral delivery of magma to the propagating ridge tip.

Chapter 4: Figures

Figure 1

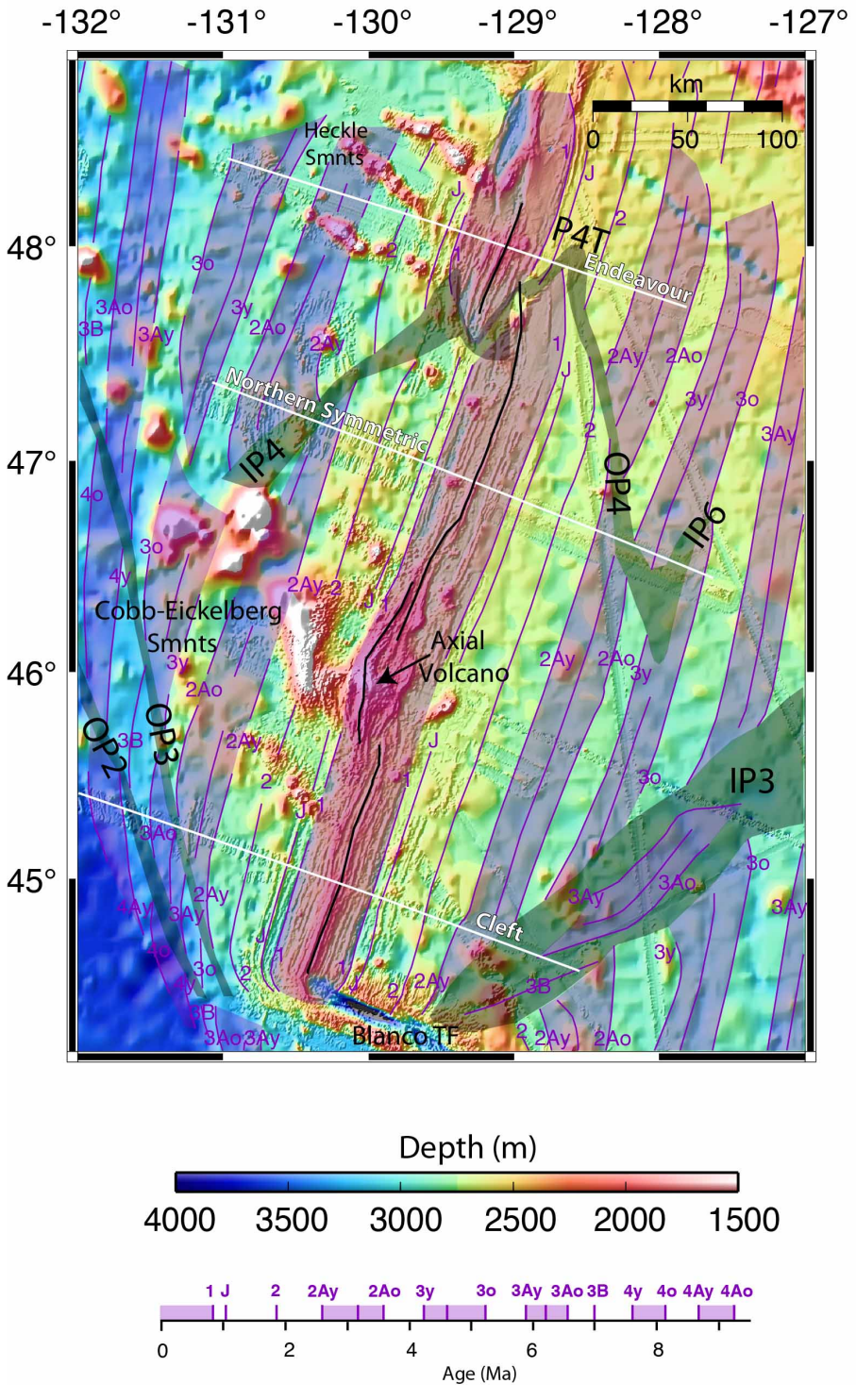
-132°
-131°
-130°
-129°
-128°
-127°
48°
47°
46°
45°
km
0
50
100
Heckle
Smnts
P4T
Endeavour
Northern Symmetric
IP4
OP4
IP6
OP2
OP3
IP3
Cobb-Eickelberg
Smnts
Axial
Volcano
Cleft
Blanco TF
Depth (m)
4000
3500
3000
2500
2000
1500
1 J 2 2Ay 2Ao 3y 3o 3Ay 3Ao 3B 4y 4o 4Ay 4Ao
0
2
4
6
8
Age (Ma)

Figure 2

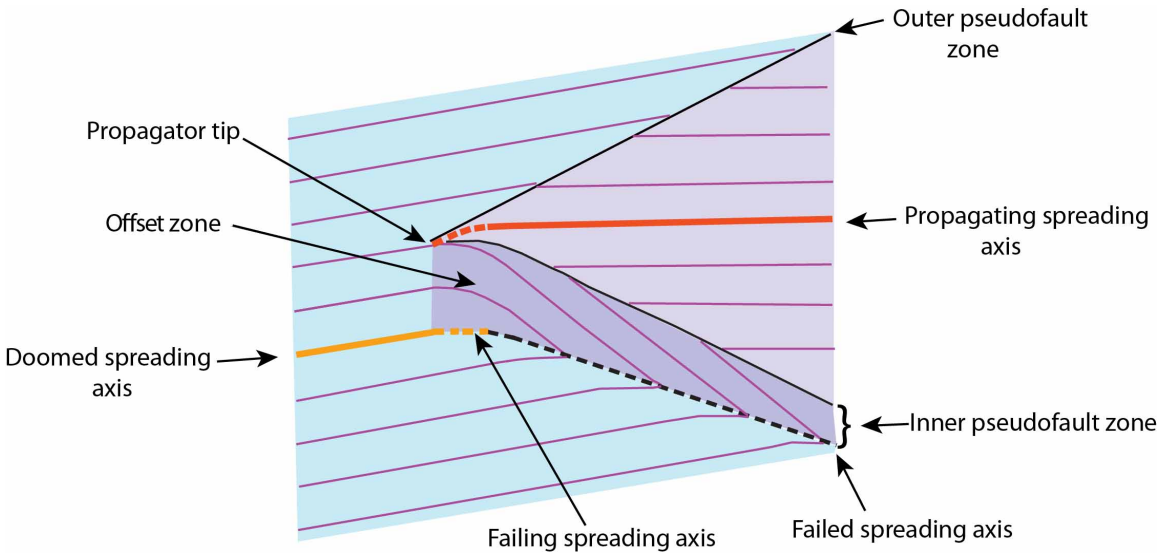
Outer pseudofault zone
Propagator tip
Offset zone
Propagating spreading axis
Doomed spreading axis
Inner pseudofault zone
Failing spreading axis
Failed spreading axis

Figure 3A

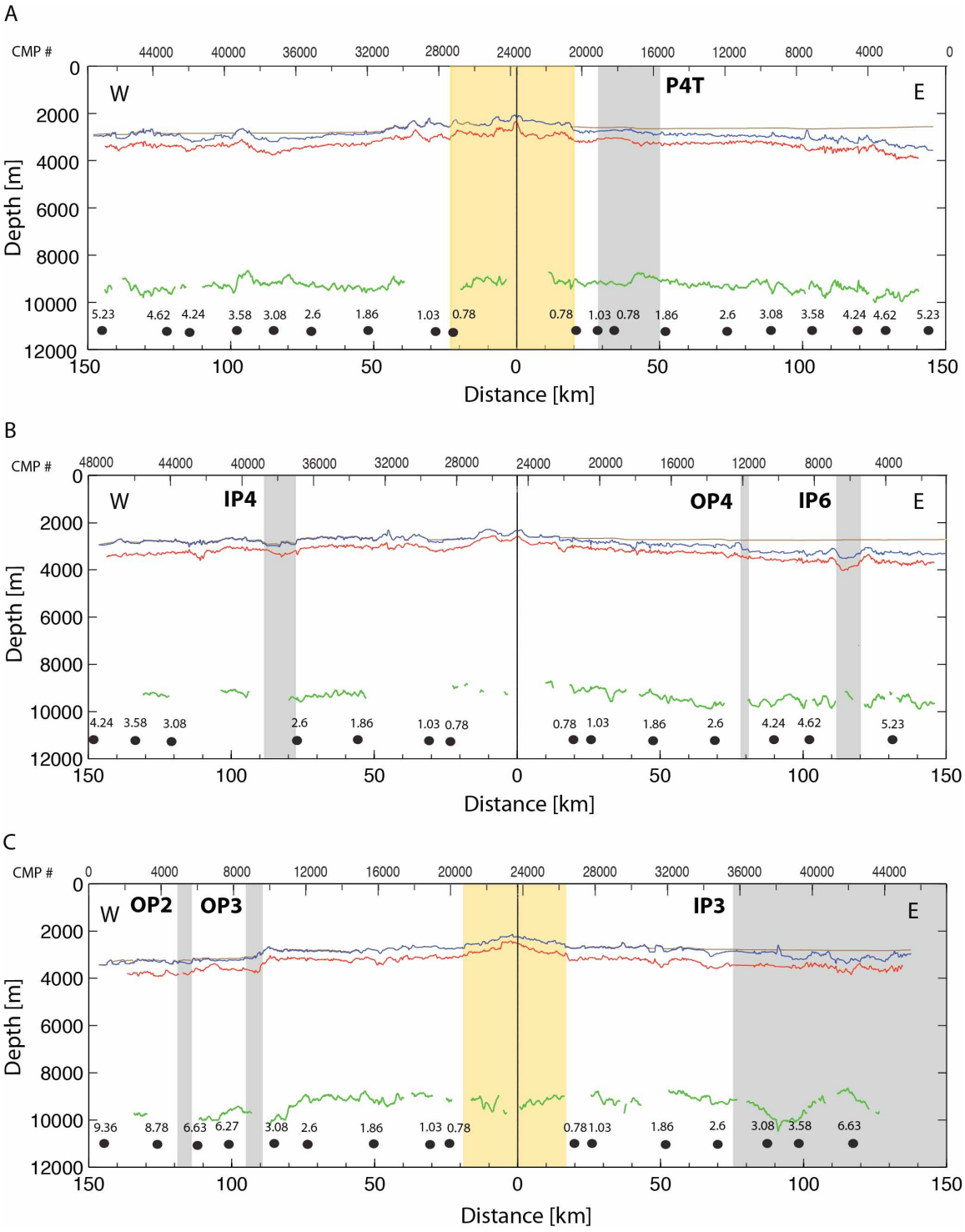
A
CMP #
44000 40000 36000 32000 28000 24000 20000 16000 12000 8000 4000 0
W
P4T
E
Depth [m]
0 2000 4000 6000 8000 10000 12000
5.23 4.62 4.24 3.58 3.08 2.6 1.86 1.03 0.78 0.78 1.03 0.78 1.86 2.6 3.08 3.58 4.24 4.62 5.23
150 100 50 0 50 100 150
Distance [km]
B
CMP #
48000 44000 40000 36000 32000 28000 24000 20000 16000 12000 8000 4000
W
IP4
OP4
IP6
E
Depth [m]
0 2000 4000 6000 8000 10000 12000
4.24 3.58 3.08 2.6 1.86 1.03 0.78 0.78 1.03 1.86 2.6 4.24 4.62 5.23
150 100 50 0 50 100 150
Distance [km]
C
CMP #
0 4000 8000 12000 16000 20000 24000 28000 32000 36000 40000 44000
W
OP2
OP3
IP3
E
Depth [m]
0 2000 4000 6000 8000 10000 12000
9.36 8.78 6.63 6.27 3.08 2.6 1.86 1.03 0.78 0.78 1.03 1.86 2.6 3.08 3.58 6.63
150 100 50 0 50 100 150
Distance [km]

Figure 3B

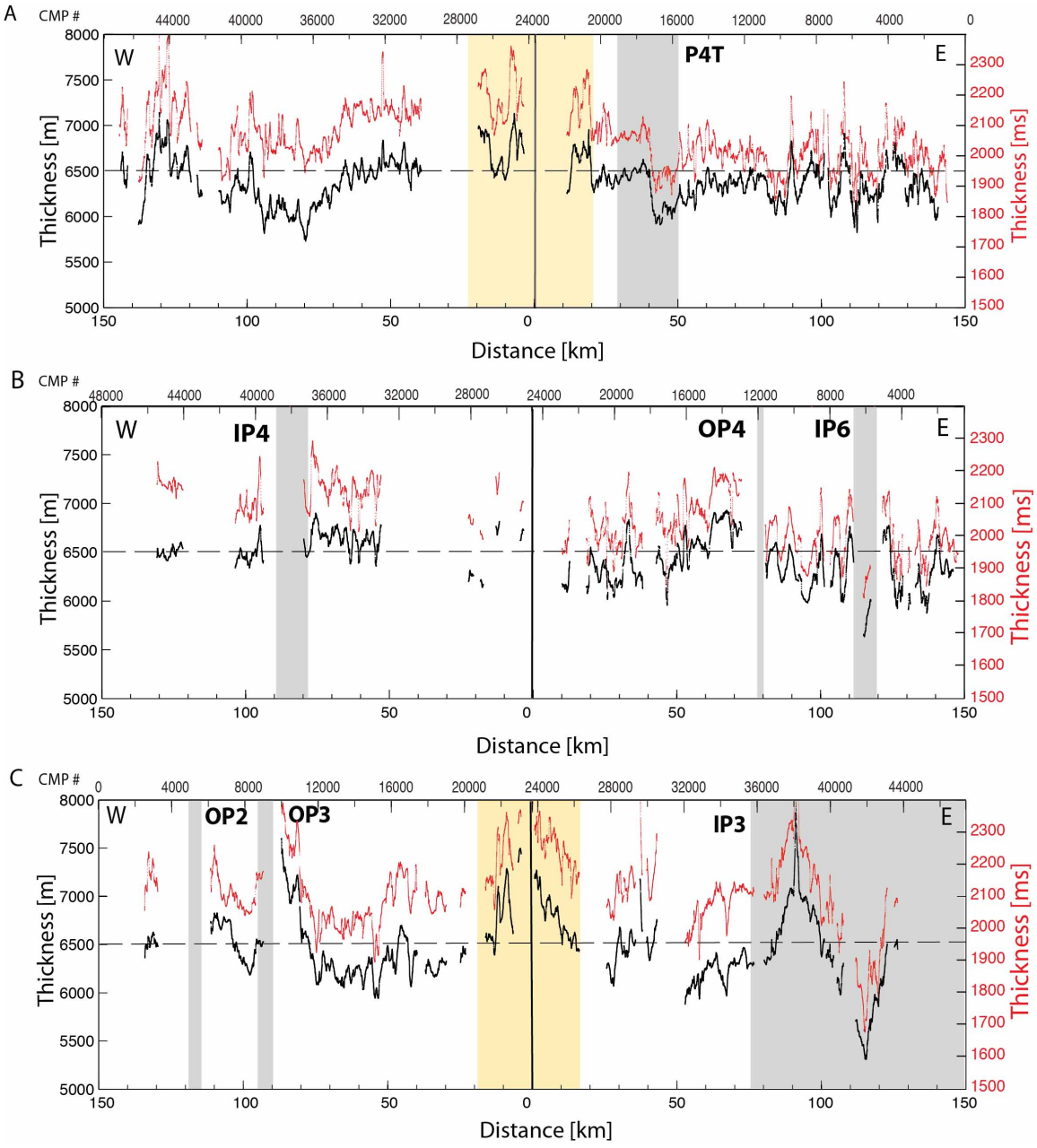
A
CMP #
W
P4T
E
Thickness [m]
Thickness [ms]
Distance [km]
B
CMP #
W
IP4
OP4
IP6
E
Thickness [m]
Thickness [ms]
Distance [km]
C
CMP #
W
OP2
OP3
IP3
E
Thickness [m]
Thickness [ms]
Distance [km]

Figure 4

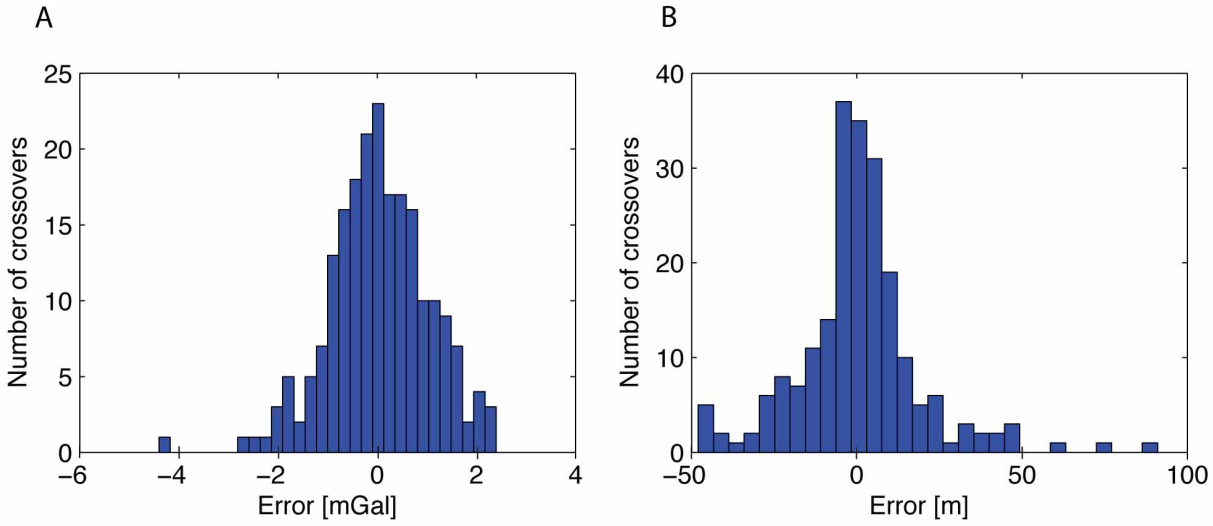
A
Number of crossovers
Error [mGal]
B
Number of crossovers
Error [m]

Figure 5

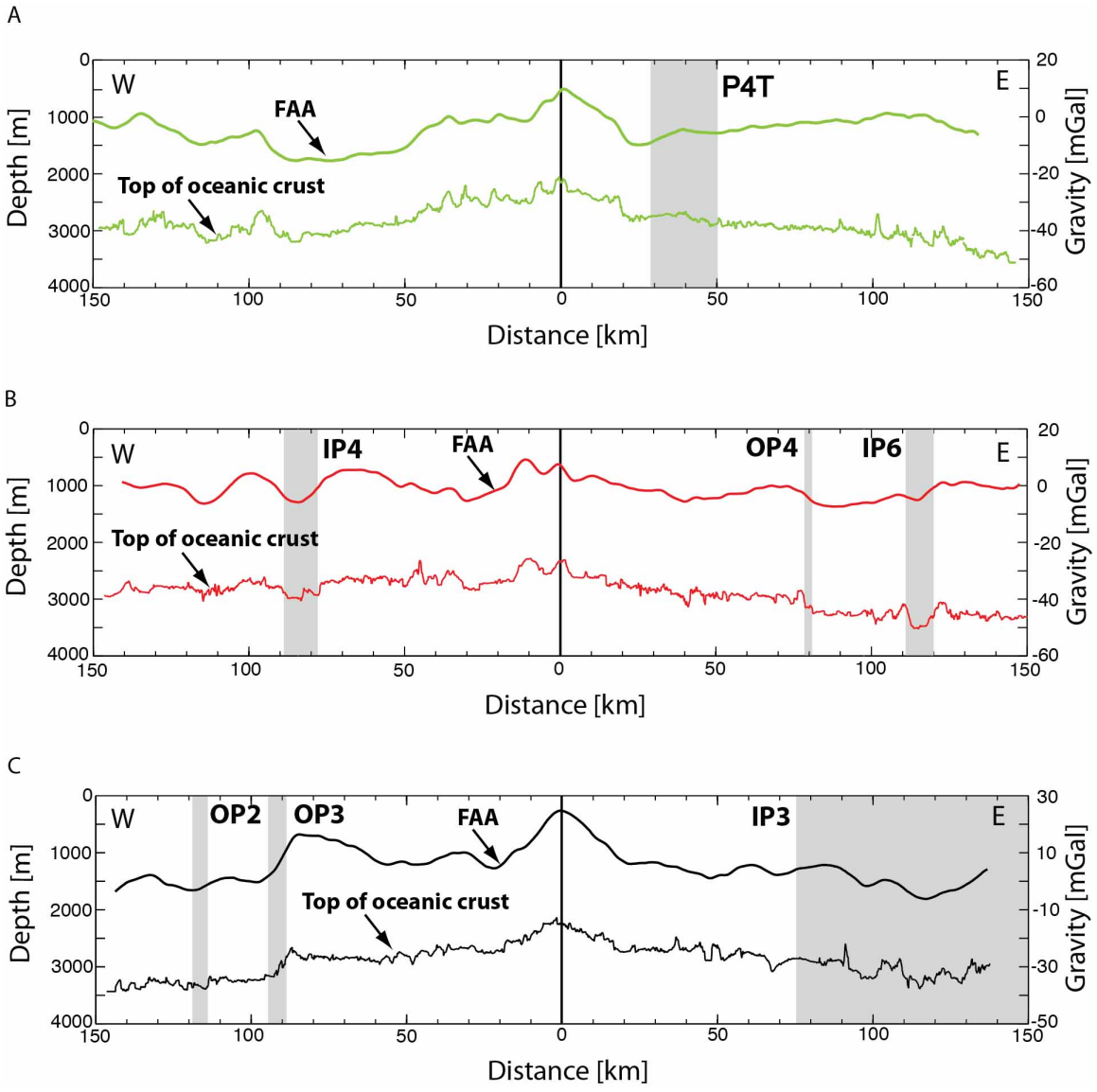
A
W
E
FAA
P4T
Top of oceanic crust
Depth [m]
Gravity [mGal]
Distance [km]
B
W
E
IP4
FAA
OP4
IP6
Top of oceanic crust
Depth [m]
Gravity [mGal]
Distance [km]
C
W
E
OP2
OP3
FAA
IP3
Top of oceanic crust
Depth [m]
Gravity [mGal]
Distance [km]

Figure 6

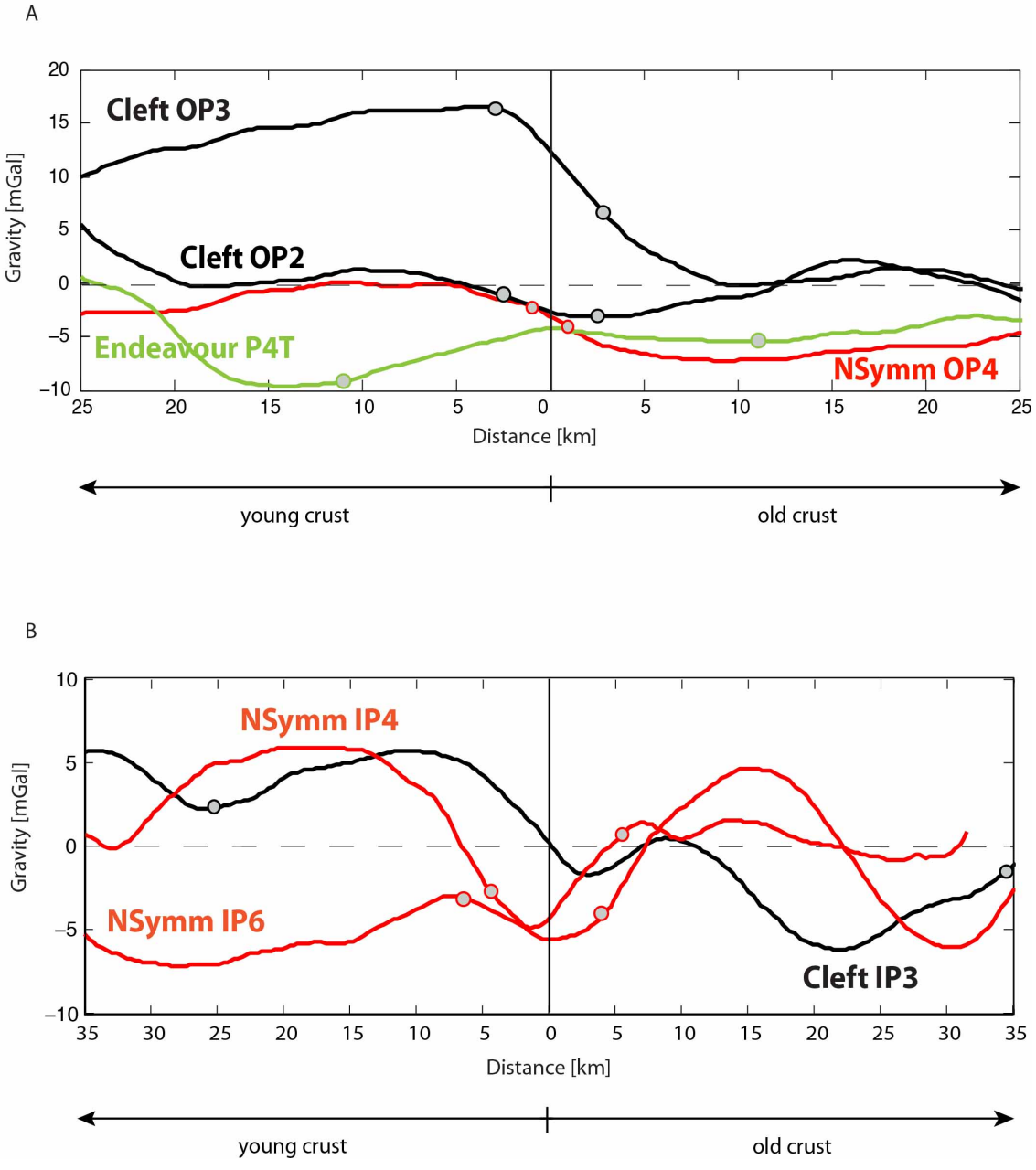
A
Cleft OP3
Cleft OP2
Endeavour P4T
NSymm OP4
Gravity [mGal]
Distance [km]
young crust
old crust
B
NSymm IP4
NSymm IP6
Cleft IP3
Gravity [mGal]
Distance [km]
young crust
old crust

Figure 7

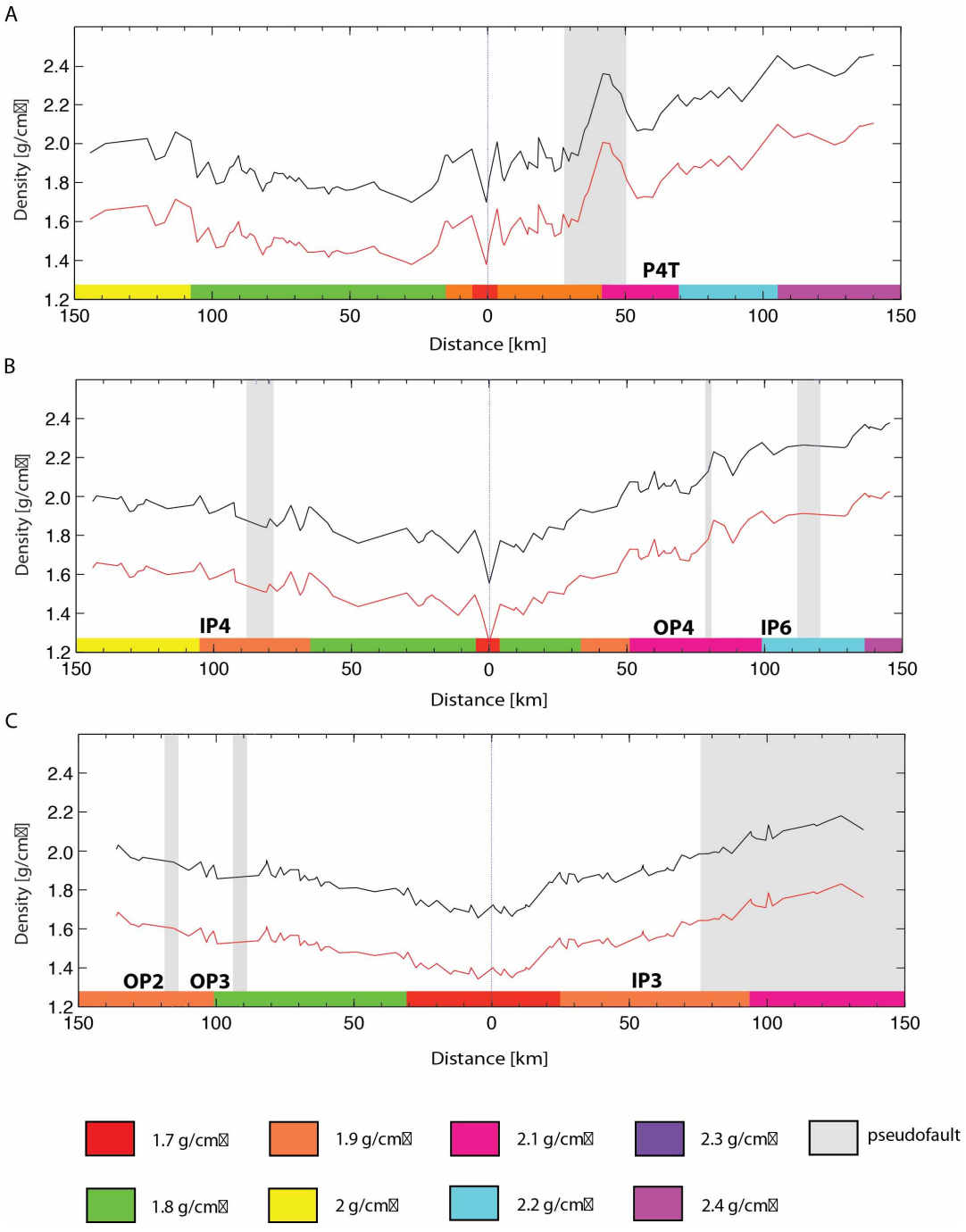
A
Density [g/cm⁻³]
2.4
2.2
2.0
1.8
1.6
1.4
1.2
P4T
150
100
50
0
50
100
150
Distance [km]
B
Density [g/cm⁻³]
IP4
OP4
IP6
Distance [km]
C
Density [g/cm⁻³]
OP2
OP3
IP3
Distance [km]
1.7 g/cm⁻³
1.9 g/cm⁻³
2.1 g/cm⁻³
2.3 g/cm⁻³
pseudofault
1.8 g/cm⁻³
2 g/cm⁻³
2.2 g/cm⁻³
2.4 g/cm⁻³

Figure 8

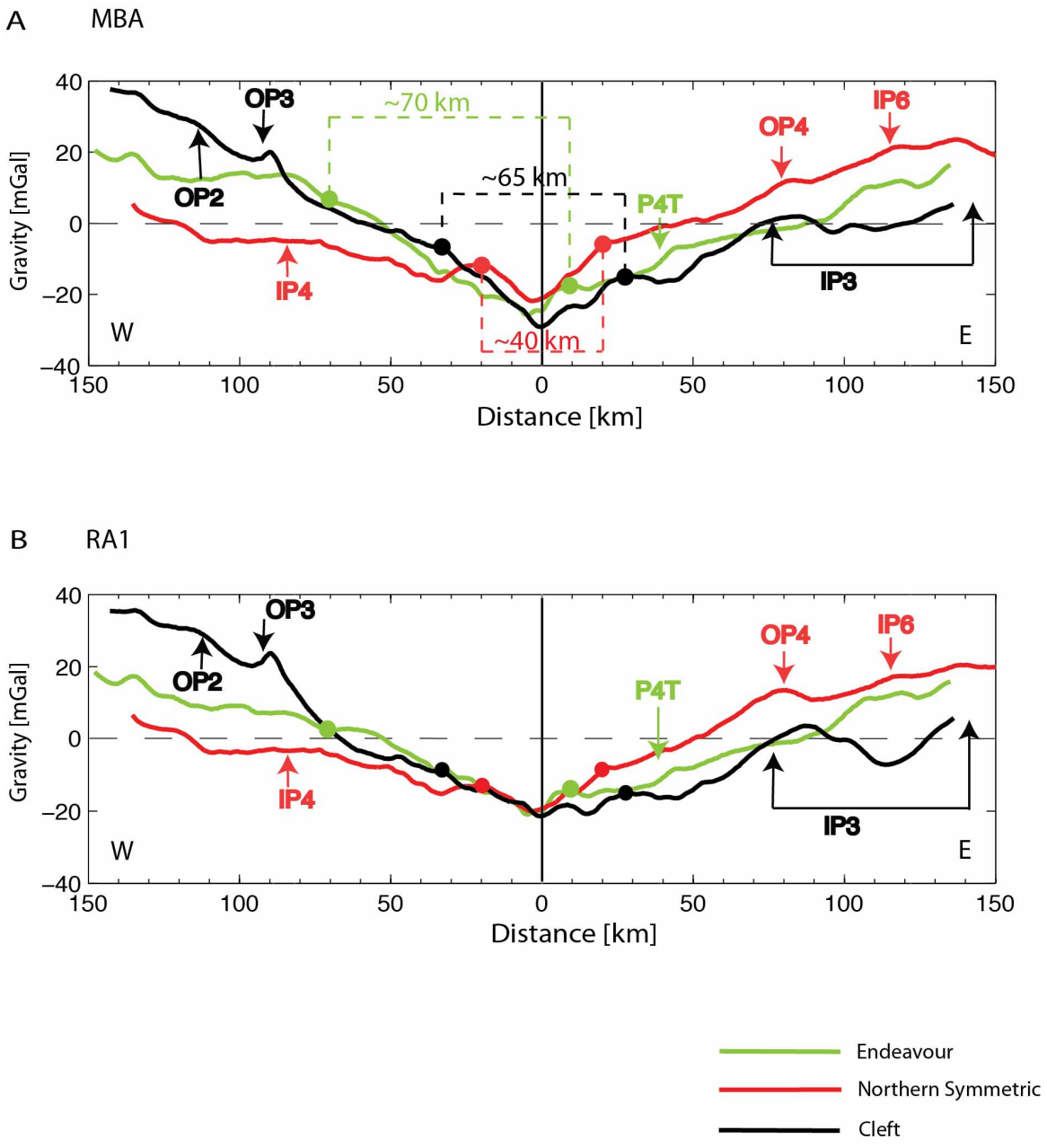
A
MBA
OP3
~70 km
OP4
IP6
OP2
~65 km
P4T
IP4
IP3
~40 km
W
E
Gravity [mGal]
Distance [km]
B
RA1
OP3
OP4
IP6
OP2
P4T
IP4
IP3
W
E
Gravity [mGal]
Distance [km]
Endeavour
Northern Symmetric
Cleft

Figure 9

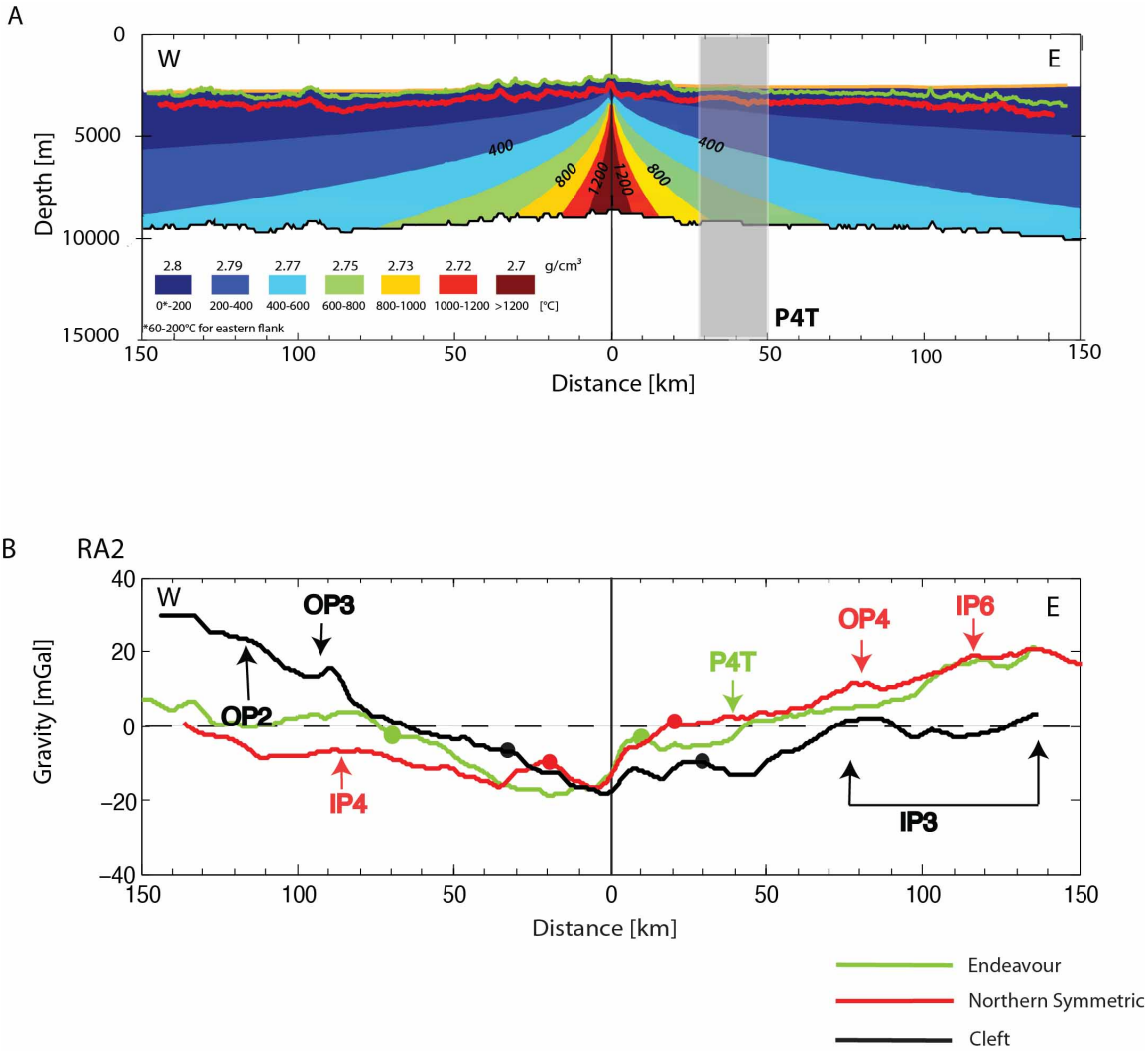
A
W
E
Depth [m]
0
5000
10000
15000
400
800
1200
1200
800
400
2.8
2.79
2.77
2.75
2.73
2.72
2.7
g/cm³
0°-200
200-400
400-600
600-800
800-1000
1000-1200
>1200
[°C]
*60-200°C for eastern flank
P4T
150
100
50
0
50
100
150
Distance [km]
B
RA2
Gravity [mGal]
40
20
0
–20
–40
W
OP3
OP2
IP4
P4T
OP4
IP6
E
IP3
150
100
50
0
50
100
150
Distance [km]
Endeavour
Northern Symmetric
Cleft

Figure 10

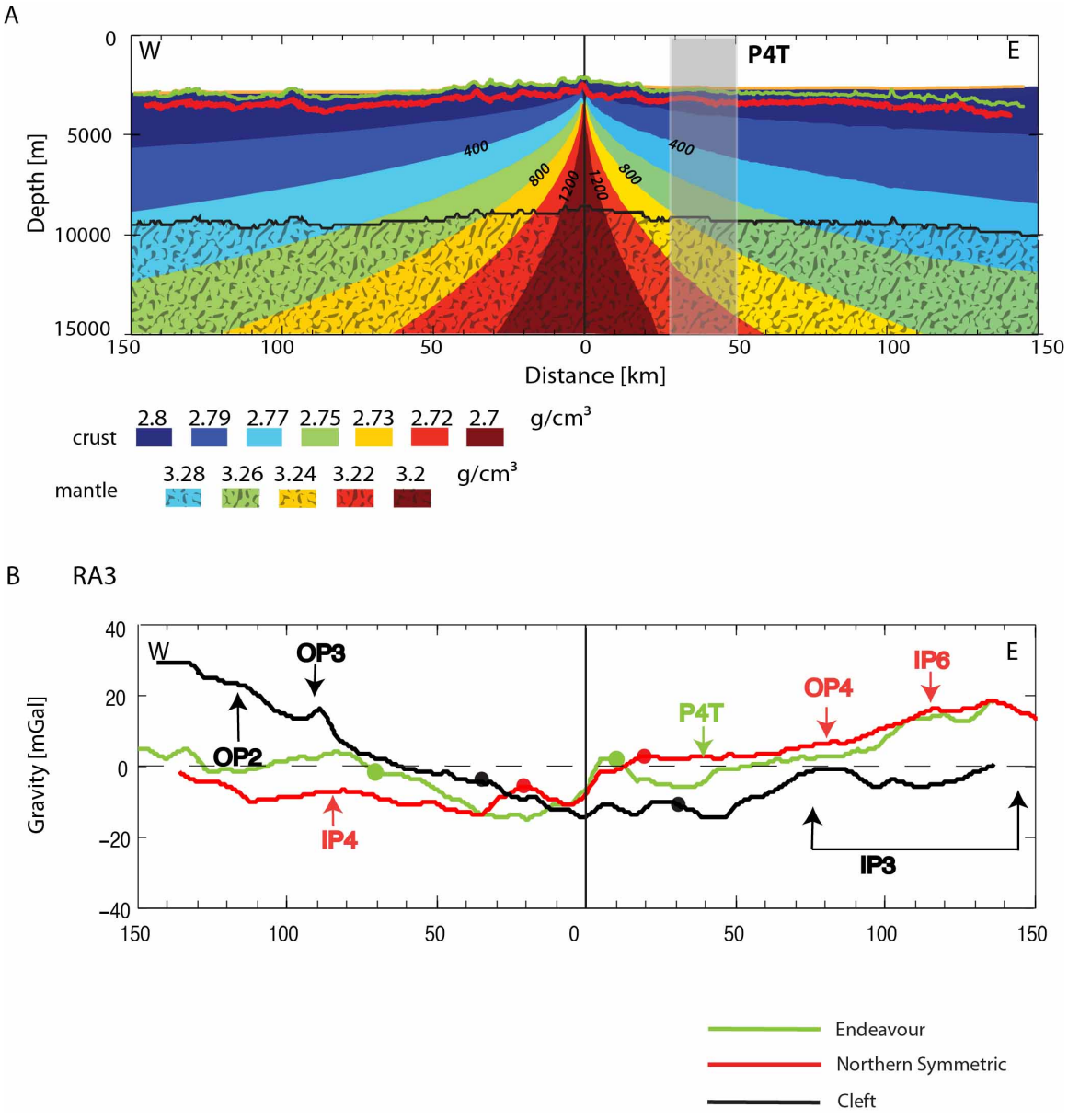
A
W
P4T
E
Depth [m]
0
5000
10000
15000
400
800
1200
1200
800
400
150
100
50
0
50
100
150
Distance [km]
crust
2.8
2.79
2.77
2.75
2.73
2.72
2.7
g/cm³
mantle
3.28
3.26
3.24
3.22
3.2
g/cm³
B
RA3
Gravity [mGal]
40
20
0
−20
−40
W
E
OP3
OP2
IP4
P4T
OP4
IP6
IP3
Endeavour
Northern Symmetric
Cleft

Figure 11

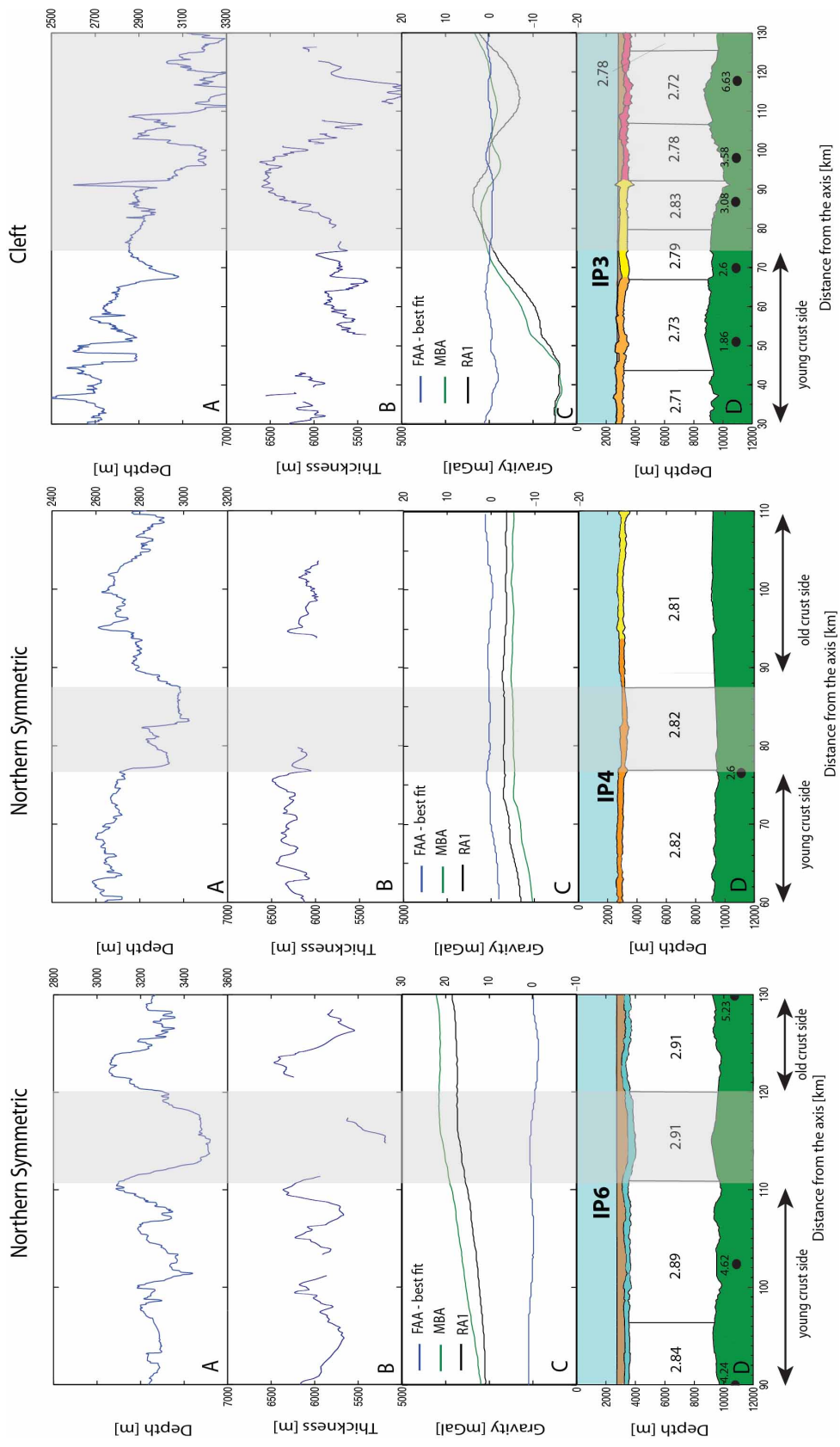
Northern Symmetric
Northern Symmetric
Cleft
Depth [m]
Thickness [m]
Gravity [mGal]
FAA - best fit
MBA
RA1
A
B
C
D
IP6
IP4
IP3
2.84
2.89
2.91
2.82
2.81
2.71
2.73
2.79
2.83
2.78
2.72
young crust side
old crust side
Distance from the axis [km]

Figure 12

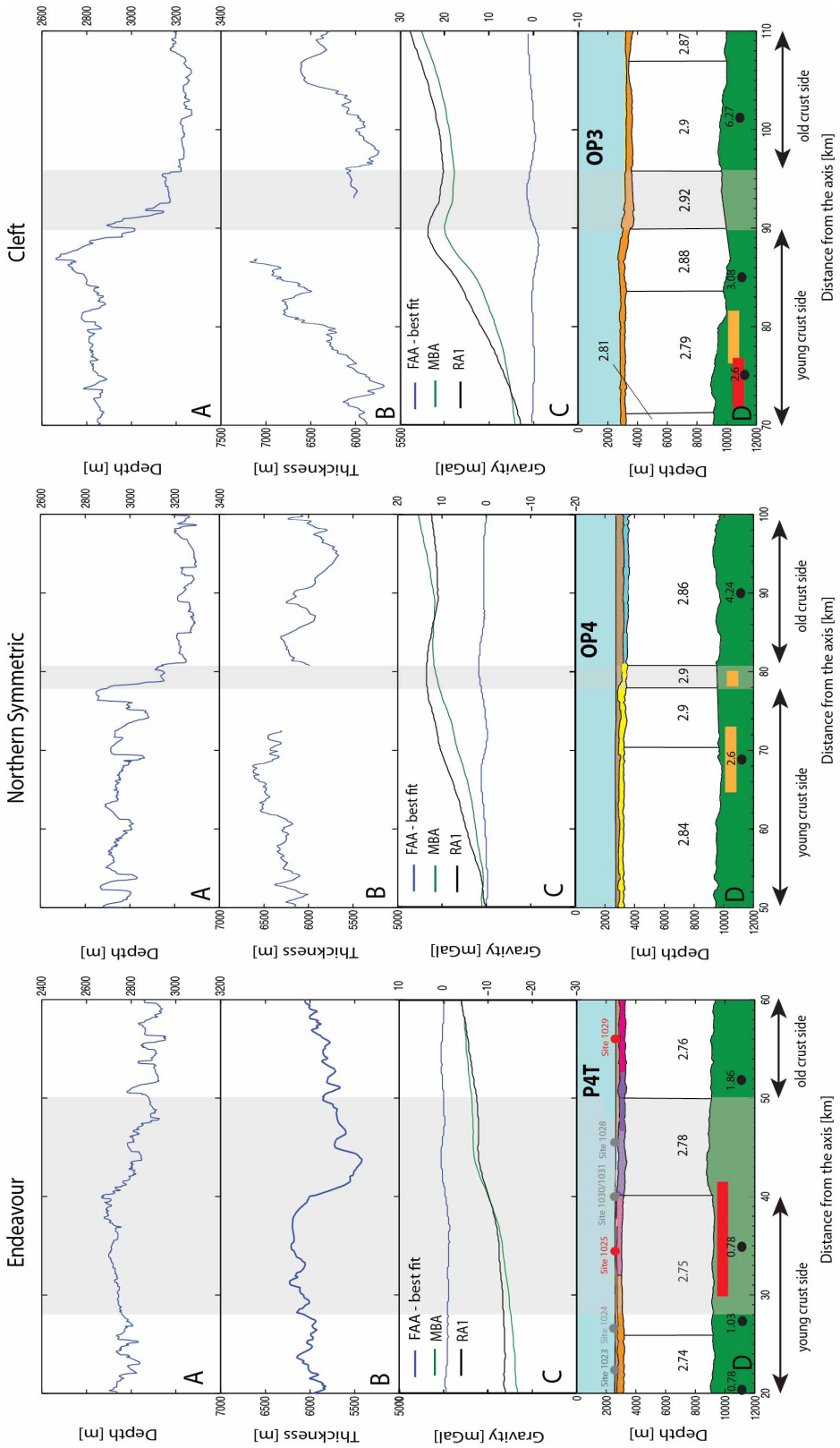
Endeavour
Northern Symmetric
Cleft
Depth [m]
Thickness [m]
Gravity [mGal]
FAA - best fit
MBA
RA1
A
B
C
D
P4T
OP4
OP3
Site 1023
Site 1024
Site 1025
Site 1030/1031
Site 1028
Site 1029
young crust side
old crust side
Distance from the axis [km]

Figure 13

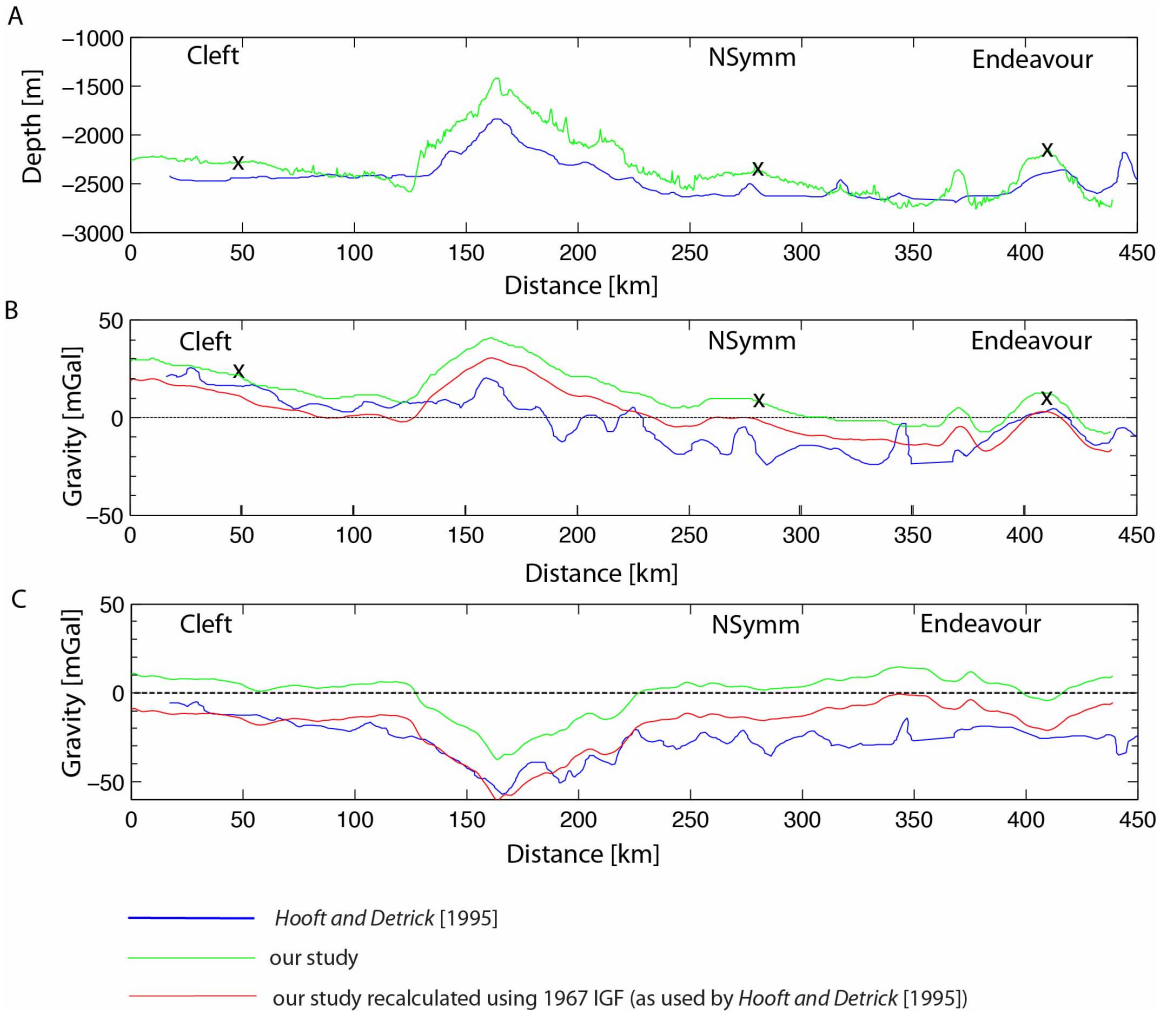
A
Depth [m]
−1000
−1500
−2000
−2500
−3000
Cleft
NSymm
Endeavour
0
50
100
150
200
250
300
350
400
450
Distance [km]
B
Gravity [mGal]
50
0
−50
Cleft
NSymm
Endeavour
Distance [km]
C
Gravity [mGal]
50
0
−50
Cleft
NSymm
Endeavour
Distance [km]
Hooft and Detrick [1995]
our study
our study recalculated using 1967 IGF (as used by Hooft and Detrick [1995])

Figure 14

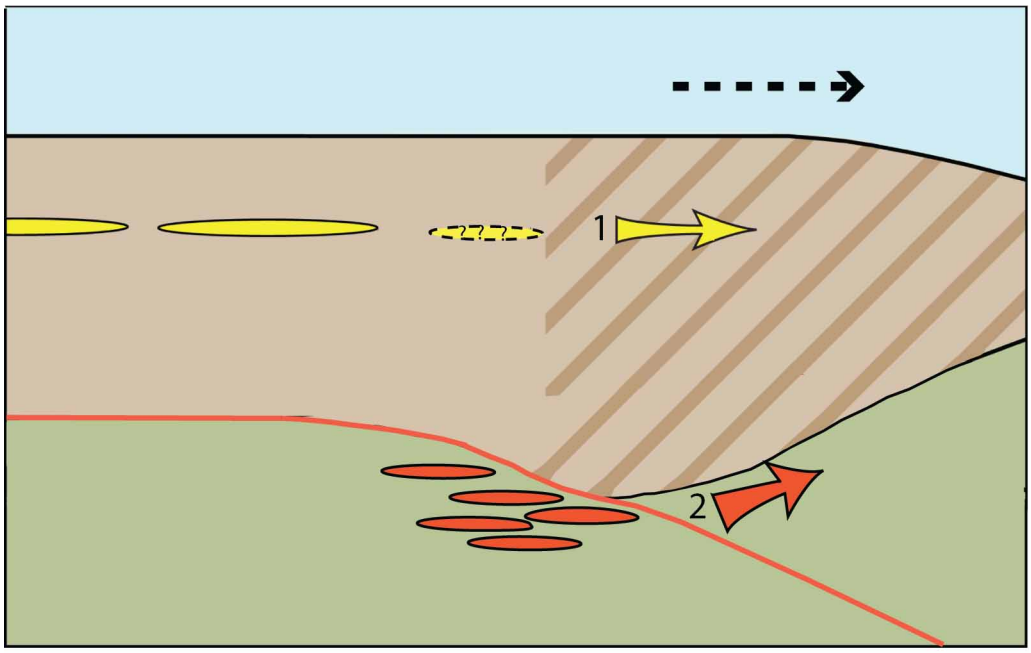

Legend:

- water column
- oceanic crust
- higher density crust
- upper mantle
- reservoir of magma at Moho level
- axial magma chamber within the crust
- boundary of the lithosphere at ridge axis